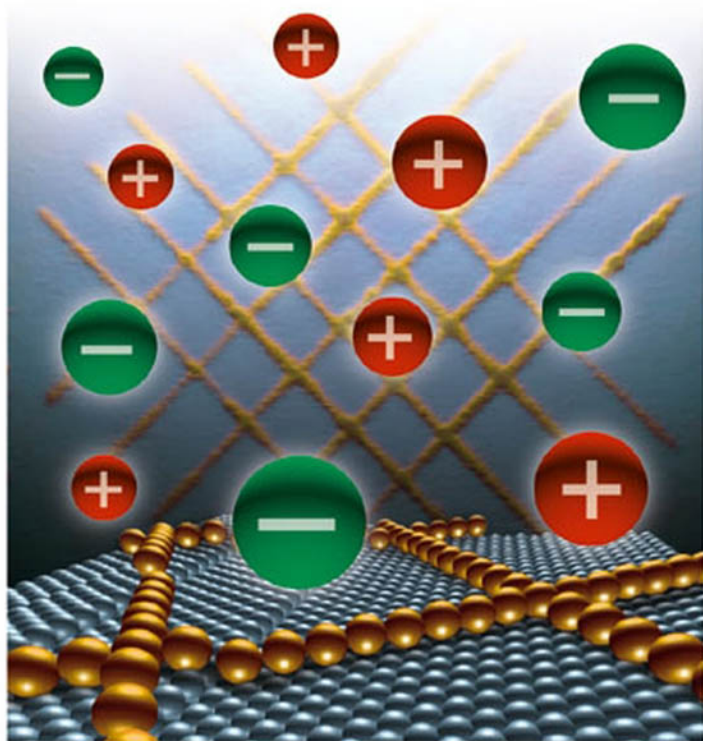


Edited by Georgi Staikov

 WILEY-VCH

Electrocrystallization in Nanotechnology



**Electrocrystallization in
Nanotechnology**

*Edited by
Georgi Staikov*

1807–2007 Knowledge for Generations

Each generation has its unique needs and aspirations. When Charles Wiley first opened his small printing shop in lower Manhattan in 1807, it was a generation of boundless potential searching for an identity. And we were there, helping to define a new American literary tradition. Over half a century later, in the midst of the Second Industrial Revolution, it was a generation focused on building the future. Once again, we were there, supplying the critical scientific, technical, and engineering knowledge that helped frame the world. Throughout the 20th Century, and into the new millennium, nations began to reach out beyond their own borders and a new international community was born. Wiley was there, expanding its operations around the world to enable a global exchange of ideas, opinions, and know-how.

For 200 years, Wiley has been an integral part of each generation's journey, enabling the flow of information and understanding necessary to meet their needs and fulfill their aspirations. Today, bold new technologies are changing the way we live and learn. Wiley will be there, providing you the must-have knowledge you need to imagine new worlds, new possibilities, and new opportunities.

Generations come and go, but you can always count on Wiley to provide you the knowledge you need, when and where you need it!



William J. Pesce
President and Chief Executive Officer



Peter Booth Wiley
Chairman of the Board

Electrocrystallization in Nanotechnology

Edited by Georgi Staikov



WILEY-VCH Verlag GmbH & Co. KGaA

The Editor

Dr. Georgi Staikov
Research Centre Jülich
Institute of Bio- and Nanosystems (IBN 3)
52425 Jülich
Germany

■ All books published by Wiley-VCH are carefully produced. Nevertheless, authors, editors, and publisher do not warrant the information contained in these books, including this book, to be free of errors. Readers are advised to keep in mind that statements, data, illustrations, procedural details or other items may inadvertently be inaccurate.

Library of Congress Card No.: applied for **British Library Cataloguing-in-Publication Data**

A catalogue record for this book is available from the British Library.

Bibliographic information published by the Deutsche Nationalbibliothek

The Deutsche Nationalbibliothek lists this publication in the Deutsche Nationalbibliografie; detailed bibliographic data are available in the Internet at <http://dnb.d-nb.de>.

© 2007 WILEY-VCH Verlag GmbH & Co.
KGaA, Weinheim

All rights reserved (including those of translation into other languages). No part of this book may be reproduced in any form – by photoprinting, microfilm, or any other means – nor transmitted or translated into a machine language without written permission from the publishers. Registered names, trademarks, etc. used in this book, even when not specifically marked as such, are not to be considered unprotected by law.

Printed in the Federal Republic of Germany
Printed on acid-free paper

Composition Asco Typesetters, Hong Kong
Printing Betz-Druck GmbH, Darmstadt
Bookbinding Litges & Dopf GmbH, Heppenheim
Cover Schulz Grafik-Design, Fußgönheim

ISBN 978-3-527-31515-4

Contents

Preface *xi*

List of Contributors *xiii*

I Fundamentals

1 The Impact of Electrocrystallization on Nanotechnology 3

Georgi Staikov and Alexander Milchev

- 1.1 Introduction 3
- 1.2 Thermodynamic Properties of Large and Small Phases 4
 - 1.2.1 The State of Thermodynamic Equilibrium 4
 - 1.2.2 Electrochemical Supersaturation and Undersaturation 6
 - 1.2.3 The Thermodynamic Work for Nucleus Formation 7
 - 1.2.3.1 Classical Nucleation Theory 8
 - 1.2.3.2 Atomistic Nucleation Theory 9
- 1.3 Kinetics of Nucleus Formation in Electrocrystallization 10
- 1.4 Energy State of the Electrode Surface and Spatial Distribution of Nanoclusters 11
- 1.5 Electrochemical Growth of Nanoparticles and Ultrathin Films 14
 - 1.5.1 Growth of 3D Nanoclusters 15
 - 1.5.2 Growth of 2D Nanoclusters and Formation of UPD Monolayers 17
- 1.6 Localization of Electrocrystallization Processes and Nanostructuring 20
- 1.7 Conclusion 24
- Acknowledgments 25
- References 25

2 Computer Simulations of Electrochemical Low-dimensional Metal Phase Formation 30

Marcelo M. Mariscal and Ezequiel P. M. Leiva

- 2.1 Introduction 30
- 2.2 Molecular Dynamics Simulations 32
 - 2.2.1 Generalities 32
 - 2.2.2 Nanostructuring of Metallic Surfaces 33

2.3	Monte Carlo Method	37
2.3.1	Generalities	37
2.3.2	Off-lattice Models	40
2.3.2.1	Stability of Metallic Nanostructures	40
2.3.3	Lattice Models	44
2.3.3.1	Introduction	44
2.3.3.2	Electrocrystallization	46
2.3.3.3	Dynamics of Crystal Growth	51
2.3.3.4	Simulation of a Complex Underpotential Deposition System	53
2.4	Brownian and Langevin Dynamics Simulations	54
2.4.1	Generalities	54
2.4.2	Applications in Electrochemical Nanostructuring and Crystal Growth	55
2.5	Conclusions and Outlook	58
	Acknowledgments	59
	References	59
3	Electrodeposition of Metals in Templates and STM Tip-generated 0D Nanocavities	61
	<i>Wolfgang Kautek</i>	
3.1	Introduction	61
3.2	Bottom-up Template Approach	61
3.3	Top-down SPM Approach	66
3.4	Thermodynamics of Low-dimensional Phases	68
3.5	Experiments on the Electrodeposition in STM-tip-generated Nanocavities	69
3.6	Underpotential Behavior of Bismuth on Gold	70
3.7	Zero-dimensional Bi Deposition	72
3.8	Conclusions	74
	Acknowledgment	75
	References	75
4	Nanoscale Electrocrystallization of Metals and Semiconductors from Ionic Liquids	79
	<i>Walter Freyland, Chitradurga L. Aravinda, and Ditimar Borissov</i>	
4.1	Introduction	79
4.2	Some Electrochemical and Interfacial Characteristics of Ionic Liquids (ILs)	80
4.3	Variable Temperature Electrochemical SPM Technique for Studies with Ionic Liquids	81
4.4	Underpotential Deposition of Metals: Phase Formation and Transitions	82
4.4.1	Ag on Au(111): Aqueous versus Ionic Liquid Electrolytes	83
4.4.2	Zn on Au(111): Spinodal Decomposition and Surface Alloying	86
4.5	Overpotential Deposition of Metals, Alloys and Semiconductors	89

4.5.1	Co–Al, Ni–Al and Ti–Al Alloy Deposition	89
4.5.2	Nanoscale Growth of Al–Sb Compound Semiconductors	92
4.6	Concluding Remarks	93
	Acknowledgment	94
	References	94
5	Superconformal Film Growth	96
	<i>Thomas P. Moffat, Daniel Wheeler, and Daniel Josell</i>	
5.1	Introduction	96
5.2	Competitive Adsorption: Inhibition versus Acceleration	98
5.3	Quantifying the Impact of Competitive Adsorption on Metal Deposition Kinetics	101
5.4	Feature Filling	104
5.5	Shape Change Simulations	107
5.6	Stability Analysis	110
5.7	Conclusions and Outlook	112
	References	113
II	Preparation and Properties of Nanostructures	
6	Localized Electrocrystallization of Metals by STM Tip Nanoelectrodes	117
	<i>Werner Schindler and Philipp Hugelmann</i>	
6.1	Electrochemistry in Nanoscale Dimensions	117
6.2	Jump-to-Contact Metal Deposition	118
6.3	Scanning Electrochemical Microscope	120
6.4	STM Tip Electrochemical Nanoelectrodes	120
6.5	Metal Deposition by STM Tip Electrochemical Nanoelectrodes	122
6.6	Metal Dissolution by STM Tip Electrochemical Nanoelectrodes	124
6.7	The Importance of Nanoelectrode Tip Shape and Surface Quality	127
6.8	Localized Electrodeposition of Single Metal Nanostructures	129
6.9	Summary and Outlook	134
	Acknowledgments	136
	References	136
7	Fabrication of Ordered Anodic Nanoporous Alumina Layers and their Application to Nanotechnology	138
	<i>Hidetaka Asoh and Sachiko Ono</i>	
7.1	Introduction	138
7.2	Self-ordered Anodic Porous Alumina	139
7.2.1	Introduction	139
7.2.2	Controlling Factor of Self-ordering of Pore Arrangement in Anodic Porous Alumina	140
7.2.3	Typical Current–Time Transients at Constant Voltages	141
7.2.4	Change in the Porosity of Anodic Alumina with Increasing Formation Voltage	142

7.2.5	Typical Self-ordering Behavior	144
7.2.6	High-current-density/High-electric-field Anodization	145
7.2.7	New Self-ordering Conditions	147
7.3	Ideally Ordered Anodic Porous Alumina	148
7.3.1	Two-step Anodization	148
7.3.2	Fabrication of Ideally Ordered Anodic Porous Alumina	150
7.3.3	Square Cell Arrangement	150
7.3.4	Detailed Observation of Square Cells	152
7.4	Anodic Porous Alumina with 3D Periodicity	154
7.4.1	Modulation of Channel Structure	154
7.4.2	2D/3D Composite Porous Alumina	154
7.5	Application of Nanoporous Alumina to a Mask for Fabrication of Nanostructures	156
7.5.1	Nanopatterning: Conventional Lithography vs. Natural Lithography	156
7.5.2	Anodization of Al on a Si Substrate	157
7.5.3	Natural Lithography of Si Surfaces Using Anodic Porous Alumina as a Mask	160
7.6	Summary	161
	Acknowledgments	162
	References	162
8	Electrochemical Fabrication of Metal Nanocontacts and Nanogaps	167
	<i>Fang Chen and N. J. Tao</i>	
8.1	Introduction	167
8.2	Electrochemical Fabrication of Metal Nanocontacts	168
8.2.1	STM/AFM Assisted Method	169
8.2.2	Electrodeposition on Surface-supported Electrodes	170
8.2.3	Self-terminated Method	172
8.2.4	Electrochemical Etching	173
8.2.5	Nanocontacts Prepared Using Nanopores	174
8.2.6	Solid State Electrochemical Reaction	174
8.2.7	Properties of Metal Nanocontacts	175
8.2.7.1	Mechanical Properties	175
8.2.7.2	Electron Transport	177
8.2.7.3	Electrochemical Properties	178
8.2.7.4	Device Properties	180
8.2.7.5	Magnetic Properties	181
8.2.7.6	Sensing Properties	182
8.3	Electrochemical Fabrication of Metal Nanogaps	183
8.3.1	AC-loop Monitoring System	185
8.3.2	DC-loop Monitoring System	186
8.3.3	Electric Double Layer as Feedback	187
8.3.4	High-frequency Impedance as Feedback	188
8.3.5	Application of Nanogaps	188
8.4	Summary	190

	Acknowledgment	191
	References	191
9	Nanowires by Electrochemical Step Edge Decoration (ESED)	195
	<i>Reginald M. Penner</i>	
9.1	Introduction	195
9.2	General Considerations	196
9.3	Direct Nanowire Electrodeposition	198
9.4	Compound Nanowires by Cyclic Electrodeposition/Stripping	200
9.5	Electrochemical/Chemical Synthesis of Nanowires	202
9.6	Nanowire “Thinning” by Electrooxidation	204
9.7	Summary	206
	Acknowledgments	206
	References	206
10	Electrochemical Fabrication of Arrayed Nanostructures	208
	<i>Takayuki Homma</i>	
10.1	Introduction	208
10.2	Formation of Metal Nanodots Along the Step Edge of the Si(111) Surface	208
10.3	Maskless Fabrication of Metal Nanodot Arrays using Electroless Deposition Induced by Controlled Local Surface Activities	210
10.4	Conclusion	215
	References	216
11	Electrodeposition of Two-dimensional Magnetic Nanostructures on Single Crystal Electrode Surfaces	217
	<i>Philippe Allongue and Fouad Maroun</i>	
11.1	Introduction	217
11.2	Ultrathin Magnetic Films	219
11.2.1	Magnetic Moment of Ultrathin Films	220
11.2.2	<i>In Situ</i> Magnetic Characterizations	223
11.2.2.1	Alternating Gradient Field Magnetometry (AGFM)	224
11.2.2.2	Magneto Optical Kerr Effect (MOKE)	225
11.2.3	Description and Exploitation of <i>in Situ</i> Magnetic Measurements	225
11.3	Electrochemical Growth and Magnetic Properties of Iron Group Films on Au(111)	227
11.3.1	Electrochemistry of Au(111) in Iron Group Metal Solutions	227
11.3.2	Ni/Au(111)	228
11.3.2.1	Morphology and Structure	228
11.3.2.2	Magnetic Properties	229
11.3.3	Co/Au(111)	230
11.3.3.1	Morphology and Structure	230
11.3.3.2	Magnetic Properties	232
11.3.4	Fe/Au(111)	235

11.3.4.1	Morphology and Structure	235
11.3.4.2	Magnetic Properties	237
11.4	Concluding Remarks	238
	Acknowledgments	239
	References	239

**12 Electrodeposition and Properties of Nanoscale Magnetic/Non-magnetic
Metallic Multilayer Films 242**

László Péter and Imre Bakonyi

12.1	Introduction	242
12.2	Electrodeposition	243
12.2.1	Electrolyte Composition	243
12.2.2	Deposition Conditions of the More Noble Layer	246
12.2.3	Deposition of the Less Noble Layer	247
12.2.4	Various Multilayer Deposition Modes	249
12.2.5	Nucleation of the Layers on Each Other	249
12.3	Properties	250
12.3.1	Structure	250
12.3.2	Magnetic Properties	253
12.3.3	Magnetoresistance	256
12.4	Summary	258
	Acknowledgments	259
	References	259

Index 261

Preface

In the last decade the scaling down of functional structures has been a dominating trend in many fields of science and technology. The size reduction of structures from the micrometer to the nanometer scale leads not only to a miniaturization of functional units but also to the development of new materials and systems with unconventional physical and chemical properties. The electrocrystallization processes, which offer over competing vapor phase deposition some unique advantages such as high selectivity and exact and easy control of the growth conditions by the electrode potential and current density, are very attractive for surface structuring and modification in modern micro- and nanotechnologies.

This book provides a comprehensive overview of recent advances in the nanostructuring and -modification of solid surfaces by electrocrystallization of metals, oxides and semiconductors. After discussing the fundamentals relevant to nanotechnology, the book focuses on the preparation and properties of various nanostructures. With chapters, written by leading experts in these fields, the book is addressed to scientists, researchers and graduate students interested in electrochemical phase formation, electrodeposition, surface science, materials science and nanotechnology.

The first chapter by Staikov and Milchev offers a general introduction to the basic concepts of electrocrystallization and their impact on nanotechnology. Mariscal and Leiva describe, in Chapter 2, different computer simulation techniques and their application to low-dimensional metal phase formation and electrochemical nanostructuring. Chapter 3 by Kautek is devoted to the preparation of low-dimensional metal systems by electrodeposition in templates and STM tip-induced 0D nanocavities. In Chapter 4 Freyland et al. discuss the specific aspects of nanoscale electrocrystallization of metals and semiconductors from ionic liquids. Chapter 5 by Moffat et al. deals with the mechanism of so-called superconformal growth, which is relevant to the nanoscale electrodeposition of on-chip metal interconnections. Schindler and Hugelmann focus, in Chapter 6, on the application of STM for tip-induced localized electrocrystallization of metals. A comprehensive overview of the fabrication of ordered nanoporous anodic alumina layers and their application is given in Chapter 7 by Asoh and Ono. In Chapter 8 Chen and Tao review different approaches for electrochemical fabrication of atomic scale contacts and nanogaps and discuss their properties and applications. An original method

for the preparation of metallic and compound nanowires by selective electrocrystallization at step edges is described by Penner in Chapter 9. Homma describes, in Chapter 10, a maskless technique for electrochemical fabrication of arrays of metal nanodots on silicon wafers, based on the formation of patterned nanodefects at the wafer surface and subsequent local electroless metal deposition. Chapter 11 by Allongue and Maroun reviews the electrochemical growth of ultrathin epitaxial films of iron group metals on single crystal substrates, correlating the structure and morphology of the films with their specific magnetic properties. Peter and Bakonyi focus, in Chapter 12, on electrodeposition of nanoscale multilayered magnetic/nonmagnetic metallic films, placing an emphasis on their structure and giant magnetoresistance behavior.

Georgi Staikov

List of Contributors

Philippe Allongue

Laboratoire de Physique de la Matière
Condensée
CNRS UMR 7643
Ecole Polytechnique
91128 Palaiseau
France

Chitradurga L. Aravinda

Institute of Physical Chemistry
University of Karlsruhe
76128 Karlsruhe
Germany

Hidetaka Asoh

Department of Applied Chemistry
Faculty of Engineering
Kogakuin University
1-24-2 Nishi-shinjuku
Shinjuku-ku
163-8677 Tokyo
Japan

Imre Bakonyi

Research Institute for Solid State Physics and
Optics
Hungarian Academy of Sciences
P.O.B. 49
1525 Budapest
Hungary

Ditimar Borissov

Institute of Physical Chemistry
University of Karlsruhe
76128 Karlsruhe
Germany

Fang Chen

Department of Electrical Engineering
Center for Solid State Electronics Research
Arizona State University
Tempe
AZ 85287
USA

Walter Freyland

Institute of Physical Chemistry
University of Karlsruhe
76128 Karlsruhe
Germany

Philipp Hugelmann

Department of Physics
Technical University München
James-Franck-Strasse 1
85748 Garching
Germany

Takayuki Homma

Department of Applied Chemistry
Waseda University
Okubo
Shinjuku
169-8555 Tokyo
Japan

Daniel Josell

Materials Science and Engineering Laboratory
National Institute of Standards and
Technology
Gaithersburg
Maryland 20899
USA

Wolfgang Kautek

Department of Physical Chemistry
University of Vienna
Währinger Strasse 42
1090 Vienna
Austria

Ezequiel P. M. Leiva

Unidad de Matemática y Física
Universidad Nacional de Córdoba
INFIQC
5016 Córdoba
Argentina

Marcelo M. Mariscal

Unidad de Matemática y Física
Universidad Nacional de Córdoba
INFIQC
5016 Córdoba
Argentina

Fouad Maroun

Laboratoire de Physique de la Matière
Condensée
CNRS UMR 7643
Ecole Polytechnique
91128 Palaiseau
France

Alexander Milchev

Rostislaw Kaischew Institute of Physical
Chemistry
Bulgarian Academy of Sciences
Acad. G. Bonchev Str., bl. 11
1113 Sofia
Bulgaria

Thomas P. Moffat

Materials Science and Engineering Laboratory
National Institute of Standards and
Technology
Gaithersburg
Maryland 20899
USA

Sachiko Ono

Department of Applied Chemistry
Faculty of Engineering
Kogakuin University,
1-24-2 Nishi-shinjuku
Shinjuku-ku
Tokyo 163-8677
Japan

Reginald M. Penner

Department of Chemistry and Institute for
Surface and Interface Science
University of California
Irvine
CA 92697-2025
USA

László Péter

Research Institute for Solid State Physics and
Optics
Hungarian Academy of Sciences
P.O.B. 49
1525 Budapest
Hungary

Werner Schindler

Technical University München
Department of Physics
James-Frank-Strasse 1
85748 Garching
Germany

Georgi Staikov

Institute of Thin Films and Interfaces (ISG 3)
and CNI-Centre of Nanoelectronic Systems for
Information Technology
Research Centre Jülich
52425 Jülich
Germany

N. J. Tao

Department of Electrical Engineering
Center for Solid State Electronics Research
Arizona State University
Tempe
AZ 85287
USA

Daniel Wheeler

Materials Science and Engineering Laboratory
National Institute of Standards and
Technology
Gaithersburg
Maryland 20899
USA

I Fundamentals

1

The Impact of Electrocrystallization on Nanotechnology

Georgi Staikov and Alexander Milchev

1.1 Introduction

Electrocrystallization processes occurring at electrochemical solid/liquid interfaces have for a long time attracted the interest of many researchers from both fundamental and applied viewpoints. After the pioneering works of Max Volmer at the beginning of the last century [1, 2], the processes of electrocrystallization have been the subject of numerous intensive studies, the results of which have been reviewed in several books [3–7].

Electrocrystallization not only represents an interesting case of phase formation and crystal growth but is also a powerful method for various technological applications because the driving force of the process can be easily controlled by the current density and the electrode potential. Additional technological advantages over the vapor deposition techniques consist in the relatively low processing temperature and the high selectivity. The low temperature is important for systems in which undesirable interdiffusion between adjacent layers or structures can occur, whereas the high selectivity of electrocrystallization processes allows uniform modification of surfaces and structures with complicated profiles.

Phase formation and crystal growth phenomena are involved in many technologically important cathodic and anodic electrochemical reactions. The most frequently studied electrocrystallization process is cathodic metal deposition on foreign and native substrates from electrolytes containing simple and/or complex metal ions [3–25]. Typical examples are the electrocrystallization of Ag from Ag⁺-containing electrolytes [5, 7, 12–15, 21], the cathodic deposition of Ag on n-Si from electrolytes containing [Ag(CN)₂][−] ions [24], and the electrodeposition of Cu [3, 9, 17–20, 22, 25], which has recently become of significant technological importance for the fabrication of Cu interconnects on integrated circuit chips [26, 27].

A process widely used for preparation of metallic alloys and semiconducting compounds is cathodic codeposition from multicomponent electrolytes [28–39]. Typical examples are the electrochemical formation of Ni–Fe alloys by codeposition from Ni²⁺- and Fe²⁺-containing electrolytes [31] and the electrodeposition of n-type CdTe from electrolytes containing Cd²⁺ and HTeO₂⁺ ions [33]. Other impor-

tant electrocrystallization processes are anodic deposition of metal oxides and anodic oxidation of metals and semiconductors [23, 40–47]. The first type of processes can be illustrated by the anodic deposition of PbO_2 from an aqueous Pb^{2+} solution [43]. The second type are substrate consuming processes, which occur in aqueous solution and usually start with adsorption of OH^- ions and place exchange reactions with the substrate [44]. Technologically important examples are the anodic oxidation of valve metals (Al, Nb, Ta, Ti) [45] and Si [46, 47].

The discovery of scanning tunneling microscopy and atomic force microscopy (STM and AFM) offered new exciting possibilities for *in situ* studies of the electrocrystallization phenomena down to an atomic level [48–50]. It would be not an overstatement to say that during the past two decades the application of these techniques has revolutionized the experimental work in this field and led to significant progress in the understanding of the atomistic aspects of electrocrystallization processes [5, 50–65]. The invention of scanning probe microscopy (SPM) also provoked a rapid development of the modern nanoscience and nanotechnology dealing with nanoscale structures and objects, including single atoms and molecules.

The application of electrocrystallization processes in nanotechnology requires a scaling down of the structures to the nanometer range. Therefore, in this chapter, we discuss some specific aspects of electrocrystallization, which are relevant for the electrochemical preparation and properties of various nanostructures. In Section 1.2 we compare the thermodynamic properties of large and small phases and introduce the concepts of supersaturation and the work for nucleus formation in electrochemical systems. The theoretical and experimental aspects of electrochemical nucleation and growth of nano-particles and ultrathin films are considered in Sections 1.3–1.5, whereas different approaches for localized electrocrystallization and preparation of nanostructures are discussed in Section 1.6. All considerations are illustrated with experimental results obtained in selected electrochemical systems.

1.2

Thermodynamic Properties of Large and Small Phases

1.2.1

The State of Thermodynamic Equilibrium

In order to describe the state of stable thermodynamic equilibrium we consider an electrochemical system consisting of an electrolyte solution of metal ions (Me^z) with a valence z and an electrochemical potential $\tilde{\mu}_{s, \infty}$, an infinitely large metal crystal of the same material (Me) with an electrochemical potential $\tilde{\mu}_{c, \infty}$ and an inert foreign substrate, which is used as a working electrode and whose Galvani potential $\phi_{we, \infty}$ can be varied by means of an external source. For the purpose of this consideration we assume that the working electrode is polarized to the Galvani potential $\phi_{c, \infty}$ of the bulk metal crystal. The temperature T is kept constant. The metal ions Me^z of the electrolyte may adsorb on the inert foreign substrate forming adatoms with an electrochemical potential $\tilde{\mu}_{ad, \infty}$. The equilibrium state of such

an electrochemical system is expressed through the equality of the electrochemical potentials $\tilde{\mu}$ of the species within coexisting phases [5, 7, 15, 23]:

$$\tilde{\mu}_{s, \infty} = \tilde{\mu}_{c, \infty} = \tilde{\mu}_{ad, \infty} \quad (1.1)$$

where

$$\tilde{\mu}_{s, \infty} = \mu_s^0 + kT \ln a_{s, \infty} + ze\phi_{s, \infty} \quad (1.2)$$

$$\tilde{\mu}_{c, \infty} = \mu_c^0 + ze\phi_{c, \infty} \quad (1.3)$$

$$\tilde{\mu}_{ad, \infty} = \mu_{ad}^0 + kT \ln a_{ad, \infty} + ze\phi_{c, \infty} \quad (1.4)$$

In Eqs. (1.2)–(1.4), μ_s^0 , μ_c^0 and μ_{ad}^0 are the standard state chemical potentials of the three species, $a_{s, \infty}$, $a_{c, \infty} = 1$ and $a_{ad, \infty}$ are their activities and $\phi_{s, \infty}$ and $\phi_{c, \infty}$ are the corresponding Galvani potentials.

Making use of the equality $\tilde{\mu}_{s, \infty} = \tilde{\mu}_{c, \infty}$ one obtains the Nernst equation,

$$E_{\infty} = E^0 + \frac{kT}{ze} \ln a_{s, \infty} \quad (1.5)$$

which gives the equilibrium potential $E_{\infty} = \phi_{c, \infty} - \phi_{s, \infty}$ of a bulk metal crystal dipped in a solution of its ions with activity $a_{s, \infty}$. The standard potential E^0 is defined by $E^0 = (\mu_s^0 - \mu_c^0)/ze$. The potential-activity ($E - a_s$) diagram in Fig. 1.1 shows schematically the equilibrium curve corresponding to Eq. (1.5) and to the equality $\tilde{\mu}_{s, \infty} = \tilde{\mu}_{c, \infty}$.

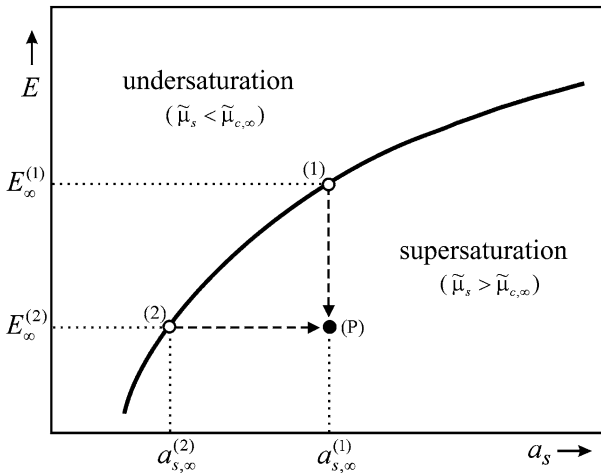


Figure 1.1. Schematic $E(a_s)$ diagram for the equilibrium of a bulk metal crystal with its own ionic solution according to Eq. (1.5).

Another formula for the equilibrium potential E_∞ could be obtained also from the equilibrium condition $\tilde{\mu}_{s, \infty} = \tilde{\mu}_{ad, \infty}$. In that case for E_∞ it results,

$$E_\infty = \frac{\mu_s^0 - \mu_{ad}^0}{ze} + \frac{kT}{ze} \ln \left(\frac{a_{s, \infty}}{a_{ad, \infty}} \right) \quad (1.6)$$

and equating the two expressions for E_∞ yields a simple formula for the equilibrium adatoms' activity: $a_{ad, \infty} = \exp[(\mu_c^0 - \mu_{ad}^0)/kT]$. The same expression for $a_{ad, \infty}$ follows from the equality of the electrochemical potentials $\tilde{\mu}_{c, \infty}$ and $\tilde{\mu}_{ad, \infty}$.

1.2.2

Electrochemical Supersaturation and Undersaturation

In order to initiate either the growth of the bulk crystal or a process of nucleus formation on the inert foreign substrate it is necessary to supersaturate the parent phase, the electrolyte solution. This means to increase its electrochemical potential to a value $\tilde{\mu}_s$ larger than that of the bulk new phase, the metal crystal ($\tilde{\mu}_s > \tilde{\mu}_{c, \infty}$). Then it is the difference $\Delta\tilde{\mu} = \tilde{\mu}_s - \tilde{\mu}_{c, \infty} > 0$, which defines the *electrochemical supersaturation*.

In Fig. 1.1 the supersaturation range is situated below the equilibrium curve corresponding to Eq. (1.5). In the opposite case, when $\tilde{\mu}_s < \tilde{\mu}_{c, \infty}$, the difference $\tilde{\mu}_s - \tilde{\mu}_{c, \infty} < 0$ defines the *electrochemical undersaturation*, which, if applied, would cause the electrochemical dissolution of the bulk crystal. Thus, the solid line in Fig. 1.1 indicates the stability limits of the infinitely large metal crystal.

As seen, the quantity $\Delta\tilde{\mu}$ is the driving force of the two opposite types of electrochemical first order phase transition, either on a native or on a foreign substrate and therefore it is of fundamental and technological importance to express it by means of physical quantities, which can be easily measured and controlled.

The general formula for $\Delta\tilde{\mu}$ that is most frequently used reads

$$\Delta\tilde{\mu} = ze\eta \quad (1.7)$$

where η is the *cathodic overpotential* defined either as¹

$$\eta = E_\infty - E \quad (1.8)$$

or as

$$\eta = \frac{kT}{ze} \ln \frac{a_s}{a_{s, \infty}} \quad (1.9)$$

Equations (1.8) and (1.9) show that the parent phase can be supersaturated with respect to the bulk crystal in two different ways, as illustrated schematically

1) In this chapter, the cathodic overpotential is defined as a positive quantity.

in Fig. 1.1. In the first way, the solution activity a_s is kept constant at the value $a_{s,\infty}^{(1)}$ and the state of the system is changed from the equilibrium point (1) to a point (P) located in the supersaturation range by changing the electrode potential from the equilibrium, $E_{\infty}^{(1)}$, to a more negative value $E \equiv E_{\infty}^{(2)}$. At this potential the bulk crystal should stay in equilibrium with a solution with an activity $a_{s,\infty}^{(2)} < a_{s,\infty}^{(1)}$. In the second way, the parent phase is supersaturated to the same state (P) but starting from the equilibrium state (2) and increasing the solution activity to a value $a_s = a_{s,\infty}^{(1)}$ larger than the equilibrium value $a_{s,\infty}^{(2)}$, the electrode potential E being kept constant at $E_{\infty}^{(2)}$. As pointed out in Refs. [7, 66–68], this second possibility of applying the supersaturation allows one to invent a modified pulse potentiostatic technique, which has certain advantages, particularly when it is necessary to preserve the energy state of the electrode surface. The increase in supersaturation by increasing the activity of metal ions at constant electrode potential has also been applied successfully for development of polarization routines for localized electro-deposition of metal nanoclusters using the STM tip as a nanotool [56, 63, 69–72].

In the above considerations the electrochemical supersaturation was defined with respect to a 3D bulk metal phase. However, in the case of foreign substrates characterized by a strong *depositing metal–substrate* interaction, various expanded (gas-like) and/or condensed (solid-like) low-dimensional metal phases can be formed in the undersaturation range with respect to the 3D bulk metal phase, a phenomenon known as underpotential deposition (UPD) [5, 11, 56, 63]. The equilibrium potential of a condensed (solid-like) 2D metal phase can be expressed by [56]

$$E_{2D} = E_{\infty} - \frac{kT}{ze} \ln a_{2D} \quad (1.10)$$

Here $a_{2D} < 1$ represents the activity of the 2D phase, which depends on the metal–substrate interaction. In this case the electrochemical supersaturation with respect to the condensed 2D metal phase is given by $\Delta\tilde{\mu}_{2D} = ze\eta_{2D}$ where the cathodic overpotential is defined as $\eta_{2D} = E_{2D} - E$.

As already mentioned, the supersaturation may initiate both the process of nucleus formation on the foreign substrate and the growth of the bulk metal crystal, depending on which phase is switched on as a working electrode. In what follows we consider the two types of electrocrystallization phenomena.

1.2.3

The Thermodynamic Work for Nucleus Formation

The formation of an n -atomic nucleus of the new phase requires one to overcome a thermodynamic barrier $\Delta\tilde{G}(n)$ called *nucleation work* and expressed by the general formula [5, 7, 12, 15]:

$$\Delta\tilde{G}(n) = -n\Delta\tilde{\mu} + \tilde{\Phi}(n) \quad (1.11)$$

Here $\tilde{\Phi}(n)$ takes into consideration the total energy excess due to the creation of new interfaces when a nucleus appears on the electrode surface.

1.2.3.1 Classical Nucleation Theory

In the particular case of sufficiently large clusters the number of atoms n can be considered as a continuous variable and the quantity $\tilde{\Phi}(n)$ could be expressed by means of the specific free *surface*, *interfacial* and *line* energies in the system *nucleus–electrolyte–working electrode*. In that case $\Delta\tilde{G}(n)$ is a differentiable function and the condition for an extremum $[d\Delta\tilde{G}(n)/dn]_{n=n_c} = 0$ yields [7, 15]

$$\Delta\tilde{\mu} = \left[\frac{d\tilde{\Phi}(n)}{dn} \right]_{n=n_c} \quad (1.12)$$

Equation (1.12) represents a general expression for the Gibbs–Thomson equation giving us the interrelation between the supersaturation $\Delta\tilde{\mu}$ and the size n_c of the so-called *critical nucleus*, which stays in unstable equilibrium with the supersaturated parent phase.

The inspection of the theoretical formula for the nucleation work shows that the $\Delta\tilde{G}(n)$ versus n relationship displays a maximum at $n = n_c$ (Fig. 1.2(a)), the values of $\Delta\tilde{G}(n_c)$, n_c and $\Delta\tilde{\mu}$ being interrelated according to

$$\Delta\tilde{G}(n_{c,3D}) = \frac{1}{3}\tilde{\Phi}(n_{c,3D}) = \frac{1}{2}n_{c,3D}\Delta\tilde{\mu} \quad (1.13)$$

when 3D clusters form on a foreign substrate and according to

$$\Delta\tilde{G}(n_{c,2D}) = \frac{1}{2}\tilde{\Phi}(n_{c,2D}) = n_{c,2D}\Delta\tilde{\mu} \quad (1.14)$$

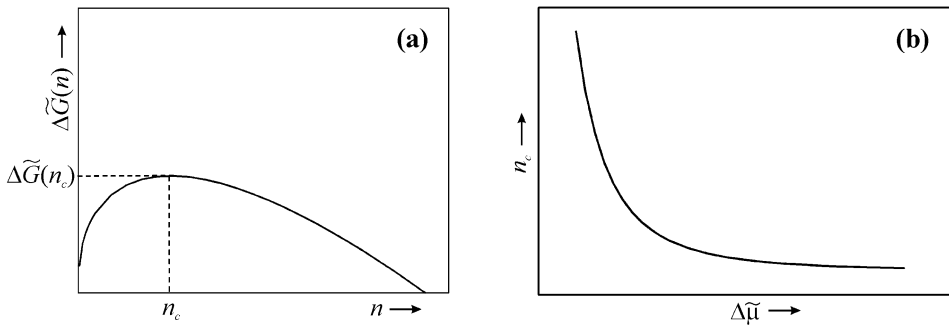


Figure 1.2. Dependence of the nucleation work $\Delta\tilde{G}(n)$ on the cluster size n (a) and dependence of the critical nucleus size n_c on the supersaturation $\Delta\tilde{\mu}$ (b) according to the classical nucleation theory (a schematic representation).

and

$$\Delta\tilde{G}(n_{c,2D}^*) = \frac{1}{2}\tilde{\Phi}(n_{c,2D}^*) = n_{c,2D}^*\Delta\tilde{\mu}_{2D} \quad (1.15)$$

when 2D clusters form on a native or on a foreign substrate, respectively. Figure 1.2(b) illustrates the supersaturation dependence of the critical nucleus size.

1.2.3.2 Atomistic Nucleation Theory

In the case of very small clusters the size n is a discrete variable and the macroscopic classical theory cannot be applied. Therefore the process of nucleus formation is described by means of atomistic considerations making use of the general formula for the nucleation work (Eq. (1.11)) [7, 15, 73, 74, 87]. The main result of the atomistic treatment is that the $\Delta\tilde{G}(n)$ vs. n relationship is not a fluent curve but displays minima and maxima, depending on the structure and energy state of the cluster (Fig. 1.3(a)). The highest maximum at a given supersaturation corresponds to the critical nucleus size.

The discrete change in the size of the clusters at small dimensions also affects the $n_c(\Delta\tilde{\mu})$ relationship. As seen from Fig. 1.3(b), in this case there corresponds to each critical nucleus a supersaturation interval and not a fixed value of $\Delta\tilde{\mu}$ as predicted by the Gibbs–Thomson equation. These special properties of small clusters influence strongly the process of phase formation during electrocrystallization and have to be taken into consideration, particularly when interpreting experimental data for electrochemical nucleation on a foreign substrate. In that case the size of the critical nuclei does not exceed several atoms [5, 7, 12, 15, 17–25, 36–39, 75–84].

Apart from the purely thermodynamic analysis, the description of the nanoscale electrocrystallization phenomena requires special consideration of the kinetics of nucleus formation and the next section is devoted to this subject.

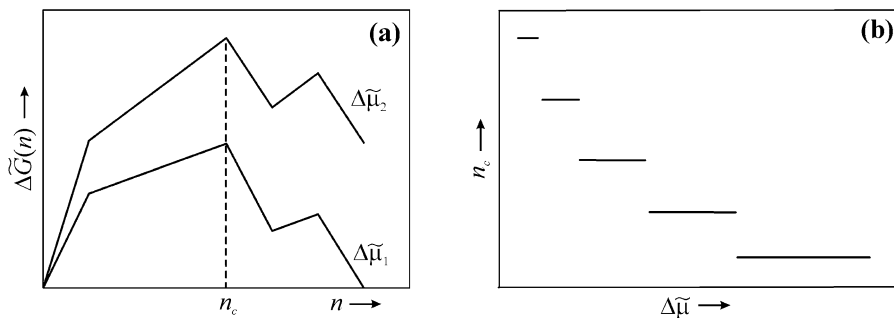


Figure 1.3. Dependence of the nucleation work $\Delta\tilde{G}(n)$ on the cluster size n (a) and dependence of the critical nucleus size n_c on the supersaturation $\Delta\tilde{\mu}$ (b) according to the atomistic nucleation theory (a schematic representation).

1.3

Kinetics of Nucleus Formation in Electrocrystallization

The nucleation work $\Delta\tilde{G}(n_c)$ is a measure of the thermodynamic barrier, which has to be overcome in order to transform n_c ions from the electrolyte solution into an n_c -atomic nucleus of the new solid or liquid phase on the electrode surface. The rate $J(t)$ of this process is a kinetic quantity and here we will comment upon its overpotential and concentration dependence in the case of a stationary nucleation when $J(t)$ attains the constant value J_0 .

The general theoretical formula for J_0 reads [2, 85, 86]

$$J_0 = Z_0 W \lambda^{-1} \exp\left[-\frac{\Delta\tilde{G}(n_c)}{kT}\right] \quad (1.16)$$

where Z_0/cm^{-2} is the number density of active sites on the substrate, W/s^{-1} is the frequency of attachment of single atoms to the critical nucleus and λ^{-1} is a non-dimensional quantity accounting for the difference between the quasi-equilibrium and the stationary number of critical nuclei. In the macroscopic classical nucleation theory λ^{-1} is given as $\lambda^{-1} = [\Delta\tilde{G}(n_c)/3\pi n_c^2 kT]^{1/2}$ and is called a ‘‘Zeldovich factor’’. It tends to unity at high supersaturations and/or very active substrates, when the critical nuclei are very small and their size remains constant over wide supersaturation intervals. For this typical case of electrochemical phase formation, particularly on foreign substrates, we shall reveal the overpotential and the concentration dependence of the stationary nucleation rate in terms of the atomistic theory of electrochemical phase formation [7, 15, 73, 87]. In this case the quantity W is given by

$$W = k_v \exp\left(-\frac{U}{kT}\right) \exp\left(-\frac{\alpha z e E}{kT}\right) \quad (1.17)$$

where k_v is a frequency factor, c is the concentration of metal ions, α is the charge transfer coefficient and U is the energy barrier to transfer of an ion from the electrolyte to the critical nucleus at an electrode potential $E = 0$. This formula for W is suitable when the supersaturation $\Delta\tilde{\mu}$ (Eq. (1.7)) is varied by changing the concentration of metal ions at a constant electrode potential E (Fig. 1.1), and substituting Eqs. (1.7), (1.9), (1.11) and (1.17) into Eq. (1.16) for the $J_0(c)$ relationship at $\lambda^{-1} \rightarrow 1$ one obtains [7, 68]:

$$J_0 = Z_0 \Omega(E) c^{n_c+1} \quad (1.18)$$

Here

$$\Omega(E) = k_v \left(\frac{\gamma}{\gamma_\infty c_\infty}\right)^{n_c} \exp\left[-\frac{U + \alpha z e E + \tilde{\Phi}(n_c)}{kT}\right] \quad (1.19)$$

where c_∞ is the equilibrium concentration of metal ions at the temperature T and γ and γ_∞ are the corresponding activity coefficients given as $\gamma = a_s/c$ and $\gamma_\infty = a_{s,\infty}/c_\infty$. Thus Eq. (1.18) shows that the size n_c of the critical nucleus can be determined from an experimental $J_0(c)$ relationship obtained at $E = \text{const}$ according to [7, 68]:

$$n_c = \frac{d \ln J_0}{d \ln c} - 1 \quad (1.20)$$

In the case when the supersaturation is varied by varying the electrode potential E at a constant concentration $c_\infty = \gamma_\infty a_{s,\infty}$ (Fig. 1.1) it turns out to be convenient to introduce the cathodic overpotential $\eta = E_\infty - E$ in Eq. (1.17). Then accounting for the $E_\infty(a_{s,\infty})$ relationship according to the Nernst equation (1.5) for the overpotential dependence of the stationary nucleation rate J_0 at $\lambda^{-1} \rightarrow 1$ one obtains [7, 68]:

$$J_0 = Z_0 \Omega(c_\infty) \exp \left[\frac{(n_c + \alpha) z e \eta}{kT} \right] \quad (1.21)$$

where

$$\Omega(c_\infty) = k_v (\gamma_\infty c_\infty)^{1-\alpha} \exp \left[- \frac{U + \alpha z e E^0 + \tilde{\Phi}(n_c)}{kT} \right] \quad (1.22)$$

As seen, in this case the size n_c of the critical nucleus can be determined from an experimental $J_0(\eta)$ relationship obtained at $c = c_\infty$ according to [7, 68]:

$$n_c = \frac{kT}{ze} \frac{d \ln J_0}{d \eta} - \alpha \quad (1.23)$$

Equations (1.16)–(1.23) are derived under the assumption of a constant number Z_0 of active sites on the working electrode, which is a most simple example of electrochemical phase formation. In reality, the number of active sites could be a *time*, *potential* and *pH* dependent quantity [7, 66, 67].

1.4

Energy State of the Electrode Surface and Spatial Distribution of Nanoclusters

The concept of “active sites” unavoidably raises the question about their physical nature and we should point out that the active sites are probably the most obscure characteristics of the nucleation kinetics. The reason is that, depending on the specific properties of the particular electrochemical system, the active sites may be entirely different nano-objects appearing on or disappearing from the electrode

surface due to various chemical and/or electrochemical reactions taking place prior to or simultaneously with the process of nucleus formation. These could be adsorption and desorption of organic and inorganic ions or molecules, surface transformations within preformed UPD layers, direct oxidation or reduction of the electrode surface etc. All this means that the assumption of an “inert” working electrode is certainly a serious approximation and a theoretical model of nucleus formation on a time-dependent number of active sites is developed in Refs. [7, 66, 67]. Without entering into detail we shall point out that if active sites appear on and disappear from the electrode surface as a result of an electrochemical reaction, parallel to the process of nucleus formation, the time dependence of the number $N(t)$ of nuclei may be expressed by means of the following second-order differential equation [7, 66, 67]:

$$\frac{d^2N}{dt^2} + A \frac{dN}{dt} + B(N - N_0) = 0 \quad (1.24)$$

Here A and B depend on the nucleation frequency $K_n = W\lambda^{-1} \exp[-\Delta\tilde{G}(n_c)/kT]$ and on the frequencies of appearance K_a^+ and disappearance K_a^- of active sites to and from the electrode surface. $N_0 = Z_a^0 + Z_l^0$ is the total number of active sites at time $t = 0$, Z_a^0 and Z_l^0 being the numbers of the available and of the latent active sites at the time moment $t = 0$.

Exact analytical solution of Eq. (1.24) is possible and yields theoretical expressions for the nucleation rate $J(t) = dN(t)/dt$ and for the number of nuclei $N(t)$ in the case of a time-dependent number of active sites. Figure 1.4 illustrates the obtained result and shows that the nucleation rate has a non-zero initial value

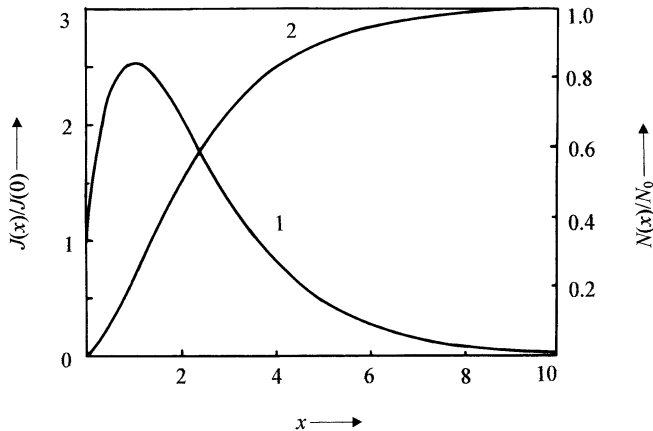


Figure 1.4. Non-dimensional plots $J(x)/J(0)$ (1) and $N(x)/N_0$ (2) versus $x = t/t_m$ calculated according to the theoretical model of nucleus formation on a time-dependent number of active sites [7, 66, 67].

$J(0) = (dN/dt)_{t=0} = K_n Z_a^0$, a zero final value, $J(\infty) = 0$, and displays a maximum, at time $t = t_m$. As for $N(t)$ it changes from zero to the maximal value $N_0 = Z_a^0 + Z_l^0$ at sufficiently long times when all latent active sites are developed and occupied by the nuclei of the new phase.

The detailed theoretical analysis carried out in Refs. [7, 66, 67] shows that, in this complex case of electrochemical phase formation, a stationary state may be established only under special circumstances and after a certain induction period. It turns out, also, that the quantity which we use to measure and to call a *stationary nucleation rate* may provide experimental information not on the *nucleation* kinetics but on the kinetics of *appearance of active sites* on the electrode surface, if this process is the rate determining step in the initial stage of the phase transition. This finding must be taken into consideration when interpreting experimental data on the kinetics of nucleus formation, both on foreign and on native substrates.

An important question closely related to the nucleation kinetics concerns the location of nuclei on the electrode surface. In particular, it turns out to be important for many practical purposes to know whether nanoclusters are randomly distributed on the substrate or whether there is a certain *cluster-cluster* correlation. The most frequently used approach to this problem consists in the statistical analysis of the distances between nearest neighbor clusters and comparison of the obtained results with theoretical formulae based on the Poisson law for a purely random distribution [88, 89]. Here we present some experimental data interpreted by means of the general theoretical expression for the probability distribution function $dP_{v,n}$ of the distances between n th neighbor clusters randomly located within a v -dimensional space, derived in Ref. [90]:

$$dP_{v,n} = \frac{v}{(n-1)!} \left[\frac{\pi^{v/2} N_{0,v}}{\Gamma(1+v/2)} \right]^n r_{v,n}^{v n - 1} \exp \left[- \frac{\pi^{v/2} N_{0,v} r_{v,n}^v}{\Gamma(1+v/2)} \right] dr_{v,n} \quad (1.25)$$

In fact Eq. (1.25) gives us the probability $dP_{v,n}$ for a given cluster to have its n th neighbor at a distance between $r_{v,n}$ and $r_{v,n} + dr_{v,n}$ and in it $N_{0,v}$ is the average cluster density, Γ is the gamma function and v is the space dimension. Thus $v = 1$ if clusters are formed on a step, $v = 2$ if clusters are formed on a surface and $v = 3$ if clusters are incorporated within a three-dimensional matrix, e.g. within the bulk of an electrically conducting medium. Correspondingly, the average distance $\bar{r}_{v,n}$ between clusters is defined as

$$\bar{r}_{v,n} = \int_0^{\infty} r_{v,n} dP_{v,n} \frac{\Gamma(n+1/v)}{(n-1)!} \left[\frac{\Gamma(n+v/2)}{\pi^{v/2} N_{0,v}} \right]^{1/v} \quad (1.26)$$

Figure 1.5 illustrates the correlation between the experimental (histograms) and theoretical (lines) distributions of the distances between first, second and third neighbor silver crystals electrodeposited on a mechanically polished glassy carbon electrode [91]. As seen, in all cases the experimentally measured smallest distances appear with a probability lower than theoretically predicted for a random distribu-

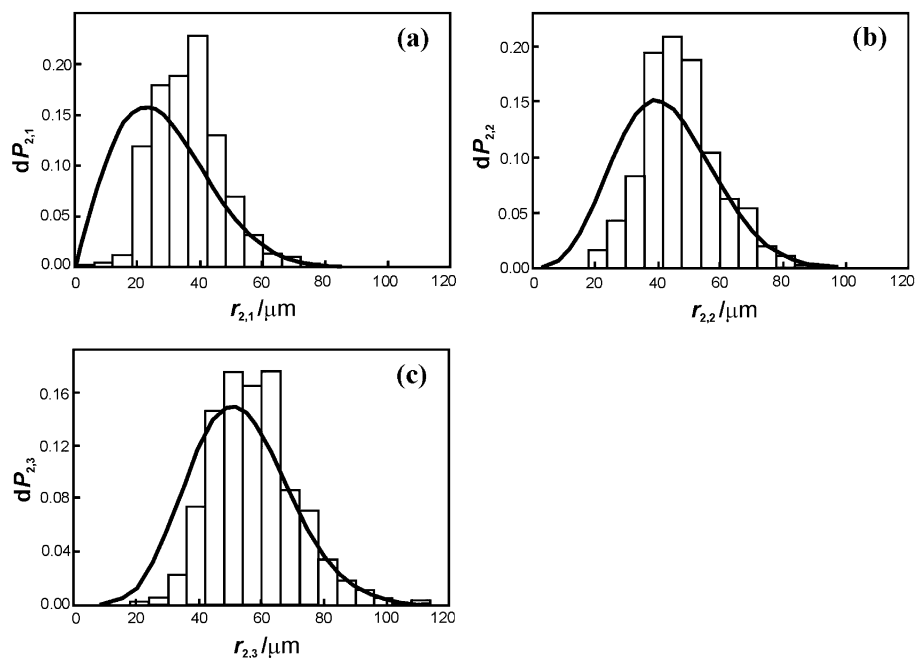


Figure 1.5. Experimental (histograms) and theoretical (lines) distribution of the distances between *first* (a), *second* (b) and *third* (c) neighbor silver crystals electrochemically deposited on a flat glassy carbon electrode, $N_{0,2} = 2.75 \times 10^4 \text{ cm}^{-2}$ [91].

tion, the effect being less pronounced for second and for third neighbor clusters. This should mean that zones of reduced nucleation rate arise around the growing stable clusters, of course, if we assume that the active sites themselves are randomly distributed on the electrode surface. This has been proven to be the case for the mechanically polished glassy carbon working electrode [91]. However, it might not necessarily be true for other amorphous or crystalline substrates.

Deviations from the random distribution were experimentally registered also in other electrochemical systems [76, 79, 92–95] and were also confirmed by means of computer simulations [96, 97]. In the next section we consider the electrochemical growth of nanoclusters and comment upon the physical nature of the zones of reduced nucleation rate.

1.5

Electrochemical Growth of Nanoparticles and Ultrathin Films

The growth kinetics of three- and two-dimensional (3D and 2D) clusters have been examined by many authors and under different experimental conditions account-

ing for various limitation factors (see e.g. Refs. [3–8] and the literature cited therein). Here we present briefly only the basic theoretical and experimental findings.

1.5.1

Growth of 3D Nanoclusters

At a constant overpotential η the current $I_1(t)$ of a single hemispherical cluster growing under the conditions of combined charge transfer and diffusion limitations is given by [98]:

$$I_1(t) = p \left[\frac{1 + nt}{(1 + 2nt)^{1/2}} - 1 \right] \quad (1.27)$$

In Eq. (1.27)

$$p = \frac{4\pi(zFDc_\infty)^2}{i_0} \left\{ \exp\left(-\frac{\alpha zF\eta}{RT}\right) - \exp\left[-\frac{(1 + \alpha)zF\eta}{RT}\right] \right\} \quad (1.28)$$

$$n = \frac{V_M i_0^2}{(zF)^2 D c_\infty} \left\{ \exp\left(\frac{2\alpha zF\eta}{RT}\right) - \exp\left[-\frac{(1 - 2\alpha)zF\eta}{RT}\right] \right\} \quad (1.29)$$

where D is the diffusion coefficient of metal ions and i_0 is the exchange current density at the *cluster–solution* interface boundary.

The growth of a single cluster affects significantly both the concentration and the overpotential distribution in the cluster vicinity [96, 99, 100]. Thus the concentration $c(\rho)$ and the overpotential $\eta(\rho)$ at a distance ρ from the cluster are given by:

$$c(\rho) = c_\infty \left[1 - \frac{I_1(t)}{2\pi\rho zFDc_\infty} \right] \quad (1.30)$$

$$\eta(\rho) = \eta + \frac{RT}{zF} \ln \left[1 - \frac{I_1(t)}{2\pi\rho zFDc_\infty} \right] \quad (1.31)$$

and substituting these two formulae into Eq. (1.21), for the stationary nucleation rate $J_0(\rho)$ at a distance ρ one obtains

$$J_0(\rho) = J_0 \left[1 - \frac{I_1(t)}{2\pi\rho zFDc_\infty} \right]^{n_c+1} \quad (1.32)$$

The solid line in Fig. 1.6 illustrates the non-dimensional distribution of the stationary nucleation rate around a growing hemispherical cluster, if the single atom adsorbed on the electrode surface is a critical nucleus ($n_c = 1$) within the entire zone of reduced concentration and overpotential. However, since the critical nucleus size is a function of the overpotential $\eta(\rho)$ it appears that, in the general case, different clusters may play the role of critical nuclei in the vicinity of the growing

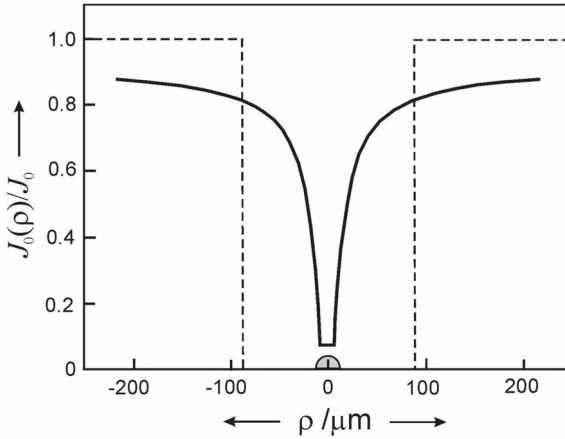


Figure 1.6. Cross section of a non-dimensional distribution of the stationary nucleation rate around a spherical cluster for the case $n_c = 1$ atom (—). Profile of a planar nucleation exclusion zone (---).

supercritical one and this yields much more complex distribution of the nucleation rate [7, 101].

If *multiple* hemispherical clusters form and grow on the electrode surface then the local zones of reduced nucleation rate spread out and gradually overlap, which means that a general theoretical model describing the overall nucleation kinetics should account for the collective interaction between a large number of growing clusters. The problem has no exact solution and a most frequently employed approximation is based on the idea of overlapping *planar diffusion zones* in which nucleation is fully arrested [14, 102–106] (Fig. 1.6). Thus, in the case of growth of clusters under the conditions of complete diffusion control, for the total current one obtains:

$$i_N(t) = \beta zFc \left(\frac{D}{\pi t}\right)^{1/2} \left\{ 1 - \exp\left[-\frac{1}{2}J_0\pi(8\pi cV_M)^{1/2}Dt^2\right] \right\} \quad (1.33)$$

if $N(t)$ clusters are *progressively* formed on the electrode surface during the time interval $(0, t)$ and

$$i_{N_0}(t) = zFc \left(\frac{D}{\pi t}\right)^{1/2} \left\{ 1 - \exp[-N_0\pi(8\pi cV_M)^{1/2}Dt] \right\} \quad (1.34)$$

if N_0 clusters appear *instantaneously* at the initial moment $t = 0$. In Eq. (1.33) β is a numerical constant, which equals 1 according to Refs. [14, 102] and $4/3$ according to Refs. [105, 106].

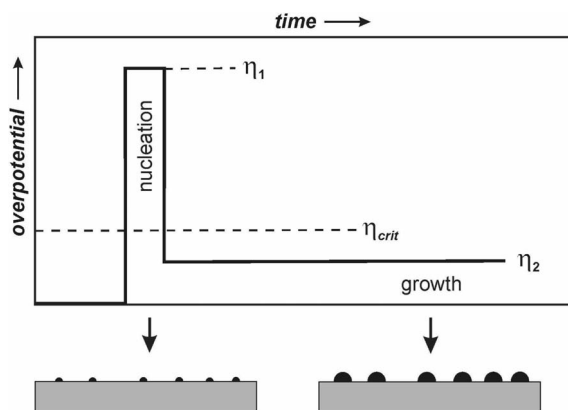


Figure 1.7. Schematic representation of the double-pulse polarization routine for preparation of metal nanoparticles and compact metal films.

A specific feature of electrochemical nucleation is the existence of an overpotential threshold (“critical overpotential” η_{crit}) below which the nucleation rate J_0 is practically zero and above which it raises exponentially (cf. Eq. (1.16)) [1–8]. Based on this feature an efficient double-pulse polarization routine for metal electrodeposition was developed, as illustrated schematically in Fig. 1.7 (see e.g. Refs. [5, 7] and the references cited therein).

The double-pulse technique allows the formation, either *progressively* or *instantaneously*, of a large number of metal clusters during the first short pulse at $\eta_1 \gg \eta_{crit}$. This pulse is followed by a second one of a much lower cathodic overpotential $\eta_2 \ll \eta_{crit}$ during which only further growth of clusters is possible. This polarization routine has been successfully applied both for electrodeposition of metal nanoparticles with a narrow size distribution [107, 108] and for electroplating of compact thin metal films [20, 109, 110].

1.5.2

Growth of 2D Nanoclusters and Formation of UPD Monolayers

As already mentioned in Section 1.2.2, in systems characterized by strong interaction energy between the depositing metal and the foreign substrate the deposition of the bulk metal phase can be preceded by UPD of different low-dimensional metal or alloy phases [5, 11, 51–65, 111–121]. In such systems, at potentials close to the equilibrium potential E_∞ , the foreign substrate is usually covered by condensed UPD monolayers, which can be either commensurate or incommensurate, depending on the crystallographic *deposit–substrate* misfit.

Figures 1.8 and 1.9 illustrate the evolution of surface morphology during the UPD of condensed Ag and Pb monolayers on stepped Au(100) and Ag(111) substrates, respectively [5, 56, 63, 111, 114–117, 120]. As seen in Fig. 1.8, the con-

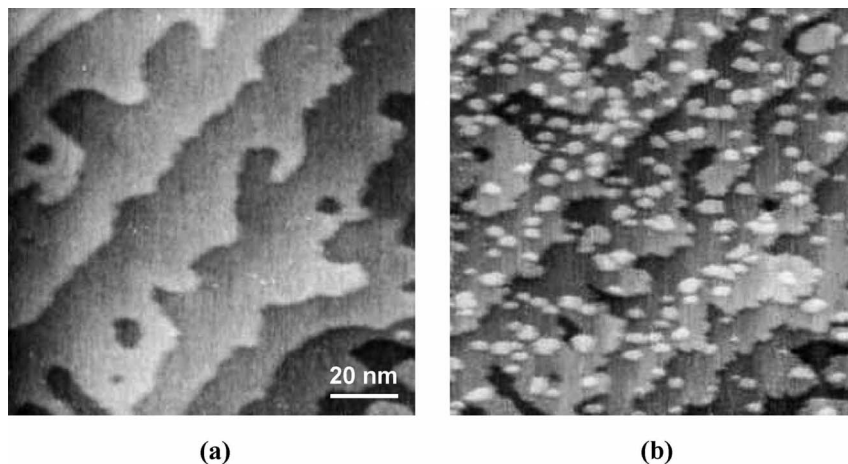


Figure 1.8. UPD of Ag on a stepped Au(100) substrate. Electrolyte: 5 mM Ag_2SO_4 + 0.1 M H_2SO_4 ($T = 298$ K). (a) *in situ* STM image of the substrate surface at underpotential $E - E_\infty = 400$ mV. (b) *in situ* STM image showing the formation of a condensed Ag monolayer at underpotential $E - E_\infty = 15$ mV.

densified Ag monolayer on Au(100) is formed by multiple nucleation and growth of 2D Ag clusters occurring simultaneously at monatomic steps and on flat terraces [116, 117]. The STM imaging with atomic resolution shows that the condensed Ag monolayer is commensurate, as expected because of the very low Ag–Au misfit. In contrast to this, a compressed close-packed incommensurate Pb monolayer is

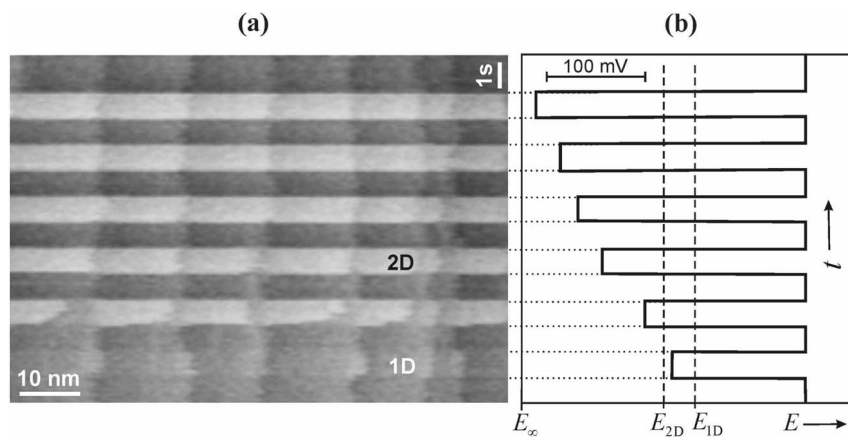


Figure 1.9. UPD of Pb on a stepped Ag(111) substrate. Electrolyte: 5 mM $\text{Pb}(\text{ClO}_4)_2$ + 0.5 M $\text{Na}(\text{ClO}_4)_2$ + 5 mM HClO_4 ($T = 298$ K). (a) *in situ* AFM image showing the 1D and 2D Pb phase formation (b) applied polarization routine.

formed on Ag(111) due to the significant Pb–Ag misfit [5, 56, 63, 111, 115, 116, 120]. Figure 1.9 shows that in this case the formation of the condensed Pb monolayer (2D Pb phase) starts exclusively at substrate monatomic steps. The linescan ($x-t$) AFM image indicates also that the monolayer growth is preceded by a decoration of the monatomic steps and formation of a “1D Pb phase” occurring at potentials more positive than the equilibrium potential E_{2D} of the condensed 2D Pb phase. These observations clearly show that substrate monatomic steps play an important role in the formation of condensed UPD monolayers and have to be taken into account in the theoretical models describing the kinetics of 2D nucleation and growth [56].

As a surface limited process, UPD offers attractive possibilities for surface modification on an atomic scale and preparation of nanomaterials with unconventional chemical and physical properties. Some important examples are summarized schematically in Fig. 1.10. Underpotential codeposition from multicomponent electrolytes is used successfully in the so-called “electrochemical atomic layer epitaxy” (EC-ALE) for a nanoscale controlled preparation of different superlattices and ultrathin films of metals, alloys and semiconducting compounds, as illustrated schematically in Fig. 1.10(a) and (b) [5, 51, 61, 122–124]. Another interesting application of the UPD phenomena is to use an UPD metal layer as a surfactant influencing the kinetics and mechanism of electrochemical growth of a more noble metal [125–128]. In this case, the UPD metal layer floats on the surface of the growing noble metal (Fig. 1.10(c)) and the growth process involves a place-exchange between the depositing metal atoms and the atoms of the UPD layer. It

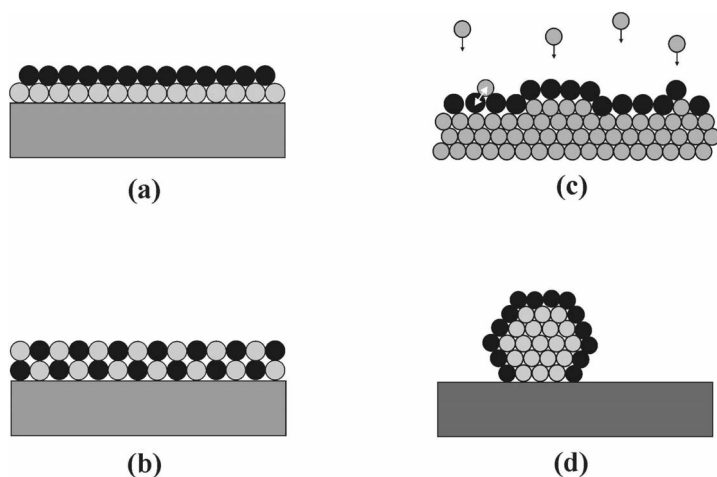


Figure 1.10. Possible applications of UPD in nanotechnology (a schematic representation). (a) deposition of superlattices and multilayers, (b) deposition of ultrathin alloy and compound films, (c) electrochemical surfactant mediated growth, (d) monolayer modification of nanoparticles.

was demonstrated that the use of Pb as a surfactant in the electrochemical deposition of Ag on Ag(111) and Au(111) facilitates a layer-by-layer growth mode [125, 126]. Recently Pb and Tl were used successfully as surfactants enhancing the electrodeposition rate of Au in order to achieve a “superfill” (perfect filling) of nano-sized trenches according to the so-called “curvature enhanced accelerator coverage” (CEAC) mechanism [127, 128]. As illustrated in Fig. 1.10(d), the UPD process can be applied also for surface modification of metal nanoparticles by a monolayer of a second metal [129–131]. The use of substrates such as graphite or glassy carbon, which are inert with respect to metal UPD, is suitable in this case. Noble metal nanoparticles with a controlled size can be electrodeposited on the inert substrate and selectively modified by a subsequent UPD of a less noble metal [131]. Recently such UPD modification was used as an intermediate step in a new technique for preparation of novel electrocatalysts based on Pt monolayers deposited on the surfaces of carbon-supported non-noble metal/noble metal (core/shell) nanoparticles (Ni/Au, Co/Pd and Co/Pt) [132]. In this technique the Pt monolayer is deposited by galvanic displacement of a pre-deposited Cu UPD monolayer. The Pt monolayer electrocatalysts prepared by this technique are characterized by a mass activity higher than that of the commercial Pt-containing catalytic materials [132].

1.6

Localization of Electrocrystallization Processes and Nanostructuring

An important property of electrocrystallization is its high selectivity. This property offers numerous possibilities for localization of electrocrystallization processes and preparation of nanostructures for fundamental research and technological applications. A widely applied method for localized electrocrystallization is based on the use of insulating templates such as lithographically patterned resist layers or nanoporous membranes (see e.g. Refs. [133, 134], Chapter 3 in this book and the references cited therein). The modification of a conducting substrate with an insulating template results in the formation of negative (recessed) structures. A single negative structure of this type is shown schematically in Fig. 1.11. For the filling of such a structure by electrodeposition, its aspect ratio h/d (depth/diameter) and the surface state of the conducting substrate are important. As already discussed in Section 1.4, the energy state of the substrate surface determines the density of active nucleation sites Z_0 and the nucleation rate J_0 . The initial stages of localized electrocrystallization in the negative structure can be characterized by the mean nucleation time $\bar{\tau}_n = \frac{1}{J_0\pi(d/2)^2}$ and the mean time $\bar{\tau}_L = \frac{d}{V_L}$ needed for the first cluster to cover the bottom surface of the structure. Here $\pi(d/2)^2$ and V_L represent the bottom area of the structure and the lateral growth rate of the crystalline cluster, respectively. Two different growth modes can generally be distinguished, depending on the electrocrystallization conditions, as illustrated schematically in Fig. 1.11: (i) a *mononuclear growth mode* occurring at $\bar{\tau}_n \gg \bar{\tau}_g$ through the formation and growth

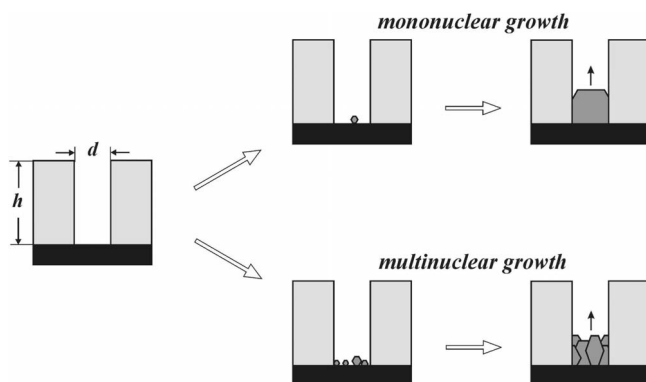


Figure 1.11. Mono- and multinuclear growth modes in a negative insulator/conductor structure (a schematic representation).

of a single nucleus and (ii) a *multinuclear growth mode* occurring at $\bar{\tau}_n \ll \bar{\tau}_g$ through the formation and growth of a large number of crystalline nuclei. The localized electrocrystallization by the mono- or multinuclear growth mode can be applied successfully for the fabrication of single- or polycrystalline metal nanowires with extremely high aspect ratios, as demonstrated recently using nanoporous polymer membranes as templates [135, 136]. Another approach to the preparation of various metal and compound nanowires is based on the preferred electrocrystallization at step edges (see e.g. Refs. [108, 137–139] and Chapter 9 in this book).

The invention of scanning probe microscopy (SPM) opened a new window not only for *in situ* surface studies of electrode surfaces at an atomic scale but also for the local nanostructuring and modification of surfaces by electrochemical phase formation using the SPM tip as a nanoelectrode (cf. Fig. 1.12(a)). In this case the ratio between the polarization resistance R_{pol} (including the resistances for the charge transfer through the new formed phase and interfaces) and the electrolyte resistance R_{el} in the electrochemical *in situ* SPM cell [140–142] is crucial for the localization. Electrochemical phase formation can be localized if $R_{pol} \ll R_{el}$ (cf. Fig. 1.12(b)). Such localized electrocrystallization was successfully realized by means of *in situ* STM in the case of metal electrodeposition from dilute electrolyte solutions (see e.g. Refs. [56, 63, 69–72] and Chapter 6 in this book). For $R_{pol} \gg R_{el}$, however, the formation of the new phase in the electrochemical *in situ* SPM cell becomes fully delocalized. Thus, no localized formation of insulating anodic oxides could be achieved by *in situ* SPM, even in pure water, due to the very high resistance of the oxide phases ($R_{pol} \gg R_{el}$). In this case the localization of the oxidation process can be realized by *ex situ* SPM in a humid atmosphere. Under these conditions the water vapors condense between the SPM tip and the substrate forming a water meniscus, which acts as electrolyte and localizes the electrochemical oxidation (Fig. 1.13a). This approach is widely used for preparation of various nanostruc-

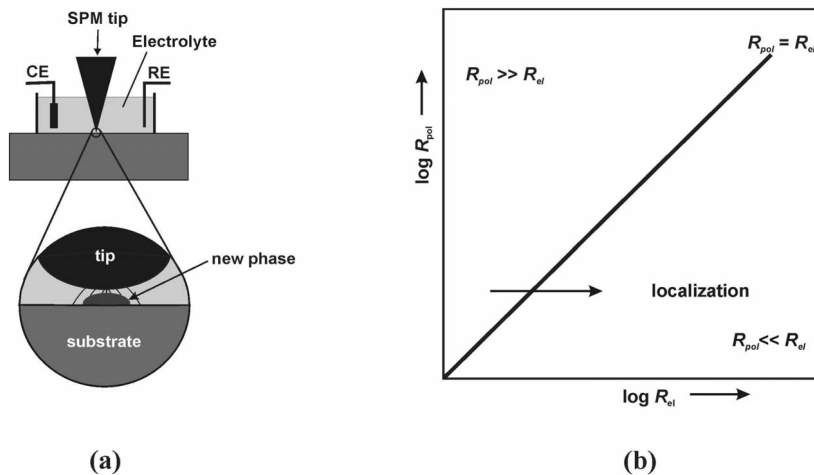


Figure 1.12. (a) Schematic representation of localized electrodeposition in the *in situ* SPM cell. (b) Schematic $\log R_{pol} - \log R_{et}$ plot showing the localization conditions.

tures by local AFM tip-induced anodic oxidation of semiconductors and valve metals [23, 46, 140–148]. Figure 1.13(b) shows, as an example, a pattern composed of linear oxide structures fabricated by scanning a conducting AFM tip on a p-Si substrate in humid air [142]. The height and the width of the oxide structures depend on the applied bias voltage ΔU , the scan rate of the AFM tip and the relative humidity of the atmosphere. Figures 1.14(a) and (b) show the voltage dependence

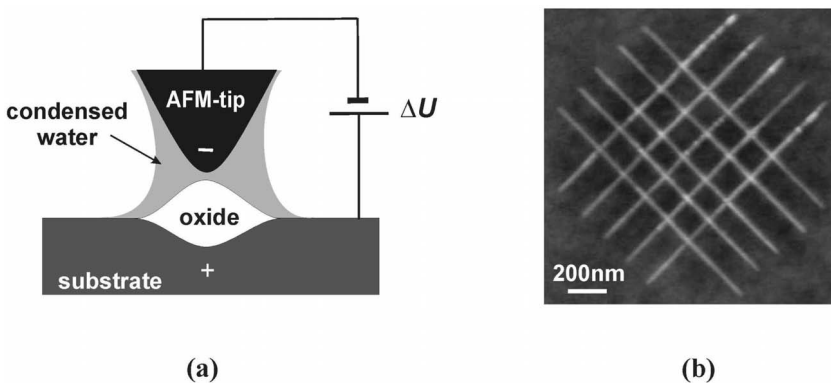


Figure 1.13. Localized anodic oxidation induced by the AFM tip. (a) Schematic representation of the electrochemical nanocell formed between the AFM tip and the substrate in humid atmosphere. (b) SiO_2 pattern fabricated by local AFM tip-induced oxidation of p-Si(111) (bias voltage $\Delta U = 8.5$ V, tip scan rate 200 nm s^{-1} , relative humidity 3%).

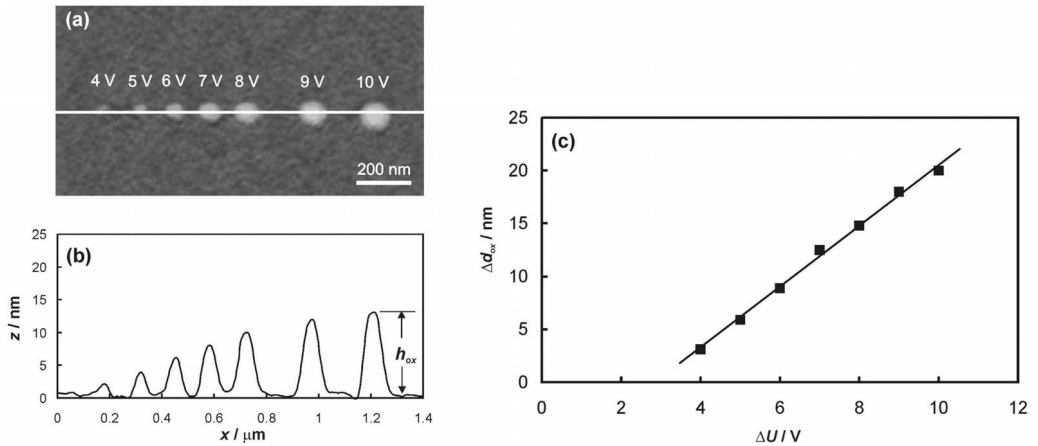


Figure 1.14. (a) Nb_2O_5 dots generated on a 20 nm thick Nb film by a fixed AFM tip applying different bias voltages ΔU (polarization time $t_p = 10$ s, relative humidity 40%). (b) Single line section of the AFM image in (a). (c) $\Delta d_{ox} - \Delta U$ dependence derived from (b).

of Nb_2O_5 dots generated by localized anodic oxidation of a thin Nb film at fixed AFM tip position (point oxidation) and constant polarization time. The anodic oxidation of Nb is a substrate-consuming electrode reaction ($2\text{Nb} + 5\text{H}_2\text{O} \rightarrow \text{Nb}_2\text{O}_5 + 10\text{H}^+ + 10\text{e}^-$), in which two moles Nb are needed for the formation of one mole Nb_2O_5 . Thus, the increase in the thickness Δd_{ox} of the generated oxide dots can be estimated from their height h_{ox} (cf. Fig. 1.14(b)) using the relation $\Delta d_{ox} = 1.56h_{ox}$ where the factor 1.56 is determined by the molar volumes of Nb and Nb_2O_5 [140]. The derived linear $\Delta d_{ox} - \Delta U$ dependence shown in Fig. 1.14(c) is in good agreement with the high-field law of the oxide growth [23, 45].

The preparation of lateral metal–insulator–metal (MIM) structures by local oxidation is of particular interest for nanoelectronics. Thus it is essential to find optimal conditions for a complete AFM tip-induced local oxidation of a thin metal film. Figure 1.15 shows an experimental routine, which has been used to control the complete local oxidation of a 5 nm thick Nb film sputtered on a thermally-oxidized silicon substrate [140]. Square structures were first fabricated with a scan rate of the AFM tip of 200 nm s^{-1} and bias voltages ΔU ranging between 6 and 12 V (Fig. 1.15(a)). In a second step, an attempt was made for a local oxidation of Nb along a 500 nm line inside each square structure in order to check if there is still an electric contact between Nb film inside and outside each square structure (Fig. 1.15(b)). The results obtained show that under the given experimental conditions a complete oxidation of the thin Nb film can be achieved at bias voltages higher than 10 V. The generated structures are presented schematically in Fig. 1.15(c). This approach can be applied successfully for the fabrication of different lateral MIM structures by local AFM tip-induced nanooxidation of ultrathin films of valve metals.

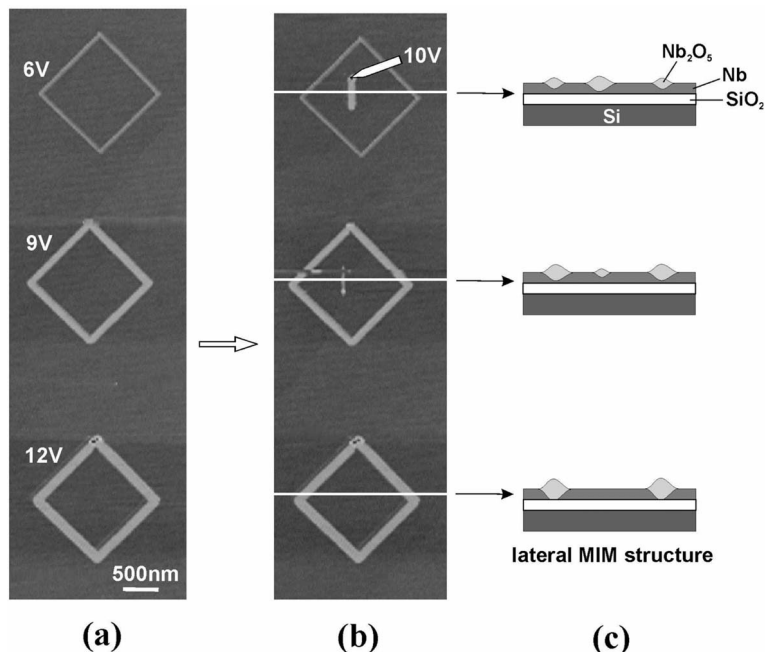


Figure 1.15. Experimental routine used for checking the complete local oxidation of a Nb thin film (Nb film thickness 5 nm, AFM tip scan rate 200 nm s^{-1} , relative humidity 40%). (a) Nb₂O₅ structures prepared by tip-induced oxidation with different bias voltages. (b) AFM image obtained after an attempt for tip-induced oxidation with $\Delta U = 10 \text{ V}$ inside the square structures in (a). (c) Schematic representation of the structures in (b).

1.7

Conclusion

In this chapter we discuss some selected aspects of electrocrystallization, which are relevant for a better understanding of both the nucleation and growth phenomena at an atomic level and the preparation of various nanostructures by electrochemical means. The presented examples demonstrate in how many respects the concepts of electrocrystallization affect the future development of nanotechnology. In particular this applies to the preparation of nanoparticles by controlled nucleation and growth, to the formation of atomic scale thin films and superlattices by underpotential deposition, to the fabrication of single- and polycrystalline nanowires by template electrodeposition and selective electrocrystallization at step edges and to the nanostructuring of metal and semiconductor substrates by SPM tip-induced electrocrystallization of metals and oxides.

Acknowledgments

The authors gratefully acknowledge the financial support given by the Research Centre Jülich, the Bulgarian Academy of Sciences and the German Research Association (DFG).

References

- 1 M. VOLMER, *Das elektrolytische Kristallwachstum*, Hermann et Cie, Paris, 1934.
- 2 M. VOLMER, *Kinetik der Phasenbildung*, Steinkopf, Dresden, 1939.
- 3 H. FISCHER, *Elektrolytische Abscheidung und Elektrokristallisation von Metallen*, Springer, Berlin, 1954.
- 4 J. O'M. BOCKRIS, G. A. RAZUMNEY, *Fundamental Aspects of Electrocrystallization*, Plenum Press, New York, 1967.
- 5 E. BUDEVSKI, G. STAIKOV, W. J. LORENZ, *Electrochemical Phase Formation and Growth – An Introduction to the Initial Stages of Metal Deposition*, VCH, Weinheim, 1996.
- 6 M. PAUNOVIC, M. SCHLESINGER, *Fundamentals of Electrochemical Deposition*, Wiley-Interscience, New York, 1998.
- 7 A. MILCHEV, *Electrocrystallization: Fundamentals of Nucleation and Growth*, Kluwer Academic Publishers, Boston/Dordrecht/London, 2002.
- 8 M. FLEISCHMANN, H. R. THIRSK, in *Advances in Electrochemistry and Electrochemical Engineering*, Vol. 3, P. DELAHAY (Ed.), Wiley, New York, 1963.
- 9 H. FISCHER, *Angew. Chem. Int. Ed. Engl.* 1969, 8, 108.
- 10 J. O'M. BOCKRIS, A. R. DESPIC, in *Physical Chemistry – An Advanced Treatise*, Vol. IXB, H. EYRING, D. HENDERSON, W. JOST (Eds.), Academic Press, New York, 1970.
- 11 D. M. KOLB, in *Advances in Electrochemistry and Electrochemical Engineering*, Vol. 11, H. GERISCHER, C. W. TOBIAS (Eds.), Wiley, New York, 1978.
- 12 E. BUDEVSKI, V. BOSTANOV, G. STAIKOV, *Annu. Rev. Mater. Sci.* 1980, 10, 85.
- 13 E. BUDEVSKI, in *Comprehensive Treatise of Electrochemistry*, Vol. 7, B. E. CONWAY, J. O'M. BOCKRIS, E. YEAGER, S. U. M. KAHN, R. E. WHITE (Eds.), Plenum Press, New York, 1983.
- 14 B. SCHARIFKER, G. HILLS, *Electrochim. Acta* 1983, 28, 879.
- 15 A. MILCHEV, *Contemp. Phys.* 1991, 32, 321.
- 16 P. ALLONGUE, in *Modern Aspects of Electrochemistry*, Vol. 23, B. E. CONWAY, J. O'M. BOCKRIS, R. E. WHITE (Eds.), Plenum Press, New York, 1992.
- 17 E. MICHAILOVA, I. VITANOVA, D. STOYCHEV, A. MILCHEV, *Electrochim. Acta* 1993, 38, 2455.
- 18 A. I. DANILOV, E. B. MOLODKINA, YU. M. POLUKAROV, *Russ. J. Electrochem.* 1994, 30, 674.
- 19 M. H. HÖLZLE, V. ZWING, D. M. KOLB, *Electrochim. Acta* 1995, 40, 1237.
- 20 G. OSKAM, J. G. LONG, A. NATARAJAN, P. C. SEARSON, *J. Phys. D: Appl. Phys.* 1998, 31, 1927.
- 21 E. BUDEVSKI, G. STAIKOV, W. J. LORENZ, *Electrochim. Acta* 2000, 45, 2499.
- 22 R. KRUMM, B. GUEL, C. SCHMITZ, G. STAIKOV, *Electrochim. Acta* 2000, 45, 3255.
- 23 G. STAIKOV, in *Electrochemical Microsystem Technologies*, J. W. SCHULTZE, T. OSAKA, M. DATTA (Eds.), Taylor & Francis, London and New York, 2002.
- 24 K. MÁRQUEZ, G. STAIKOV, J. W. SCHULTZE, *Electrochim. Acta* 2003, 48, 875.
- 25 A. MILCHEV, T. ZAPRYANOVA, *Electrochim. Acta* 2006, 51, 2926.

- 26 P. C. ANDRICACOS, C. UZOH, J. O. DUKOVIC, J. HORKANS, H. DELIGIANNI, *IBM J. Res. Develop.* **1998**, *42*, 567.
- 27 P. C. ANDRICACOS, *Interface* **1999**, *8*, 32.
- 28 A. BRENNER, *Electrodeposition of Alloys*, Academic Press, New York, **1963**.
- 29 K. M. GORBUNOVA, YU. M. POLUKAROV, in *Advances in Electrochemistry and Electrochemical Engineering*, Vol. 5, P. DELAHAY (Ed.), Wiley, New York, **1967**.
- 30 F. A. KRÖGER, *J. Electrochem. Soc.* **1978**, *125*, 2028.
- 31 P. C. ANDRICACOS, C. ARANA, J. TABIB, J. DUKOVIC, L. T. ROMANKIW, *J. Electrochem. Soc.* **1989**, *136*, 1336.
- 32 A. MILCHEV, R. LACMANN, *J. Cryst. Growth* **1991**, *110*, 919, 925.
- 33 K. RAJESHWAR, *Adv. Mater.* **1992**, *4*, 23.
- 34 D. LANDOLT, *Electrochim. Acta* **1994**, *39*, 1075.
- 35 G. HODES, in *Physical Electrochemistry*, I. RUBINSTEIN (Ed.), Marcel Dekker, New York, **1995**.
- 36 E. MICHAILOVA, A. MILCHEV, R. LACMANN, *Electrochim. Acta* **1996**, *41*, 329.
- 37 A. MILCHEV, *Electrochim. Acta* **1997**, *42*, 1533.
- 38 A. MILCHEV, E. MICHAILOVA, T. ZAPRYANOVA, *Electrochem. Commun.* **2004**, *6*, 713.
- 39 A. MILCHEV, G. STAIKOV, *Indian J. Chem.* **2005**, *44A*, 899.
- 40 L. YOUNG, *Anodic Oxide Films*, Academic Press, London, **1961**.
- 41 D. A. VERMILYEA, in *Advances in Electrochemistry and Electrochemical Engineering*, Vol. 3, P. DELAHAY (Ed.), Wiley, New York, **1963**.
- 42 M. J. DIGNAM, in *Comprehensive Treatise of Electrochemistry*, Vol. 4, J. O'M. BOCKRIS, B. E. CONWAY, E. YEAGER, R. E. WHITE (Eds.), Plenum Press, New York, **1981**.
- 43 M. FLEISCHMANN, L. J. LI, L. M. PETER, *Electrochim. Acta* **1989**, *34*, 475.
- 44 B. E. CONWAY, B. BARNETT, H. ANGERSTEIN-KOZLOWSKA, B. V. TILAK, *J. Chem. Phys.* **1990**, *93*, 8361.
- 45 J. W. SCHULTZE, M. M. LOHRENGEL, *Electrochim. Acta* **2000**, *45*, 2499.
- 46 H. BLOEß, G. STAIKOV, J. W. SCHULTZE, *Electrochim. Acta* **2001**, *47*, 335.
- 47 V. LEHMANN, *Electrochemistry of Silicon: Instrumentation, Science, Materials and Applications*, Wiley-VCH, Weinheim, **2002**.
- 48 G. BINNIG, H. ROHRER, *Helv. Phys. Acta* **1982**, *55*, 726.
- 49 P. LUSTENBERGER, H. ROHRER, R. CHRISTOPH, H. SIEGENTHALER, *J. Electroanal. Chem.* **1988**, *243*, 225.
- 50 H. SIEGENTHALER, in *Scanning Tunneling Microscopy II*, Springer Ser. Surf. Sci., Vol. 28, R. WIESENDANGER, H.-J. GÜNTHERODT (Eds.), Springer, Berlin, **1992**.
- 51 G. STAIKOV, K. JÜTTNER, W. J. LORENZ, E. BUDEVSKI, *Electrochim. Acta* **1994**, *39*, 1019.
- 52 A. A. GEWIRTH, H. SIEGENTHALER (Eds.), *Nanoscale Probes of the Solid/Liquid Interface*, Kluwer Academic Publishers, Dordrecht/Boston/London, **1995**.
- 53 P. ALLONGUE, in *Advances in Electrochemical Science and Engineering*, Vol. 4, H. GERISCHER, C. W. TOBIAS (Eds.), VCH, Weinheim, **1995**.
- 54 W. PLIETH, W. J. LORENZ (Eds.), *Electrochemical Nanotechnology*, Wiley-VCH, Weinheim, **1998**.
- 55 K. ITAYA, *Prog. Surf. Sci.* **1998**, *58*, 121.
- 56 G. STAIKOV, W. J. LORENZ, E. BUDEVSKI, in *Imaging of Surfaces and Interfaces (Frontiers in Electrochemistry*, Vol. 5), J. LIPKOWSKI, P. N. ROSS (Eds.), Wiley-VCH, New York, **1999**.
- 57 R. J. NICHOLS, in *Imaging of Surfaces and Interfaces (Frontiers in Electrochemistry*, Vol. 5), P. N. ROSS, J. LIPKOWSKI (Eds.), Wiley-VCH, New York, **1999**.
- 58 T. P. MOFFAT, in *Electroanalytical Chemistry*, Vol. 21, A. J. BARD, I. RUBINSTEIN (Eds.), Marcel Dekker, New York, **1999**.
- 59 D. M. KOLB, *Electrochim. Acta* **2000**, *45*, 2387.
- 60 D. M. KOLB, in *Advances in Electrochemical Science and Engineering*, Vol. 7, R. C. ALKIRE, D. M. KOLB (Eds.), Wiley-VCH, Weinheim, **2001**.

- 61 J. L. STICKNEY, in *Advances in Electrochemical Science and Engineering*, Vol. 7, R. C. ALKIRE, D. M. KOLB (Eds.), Wiley-VCH, Weinheim, 2001.
- 62 D. P. BARKEY, in *Advances in Electrochemical Science and Engineering*, Vol. 7, R. C. ALKIRE, D. M. KOLB (Eds.), Wiley-VCH, Weinheim, 2001.
- 63 W. J. LORENZ, G. STAIKOV, W. SCHINDLER, W. WIESBECK, *J. Electrochem. Soc.* **2002**, 149, K47.
- 64 W. POLEWSKA, R. J. BEHM, O. M. MAGNUSSEN, *Electrochim. Acta* **2003**, 48, 2915.
- 65 W. FREYLAND, C. A. ZELL, S. ZEIN EL ABEDIN, F. ENDRES, *Electrochim. Acta* **2003**, 48, 3053.
- 66 A. MILCHEV, *J. Electroanal. Chem.*, **1998**, 457, 35.
- 67 A. MILCHEV, *J. Electroanal. Chem.*, **1998**, 457, 47.
- 68 A. MILCHEV, E. MICHAILOVA, *Electrochem. Commun.*, **2000**, 2, 15.
- 69 R. T. PÖTZSCHKE, G. STAIKOV, W. J. LORENZ, W. WIESBECK, *J. Electrochem. Soc.*, **1999**, 146, 141.
- 70 W. SCHINDLER, D. HOFMANN, J. KIRSCHNER, *J. Electrochem. Soc.*, **2001**, 148, C124.
- 71 W. SCHINDLER, P. HUGELMANN, M. HUGELMANN, F. X. KÄRTNER, *J. Electroanal. Chem.*, **2002**, 522, 49.
- 72 R. WIDMER, H. SIEGENTHALER, *Electrochem. Commun.*, **2005**, 7, 421.
- 73 A. MILCHEV, S. STOYANOV, *J. Electroanal. Chem.*, **1976**, 72, 33.
- 74 S. STOYANOV, in *Current Topics in Materials Science*, Vol. 3, E. KALDIS (Ed.), North-Holland, Amsterdam, 1978.
- 75 J. MOSTANY, J. PARRA, B. R. SCHARIFKER, *J. Appl. Electrochem.*, **1986**, 16, 333.
- 76 A. SERRUYA, B. R. SCHARIFKER, I. GONZALEZ, M. T. OROPEZA, M. PALOMAR-PARDAVE, *J. Appl. Electrochem.*, **1996**, 26, 451.
- 77 M. PALOMAR-PARDAVE, M. TERESA RAMIREZ, I. GONZALEZ, A. SERRUYA, B. R. SCHARIFKER, *J. Electrochem. Soc.*, **1996**, 143, 1551.
- 78 A. KELAIDPOULOU, G. KOKKINIDIS, A. MILCHEV, *J. Electroanal. Chem.* **1998**, 444, 195.
- 79 A. SERRUYA, J. MOSTANY, B. R. SCHARIFKER, *J. Electroanal. Chem.*, **1999**, 464, 39.
- 80 A. MILCHEV, D. STOYCHEV, V. LAZAROV, A. PAPOUTSIS, G. KOKKINIDIS, *J. Cryst. Growth*, **2001**, 226, 138.
- 81 M. ARBIB, B. ZHANG, V. LAZAROV, D. STOYCHEV, A. MILCHEV, C. BUSSHERMAN, *J. Electroanal. Chem.*, **2001**, 510, 67.
- 82 L. H. MENDOZA-HUIZAR, J. ROBLES, M. PALOMAR-PARDAVE, *J. Electroanal. Chem.*, **2002**, 521, 95.
- 83 L. H. MENDOZA-HUIZAR, J. ROBLES, M. PALOMAR-PARDAVE, *J. Electroanal. Chem.*, **2003**, 545, 39.
- 84 L. H. MENDOZA-HUIZAR, J. ROBLES, M. PALOMAR-PARDAVE, *J. Electrochem. Soc.*, **2005**, 152, 95.
- 85 R. BECKER, W. DÖRING, *Ann. Phys.*, **1935**, 24, 719.
- 86 Ya. B. ZELDOVICH, *Acta Physicochim. USSR*, **1943**, 18, 1.
- 87 A. MILCHEV, S. STOYANOV, R. KAISCHEW, *Thin Solid Films*, **1974**, 22, 255, 267.
- 88 P. HERTZ, *Math. Ann.*, **1909**, 67, 387.
- 89 S. CHANDRASEKHAR, *Rev. Mod. Phys.*, **1943**, 15, 1.
- 90 A. MILCHEV, *J. Chem. Phys.*, **1994**, 100, 5160.
- 91 A. MILCHEV, E. MICHAILOVA, I. LESIGIRASKA, *Electrochem. Commun.*, **2000**, 2, 407.
- 92 W. S. KRUIJT, M. SLUYTERS-REHBACH, J. H. SLUYTERS, A. MILCHEV, *J. Electroanal. Chem.*, **1994**, 371, 13.
- 93 J. MOSTANY, A. SERRUYA, B. R. SCHARIFKER, *J. Electroanal. Chem.*, **1995**, 383, 33.
- 94 U. SCHMIDT, M. DONTEN, J. G. OSTERYOUNG, *J. Electrochem. Soc.*, **1997**, 144, 2013.
- 95 S. IVANOV, V. TSAKOVA, *J. Appl. Electrochem.*, **2002**, 32, 709.
- 96 A. MILCHEV, W. S. KRUIJT, M. SLUYTERS-REHBACH, J. H. SLUYTERS, *J. Electroanal. Chem.*, **1993**, 362, 21.
- 97 V. TSAKOVA, A. MILCHEV, *J. Electroanal. Chem.*, **1998**, 451, 211.
- 98 S. FLETCHER, *J. Cryst. Growth*, **1983**, 62, 505.
- 99 A. MILCHEV, *J. Appl. Electrochem.*, **1990**, 20, 307.

- 100 A. MILCHEV, J. *Electroanal. Chem.*, **1991**, 312, 267.
- 101 A. MILCHEV, L. HEERMAN, *Electrochim. Acta*, **2003**, 48, 2903.
- 102 G. GUNAWARDENA, G. HILLS, I. MONTENEGRO, B. SCHARIFKER, *J. Electroanal. Chem.*, **1982**, 138, 225.
- 103 B. R. SCHARIFKER, J. MOSTANY, *J. Electroanal. Chem.*, **1984**, 177, 13.
- 104 M. V. MIRKIN, A. P. NILOV, *J. Electroanal. Chem.*, **1990**, 283, 35.
- 105 L. HEERMAN, A. TARALLO, *J. Electroanal. Chem.*, **1999**, 470, 70.
- 106 L. HEERMAN, E. MATTHIJS, S. LANGEROCK, *Electrochim. Acta*, **2000**, 47, 905.
- 107 H. LIU, F. FAVIER, K. NG, M. P. ZACH, R. M. PENNER, *Electrochim. Acta*, **2001**, 47, 671.
- 108 R. M. PENNER, *J. Phys. Chem. B*, **2002**, 106, 3339.
- 109 K. MÁRQUEZ, G. STAIKOV, J. W. SCHULTZE, *Trans. IMF*, **2002**, 80, 73.
- 110 K. MÁRQUEZ, R. ORTIZ, J. W. SCHULTZE, O. P. MÁRQUEZ, J. MÁRQUEZ, G. STAIKOV, *Electrochim. Acta*, **2003**, 48, 711.
- 111 D. CARNAL, P. I. ODEN, U. MÜLLER, E. SCHMIDT, H. SIEGENTHALER, *Electrochim. Acta*, **1995**, 40, 1223.
- 112 G. STAIKOV, in *Nanoscale Probes of the Solid/Liquid Interface*, A. A. GEWIRTH, H. SIEGENTHALER (Eds.), Kluwer Academic Publishers, Dordrecht/Boston/London, **1995**.
- 113 U. SCHMIDT, S. VINZELBERG, G. STAIKOV, *Surf. Sci.*, **1996**, 348, 261.
- 114 G. STAIKOV, W. J. LORENZ, *Can. J. Chem.*, **1997**, 75, 1624.
- 115 J. SACKMANN, A. BUNK, R. T. PÖTZSCHKE, G. STAIKOV, W. J. LORENZ, *Electrochim. Acta*, **1998**, 43, 2863.
- 116 S. GARCIA, D. SALINAS, C. MAYER, E. SCHMIDT, G. STAIKOV, W. J. LORENZ, *Electrochim. Acta*, **1998**, 43, 3007.
- 117 G. STAIKOV, W. J. LORENZ, *Z. Phys. Chem.*, **1999**, 208, 17.
- 118 S.-J. HSIEH, A. A. GEWIRTH, *Langmuir*, **2000**, 9501.
- 119 R. VIDU, S. HARA, *Surf. Sci.*, **2000**, 452, 229.
- 120 R. WIDMER, H. SIEGENTHALER, *J. Electrochem. Soc.*, **2004**, 151, E238.
- 121 S. GARCIA, D. R. SALINAS, G. STAIKOV, *Surf. Sci.*, **2005**, 576, 9.
- 122 J. L. STICKNEY, in *Electroanalytical Chemistry*, Vol. 21, A. J. BARD, I. RUBINSTEIN (Eds.), Marcel Dekker, New York, **1999**.
- 123 H. J. PAULING, K. JÜTTNER, *Electrochim. Acta*, **1992**, 37, 2237.
- 124 H. J. PAULING, G. STAIKOV, K. JÜTTNER, *J. Electroanal. Chem.*, **1994**, 376, 179.
- 125 K. SIERADZKI, S. R. BRANKOVICH, N. DIMITROV, *Science*, **1999**, 284, 138.
- 126 S. R. BRANKOVICH, N. DIMITROV, K. SIERADZKI, *Electrochem. Solid-State Lett.*, **1999**, 2, 443.
- 127 D. JOSELL, C. R. BEAUCHAMP, D. R. KELLEY, C. A. WITT, T. P. MOFFAT, *Electrochem. Solid-State Lett.*, **2005**, 8, C54.
- 128 D. JOSELL, D. WHEELER, T. P. MOFFAT, *J. Electrochem. Soc.*, **2006**, 153, C11.
- 129 K. SASAKI, Y. MO, J. X. WANG, M. BALASUBRAMANIAN, F. URIBE, J. MCBREEN, R. R. ADZIC, *Electrochim. Acta*, **2003**, 48, 3841.
- 130 J. ZHANG, Y. MO, M. B. VUKMIROVIC, R. KLIE, K. SASAKI, R. R. ADZIC, *J. Phys. Chem. B*, **2004**, 108, 10995.
- 131 L. KOMSIYSKA, G. STAIKOV, unpublished results.
- 132 J. ZHANG, F. H. B. LIMA, M. H. SHAO, K. SASAKI, J. X. WANG, J. HANSON, R. R. ADZIC, *J. Phys. Chem. B*, **2005**, 109, 22701.
- 133 J. O. DUKOVIC, in *Advances in Electrochemical Science and Engineering*, Vol. 3, H. GERISCHER, C. W. TOBIAS (Eds.), VCH, Weinheim, **1994**.
- 134 C. R. MARTIN, *Science*, **1994**, 266, 1961.
- 135 G. YI, W. SCHWARZACHER, *Appl. Phys. Lett.*, **1999**, 74, 1746.
- 136 T. W. CORNELIUS, J. BRÖTZ, N. CHTANKO, D. DOBREV, G. MIEHE, R. NEUMANN, M. E. TOIMIL MOLARES, *Nanotechnology*, **2005**, 16, S246.
- 137 E. C. WALTER, B. J. MURRAY, F. FAVIER, G. KALTENPOTH, M. GRUNZE, R. M. PENNER, *J. Phys. Chem. B*, **2002**, 106, 11407.

- 138 Q. LI, J. T. NEWBERG, E. C. WALTER, J. C. HEMMINGER, R. M. PENNER, *Nano Lett.*, **2004**, 4, 277.
- 139 E. J. MENKE, Q. LI, R. M. PENNER, *Nano Lett.*, **2004**, 4, 2009.
- 140 A. HEIDELBERG, C. ROZENKRANZ, J. W. SCHULZE, Th. SCHÄPERS, G. STAIKOV, *Surf. Sci.*, **2005**, 597, 173.
- 141 J. W. SCHULZE, A. HEIDELBERG, C. ROZENKRANZ, Th. SCHÄPERS, G. STAIKOV, *Electrochim. Acta*, **2005**, 51, 775.
- 142 H. BLOESS, PhD Thesis, University of Düsseldorf, **2002**.
- 143 J. A. DAGATA, J. SCHNEIR, H. H. HARARY, C. J. EVANS, M. T. POSTEK, J. BENNET, *Appl. Phys. Lett.*, **1990**, 56, 2001.
- 144 H. SUGIMURA, T. UCHIDA, N. KITAMURA, H. MASUHARA, *Appl. Phys. Lett.*, **1993**, 63, 1288.
- 145 J. A. DAGATA, T. INOUE, J. ITOH, K. MATSUMOTO, H. YOKOYAMA, *J. Appl. Phys.*, **1998**, 84, 6891.
- 146 E. DUBOIS, J. L. BUBENDORFF, *J. Appl. Phys.*, **2000**, 87, 8148.
- 147 E. S. SNOW, G. G. JEMIGAN, P. M. CAMPBELL, *Appl. Phys. Lett.*, **2000**, 76, 1782.
- 148 N. FARKAS, G. ZHANG, E. A. EVANS, R. D. RAMSIER, J. A. DAGATA, *J. Vac. Sci. Technol. A*, **2003**, 21, 1188.

2 Computer Simulations of Electrochemical Low-dimensional Metal Phase Formation

Marcelo M. Mariscal and Ezequiel P. M. Leiva

2.1 Introduction

The understanding of surface processes at the atomic level has undergone a dramatic change after the invention of scanning tunneling microscopy (STM) [1] and atomic force microscopy (AFM) [2] techniques. Other related techniques have also been developed, that share the common feature that a solid probe with a sharp tip is physically scanned, by means of piezoelectric translators, over the surface of a sample, with a tip/sample separation of the order of ångströms. The measuring instrument related to these techniques is generally called a scanning probe microscope (SPM). These new developments, which have attracted the attention of many surface scientists around the world, rapidly found application in electrochemistry [3], opening the gate to a new era that we could call the era of surface nanoelectrochemistry. In the conventional electrochemical techniques the information obtained is global, in the sense that the information obtained after the application of a perturbation is an average of the answer from the different parts of the surface. On the other hand, electrochemical SPM techniques give detailed information from a limited region of the surface, which in some cases, when atomic resolution is obtained, comes down to the behavior of single atoms. Thus, in many cases atomic or molecular information must be made compatible with an average response of the whole system. In some sense, this is similar to the problem subject of statistical thermodynamics: a link must be found between the fine grained molecular information and the emerging thermodynamic properties. However, the main problem with straightforward application of the well-known statistical mechanics machinery is that very few systems are exactly solvable. The partition function of the system, that is, the sum over the possible states of the systems, usually involves so many terms (often infinitely many) that the problem is not tractable analytically. After the invention of digital machines capable of performing numerical calculations, a new way to study many physical, chemical and biological systems was generated, the so-called "computer simulation". Up to now many different approaches have been taken, depending on the problem to be solved. In general, the methods can be divided into three groups: deterministic, quasi-deterministic and stochastic.

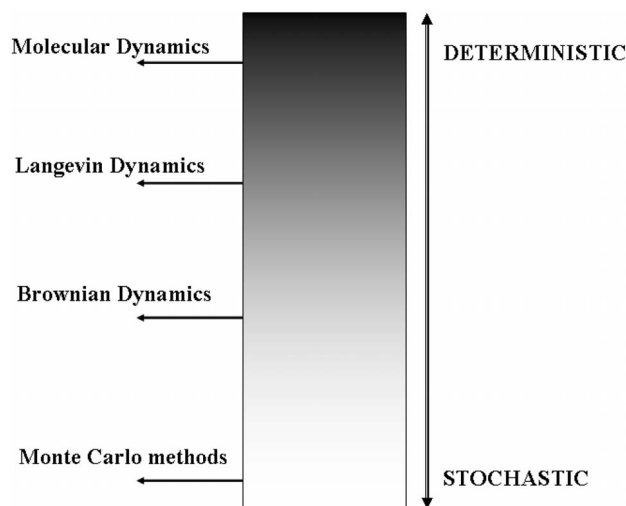


Figure 2.1. Computer simulation techniques frequently used to model electrochemical systems.

The first refers to the classical mechanics method called “molecular dynamics”, the second to a variety of methods such as Brownian dynamics and Langevin dynamics and the third, a purely stochastic method that is classified as a “Monte Carlo” technique. Figure 2.1 shows schematically the variety of methods available to perform computer simulations.

As in the case of other branches of nanotechnology, the future of nanoelectrochemical technology will rest on the fabrication, assembly and stability of nanoscale structures. However, a coherent picture of many of the fundamental phenomena leading to the formation, stability and structure evolution of electrochemically generated nanostructures is still lacking. For this reason, a suitable combination of experiment and modeling of the driving forces involved in the synthesis and organization of nanostructures will play a fundamental role in providing this knowledge in the near future.

The kinds of structures generated on surfaces are sometimes characterized by their dimensionality, ranging from 2D down to 0D. This classification refers to the periodicity of a certain motif made up of a single atom or group of atoms that form an array. Eventually, this definition is also extended to defects. For example, a single cluster made of N atoms is called a 0D object, although the cluster itself has a 3D structure. This means that the cluster is an object without periodicity (no repetition) in space. Similarly, a step edge extending infinitely is 1D object, while a perfect (infinite) atomic layer is considered to be 2D. However, since in experiment “infinite” is rather an abstract extrapolation, these concepts are more loosely used. For example, atoms adsorbed at island edges extending over several tens of nanometers may behave as 1D objects, although strictly speaking these systems are finite.

In the present chapter we will briefly describe the foundations of the three types of simulation techniques mentioned above, and discuss their application to low-dimensional metal phase formation and electrochemical nanostructuring.

2.2

Molecular Dynamics Simulations

2.2.1

Generalities

The main idea underlying classical molecular (or atom) dynamics is straightforward. To exemplify this for the simple case of an ensemble of atoms, let us consider a system of N particles, each having mass m_i with Cartesian coordinates $\{\mathbf{r}_i\}$. The trajectory of this system of particles can be obtained by solving the equations given by Newton's second law $\left(m_i \frac{d^2 \mathbf{r}_i}{dt^2} = \mathbf{F}_i\right)$, where \mathbf{F}_i is the force exerted on particle i , that can be calculated from the potential energy of the system $U(\{\mathbf{r}_i\})$ according to:

$$\mathbf{F}_i = -\nabla_i U(\{\mathbf{r}_i\}) = -\frac{\partial U(\{\mathbf{r}_i\})}{\partial x_i} \hat{x} - \frac{\partial U(\{\mathbf{r}_i\})}{\partial y_i} \hat{y} - \frac{\partial U(\{\mathbf{r}_i\})}{\partial z_i} \hat{z} \quad (2.1)$$

where (x_i, y_i, z_i) are the coordinates of particle i and $\hat{x}\hat{y}\hat{z}$ are unit vectors. According to the previous equations, once the interactions between the particles are given through the interaction potential $U(\{\mathbf{r}_i\})$, the integration of Newton's equation allows the prediction of the behavior of the system at all times, provided some boundary conditions are given. Since Newton's equation is a set of $3N$ differential second-order equations, $6N$ of such conditions are required to solve the problem. The most common physical situation is one where the positions $\{\mathbf{r}_i\}$ and velocities $\left\{\frac{d\mathbf{r}_i}{dt}\right\}$ are known at a certain time t , and the evolution of the system for $t > t_0$ is sought, so that the $6N$ boundary conditions are fixed by the initial positions and velocities of the particles. Once the trajectory of the system has been obtained, that is, the set $\{\mathbf{r}_i(t)\}$ for all t , the properties of the system can be calculated from this information. Thus, the problem reduces to finding a suitable method to integrate the set of Newton's equation with the forces given by Eq. (2.1). Since even for very simple forms of $U(\{\mathbf{r}_i\})$ this is not possible to perform analytically for more than two particles, approximate methods are required. The basic idea is to write two third-order Taylor expansions $\mathbf{r}_i(t)$, one forward and one backward in time, from which after addition we get:

$$\mathbf{r}_i(t + \Delta t) = 2\mathbf{r}_i(t) - \mathbf{r}_i(t - \Delta t) + \left(\frac{d^2 \mathbf{r}_i}{dt^2}\right)_t \Delta t^2 + \dots \quad (2.2)$$

According to this equation, the positions of the particles at time $t + \Delta t$ can be computed from the positions at the time t and $t - \Delta t$, and the second derivative $\left(\frac{d^2\mathbf{r}_i}{dt^2}\right)_t$, that correspond to the acceleration. The latter can be computed via Eq. (2.1). Equation (2.2) is known as a Verlet algorithm. A number of methods are discussed in specific textbooks [4], and the choice must be taken by making a balance between accuracy and cost in execution speed. In general the Verlet algorithm has a good energy conservation at long times, however predictor-correctors ones have very good local energy conservation.

We see that the numerical integration of Newton's equation is not a problem, so the question arises as to whether classical molecular dynamics simulations can be used to truthfully describe a real electrochemical system. As long as we deal with particles heavier than hydrogen, quantum mechanical effects in the motion of the particles are not important, and the main handicap to getting a proper description of the real physical system is the knowledge of the function $U(\{\mathbf{r}_i\})$. There are some cases where reasonably good approximations to the exact $U(\{\mathbf{r}_i\})$ are available. Typical examples are ionic systems, closed shell molecular systems and transition metals and their alloys. To the latter group belong the so-called glue model or the embedded atom method described below. These are essentially semi-empirical approaches, where $U(\{\mathbf{r}_i\})$ is fitted to reproduce a number of experimental properties, like binding energies, heat of formation of alloys, etc.

Systems where chemical bonds of molecules are broken or created are much more difficult to describe, since the only way to get a proper description of a reaction all the way between reactant and products would be to solve the quantum mechanical problem at each step of the reaction. With this purpose, *ab initio* molecular dynamics [5] was devised as a method to solve the electronic and nuclear problems all at the same time, for every time step of a molecular dynamics simulation. Within this approach, the forces acting on the nuclei are obtained from density functional calculations.

2.2.2

Nanostructuring of Metallic Surfaces

Different types of techniques have been employed for the electrochemical nanostructuring of solid surfaces, involving a common instrument for their implementation: the scanning tunneling microscope. While this instrument is usually employed to yield information on the structure of the surface, a number of applications have appeared that allow nanostructuring at the electrochemical interphase [6]. These applications have been discussed in several review articles [7–9] and we mention here those which are relevant for the present chapter. In one of them, developed by Kolb and coworkers [10] and called tip induced local metal deposition (TILMD), nanoclusters are generated on the surface of a substrate by transfer of matter from the tip of the STM. The material on the tip is continuously renewed by deposition from a solution containing ions of the metal to be deposited. In another method, 0D defects are generated on a metal surface, and the holes gener-

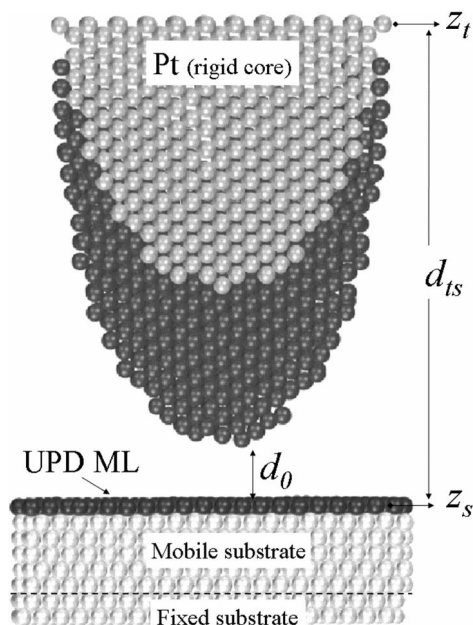


Figure 2.2. Typical starting configuration employed in the atom dynamics simulation of cluster deposition. The system has been projected onto the $(X - Y)$ plane. Gray circles denote Pt atoms belonging to the STM tip. Black circles represent the atoms of the material M being deposited and light gray circles indicate the substrate atoms. In this case the scheme includes a monolayer adsorbed on the electrode. d_{ts} indicates the distance between the surface and the upper part of the tip. d_0 is the initial distance between the surface and the lower part of the tip. Fixed and mobile substrate layers are also marked on the figure. Taken from Ref. [58].

ated in this way are later decorated through deposition of the foreign metal. In this section we will deal with the simulation of the processes involved in the first of these techniques (TILMD), by means of atom dynamics. The initial state (Fig. 2.2) corresponds to the STM tip located in front of the surface of the substrate on which the material is to be deposited. The surface may be naked, or covered by a metal monolayer. This is for example the case where a monolayer of a metal can be deposited at potentials more positive than the Nernst reversible potential (underpotential deposition, UPD). In a second stage, metal from the solution is electrodeposited on the uncovered part of the STM tip. In a third stage, a connective neck is formed between the tip and the surface, and finally the tip is moved away from the electrode leaving, in many cases, a cluster on the surface which typically contains 20–100 atoms, and is a few monolayers high. Seemingly simple, experiments performed by this technique are not always successful for cluster generation, depending very strongly on the kind of materials involved. The method performs

well for several combinations of metals, in particular for copper and palladium clusters on Au(111) [10, 11]. For other combinations, such as Cu on Ag(111) and Ni on Au(111), cluster formation is not observed [12, 13]. Since the number of atoms involved is relatively small, this appears to be an interesting problem to tackle by the atom dynamics techniques described above. Pioneering work in this area was carried out by Landman et al. [14] for the interaction of an Au tip with a Ni surface and vice versa. Application to different electrochemical systems was developed by Del Pópolo et al. [15–19], and we discuss here mainly their work.

The process of cluster generation was simulated in a large microcanonical ensemble including three kinds of atoms: Pt atoms for the STM tip, atoms of type A for the deposit, and atoms B for the substrate. A typical initial configuration is displayed in Figure 2.2. In this figure the Pt atoms (gray circles) forming the tip are arranged in a roughly semi-ellipsoidal shape that has been cut out of a Pt crystal oriented with a (110) surface in the z direction parallel to the electrode surface. These atoms are kept fixed during the simulation. Mobile atoms A (black circles) are arranged in semi-ellipsoidal shape on the tip and oriented with the (110) surface parallel to the electrode. Different tip geometries were employed in the simulations. This one has the highest density of surface atoms and the lowest surface energy, and should therefore be particularly stable.

The substrate is made of 8 layers of atoms B (gray-light circles) arranged in fcc(111) geometry, of which the upper six layers are mobile. In some systems the substrate is already covered with a monolayer of atoms A before the cluster is generated. Such a monolayer is indicated in Figure 2.2, but it may be present or not depending on the combination of A and B in order to mimic the experimental situation.

The interactions between the atoms were treated by the *embedded atom method* (EAM) [20]. This is a many-body potential which provides a reliable description of static and kinetic properties of transition metals for bulk systems, as well as for systems involving surfaces. The EAM represents an improvement on pair potentials such as the Lennard-Jones one, since the consideration of many-body properties by the former yields a better description of cohesion away from equilibrium.

The solution was absent in this model. All the metals investigated interact weakly with water, so that it can be expected that cluster formation should be dominated by metal–metal interactions.

The atom dynamics simulations followed the procedure established by the group of Landman [14]: The tip was brought slowly towards the electrode surface. At a certain distance the tip and the electrode became linked by a bridge of atoms. This is the so-called *jump to contact*, and the corresponding position of the tip was taken as the reference point from which further tip movement was measured. The tip was then moved an additional distance Δz towards the surface, and then withdrawn. A typical run extended over 5–10 ns. Electrochemical adatom deposition was not considered within this time, more details can be found in Refs. [15–19].

Figure 2.3 shows snapshots of a typical simulation where cluster nanostructuring is successful. It can be observed that the general qualitative picture is as described above. However, an additional feature appears: some mixing between the

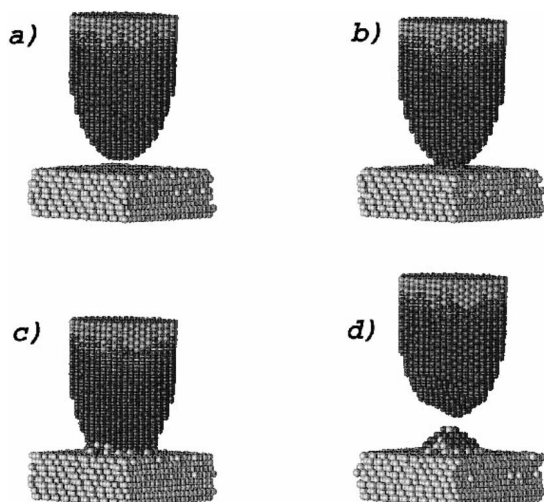


Figure 2.3. Snapshots of an atom dynamics simulation taken during the generation of a Pd cluster on Au(111). (a) Initial state with $d_0 = 6.25 \text{ \AA}$, (b) jump-to-contact from the tip to the surface, (c) closest approach distance $d_0 = -8.78 \text{ \AA}$, (d) final configuration after tip retraction. The resulting cluster had 256 atoms, was 8 layers high and its composition was 16% in Au. Taken from Ref. [17].

material from the tip and the surface occurs. A quantitative analysis shows that the size of the clusters and the degree of alloying increase with the penetration of the tip. This is shown in Figure 2.4, where both cluster size and the degree of alloying are shown as a function of Δz . As will be discussed in the section on Monte Carlo simulations, the alloying in the clusters may be a reason for their unusual stability.

The previous results show that atom dynamics simulations were useful to understand the mechanism by which Pd clusters are generated on Au surfaces. Something similar can be stated on the generation of Cu clusters on Au surfaces. On the other hand, simulations can also be helpful in understanding why, in some cases, nanostructuring *is not* successful. This is for example when Cu nanostructuring on Ag is attempted. In this case, the experiments shows only disperse 2D structures. When simulations are carried out with a Cu loaded tip oriented with the (111) face pointing towards the Ag(111) surface only holes are obtained on the surface [19]. When other tip orientations are used, small clusters result, indicating that the Ag surface has a very low affinity for Cu atoms.

A systematic study with different metal couples shows that a necessary condition for nanostructuring is that the binding energies of the metals involved are similar [18, 19].

An interesting issue that deserved further study was the effect of the crystalline nature of the tip on the nanostructuring process. Mariscal et al. [21] have studied the effect of the crystalline structure of the tip for a homoatomic system, namely

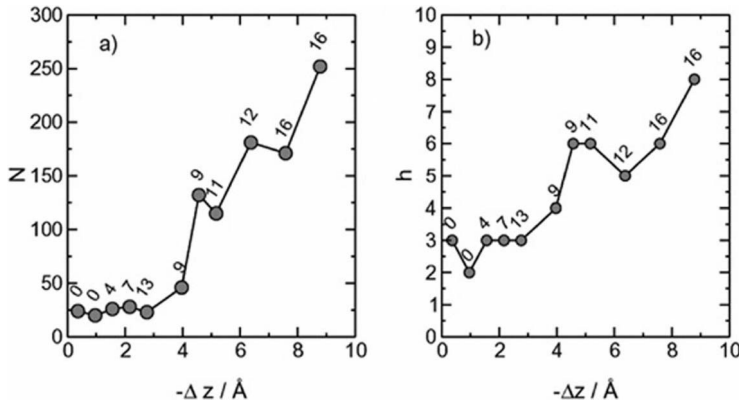


Figure 2.4. Cluster size and composition for Pd nanostructuring on Au(111) showing alloy formation as a function of maximum tip displacement Δz for a typical set of runs. (a) Number of particles in the cluster, (b) cluster height in layers. The numbers close to the circles denote the Au atomic percentage in the clusters. Taken from Ref. [18].

Cu deposition on Cu(111) substrate surfaces. Two types of tip were used, which were oriented with a (111) or a (110) single-crystal face facing the surface of the substrate. Depending on the structure of the tip, strong differences in the behavior of the forces on the tip upon retraction were observed in the case of this homoatomic system. In the case of the [111] tip, the approach produced the indentation of atoms belonging to the tip into the substrate, and reciprocally, some atoms are expelled from the surface, so that a mixing resulted. This behavior was contrasted with that of the [110] tip, where no indentation of the atoms from the tip was produced. Similar behavior is expected in the case of heteroatomic systems.

2.3 Monte Carlo Method

2.3.1 Generalities

In statistical mechanics the properties of a system in equilibrium are calculated from the partition function [22] that, depending on the choice for the ensemble considered, involves a sum over different states of the system. In the frequently used canonical ensemble that implies a constant number of particles N , volume V and temperature T , the partition function Q is:

$$Q = \sum_{\mathbf{c}} \exp[-H(\mathbf{c})/k_B T] \quad (2.3)$$

where $H(\mathbf{c})$ is the Hamiltonian of the system for state \mathbf{c} , k_B and T are Boltzmann's constant and the absolute temperature respectively. The expectation value of a quantity $Y(\mathbf{c})$ is calculated according to:

$$\langle Y \rangle = \sum_{\{\mathbf{c}\}} Y(\mathbf{c}) \frac{\exp[-H(\mathbf{c})/k_B T]}{Q} \quad (2.4)$$

where the sum is extended over all the states $\{\mathbf{c}\}$ of the system. The quasi-classical forms of Eqs. (2.3) and (2.4) for an atomic system are:

$$Q = \frac{1}{N!h^{3N}} \int \exp[-H(\mathbf{r}, \mathbf{p})/k_B T] \, d\mathbf{r} \, d\mathbf{p} \quad (2.5)$$

$$\langle Y \rangle = \frac{1}{Q} \frac{1}{N!h^{3N}} \int Y(\mathbf{r}, \mathbf{p}) \exp[-H(\mathbf{r}, \mathbf{p})/k_B T] \, d\mathbf{r} \, d\mathbf{p} \quad (2.6)$$

where h is Planck's constant, N is the number of particles, \mathbf{r} and \mathbf{p} denote the coordinates and momentum of the particles respectively. Separating the \mathbf{r} and \mathbf{p} -dependent parts of $H(\mathbf{r}, \mathbf{p})$, Q can be written as:

$$Q = \left[\frac{V^N}{N!A^{3N}} \right] \int \frac{\exp[-U(\mathbf{r})/k_B T]}{V^N} \, d\mathbf{r} \quad (2.7)$$

where $A = (h^2/2\pi m k_B T)^{1/2}$. The part in parentheses in Eq. (2.7) is called the "ideal gas" part of the partition function, since it corresponds to the integration of the pure kinetic part only. On the other hand, the integral in this equation runs over all the configurations of the system, and is termed the excess part. When the property Y in Eq. (2.4) depends only on the coordinates \mathbf{r} , the calculation of Y involves "just" an integration over the configuration space of the system:

$$\langle Y \rangle = \frac{1}{Q} \left[\frac{V^N}{N!A^{3N}} \right] \int Y(\mathbf{r}) \frac{\exp[-U(\mathbf{r})/k_B T]}{V^N} \, d\mathbf{r} \quad (2.8)$$

The configuration integral in Eq. (2.7) is, even for very simple interatomic potentials, a formidable task, and it is in this respect that Monte Carlo Methods come to our aid. However, the application of the Monte Carlo method is not a straightforward integration to get Q , but a somehow more sophisticated way to get the average $\langle Y \rangle$ without needing to calculate Q . The idea is that one is able to get a succession of configurations, each having a weight proportional to the probability ρ_i of their occurrence, like for example:

$$\rho_i = \frac{\exp[-U(\mathbf{r})/k_B T]}{\int \exp[-U(\mathbf{r})/k_B T] \, d\mathbf{r}} \quad (2.9)$$

If this is possible, the quantity $\langle Y \rangle$ can be calculated by taking an average of the value of $Y(\mathbf{r})$ over the configurations generated. Such a succession of states is achieved by generating a Markov chain of states. To discuss more concretely this point, let us think of the configuration of the system $\{\mathbf{r}\}$ as a random variable, where the probabilities for the occurrence of all the individual configurational states of the system can be stored in a vector $\boldsymbol{\rho}$. Each component ρ_i of this vector will contain the probability for the occurrence of a given configuration of the system \mathbf{r}_i . If the ensemble corresponds to the equilibrium state, the components of the vector $\boldsymbol{\rho}$ will be given by Eq. (2.9). On the other hand, if the ensemble does not correspond to the equilibrium state, a chain of states can be generated leading to the equilibrium distribution. A suitable choice for this is to let the vector $\boldsymbol{\rho}(t)$ evolve by generating a new configuration $\boldsymbol{\rho}(t+1)$ that depends only on $\boldsymbol{\rho}(t)$ (and not on other previous configurations). This can be done by multiplying the vector $\boldsymbol{\rho}(t)$ by a matrix $\mathbf{\Pi}$ according to: $\boldsymbol{\rho}(t)\mathbf{\Pi} = \boldsymbol{\rho}(t+1)$. If one, and only one, of the eigenvalues of the matrix is unity and the others are less than unity, then it can be shown that a steady state is found where $\boldsymbol{\rho}(t)$ becomes independent of t . In other words: $\boldsymbol{\rho}\mathbf{\Pi} = \boldsymbol{\rho}$.

Thus, implies the equation:

$$\sum_i \rho_i \Pi_{ij} = \rho_j \quad (2.10)$$

where the Π_{ij} are the elements of the matrix $\mathbf{\Pi}$. Since the steady state sought is the Boltzmann probability of state, then the problem is reduced to that of finding a suitable matrix $\mathbf{\Pi}$ fulfilling Eq. (2.10) that performs this task. The most popular algorithm is that by Metropolis et al. [23].

$$\Pi_{ij} = \frac{1}{N_i} \min \left\{ 1, \exp \left(\frac{U_{N,j} - U_{N,i}}{k_B T} \right) \right\}$$

$$\Pi_{ii} = 1 - \sum_{j \neq i} \Pi_{ij} \quad (2.11)$$

where the function (min) selects the minimal value inside the bracket. Note that this algorithm not only fulfills Eq. (2.10) but also the more restrictive condition: $\rho_i \Pi_{ij} = \rho_j \Pi_{ji}$, which is called “microscopic reversibility”.

A computer simulation using the transition probabilities in Eq. (2.11) can be performed in the following way: an initial configuration $\boldsymbol{\rho}$ must be chosen, and from it a chain of new configurations are generated where the transitions probabilities between them are given by Eq. (2.11). In each step of the simulation the transition probability Π_{ij} is calculated and compared with a random number η , generated with a uniform probability between 0 and 1. If $\eta < \Pi_{ij}$ the new configuration is accepted, otherwise it is rejected. Since the early states of the chain may be strongly influenced by the initial state chosen, it is of practical use to discard the first k states, for some suitable choice of k . In the case of the NVT ensemble under con-

sideration, where the particles may take virtually any position in space, it is usual that the different configurations are generated by small displacements of the particles in the simulation box. The energy changes associated with these displacements are those introduced in Eq. (2.11) to calculate the Π_{ij} . On the other hand, it can be assumed that the particles in the system may take only definite positions in space; these are the so-called “*lattice models*”. To differentiate from these, the former simulations are called “*off lattice simulations*”.

As is the case in statistical thermodynamics, other ensembles exist where the simulations can be performed. Among others, it is worth mentioning *NPT* (isothermal–isobaric) simulations, where the number of particles N , the pressure P and the temperature T are fixed and the volume of the system is allowed to fluctuate, and μVT (Grand Canonical) simulations. The latter ensemble is particularly useful in electrochemistry and crystal growth, since in many cases the control of the electrostatic potential difference involves the control of the chemical potential of some of the species present at the electrochemical interface.

2.3.2

Off-lattice Models

Off-lattice models allow the chemical species under consideration to occupy, in principle, any position in space, so that relevant information concerning the relaxation and space distribution of the constituents of the system can be obtained. We discuss now some applications of these models to electrochemical problems.

2.3.2.1 Stability of Metallic Nanostructures

The Monte Carlo methods described in this section are complementary to the atom dynamics simulations described in Section 2.2, and may provide an alternative explanation for the unusual stability of clusters generated by electrochemical nanostructuring [24]. Cluster stability in the UPD region is not easy to understand, since on thermodynamic grounds clusters should be less stable than the bulk material because they present a surface and surface atoms are energetically less stable than bulk ones. As we saw in Section 2.2, the clusters generated by electrochemical nanostructuring may present a certain degree of alloying with the material of the surface, that could make them more stable than pure clusters of the metal being deposited. The situation is represented schematically in Figure 2.5. The cluster contains atoms of type M , which is the material being deposited, and atoms of type S , which is the material of the substrate. The M atoms are in equilibrium with the electrolyte containing M^{+z} cations when the potential of the electrode is ϕ_s . On the other hand the bulk metal M is in equilibrium with the same solution at the potential ϕ_M . If $\phi_s > \phi_M$ the cluster is more stable than the bulk metal. As we shall see in this section, Monte Carlo methods may be employed to check if the occurrence of surface alloying may influence the stability of clusters towards dissolution.

As long as the atoms in the clusters may exchange with the corresponding ions in solution, the natural choice of the parameter that controls the stability of the

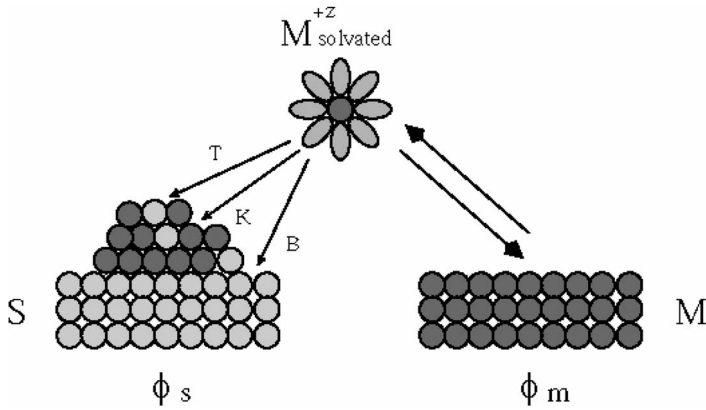


Figure 2.5. Scheme of an alloyed cluster on an electrode S (left). The cluster is in equilibrium with the electrolyte containing M^{+z} cations at an electrode potential ϕ_s . The bulk metal M is in equilibrium with the same solution at the potential ϕ_M . Taken from Ref. [59].

atoms in the clusters is the chemical potential μ . The electrode potential is related to μ according to:

$$\phi = (E_c - \mu)/z \quad (2.12)$$

where E_c is the cohesive energy of the metal being deposited, z is its valence and the standard equilibrium potential for the M deposition and dissolution reaction has been taken as zero.

Thus, the relative stability of the clusters can be analyzed by means of Monte Carlo Grand Canonical simulations, where the parameters fixed during a simulation are the volume of the simulation cell V , the temperature T , and the chemical potential of the deposited atoms μ . Three types of trial moves are allowed in the cluster/surface system:

- Motion of a particle. This is attempted within a small cube in relation to the size of the system and accepted according to the Metropolis criterion (Eq. (2.11)).
- Particle insertion. An attempt is made to insert a particle at a random position in the simulation box.
- Particle removal. A particle is chosen at random and its removal is attempted.

Insertion–removal trials were applied only to atoms of the deposited material.

In the electrochemical experiments, potential steps or potential sweeps can be applied to the working electrode. Both types of experiments can be simulated by making the proper changes in μ . In all cases, the starting conditions of the cluster corresponded to those of the final state of the nanostructuring process, as performed in the atom dynamic simulations described in the previous section. We

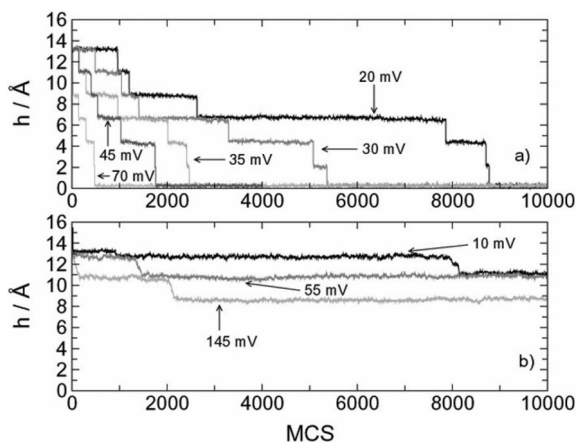


Figure 2.6. Evolution of cluster height as a function of the number of Monte Carlo steps (a) for a pure Pd cluster, (b) for a Pd–Au cluster with 16% gold. Taken from Ref. [18].

have seen in Section 2.2 that, in many cases, alloyed clusters result from the AD simulation. In these cases, comparative simulations were performed where the atoms in the cluster coming from the surface were replaced by atoms of the same type as those being deposited. The comparison of the behavior of these “pure” clusters with that of their alloyed clones allowed us to draw important conclusions on the influence of alloying on cluster stability, keeping the geometrical factors about the same. In addition, these simulations provide a qualitative idea of the dissolution mechanism, especially relative to the sequence in which the atoms should dissolve from the cluster.

Figure 2.6 shows cluster height as a function of the number of MC steps for the dissolution of both a pure and an alloyed palladium cluster on Au(111) at different chemical potentials. The pure cluster was obtained by substitution of all gold atoms by palladium atoms in an alloyed cluster generated with a tip. The curve at the lowest potential, $\phi = 20$ mV, provides a representative example of pure metal cluster dissolution. At first, there is little dissolution, but mainly a rearrangement of atoms, and the cluster takes on the shape of a truncated pyramid three layers high (1 layer ≈ 2.2 Å). It remains in this metastable state for a few simulation steps, then it starts to dissolve, and the last two layers disappear rapidly. The dissolution is found to proceed from kink sites at all levels of the cluster. Some snapshots of the simulation are shown in Figure 2.7. Similar behavior is found at higher potentials, but the dissolution proceeds more rapidly. For the alloyed cluster, the dissolution at 10 mV proceeds similarly, but the cluster, which at the beginning contained 16% gold, becomes progressively richer in gold, and finally reaches a steady state that, depending on the potential, is three to four layers high. Snapshots of this simulation are shown in Figure 2.8. In agreement with the experi-

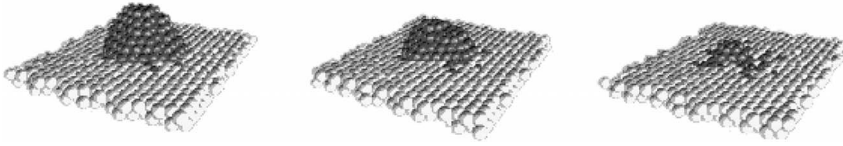


Figure 2.7. Different stages in the dissolution of a pure Pd cluster on a Au(111) surface. The simulation corresponds to the curve at 20 mV of Fig. 2.6(a).

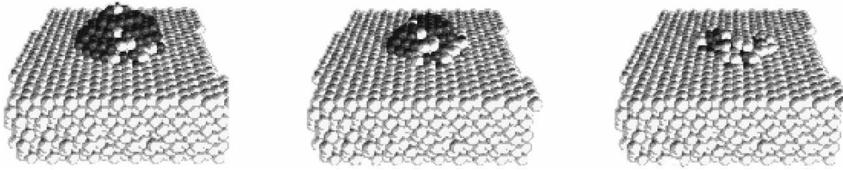


Figure 2.8. Different stages in the dissolution of an alloyed Pd/16% Au cluster on a Au(111) surface. The simulation corresponds to the curve at 10 mV of Fig. 2.6(b).

mental results [25], the cluster is the smaller, the higher the potential. The simulation shows that the boundary of the final clusters consists mainly of gold atoms.

Grand Canonical Monte Carlo simulations may also be applied to study cluster growth on metal surfaces. Depending on the value of μ , a cluster may dissolve, remain in a stationary state or grow, as considered in Ref. [18]. In the case of Cu cluster growth inside Au(111) nanocavities, the simulations show [26], like the experimental work [27], that this process is confined to the inside of the hole generated on the surface.

The same kind of computer simulations can be used to study the stability of metal nanowires suspended between a STM tip and a substrate surface, where matter exchange is allowed with the solution. For instance, Figure 2.9 shows snapshots taken after 10^5 MC steps at different chemical potentials. It can be seen

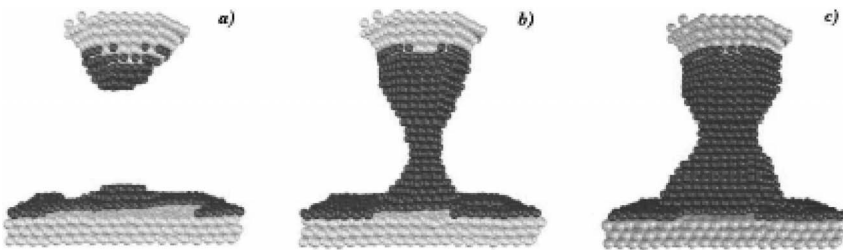


Figure 2.9. Final configuration after 10000 MCS of a Cu nanowire suspended between a Au STM tip and a Au(111) substrate, (a) $\mu = -3.60$ eV, (b) $\mu = -3.50$ eV and (c) $\mu = -3.35$ eV. Taken from Ref. [58].

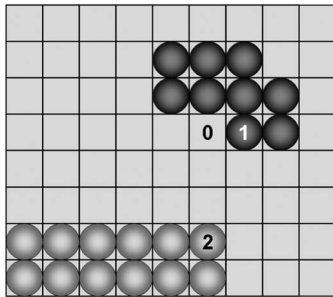


Figure 2.10. Scheme of the substitution of a surface by a lattice of adsorption sites. The site occupied by an adsorbate is marked with 1, a substrate site by 0 and a substrate atom on a substrate site by 2.

how a connecting neck can be formed or dissolved, depending on the chemical potential.

2.3.3

Lattice Models

2.3.3.1 Introduction

The main idea of a lattice model is to assume that atomic or molecular entities constituting the system occupy well defined sites in space. For example, to represent the adsorption of atoms on a surface, the adsorption sites are represented by points of a two-dimensional lattice, that may be occupied or unoccupied. (See Figure 2.10). The use of Monte Carlo simulations of lattice-gas models as a tool for understanding interfacial electrochemistry has been recently addressed by Brown et al. [28] in a concise and didactic approach. Among the motivations for the use of Monte Carlo simulations are the accuracy over mean field methods, which involve the analytical or numerical resolution of a small set of equations. Furthermore, Monte Carlo simulations allow the analysis of fluctuations, opening the way to the calculation of a wider number of properties of the system.

As stated above, the close relationship between electrode potential and electrochemical potential of adsorbed species makes the Grand Canonical ensemble an attractive choice for the simulation of surface electrochemical processes. The Hamiltonians H of the lattice gas for one and two adsorbed species from which the transition probabilities Π_{ij} can be calculated have been discussed by Brown et al. [28]. For example, for two adsorbed species, A and B we have:

$$H(c) = -\tilde{\mu}_A \sum_i c_i^A - \tilde{\mu}_B \sum_i c_i^B - \sum_n \left[\Phi_{AA}^{(n)} \sum_{\{i,j\}} c_i^A c_j^A + \Phi_{BB}^{(n)} \sum_{\{i,j\}} c_i^B c_j^B + \Phi_{AB}^{(n)} \sum_{\{i,j\}} c_i^A c_j^B + c_i^B c_j^A \right] - H_3 \quad (2.13)$$

where $\tilde{\mu}^I$ denote the chemical potential of species I , c_i^I the occupation number (0 or 1) of site i by the species I , (n) indicates the rank of the neighborhood between sites (first, second, etc), and $-\Phi_{IJ}^{(n)}$ is the pairwise interaction energy between particles of type I and J that are nearest neighbors. The term H_3 denotes other interactions than the pairwise ones considered in the previous terms. Since particles are restricted to adsorb on N well-defined lattice sites, the coverage can be easily calculated from: $\theta_I = \sum_i c_i^I / N$ and the charge flowing upon adsorption of the species of type I is: $q_I = -e_0 z_I \theta_I$ where e_0 is the elementary charge unit and z_I is the effective electrovalence of I .

According to this, voltammetric quasi-equilibrium currents i , may be derived yielding, in the case of two adsorbed species:

$$i = e_0 F \left[z_A^2 \frac{\partial \theta_A}{\partial \tilde{\mu}_A} + 2z_A z_B \frac{\partial \theta_B}{\partial \tilde{\mu}_A} + z_B^2 \frac{\partial \theta_B}{\partial \tilde{\mu}_B} \right] v \quad (2.14)$$

where v is the potential sweep rate.

The Monte Carlo method, as described so far, is useful to evaluate equilibrium properties, but says nothing about the time evolution of the system. However, it is in some cases possible to construct a Monte Carlo algorithm that allows the simulated system to evolve like a physical system. This occurs when the dynamics can be described as thermally activated processes, such as adsorption, desorption and diffusion. Since these processes are particularly well defined in the case of lattice models, they are particularly well suited for this approach. The foundations of dynamical Monte Carlo [DMC] or kinetic Monte Carlo [KMC] simulations have been discussed by Fichtorn and Weinberg [29] in terms of the theory of Poisson processes. The main idea is that the rate of each process that may eventually occur on the surface can be described by an equation of the Arrhenius type:

$$k_f = A e^{-E^\ddagger/k_B T} \quad (2.15)$$

where k_f is the experimental rate constant for the forward reaction and A is called the *frequency factor*. The theoretical basis for the evaluation of the parameters in Eq. (2.15) is given by transition state theory (TST, also denoted activated-complex, absolute-reaction-rate), the temperature dependence being somewhat more complicated than that expected from Eq. (2.15). However, it is customary to think of each of the processes under consideration in terms of the system oscillating in the neighborhood of a minimum of a potential energy surface, performing A attempts to cross over a barrier per unit time, the probability of success depending on the temperature and the height of the barrier. Once all the processes that may occur at a certain step of the simulation have been identified, each one is assigned a rate v_i . The probability of a process occurring can be thus represented on a straight line by a segment proportional to its rate, as shown schematically in Figure 2.11 for a system where only three processes may occur at the time t . If the sum of all the segments is normalized to unit length, then the occurrence of a process can be selected by generating a random number between 0 and 1, and choosing the pro-

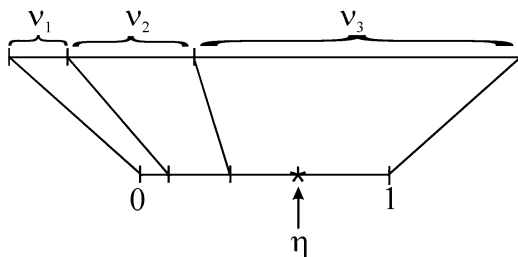


Figure 2.11. Illustration of the way in which a given process is selected in a kinetic Monte Carlo simulation where only three processes may occur. The probability of each process to occur is represented on a straight line by a segment proportional to its rate v_i . The sum of all the segments is normalized to unit length, so that the occurrence of a process can be selected by generating a random number η between 0 and 1, and then choosing the process corresponding to the segment on which the random number is found to fall. Here η falls in the segment corresponding to the rate v_3 .

cess corresponding to the segment on which the random number has been found to fall. In the figure the random number fell on the segment corresponding to the process v_3 . Since the probability of changing the current state has a constant rate, the elapsed time Δt until the accepted change has an exponential distribution. Thus, Δt will be calculated from:

$$\Delta t = -\frac{\ln(\eta)}{\sum_i v_i} \quad (2.16)$$

where η is a random number uniformly distributed on $(0, 1)$ and the sum index runs over all possible processes at a given time step. After letting the time advance by Δt , the configuration of the system is updated, a new set of rates $\{v_i\}$ is calculated, a new process is chosen by chance again and so on.

2.3.3.2 Electrocristallization

The use of electrochemical techniques like cyclic voltammetry along with *in situ* microscopy techniques has opened new horizons in the last decade concerning the understanding of metal electrodeposition processes. Among these, scanning tunneling microscopy (STM) has allowed the observation in direct space and real time of the formation and growth of a new phase during the electrocrystallization of a metal from an electrolytic solution. In this context it is worth mentioning the so-called underpotential deposition (UPD), which implies the deposition of a metal M on the surface of an electrode or substrate S of different nature at potentials more positive than those predicted from the Nernst equation [30, 31].

The possibility that UPD takes place can be quantified through the so-called underpotential shift $\Delta\phi_{UPD}$, which is related to the difference in the chemical po-

tential of M adsorbed on S at a coverage degree Θ , say $\mu(M_\Theta/S)$ and the chemical potential of M in the bulk phase, say $\mu(M/M)$, through the following equation:

$$\Delta\phi_{UPD} = \frac{1}{ze_0} [\mu(M/M) - \mu(M_\Theta/S)] \quad (2.17)$$

where z is the charge of the ion M in the solution and e_0 is the elemental charge. Criteria for the experimental estimation of $\Delta\phi_{UPD}$ have been given in the literature by Kolb et al. [32] and Trasatti [33]. Since $\Delta\phi_{UPD}$ depends on the valence of the ion being deposited, it may be preferable to use the excess of chemical potential $\Delta\mu$ as a stability criterion for adsorbed monolayers which we define as:

$$\Delta\mu = \mu(M_\Theta/S) - \mu(M/M) \quad (2.18)$$

According to Eqs. (2.17) and (2.18), negative values of $\Delta\mu$ indicate underpotential deposition, while positive ones predict overpotential deposition.

Concerning the modeling of UPD as a thermodynamic process, different interesting approaches have been taken by several authors in the 1970s [6, 34–37]. The most widespread idea is to envisage this phenomenon as related to the formation of different adsorbed phases, involving in some cases, phases of low dimensionality that differ in their properties and can be detected as separate entities by given experimental techniques, that is peaks in a voltammogram. The interpretation of UPD as a phase transition has been employed by Blum et al. [37] to develop a model for the underpotential deposition of Cu on Au(111) in the presence of sulfate anions and has also been recently brought into a more general context by Lorenz and coworkers [38, 39]. According to these ideas, the dimensionality of the phases involved in the UPD phenomena is between 0 and 2. The 0D phases correspond to the adsorption of isolated metal atoms, the adsorption on kink sites, and the adsorption on vacancies of the first lattice plane of the substrate or on some other type of point defects. The 1D phases are related to the adsorption at the border of steps or monoatomic terraces and the 2D phases are related to the formation of monolayers and submonolayers of adsorbate building compressed, (1×1) or even expanded structures. The relative abundance of 0D and 1D phases is determined by the presence of defects on the electrode surface. Their existence has been related to the existence of small shoulders in the voltammograms, as postulated by Siegentaler et al. [40] and Staikov et al. [41]. In the case of the 2D phases that are formed on the flat terraces or defect-free surfaces there is clear experimental evidence for the existence of compressed [42], compact and expanded structures [6, 38]. The formation and growth of a compact, defect-free 2D structure can be described as a first-order phase transition that takes place at the electrode/solution interface and its occurrence should be characterized by a discontinuity in the adsorption isotherm, with a concomitant very sharp peak (more properly speaking a Dirac delta function) in the voltammetric profiles [37]. Thus, it is quite remarkable that although UPD has been often related to the presence of first-order phase transitions, the real existence of these phenomena in experimental systems is still not

completely free from controversy, since discontinuities in the experimental isotherms are usually not obtained when specific anion adsorption is avoided [6]. Higher order phase transitions should be characterized by the presence of rather wide and flat voltammetric peaks [37], though there is no experimental evidence for the occurrence of this type of phenomenon in electrochemical systems [6]. In this respect, computer simulations could also deliver enlightening information. As mentioned above, many approaches can be taken for the study of surface-related problems, like deterministic molecular dynamics simulations and the stochastic Monte Carlo method based on continuum Hamiltonians (off-lattice). In this section, we consider Monte Carlo techniques in which the surface is modeled through a lattice Hamiltonian (on-lattice simulations) [43]. Within this approach, a surface is replaced by a regular array of lattice points where particles may adsorb, as we have shown in Fig. 2.10. An occupation number is defined (that is, 0 for an unoccupied site, 1 for a site occupied by an adsorbate type atom, 2 for a site occupied by a substrate type atom) and some assumption is made concerning the interaction between the atoms on the surface. If pairwise additive interaction between nearest neighbors is assumed and interactions between more distant atoms are neglected, it can be demonstrated that the thermodynamic properties of the lattice gas can be obtained from the thermodynamics of the Ising model [44], which have been extensively investigated. Lattice gas models allow one to deal with a relatively large number of particles at a relatively low computational cost, and are widely used in computer simulations to study nucleation and growth. In principle, simulations can be made for many heterometallic systems, but difficulties will arise if the atoms participating are of greatly different sizes. Rojas [45] has examined the stability of some adsorbate/substrate systems with different misfits (see Table 2.1) by means of off-lattice simulations, finding that, for example, a monolayer of Ag on Pt(111) still holds in a 1×1 structure in spite of the misfit. However, systems

Table 2.1. Misfits ($e_{mf}\% = (a_{Sus} - a_{Ads}/a_{Sus}) \times 100$) for some substrate/adsorbate systems of interest in electrochemistry. The numbers marked in boldface are systems where the adsorbate monolayer remains commensurate with the substrate in off-lattice simulations [45]. These systems are reasonable candidates for lattice model simulations.

Subs/Ads	Ni	Cu	Pd	Pt	Au	Ag	Pb
Ni	0.0	-2.69	-10.51	-11.36	-15.91	-16.19	-40.62
Cu	2.63	0.0	-7.61	-8.44	-12.86	-13.14	-36.93
Pd	9.51	7.07	0.0	-0.77	-4.88	-5.14	-27.25
Pt	10.20	7.78	0.76	0.0	-4.08	-4.34	-26.27
Au	13.72	11.39	4.65	3.92	0.0	-0.24	-21.32
Ag	13.93	11.61	4.89	4.15	0.24	0.0	-21.02
Pb	28.88	26.97	21.41	20.80	17.57	17.37	0.0

with larger misfits (like Au on Cu(111)) results in the expulsion of some adsorbate atoms from the monolayer with the subsequent appearance of defects. In these cases a lattice model would be quite unrealistic and should not be employed.

In principle, it must be kept in mind that continuum Hamiltonians, where particles are allowed to take any position in space, are much more realistic in cases where epitaxial growth of an adsorbate leads to incommensurate adsorbed phases or to adsorbates with large coincidence cells. On the other hand, to assume that particle adsorption can only occur at definite sites is a good approximation for some systems. Such is the case of silver on gold, where there is practically no crystallographic misfit.

A further important point that must be considered is that the interaction between the metallic atoms should be described by a suitable (many body) potential such as that we presented in Section 2.2, and this seems difficult to compute with a lattice model. For this purpose, we considered the adsorption (desorption) of a particle at a site immersed in a certain environment surrounding it, as shown in Figure 2.12. The adsorption site for the particle is located in the central box, and the calculation of the interactions is limited to a circle of radius R . The adsorption energy for all the possible configurations of the environment of the central atom was calculated prior to the simulation, so that during the MC simulation the most expensive numerical operations are reduced to the reconstruction of the index that characterizes the configuration surrounding the particle on the adsorption site.

In the case of electrochemical techniques, potentiostatic control is, in many cases, applied to fix the chemical potential of species at the metal/solution interface. Since the natural counterparts of potentiostatic experiments are Grand

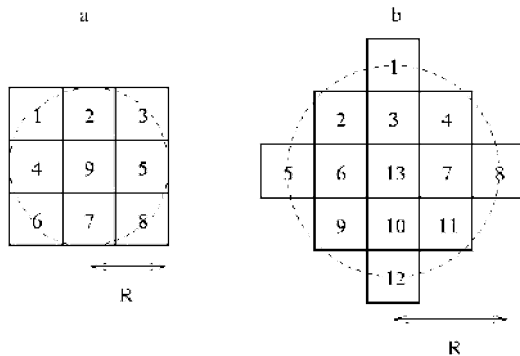


Figure 2.12. Environment of S sites (a) $S = 9$, (b) $S = 13$ surrounding an adsorption site. These were employed for the calculation of the adsorption/desorption energies of an adsorbate atom on a substrate) for a cutoff radii corresponding to the distance between second (a) and third (b) nearest neighbors. The particle is adsorbed on the central box (9 and 13 respectively) and the remaining sites may be occupied by adsorbate or substrate like atoms. A total number of $3^{(S-1)}$ configurations result.

Canonical Monte Carlo ($\mu VT/MC$) simulations, where the chemical potential μ is one of the parameters fixed in the simulations, this was the methodology applied by Giménez and Leiva [46] to study the formation and growth of low-dimensionality phases on surfaces with defects. To emulate (100) surfaces, the system was characterized by a square lattice with M adsorption sites. Different arrangements of substrate atoms allowed for the simulation of various types of surface defects. Within the procedure described in Section 2.3.2.1 (Metropolis algorithm), thermodynamic properties were obtained, after some equilibration steps, as average values of instantaneous magnitudes stored along a simulation run. One of these quantities is the average coverage degree of the adsorbate atoms $\langle \theta \rangle_{Ads}$ at a given chemical potential μ . To imitate different surface defects, substrate islands of various sizes and shapes were generated by means of the technique of simulated annealing. Within this approach, a fixed number of substrate atoms are set on the surface, and a MC simulation is started at a very high initial temperature T_0 , of the order of 10^4 K. The system is later cooled down following a logarithmic law ($T_{n+1} = T_n K$), where K is a positive constant lower than one and T_n is the temperature at the n th iteration step. A certain number of MC steps, N_{MCS} , are run at each temperature and the simulation is stopped when T_f is reached. By changing N_{MCS} , different kinds of structures may be obtained, as shown in Figure 2.13. Gimenez and Leiva [46] considered several systems involving Ag, Au, Pt and Pd. It was found that, taking into account some general trends, such systems can be classified into two large groups. The first comprises Ag/Au(100), Ag/Pt(100), Au/Pt(100) and Au/Pd(100), which have favorable binding energies as compared with the homoepitaxial growth of adsorbate-type atoms, as shown in Table 2.2. For this family of systems, when the simulations are performed in the presence of substrate-type islands in order to emulate surface defects, the islands remain almost unchanged, and the adsorbate atoms successively

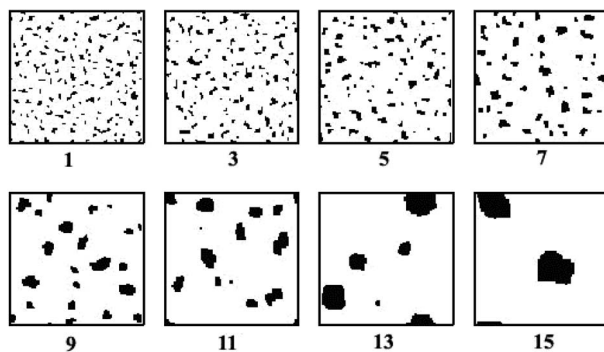


Figure 2.13. Final configurations for the simulated annealing simulations performed to obtain a surface with different types of defects. The number of Monte Carlo steps N_{MCS} increases from upper left to lower right. $N_{MCS} = 20 \times 2^{m-1}$, where m is the ordinal number of the configuration in the figure.

Table 2.2. Excess of chemical potential in eV, as calculated from the adsorption isotherms according to Eq. (2.18).

Subs/Ads	Ag	Au	Pt	Pd
Ag	0.00	0.08	0.53	–
Au	–0.17	0.00	0.54	0.14
Pt	–0.55	–0.42	0.00	–
Pd	–	–0.26	–	0.00

occupy kink sites, step sites and the complete monolayer. This is illustrated in Figure 2.14 for the surface atomic arrangement of Ag on Pt(100), and for the adsorption isotherms of this system in Figure 2.15. To produce this figure, partial coverage degrees for step and kink sites were defined, relative to the total number of step and kink sites available. The sequential filling of kink sites, steps and the rest of the surface can also be appreciated in the partial isotherms. The second group is composed of Au/Ag(100), Pt/Ag(100), Pt/Au(100), and Pd/Au(100), for which monolayer adsorption is more favorable on substrates of the same nature than on the considered substrates (see Table 2.2). When simulations are carried out in the presence of islands of substrate-type atoms, these tend to disintegrate in order to form 2D alloys with adsorbate atoms, as illustrated in Fig. 2.16 for Pt deposition on Ag(100). For this second type of system the partial adsorption isotherms do not show any particular sequential filling, as can be observed in Fig. 2.17.

A detailed analysis of the environment of adatoms and substrate atoms as a function of adatom coverage degree was also found very helpful in understanding the different behavior of the two families of system described above [46].

2.3.3.3 Dynamics of Crystal Growth

In the previous section we analyzed the use of a lattice Monte Carlo method related to the study of equilibrium properties. However, it is possible, by means of the

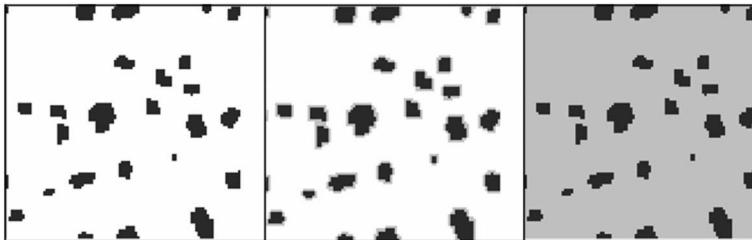


Figure 2.14. Snapshots of the final state of the surface at three different chemical potentials (-4.27 eV, -3.44 eV, and -3.06 eV) for the Ag on Pt(100) simulation. The average island size is 48 atoms.

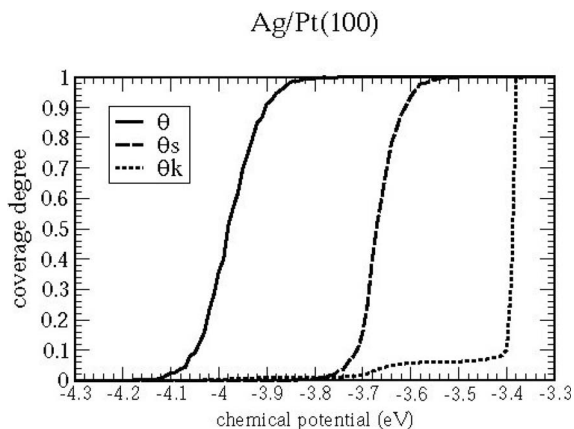


Figure 2.15. Adsorption isotherms for the deposition of Ag on Pt(100) in the presence of surface defects. Coverage degree of the submonolayer (θ), step sites (θ_s) and kink sites (θ_k) as a function of chemical potential. Taken from Ref. [46].

KMC method discussed above, to use it to compute the time evolution of a system. This method has been applied to the electrochemical nucleation and growth phenomena by Giménez et al. [47], where two types of processes related to the growth of the new phase were considered: adsorption of an adatom on the surface and its diffusion in different environments. The embedded atom method potential was employed, considering a system with a negligible lattice misfit: Ag deposition on Au(111) and Au(100) surfaces, simulated using rectangular and hexagonal lattices respectively. These dynamic calculations considered the closest environment of an atom undergoing diffusion, and the potential energy curves for its motion were calculated for all possible occupations of neighboring sites. From these curves the at-

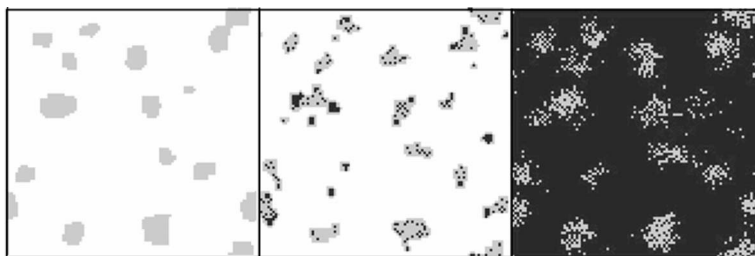


Figure 2.16. Snapshots of the final state of the surface at three different chemical potentials (-5.74 eV, -5.32 eV and -5.21 eV) for the Pt on Ag(100) lattice model simulation. Average island size 53 atoms.

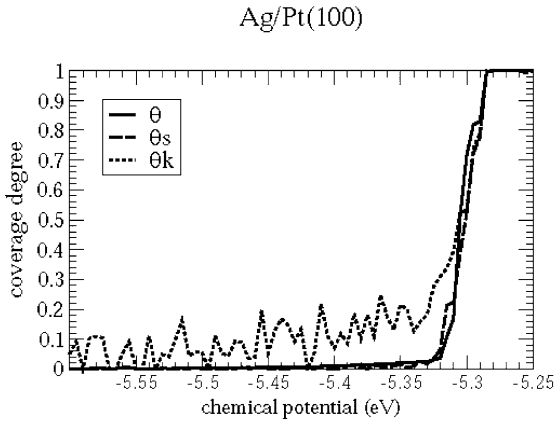


Figure 2.17. Adsorption isotherms for the deposition of Pt on Ag(100) in the presence of surface defects. Coverage degree of the submonolayer (θ), step sites (θ_s) and kink sites (θ_k) as a function of chemical potential. Taken from Ref. [46].

tempt frequency for overcoming the diffusion barrier v_0 , and the activation energy E_a , were obtained. Thus, the rates v_i for all the possible diffusion processes were calculated according to $v_i = v_0 \exp\left(-\frac{E_a}{kT}\right)$.

The activation barriers for Ag single adatom diffusion were found to be markedly different on the Au(111) and Au(100) faces, the latter being considerably larger, due to the more open nature of the surface. This resulted in a diffusion coefficient on Au(111) that was several orders of magnitude larger than on Au(100). The model led to the conclusion that, on energetically rough surfaces, island formation should prevail, while on the smoothest surfaces, the growth of the new phase should take place predominantly at steps. In the case of the adsorption rates, this model assumed the same rate for electrodeposition on all free sites. A more realistic calculation taking into account different rates on different environments was subsequently developed by Giménez et al. [48].

2.3.3.4 Simulation of a Complex Underpotential Deposition System

In the previous sections we have discussed Monte Carlo simulations where the potentials describing the interactions between the constituents of the system were taken from a previously existing model, with the aim of predicting the behavior of the different systems on the basis of this knowledge. This information is very difficult to obtain for more complicated systems, like for example those where the solvation of the particles plays an important role, or where interactions between several types of particles occur. In these cases, a different approach can be taken. Instead of attempting the calculation of the interactions from a model, these are treated as adjustable parameters. The rewards and the pitfalls of this approach have been discussed by Brown et al. [28], who have reviewed the application of

the methods described in Section 2.2 to Cu underpotential deposition on Au(111) in the presence of adsorbed sulfate. Cu and sulfate adsorption was assumed to take place on a triangular lattice, with a hamiltonian like that given in Eq. (2.19). Ground states calculations were performed, and the phase diagram was determined for this system. The review by Brown [28] includes dynamic simulation for this system, where the stationary currents were compared with non-equilibrium profiles. Although this simulation method was employed only for 2D systems, it could, in principle, be extended to simulate metal deposition on surface defects.

2.4 Brownian and Langevin Dynamics Simulations

2.4.1 Generalities

Molecular or atom dynamics simulation as discussed above is a deterministic technique that allows us to predict the “real” trajectories of motion in real time. However, in order to capture many relaxation processes, the integration time step must be very small, of the order of ps, and therefore the period of time explored cannot usually be greater than nanoseconds when a reasonable number of particles is employed. Of course, as discussed in the previous section, this time scale is not suited to the study of many physical problems involved in crystallization. Furthermore, in some cases, not all the degrees of freedom considered are relevant for the process under study. Taking again metal deposition as an example, in some cases the simulator may be interested in the structure of the deposit being formed. While the coordinates of the discharged metal atoms are relevant for this purpose, the coordinates of the solvent molecules do not play any relevant role, since the solvent rather participates as a thermal bath in which the depositing ions are immersed. In this respect, Langevin dynamics (LD) and Brownian dynamics (BD) methods are relatively simple methods, developed to follow the trajectories of ions or neutral atoms in a fluid at relatively low computational cost. The algorithm for LD is conceptually simple: the motion of the i th atom with mass m_i is governed by the Langevin equation:

$$m_i \frac{d^2 r_i}{dt^2} = -\gamma_i \frac{dr_i}{dt} + F_{sist} + F_{rand} \quad (2.19)$$

The terms on the right-hand side of Eq. (2.19) describe the effects of collisions with the surrounding solvent molecules. The first term corresponds to an average frictional force with a macroscopic friction coefficient given by γ_i . The second term F_{sist} represents the force on the i th atom caused by the interactions with other neighbor's atoms. The last term is a random Gaussian force obeying the fluctuation-dissipation theorem [49]. Ermak's algorithm [4] is an attempt to treat properly both the systematic dynamic and the stochastic elements of the Langevin equation.

A simple algorithm of this type, which reduces to the velocity Verlet algorithm, is obtained if, on integrating the velocity equation, the systematic force is assumed to vary linearly with time:

$$r(t + \delta t) = r(t) + c_1 \delta t v(t) + c_2 \delta t^2 a(t) + \delta r^G \quad (2.20)$$

$$v(t + \delta t) = c_0 v(t) + (c_1 - c_2) \delta t a(t) + c_2 \delta t a(t + \delta t) + \delta v^G \quad (2.21)$$

After the selection of the random components δr^G and δv^G for a given step, the algorithm is implemented in the usual way. The numerical coefficients in Eqs. (2.20) and (2.21) are ($c_0 = e^{-\gamma \delta t}$, $c_1 = (\gamma \delta t)^{-1}(1 - c_0)$, $c_2 = (\gamma \delta t)^{-1}(1 - c_1)$).

When the friction is large and the motions are overdamped, the acceleration term, left-hand side of Eq. (2.19) may be neglected. This approximation yields the so-called Brownian equation:

$$\gamma_i \frac{dr}{dt} = F_{sist} + F_{rand} \quad (2.22)$$

Brownian dynamics simulations allow us to use larger time steps, and therefore, to explore long times, of the order of μs .

2.4.2

Applications in Electrochemical Nanostructuring and Crystal Growth

Li et al. [50] have developed an electrochemical nanostructuring technique that consists of a polymer-coated Pt ultramicroelectrode (STM tip) and graphite as substrate. Ag atoms are deposited on the tip at underpotentials, so that approximately one atomic monolayer is deposited on the tip. After this, a first bias pulse is applied to the tip, causing the formation of a shallow pit. Then, a second bias pulse with a smaller amplitude is applied to cause the desorption of silver from the tip. The desorbed silver ions diffuse and migrate across the tip-sample gap and deposit on the high coordination sites present at the edge of the pit. The final result is a silver particle having typical dimensions of 100–500 Å in diameter and 5–40 Å in height. Besides the experiments, Li et al. [50] developed a model for this process that was tested by means of Brownian Dynamics (BD) simulations. The main points addressed by these simulations were the relative role of adsorbed and dissolved Ag in supplying the silver required for the nanostructuring on the time scale of the experiment, the ion flux as a function of the tip-sample separation and the importance of the electric field in promoting silver transport by migration for dissolved and adsorbed silver components.

BD simulations have also been used by Fransaer et al. [51] and Penner [52] to study some aspects of particle size dispersion (PSD) during the growth of metal nanocrystal ensembles on electrode surfaces.

Schmickler et al. [53] have employed Langevin dynamics simulations to study the first stages of metal deposition. In their model, the electrochemical interface, that is, the electrode surface in contact with an electrolyte solution containing

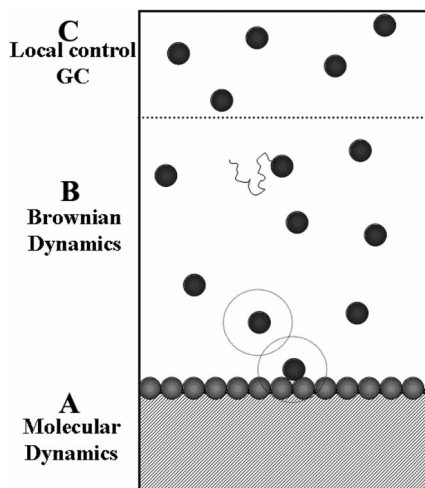


Figure 2.18. Schematic representation of the Grand Canonical atom dynamics simulation box in which three regions can be observed. Particles represented by black spheres move according to Langevin equation (B and C region). However, substrate particles (gray spheres) obey classical molecular dynamics (A region). The chemical potential μ is controlled by means of a reservoir of particles far from the surface (C region).

metal ions was represented by three subsystems in contact, namely A, B and C (see Fig. 2.18). The region A represented the electrode surface and was modeled by means of classical atom dynamics. The regions B and C represented the electrolyte solution and were modeled by means of the Langevin equation of motion (Eq. (2.19)), emulating the stochastic displacements of the ions due to friction with solvent particles (e.g. water). The C part, emulates the bulk-solution and the background chemical potential μ_0 of the species was controlled by adding or deleting particles. In this model, the activation energy required to adsorb a particle coming from the solution has been neglected in order to save computer time. A schematic plot of the potential energy is shown in Figure 2.19. At each time step the interaction potential ϕ_i of each particle i in region B with the metal surface is calculated from the semi-empirical embedded atom method described in Section 2.2 and compared with the background potential μ_0 . If $\phi_i(r_i) < \mu_0$, the particle is deposited onto the surface. This means that the particle switches from Langevin to deterministic dynamics, keeping its old velocity. The particle is then in the attractive part of the potential (see left-hand side of Figure 2.19), so that backscattering is unlikely. Conversely, if a surface particle of metal M reaches the crossing point (vertical dotted line in Figure 2.19), where its potential energy equals the background potential μ_0 it is dissolved and starts to move according to Langevin dynamics.

The model has been tested for different systems of interest in electrochemical deposition and ultrahigh vacuum (UHV) experiments. Different growth modes

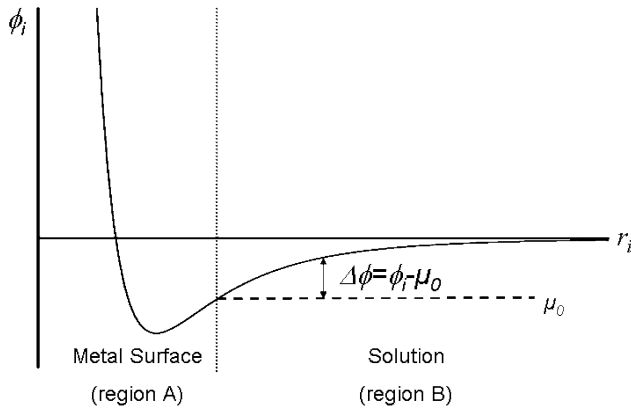


Figure 2.19. Schematic plot of the potential energy $\phi_i(r_i)$ of a particle near the surface. The dotted vertical line, where $\phi_i(r_i) = \mu_0$ denotes the transition between deterministic and stochastic.

and diffusion mechanisms have been found in good agreement with UHV metal deposition.

Electrochemical deposition of Pd on Au(111) has been studied by several experimental techniques, especially deposition of the first Pd monolayer onto Au(111), which starts at underpotentials. The influence of anions (chloro complex) has been reported to play a key role in the stabilization of the monolayer [54]. In the case of metal beam epitaxy (MBE) in UHV, different results have been obtained [55]. At 150 K, the deposition of Pd on Au(111) follows a layer-by-layer growth mode. However, at temperatures above 300 K, surface alloy formation has been observed by means of the LEISS technique.

Computer simulations for this system at different deposition potentials μ_0 revealed the very early atomistic mechanism taking place during the formation of the first monolayer [56]. Overpotential deposition (OPD) is predicted with this method, in accordance with previous EAM calculations [57]. Figure 2.20 shows

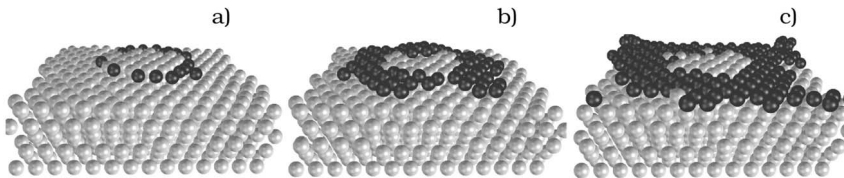


Figure 2.20. Snapshots taken after 20 ns at different background chemical potential. Grand Canonical atom dynamics simulation of Pd deposition on Au(111) with surface defects, (a) $\mu_0 = 0.78$ V, (b) 0.98 V and (c) 1.18 V with respect to Pd bulk deposition. (The solution particles are not represented for a better visualization.)

the final configurations of the Au(111) substrate surface at different μ_0 after 20 ns. Note that the surface includes defects, in this case a two-dimensional island containing kink sites and monoatomic steps. As observed in Fig. 2.20, at $\mu_0 = 0.78$ V arrival and deposition of palladium atoms occurs at kink sites or monoatomic steps only. As the electrode potential becomes more negative, Pd atoms start to grow at the flat terraces also (Figure 2.20(b)). At $\mu_0 = 1.18$ V palladium atoms start to grow also at terraces; fast mixing between Pd atoms and Au atoms can be observed from the trajectories, preferentially at the borders of monoatomic steps, leading to a surface alloy in the first layer (see Figure 2.20(c) at the border of the island). Different diffusion pathways can be noticed during the early stages of metal deposition. In the case of Pt deposition on Au(111) the computer simulations performed by Schmickler and coworkers [53] showed, at high overpotentials, a very fast exchange between Au atoms from the first layers of the electrode surface with Pt atoms coming from the solution. The exchange rate was reported to be of the order of a fraction of a nanosecond. From the computer simulations it was observed that after 7% exchange, Pt atoms start to join other Pt atoms to form 3D clusters.

2.5

Conclusions and Outlook

We have discussed in this chapter a wide diversity of computer simulation techniques applied to low-dimensional metal phase formation and electrochemical nanostructuring. Methods considering purely stochastic motion (i.e. Monte Carlo) allow access to the thermodynamics of the system, providing information about the energetic and entropic aspects of the system of interest, ignoring in most cases the kinetics. On the other hand, entirely deterministic methods (i.e. molecular (atom) dynamics) can be applied to study dynamic processes on the nanosecond scale. A typical example of the latter is the atomistic picture of the tip-induced local metal deposition method, revealing alloy formation on the generated clusters for strong tip–substrate interactions. Some of the predictions made have, until today, no experimental evidence, due to experimental limitations in observing different types of metals with atomic precision. Intermediate types of computer simulations are the quasi-stochastic Langevin or Brownian Dynamics, which were used in recent years to consider stochastic effects and friction with solvent particles. Interesting predictions have been reported in the literature, in particular for electrocrystallization on different metal surfaces. The absence of improved interatomic potentials to describe realistically the interaction between metal atoms, water and ions make the computer experiments a purely metallic atomistic approach. Thus, while metal phase formation in ultrahigh vacuum experiments can be directly compared with the computer simulation presented in the present chapter, the behavior of systems where solvent or ions play a decisive role must still await further developments to be properly simulated. Intermediate cases, where solvent and ions play a secondary role may be successfully understood at a qualitative level.

In conclusion, realistic models are starting to be constructed to perform numerical simulations with the help of computers, in order to explore the atomistic and

elemental processes involved in the first stages of metal deposition and electrochemical nanostructuring. Thermodynamics and kinetics can be taken into account, and new methodologies, together with the enormous growth in computer power, promise a prosperous future in the field.

Acknowledgments

The authors wish to thank Consejo Nacional de Investigaciones Científicas y Técnicas (CONICET), Agencia Córdoba Ciencia, Secyt UNC, Program BID 1201/OC-AR PICT No. 06-12485 for financial support.

References

- 1 G. BINNING, H. ROHRER, Ch. GERBER, E. WEIBEL, *Appl. Phys. Lett.* **1981**, *40*, 178–180.
- 2 G. BINNIG, C. F. QUATE, Ch. GERBER, *Phys. Rev. Lett.* **1986**, *56*, 930–933.
- 3 R. J. SONNENFELD, P. K. HANSMA, in *Modern Aspects of Electrochemistry*, J. O'M. BOCKRIS et al. (Eds.), Vol. 21, Kluwer, New York, **1990**.
- 4 M. P. ALLEN, D. J. TILDESLEY, *Computer Simulation of Liquids*, Oxford University Press, Oxford, **1987**.
- 5 R. CAR, M. PARRINELLO, *Phys. Rev. Lett.*, **1985**, *55*, 2471–2474.
- 6 E. BUDEVSKI, G. STAIKOV, W. J. LORENZ, *Electrochemical Phase Formation and Growth*, VCH, Weinheim, **1996**.
- 7 W. J. LORENZ, G. STAIKOV, W. SCHINDLER, W. WIESBECK, *J. Electrochem. Soc.*, **2002**, *49*, K47–59.
- 8 N. B. LUQUE, E. P. M. LEIVA, *Electrochim. Acta*, **2005**, *50*, 3161–3178.
- 9 D. M. KOLB, F. C. SIMEONE, *Electrochim. Acta*, **2005**, *50*, 2989–2996.
- 10 D. M. KOLB, R. ULLMANN, T. WILL, *Science* **1997**, *275*, 1097–1099.
- 11 G. E. ENGELMANN, J. C. ZIEGLER, D. M. KOLB, *J. Electrochem. Soc.* **1998**, *145*, L33–L35.
- 12 D. M. KOLB, R. ULLMANN, J. C. ZIEGLER, *Electrochim. Acta*, **1998**, *43*, 2751–2760.
- 13 D. M. KOLB, G. E. ENGELMANN, J. C. ZIEGLER, *Solid State Ionics*, **2000**, *131*, 69–78.
- 14 U. LANDMAN, W. D. LUEDTKE, *Consequences of Tip-Sample Interactions, in: Scanning Tunneling Microscopy III*, R. WIESENDANGER, H. J. GÜNTHERODT (Eds.), Springer Verlag, Berlin, **1993**; U. LANDMAN, W. D. LUEDTKE, N. A. BURNHAM, R. J. COLTON, *Science* **1990**, *248*, 454–461.
- 15 M. G. DEL PÓPOLO, E. P. M. LEIVA, W. SCHMICKLER, *Angew. Chem.* **2001**, *113*, 4807–4809.
- 16 M. G. DEL PÓPOLO, E. P. M. LEIVA, H. KLEINE, J. MEIER, U. STIMMING, M. MARISCAL, W. SCHMICKLER, *App. Phys. Lett.*, **2002**, *81*, 2635–2637.
- 17 M. G. DEL PÓPOLO, E. P. M. LEIVA, H. KLEINE, J. MEIER, U. STIMMING, M. MARISCAL, W. SCHMICKLER, *Electrochim. Acta* **2003**, *48*, 1287–1294.
- 18 M. G. DEL PÓPOLO, E. P. M. LEIVA, M. MARISCAL, W. SCHMICKLER, *Nanotechnology*, **2003**, *14*, 1009–1013.
- 19 M. G. DEL PÓPOLO, E. P. M. LEIVA, M. MARISCAL, W. SCHMICKLER, *Surf. Sci.*, **2005**, *597*, 133–155.
- 20 S. M. FOILES, M. I. BASKES, M. S. DAW, *Phys. Rev. B*, **1986**, *33*, 7983–7991.
- 21 M. MARISCAL, C. NARAMBUENA, M. G. DEL PÓPOLO, E. P. M. LEIVA, *Nanotechnology*, **2005**, *16*, 974–980.
- 22 T. L. HILL, *Intruducción a la Termodinámica Estadística*, Paraninfo, España, **1970**.

- 23 N. METROPOLIS, A. ROSENBLUTH, M. ROSENBLUTH, A. H. TELLER, E. TELLER, *J. Chem. Phys.*, **1953**, *21*, 1087–1092.
- 24 D. M. KOLB, G. ENGELMANN, J. C. ZIEGLER, *Angew. Chem. Int. Ed. Engl.*, **2000**, *39*, 1123–1125.
- 25 S. MAUPAI, Ph.D. Thesis, Technical University of Erlangen, **2001**.
- 26 N. B. LUQUE, E. P. M. LEIVA, *Surf. Sci.*, **2004**, *571*, L319–L324.
- 27 X. H. XIA, R. SCHUSTER, V. KIRSCHNER, G. ERTL, *J. Electroanal. Chem.*, **1999**, *461*, 102–109.
- 28 G. BROWN, P. A. RIKVOLD, S. J. MITCHELL, M. A. NOVOTNY, in *Interfacial Electrochemistry*, Ch. 4, A. WIECKOWSKI (Ed.), Marcel Dekker, New York, **1999**.
- 29 K. A. FICHTHORN, W. H. WEINBERG, *J. Chem. Phys.*, **1991**, *95*, 1090–1096.
- 30 E. P. M. LEIVA, in *Current Topics in Electrochemistry*, Vol. 2, pp. 269–291, Council of Scientific Information, Trivandrum, India, **1993**.
- 31 E. P. M. LEIVA, *Electrochim. Acta*, **1996**, *41*, 2185–2206.
- 32 D. M. KOLB, in *Advances in Electrochemistry and Electrochemical Engineering*, H. GERISCHER, C. W. TOBIAS (Eds.), Vol. 11, Wiley, New York **1978**.
- 33 S. TRASATTI, *Z. Phys. Chem. NF* **1975**, *98*, 75.
- 34 K. K. JUTTNER, G. STAIKOV, W. J. LORENZ, E. SCHMIDT, *J. Electroanal. Chem.*, **1977**, *80*, 67–70.
- 35 A. BEWICK, B. THOMAS, *J. Electroanal. Chem.*, **1975**, *65*, 911–931.
- 36 A. BEWICK, B. THOMAS, *J. Electroanal. Chem.*, **1976**, *70*, 239–244.
- 37 L. BLUM, D. A. HUCKABY, M. LEGAULT, *Electrochim. Acta*, **1996**, *41*, 2207–2227.
- 38 G. STAIKOV, W. J. LORENZ, E. BUDEWSKI, in *Imaging of Surfaces and Interfaces*, Ch. 1, J. LIPKOWSKI, P. N. ROSS (Eds.), New York, **1999**.
- 39 S. G. GARCIA, Ph.D. Thesis, Universidad Nacional del Sur, Bahia Blanca, Argentina, **1997**.
- 40 D. CARNAL, P. I. ODEN, U. MULLER, E. SCHMIDT, H. SIGENTALER, *Electrochim. Acta*, **1995**, *40*, 1223–1235.
- 41 G. STAIKOV, K. JUTTNER, W. J. LORENZ, E. BUDEWSKI, *Electrochim. Acta*, **1978**, *23*, 319–324.
- 42 M. F. TONEY, J. G. GORDON, M. G. SAMMANT, G. L. BORGES, O. R. MERLOY, D. YEE, L. B. SORENSEN, *J. Phys. Chem.*, **1995**, *99*, 4733–4744.
- 43 F. CELESTINI, D. PASSERONE, F. ERCOLESI, E. TOSATTI, *Surf. Sci.* **1998**, *402*, 886–890.
- 44 N. GOLDENFELD, *Lectures in Phase Transitions and the Renormalization Group*, Addison Wesley Publishing Company, New York, **1992**.
- 45 M. I. ROJAS, *Surf. Sci.*, **2004**, *14*, 76–88.
- 46 M. C. GIMÉNEZ, E. P. M. LEIVA, *Langmuir*, **2003**, *19*, 10538–10549.
- 47 M. C. GIMÉNEZ, M. G. DEL POPOLO, E. P. M. LEIVA, S. G. GARCÍA, D. R. SALINAS, C. E. MAYER, W. J. LORENZ, *J. Electrochem. Soc.* **2002**, *149*, E109–116.
- 48 M. C. GIMÉNEZ, M. G. DEL PÓPOLO, E. P. M. LEIVA, *Langmuir* **2002**, *18*, 9087–9094.
- 49 F. REIF, *Fundamentals of Statistical and Thermal Physics*, McGraw-Hill Kogakusha, Tokyo, **1965**.
- 50 W. LI, G. S. HSIAO, D. HARRIS, R. M. NYFFENEGGER, J. A. VIRTANEN, R. M. PENNER, *J. Phys. Chem.* **1996**, *100*, 20103–20113.
- 51 J. L. FRANSAER, R. M. PENNER, *J. Phys. Chem. B*, **1999**, *103*, 7643–7653.
- 52 R. M. PENNER, *J. Phys. Chem. B*, **2001**, *105*, 8672–8678.
- 53 W. SCHMICKLER, K. POETTING, M. MARISCAL, *Chem. Phys.* **2006**, *320*, 149–154.
- 54 L. A. KIBLER, M. KLEINERT, R. RANDLER, D. M. KOLB, *Surf. Sci.* **1999**, *443*, 19–30.
- 55 E. KOEL, A. SELLIDJ, M. T. PAFFETT, *Phys. Rev. B.*, **1992**, *46*, 7846–7856.
- 56 M. M. MARISCAL, K. PÖTTING, W. SCHMICKLER, in preparation.
- 57 M. I. ROJAS, C. G. SANCHEZ, M. G. DEL PÓPOLO, E. P. M. LEIVA, *Surf. Sci.* **2000**, *453*, 225–228.
- 58 M. M. MARISCAL, Ph.D. Thesis, Universität Ulm, Germany, **2004**.
- 59 M. G. DEL PÓPOLO, Ph.D. Thesis, Universidad Nacional de Córdoba, Argentina, **2002**.

3

Electrodeposition of Metals in Templates and STM Tip-generated 0D Nanocavities

Wolfgang Kautek

3.1

Introduction

Low-dimensional metal systems are of crucial importance for nanotechnology. They may be produced lithographically, by physical vapor deposition delocalised on substrates, or by electrochemical *in situ* scanning probe microscopy (SPM) techniques [1]. Electrochemical nanotechnology is a wide ranging and expanding multi-disciplinary area. Electrochemical materials science in nanoscopic dimensions yields a high technological potential. The electrochemical approach has been proven successful not only in the fabrication of nanostructures and nano-assemblies, addressing molecular electronics, nanostructured materials, nanoelectrodes, photonic crystal nanocavities, 2D and 3D assemblies of nanoparticles and q-dots, but also in electron transport across nanostructured materials [2–7]. There is evidence that localized metal nanostructures of less than 10 nm width can only be reproducibly formed by electrochemical approaches [8–10].

The promise and reality of electrochemical nanotechnology currently do not align due to the lack of theoretical models to predict electrochemical activity of nanostructures and the lack of synthesis techniques to construct a variety of microstructures from the atom up. Further research is necessary and under way in several laboratories.

3.2

Bottom-up Template Approach

Nanosize metallic structures are very promising materials for new physical and chemical applications. Structure sizes below the Fermi wavelength cause the localization of the electrons and change the physical and chemical behavior. Various technologies have been developed to fabricate metallic nanostructures. Among these the use of templates for localized metal deposition is particularly promising, for example for the growth of nanowires or dots in polymer membrane nanochannels [11–20]. This approach is illustrated schematically in Fig. 3.1 and has been

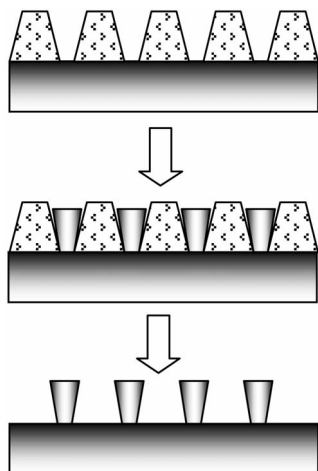


Figure 3.1. Schematics of electrochemical metal deposition (ECD) in templates.

applied successfully for the preparation of various metal nanowires and heterostructured multilayered nanowires. It was shown that single- or polycrystalline metal nanowires can be prepared by applying appropriate polarization routines. An electrochemical jet cell was used, for example, to deposit metal nanowires in a polycarbonate track-etched (PCTE) membrane template contacted by laser-deposited gold which itself was reinforced by electrodeposited gold (Fig. 3.2) [13]. Remarkably, the resulting nanowires exhibited single crystalline {111} orientation (Fig. 3.3). The possibility for fabrication of single- and polycrystalline Bi nanowires

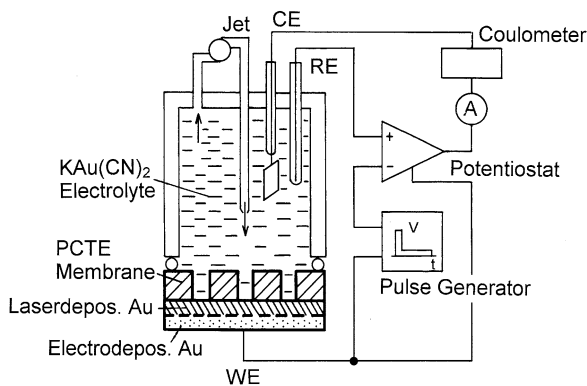


Figure 3.2. Electrochemical jet cell used to deposit metal nanowires in a polycarbonate track-etched (PCTE) membrane template contacted by laser-deposited gold reinforced by electrodeposited gold. WE: working electrode. RE: reference electrode. CE: counter electrode. The jet provides reproducible convection conditions in front of the template [13].

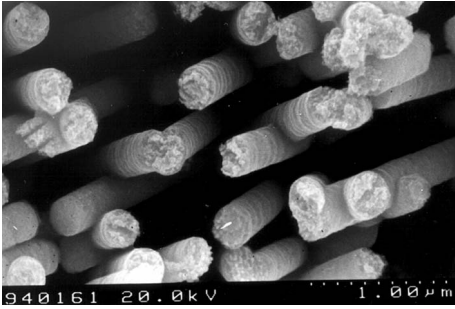


Figure 3.3. Single crystalline gold nanowires in a poly-carbonate track-etched (PCTE) membrane template after dissolution of the template [13].

by electrodeposition in single-channel polymer membranes has also been demonstrated recently [19, 20].

Another technique based on the approach shown in Fig. 3.1 utilizes highly ordered anodized aluminum oxide (AAO) porous membranes as a template for electroless [21] and electrodeposition of metals, alloys, and metal-organic phases [22–24]. It is employed as a general fabrication means for the formation of an array of two-dimensional lateral superlattice nanostructures. The flexibility of using a variety of materials gives the freedom of engineering various physical properties determined by the shape, size, composition, and doping of the nanostructures.

Conductive surface templates have also been employed to control the local electrochemical deposition of metals in nanoscale dimensions, for example via preferred nucleation at defects and step edges [25].

An approach combining top-down structuring with a bottom-up strategy is the fabrication of electrochemical surface templates based on the patterning of self-assembled monolayers (SAMs). By modification of the molecular structure, SAMs provide a flexible route to control the electron transfer [26, 27] and, thus the electrochemical properties of the SAM-coated surface [28, 29]. Patterning of SAMs can be performed not only by conventional lithographic tools (light, electrons, ions) as well as by soft lithography [30, 31], but also by local electrochemical removal of a SAM of for instance dodecanethiol on flame-annealed gold by an electrochemical desorption procedure [32]. Nanoscale SAM structures with lateral dimensions of ~ 10 nm have been fabricated by scanning probe [33, 34], as well as by electron beam lithography [35–39]. To pattern large arrays with nanoscale elements, proximity printing with low energy electrons has been demonstrated to be a fast parallel method [40, 41]. SAMs of aliphatic and aromatic thiols are most commonly used to modify gold surfaces. When irradiated with electrons, 1-octadecanethiol (ODT) acts as a positive resist and 1-1'-biphenyl-4-thiol (BPT) films as a negative resist [42, 43]. The non-irradiated ODT films and the irradiated BPT films resist aqueous cyanide etching solutions and thereby generate contrast on the locally irradiated surfaces.

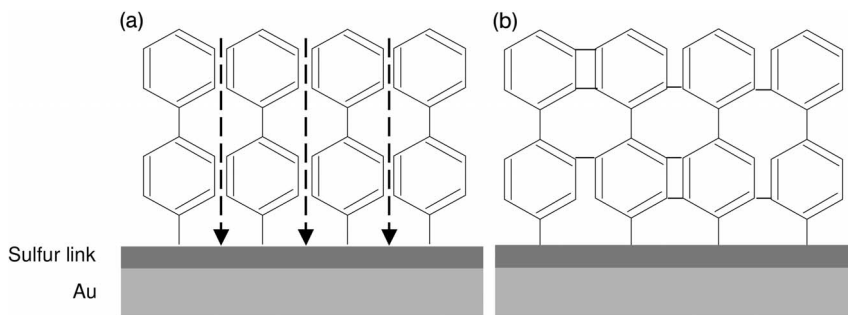


Figure 3.4. 1,1'-biphenyl-4-thiol on gold. Metal ion penetration is possible through the non-irradiated layer (a), and can block penetration acting as “negative” template when crosslinked (b).

Recently, the electrodeposition of copper was investigated in electron beam patterned thiol SAMs on gold electrodes. Patterned alkanethiols act as a “positive” template, that is Cu was only deposited in the irradiated areas [44, 45]. In contrast, SAMs of ω -(4'-methyl-biphenyl-4-yl)-dodecyl thiol and of 1-1'-biphenyl-4-thiol act as “negative” templates where Cu is only deposited in the non-irradiated areas [41, 46].

Cobalt nanoclusters electrodeposited on non-magnetic surfaces are another technologically important system due to their magnetic properties. The size dependence of the magnetic properties, which leads to a transition from ferromagnetic behavior (bulk Co) to superparamagnetic behavior for small isolated clusters [47, 48] can be utilized to increase the data storage capacity of magnetic recording media. Small Co clusters may further be applied in reading heads based on giant magneto-resistance and antiferromagnetic coupling [49, 50], or in tunnel magnetic junctions [51]. Co could be selectively deposited on biphenylthiol negative templates (Fig. 3.4) [52]. Using e-beam patterned BPT as template a continuous metal film could be fabricated. For both Cu and Co, the smallest structures produced this way were 30 nm wide lines and 30 nm dots. Within grating structures a 40–50 nm resolved line width was achieved (Fig. 3.5). Strong evidence was found that highly selective cobalt deposition on BPT is only possible under hydrogen coevolution, which locally influences the pH. This results in precipitation of $\text{Co}(\text{OH})_2$ that can act as a local inhibitor for cobalt deposition.

An example of a self-assembly bottom-up approach without a top-down structuring step is the electrochemical deposition through a self-assembled latex template [53, 54]. The result is near-spherical gold nanocavities within the resulting porous gold films which support localized surface plasmons coupling strongly to incident light with a sharp spectral resonance. The energy of this is tuneable from ultraviolet to near infrared by controlling the diameter and height of the nanocavities. Thus tuneable metallic opto-molecular sensors and filters are a prospect which may find application in magnetic recording media, photonic crystals and biosensors.

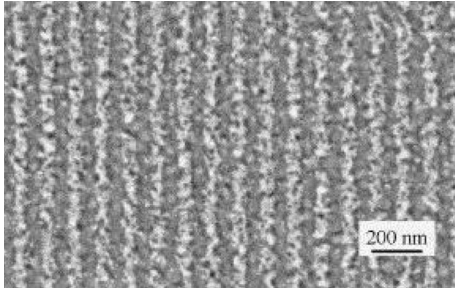


Figure 3.5. SEM micrograph of a Co line grating electro-deposited in a BPT-SAM template patterned by direct e-beam writing [52].

Biological naturally self-assembled templates can be ideal templates. Bacterial surface (S-)layer lattices of for instance *Bacillus sphaericus* can serve as molecular templates for the electroless nucleation of ordered two-dimensional arrays of gold nanoparticles with a size of 5 nm (Fig. 3.6) [55, 56]. Mineralization of the exposed inner face of the self-assembled S-layer was achieved by placing TEM grids covered by S-layer protein monolayers onto drops of an HAuCl_4 solution. H_2S gas treatment resulted in a regularly arranged array of gold nanoparticles in register with the lattice geometry of the protein template. Precipitation of the inorganic phase was confined to the pores of the S-layer with the result that the gold clusters were discrete and relatively uniform in size (mean values, 4.5 nm) with a round shape. Systematic X-ray photoelectron emission spectroscopy (XPS) yielded a detailed chemical analysis of the S-layers during various processing steps and indicated that topography and functional groups are important for a superlattice formation.

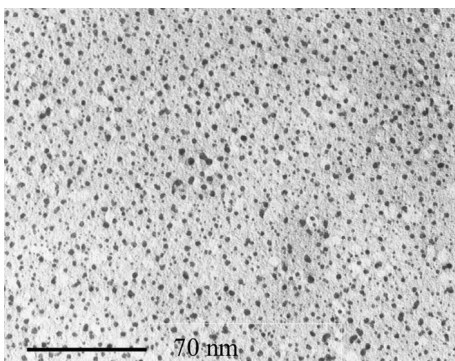


Figure 3.6. Transmission electron micrograph of Au clusters formed on a Pt grid coated with Pioloform® film and S-layer + glutaraldehyde fixation + H_2S treatment [56].

3.3

Top-down SPM Approach

Several electrochemical SPM techniques have evolved to generate low-dimensional metal or oxide systems [57]. The first successful attempts at electrochemical nanostructuring were based on the generation of surface defects by a scanning tunneling tip. The defects were created either by a mechanical contact between tip and substrate, that is a tip crash, or by some sort of sputtering process initiated by the high-voltage pulses applied to the tip [58, 59]. These artificially created defects then acted as nucleation centers for metal deposition, which allowed the decoration of electrode surfaces by metal clusters on a nanometer scale.

Another early probe-induced technique was the initial metal deposition at the SPM probe and the subsequent mechanical transfer of a small Me cluster to the substrate surface below the probe. This technique is based again on the “jump-to-contact” between tip and substrate [60–67]. By applying an electrode potential to the STM tip slightly negative of the bulk deposition potential of the metal ions in solution, metal is deposited from the electrolyte onto the tip. This metal-loaded tip then approaches the surface close enough for the jump-to-contact to occur. A connective neck, a metal bridge between tip and substrate, will break upon the subsequent retreat of the tip. This leaves a small metal cluster on the substrate surface. The tip is then again recoated due to the ongoing metal deposition and becomes ready for the next cluster formation. Provided that the metal deposition is a fast process, cluster generation can be performed at kHz rates: that means an array of 10 000 Cu clusters on Au(111) can be made in minutes [63]. Typical parameters are 10–20 ms pulses at a rate of 50–80 Hz. The cluster size can be varied by changing the tip approach. An electrochemical scanning tunnelling microscope (EC-STM) tip was used to fabricate nanometer-sized Cd clusters on Au(111) electrode surfaces at preselected positions. Cd nanoclusters were formed at different substrate potentials and were studied using electrochemical and topological characterization in the *in situ* STM [67]. The height and stability of nanometer-sized Cd clusters on Au(111) electrode surfaces for instance depended strongly on the applied substrate potential. This was ascribed to potential-dependent surface alloying leading also to a variable composition of the clusters due to intermixing of Cd from the tip with the substrate during the jump-to-contact process.

This tip-induced metal deposition was also investigated on alloy surfaces of AuCu single crystals of various surface composition and orientation [68]. Varying composition of the substrate surface drastically changed the cluster formation behavior and the cluster stability. The cluster stability is explained by an alloy formation during the jump-to-contact process. The alloy like behavior of the clusters becomes obvious when observing the cluster dissolution as a function of the applied potential to selective dealloying of the substrate. The presence of a Cu underpotential deposition layer can have an additional effect in stabilizing the clusters by hampering Au surface diffusion. Such stabilizations seem to be limited to systems where strong attractive interactions are present.

Defect-induced techniques are characterized by a mechanical production of small surface defects of different dimensionality, which can act as nucleation centers in the subsequent metal phase formation process [58, 69, 70].

An approach less harmful to the substrate is the local removal of an overlayer that causes a high overpotential for metal deposition. By choosing an electrode potential slightly negative of the Nernst potential, where no metal deposition will take place on top of the overlayer, deposition will immediately set in upon removal of the overlayer by the tip of an STM or AFM sliding across the surface. This has been demonstrated in an AFM study for Cu deposition onto an oxide covered Cu surface [71, 72] and in an STM study for Cu deposition onto Au(111) covered by a monolayer of sodium dodecyl sulfate [73]. The scanning force microscopy (SFM) cantilever pressure caused deposition of e.g. a small Cu cluster on Au(100) terraces in the scan region, but no surface damage was observed after lifting [71–73]. This means that the nucleation was induced by either an elastic deformation of the surface or by creation of fresh surface areas free of adsorbed contaminants. Although the precision of the metal nanostructures generated in such a way was comparatively poor [74], this method bears the potential of decorating semiconductor surfaces with metal nanostructures, while so far studies have been mostly restricted to metal on metal. This approach requires dense monolayers with sufficient inhibition for metal deposition which can be removed by the tip without damaging the substrate.

Another approach is field-induced SPM techniques. They make use of the inhomogeneous electric field distribution between the SPM probe and the substrate. Thus the structure of the STM tunnelling gap and of the electrochemical double layers is changed locally, and the metal ion concentration within the gap, and/or the charge carrier density and distribution of the underlying substrate domain are modified [75, 76]. This is based on a burst-like dissolution of metal from the tip, onto which it had been deposited from solution, and the redeposition onto the substrate within a narrow region directly underneath the tip. The key lies in the momentarily high metal ion concentration after the sudden metal dissolution at the tip, which causes a more positive Nernst potential for the surface region underneath the tip.

A related nanostructuring method for the fabrication of 0-dimensional metal structures used the solid electrochemical reaction, the local oxidation/reduction reaction of mobile metal ions in an ionic/electronic mixed conductor induced by an STM tip [77]. Silver sulfide (Ag_2S) was used as the tip material. A nanoscale Ag cluster was formed at the apex of the Ag_2S tip when a negative bias voltage was applied to the sample. The Ag ions in the Ag_2S tip were reduced to Ag atoms by the tunnelling electrons from the sample.

Finally, the majority of this chapter is dedicated to a template-induced technique that relies on the localized electrochemical formation of irreversible cavities or voids as templates for the subsequent electrochemical deposition [78–82]. This makes use of the concept to create zero-dimensional (0D) metal clusters where nanoscaled cavities have to be formed by local corrosion via low-dimensional anion

systems. In this chapter, this method is described for the Bi on Au system. Bismuth nanostructures are of considerable interest, both from a fundamental, as well as from a technological (device applications) points of view [83].

3.4

Thermodynamics of Low-dimensional Phases

Electrodeposition of metals in STM tip-generated template cavities can be appropriately discussed when one considers the important role of nanosized anodically formed cavities. Low dimensional, 0-dimensional (0D), 1-dimensional (1D), and 2-dimensional (2D) metal phases in the underpotential deposition (UPD) range can be directly observed by *in situ* STM and SFM [8, 10, 82, 84]. The formation of low-dimensional anion (or oxide) systems at 0D and 1D substrate surface inhomogeneities as well as the formation of 2D oxide overlayers and 3D passive films determines both the rate determining step of the dissolution kinetics and the dissolution and passivation mechanism. The equilibrium potentials of these are given by [10]

$$U_{iD A} < U_{3D A}^0 + RT/nF \ln[(a_{iD A} a_{H^+}^n)/a_{H_2O}] \quad (3.1)$$

with $i = 0, 1, 2, 3$ and $n = 1, 2$. Since $a_{iD A}$ decreases with decreasing dimensionality i , the equilibrium potential is shifted into the negative direction:

$$U_{0D A} < U_{1D A} < U_{2D A} < U_{3D A} \quad (3.2)$$

Moreover, kinetic results show that the exchange current density of the dissolution of 0D and/or 1D kinks (in the so-called active potential region) is less than that of a 2D kink (in the so-called prepassive potential region).

Low-dimensional metal phases, on the other hand, exist on an ideally polarisable and foreign substrate in the undersaturation range $U > U_{3D Me}$ if the binding energy of Me adatoms on the substrate is stronger than that of the metal on the native substrate. The metal phase formation process usually starts at high underpotentials, ΔU_{UPD} , by a decoration of 0D surface point defects such as kinks, vacancies, interstitials, chemical impurities, and emergence points of edge and screw dislocations. This is followed by the decoration of 1D monatomic steps, intersection lines of grain boundaries and stacking faults. The phase formation process proceeds by the formation of 2D expanded commensurate or gas-like metal adlayers on atomically flat terraces. The last step is the formation of condensed commensurate, high order commensurate or incommensurate 2D monolayers via a first order phase transition. The stability ranges of expanded (gas-like) or condensed (liquid-like or solid-like) Me phases of different dimensionality, iD (with $i = 1, 2, 3$), are characterized by Nernst-type equations [10]:

$$U_{iD Me} = U_{3D Me}^0 + RT/zF \ln(a_{Mez^+}/a_{iD Me}) \quad (3.3)$$

where $U_{iD\text{ Me}}$ denotes the respective equilibrium potential, $U_{3D\text{ Me}}^0$ is the standard potential of the 3D Me bulk phase, $a_{\text{Me}^{z+}}$ the activity of Me^{z+} in the electrolyte, and $a_{iD\text{ Me}}$ the activity of an iD Me phase. In the case of condensed iD Me phases ($i = 0-2$), $a_{iD\text{ Me}}$ are constants and less than unity. $a_{iD\text{ Me}}$ usually decreases with decreasing i so that the corresponding equilibrium potentials are shifted in the positive direction in analogy to the anion systems described above:

$$U_{3D\text{ Me}} < U_{2D\text{ Me}} < U_{1D\text{ Me}} < U_{0D\text{ Me}} \quad (3.4)$$

iD phases are stable at $U < U_{iD\text{ Me}}$. The higher the Me–surface interaction energy, the smaller can be the iD metal phase. The activity term $a_{iD\text{ Me}}$ is related to this interaction energy, so that it is expected to decrease with decreasing dimensionality, giving higher (i.e., more positive) equilibrium potentials for phases of lower dimensionality i .

This thermodynamic situation is of fundamental importance for the electrodeposition of metals in STM-tip-generated 0D nanocavities described here. In the presence of specifically active 0D substrate surface inhomogeneities, a formation of a small 0D Me cluster with defined energetics, size, and structure can be induced. A small localized and stable cluster of Me adatoms with specific energetics and structure different from those of the Me bulk phase, is formally considered as an “0D Me cluster”. This behavior is also supported by first-principle calculations [85, 86]. The adsorption isotherms calculated indicated that Ag adsorption on Au(111) should occur in three well-defined stages: first, adsorption on 0D kink sites, second, adsorption at monatomic steps (1D) and finally formation of the monolayer or 2D phase. In all cases, the presence of inhomogeneities shift the adsorption isotherms towards more negative chemical potentials thus increasing ΔU_{UPD} with respect to that predicted at perfect surfaces.

The stability of small Me clusters and defined Me nanostructures on foreign substrate surfaces is still an open problem. Generally, small 3D clusters have a more negative equilibrium potential than the corresponding infinitely large phases. This effect is related to the Gibbs–Thomson or Kelvin equation and leads to a dissolution of small 3D phases at the corresponding equilibrium potentials. It is evident that a stabilization of iD metal phases ($i = 0, 1, 2$) at open circuit conditions needed for long-time stable nanostructures can be achieved by the low-dimensional system concept using stabilizing effects such as adsorption of interface inhibitors, passivation, and inclusion of contaminants.

3.5

Experiments on the Electrodeposition in STM-tip-generated Nanocavities

The experiments were performed with a scanning tunnelling microscope for *in situ* electrochemical measurements [78, 79, 87]. STM tips were made from electrochemically inert iridium wires by mechanical grinding and were covered, except for the apex of the tip, with Apiezon wax. An open cell made of PCTFE (Kel-F®)

with a volume of ~ 0.2 ml was employed for the *in-situ* STM experiments [78, 79]. A 300 nm thick Au film evaporated onto a borosilicate glass served as the working electrode. This was flame-annealed to about 500 °C in order to obtain large Au(111) terraces. Two platinum wires served as counter and quasi-reference electrodes. Potentials are reported relative to the 3D equilibrium potentials of the metal deposits in the same electrolyte. The electrolytes were prepared from $\text{Bi}(\text{NO}_3)_3 \cdot 5\text{H}_2\text{O}$ and HNO_3 . Nanometer-sized cavities on the gold surface were produced by switching the tip from the input of the STM current amplifier to a pulse generator that provides pulses with duration down to 20 ns and pulse height up to ± 4 V. The STM images were obtained in the constant current mode.

3.6 Underpotential Behavior of Bismuth on Gold

The controlled electrodeposition of 0D phases needs detailed knowledge of the UPD behavior. Bi exhibits two different Bi monolayer structures on Au(111) in the UPD region [88–91]. At a UPD potential $\Delta U_{\text{UPD}} \approx 0.20$ V, a (2×2) -Bi adlattice with a moderate coverage ($\theta_{\text{Bi}} = 0.25$) occurs. There is indication that hydroxide is co-adsorbed with the Bi in a 1:2 ratio [90]. At $\Delta U_{\text{UPD}} \approx 0.10$ V, a condensed uniaxially commensurate structure ($\theta_{\text{Bi}} = 0.64$) is formed before the onset of the bulk metal deposition. The latter fact is significant with respect to the deposition of Bi on Au terraces and in nanocavities, since it indicates that the further Bi deposition onto the condensed Bi monolayer requires a significant additional electrochemical energy, because the monolayer is compressively strained. The Stranski–Krastanov growth model can be expected for the overpotential deposition due to the strong mismatch in the atomic radii of about 22% ($r_{\text{Au}} = 0.144$ nm; $r_{\text{Bi}} = 0.175$ nm) [92].

A cyclic voltamogram for Bi UPD on Au(111) from deaerated BiO^+ (formally also Bi^{3+}) in HNO_3 is depicted in Fig. 3.7. The dashed curves represent deposition and stripping current traces of the 3D metal phases, and allow location of the observed equilibrium potentials of the respective electrode reactions versus the Ag/Ag⁺ electrode potential in the same electrolyte. The Bi/BiO⁺ equilibrium potential theoretically is $U_{3\text{D}} = -0.48$ V(Ag^{0/+}), and has been observed at $U_{3\text{D}} \approx -0.41$ V(Ag^{0/+}) in 0.001 M Me^{z+} (Fig. 3.7). In this context, potentials are conveniently given relative to $U_{3\text{D}}$ i.e. as underpotentials, ΔU_{UPD} .

Bi shows the two characteristic UPD peak groups (Fig. 3.7), the first due to the low coverage (2×2) -Bi adlattice at $\Delta U_{\text{UPD}1} \approx 0.25$ V, and the second at $\Delta U_{\text{UPD}2} \approx 0.19$ V, due to the condensed uniaxially commensurate $(p \times \sqrt{3})$ structure (see above [88–91]). The Au surface of the Bi experiment in Fig. 3.7 exhibited not only pure (111) orientation, but also several shifted peaks were observed in contrast. The small current features at $U > U_{\text{UPD}1}$ can be correlated to the formation of a higher quantity of 1D phases, i.e. the decoration of steps, which exhibit a higher concentration on a misoriented low-index plane.

The point of zero charge (pzc) of the substrate Au is of major importance for any UPD reactions since it determines the nature and surface excess of adsorbed

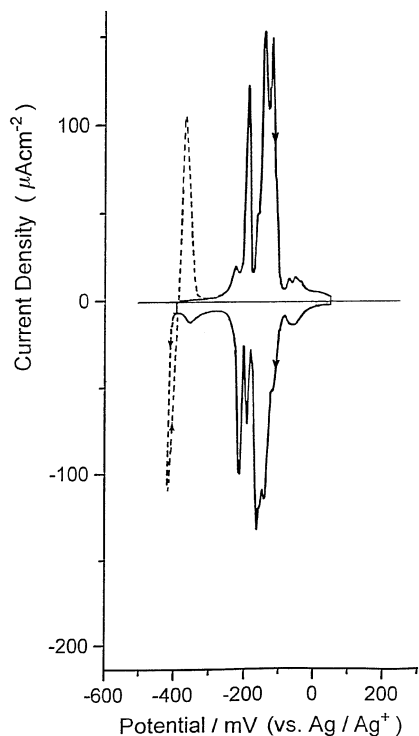


Figure 3.7. Representative cyclic voltammograms for Bi underpotential deposition (UPD) on Au(111). Electrolyte: deaerated, 0.001 M Me^{z+} + 0.01 M HNO_3 . Scan rate: 0.03 V s^{-1} . Potential versus the Ag/Ag^+ electrode in this electrolyte. Dashed curves represent current traces when 3D Me phases have been deposited [82].

cations and/or anions that compete with underpotential deposits for surface sites. Au(111) exhibits pzc's at $U_{\text{pzc}} = 0.47 \text{ V(SHE)} = -0.15 \text{ V(Ag}^{0/+})$ [86–88], and Au(210) at $U_{\text{pzc}} \approx -0.40 \text{ V(Ag}^{0/+})$ [93]. Au(111) shows the most anodic and Au(210) the most cathodic pzc [94]. The entire UPD range of Bi therefore overlaps with the double layer region of Au(111) where Au oxide is not stable (Fig. 3.6). Only NO_3^- anion adsorption competes with the formation of the low coverage (2×2)-Bi adlattice at $\Delta U_{\text{UPD}1} \approx 0.25 \text{ V}$, that is $U \approx -0.16 \text{ V(Ag}^{0/+})$ almost coincident with the Au pzc $U_{\text{pzc}} = -0.15 \text{ V(Ag}^{0/+})$ [94–97]. That means that the formation of the condensed uniaxially commensurate ($p \times \sqrt{3}$) structure down to $\Delta U_{\text{UPD}2} \approx 0.19 \text{ V}$, that is $U \approx -0.22 \text{ V(Ag}^{0/+})$, occurs on a Au surface with about equal surface concentrations of NO_3^- anions and cations, such as hydronium cations, and the Bi source, hydrated BiO^+ cations. The generation of the 3D Bi phase, however has to compete with anion adsorption on the Bi monolayer which is expected to exhibit a much more negative pzc as naked Ag ($U_{\text{pzc}}(\text{Ag}) \approx -1.10 \text{ V(Ag}^{0/+})$), or even Au ($U_{\text{pzc}} = -0.15 \text{ V(Ag}^{0/+})$).

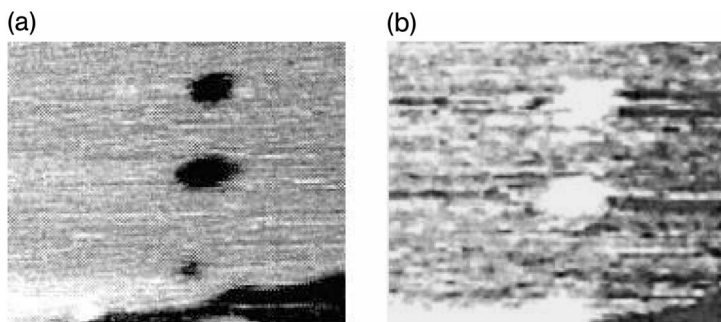


Figure 3.8. STM images ($60 \times 25 \text{ nm}^2$) obtained on Au(111) in 0.01 M $\text{Bi}(\text{NO}_3)_3 + 1 \text{ M HNO}_3$. (a) $U = 0.52 \text{ V}$ ($\text{Bi}^{0/3+}$) after application of potential pulses of 80 ns duration and 2.8 V between tip (tip negative) and sample; (b) after potential step from +0.52 to +0.15 V ($\text{Bi}^{0/3+}$), 16.5 min [82].

3.7 Zero-dimensional Bi Deposition

The formation of the nanocavities on Au in a 0.01 M $\text{Bi}(\text{NO}_3)_3 + 1 \text{ M HNO}_3$ electrolyte was carried out at $U \approx +0.10 \text{ V}(\text{Ag}^{0/+})$ or $U \approx +0.52 \text{ V}(\text{Bi}/\text{BiO}^+)$, that is more than 0.2 V positive of the Bi-UPD range, which sets in below $\Delta U_{\text{UPD}1} \approx -0.17 \text{ V}(\text{Ag}^{0/+})$. The STM image in Fig. 3.8(a) shows a Au(111) terrace on which three nanocavities were created by the application of three 2.8 V 80 ns pulses (tip negative) between the tip and the sample. The diameters range between about 3 and 5 nm. Though the curvature of the tip interferes with the true topography of the nanocavities, one can conclude that the two upper cavities are at least 2 monolayers deep (Fig. 3.8(a)).

After the cavity formation, the electrode potential was reduced to $U \approx 0.27 \text{ V}(\text{Ag}^{0/+})$ or $U \approx +0.15 \text{ V}(\text{Bi}/\text{BiO}^+)$ near the UPD potential, $\Delta U_{\text{UPD}2} \approx +0.19 \text{ V}$, where a condensed Bi layer is formed, not only on the terraces, but with high probability also on the bottoms and walls of the cavities. The STM image in Fig. 3.8(b) was obtained after this potential step. Progressive and preferential filling of the nanocavities with Bi is evident from the cross sections in Fig. 3.9, as well as from the more extensive data plot of the depths of the three cavities as a function of the deposition time (Fig. 3.10). The data in Fig. 3.10 were evaluated from a set of twelve consecutive STM images each requiring 90 s. At $U \approx +0.15 \text{ V}(\text{Bi}/\text{BiO}^+)$, almost coincident with $\Delta U_{\text{UPD}2} \approx +0.19 \text{ V}$, the deposition ceased (in less than half an hour) as the cavities were filled with Bi, that means as soon as the growing Bi nanoclusters reached the surface of the compact UPD Bi layer on the terraces. These embedded clusters appear as about 0.1 nm high protrusions above the surface in the STM images (Figs. 3.8 and 3.9). Considering the substantial atomic radii difference of about 22% of Bi (0.175 nm) and Au (0.144 nm), this height difference can be mainly explained topographically without the necessity of invoking

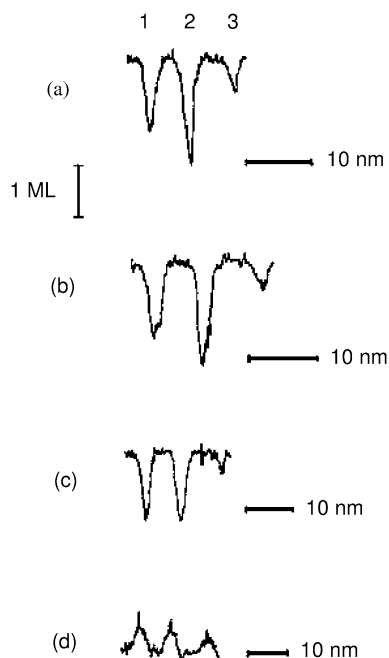


Figure 3.9. Cross sections of three nanocavities imaged in Fig. 3.8(a). (a) $U \approx +0.52 \text{ V}(\text{Bi}^{0/3+})$; (b) immediately after potential step to $+0.15 \text{ V}(\text{Bi}^{0/3+})$; (c) after 7.5 min; (d) after 16.5 min. Horizontal bars: 10 nm. Vertical bars: Au monolayer units (= 0.29 nm) [82].

electronic effects such as workfunction differences. From this protrusion height, one can deduce the deposition of two Bi monolayers in addition to the first UPD layer present on the bottom of the middle cavity which is two Au monolayers deep.

0D metal clusters could not be formed on gold 0D cavities that were always covered by oxide, hydroxide or nitrate. Only once the entire Au surface, including the 0D cavities, was covered by a dense monolayer of the deposit metal, and no direct interaction with Au was possible, could 0D Bi clusters on Bi-“clad” 0D cavities be generated. However, the Bi surface also exhibits more or less strong nitrate adsorption over the entire UPD range down to the bulk deposition. This obviously is no inhibitor for the 0D species.

The fundamental reason for the privileged properties of Bi lies in the fact that the pzc of Au is almost 0.2 V positive of the 3D-Bi/BiO⁺ potential $U_{3D}(\text{Bi})$ so that anions cannot inhibit the formation of the close-packed adlayer in the range between $U_{3D}(\text{Bi})$ and $U_{pzc}(\text{Au}) \approx U_{\text{UPD } 2}(\text{Bi})$. 0D clusters can be generated. However, Bi with the larger atomic radius than the host Au always results in morphologically observable features with finite vertical heights whereas the commensurate Ag, with a radius practically equal to that of the template, leads to a flat filling of the 0D void

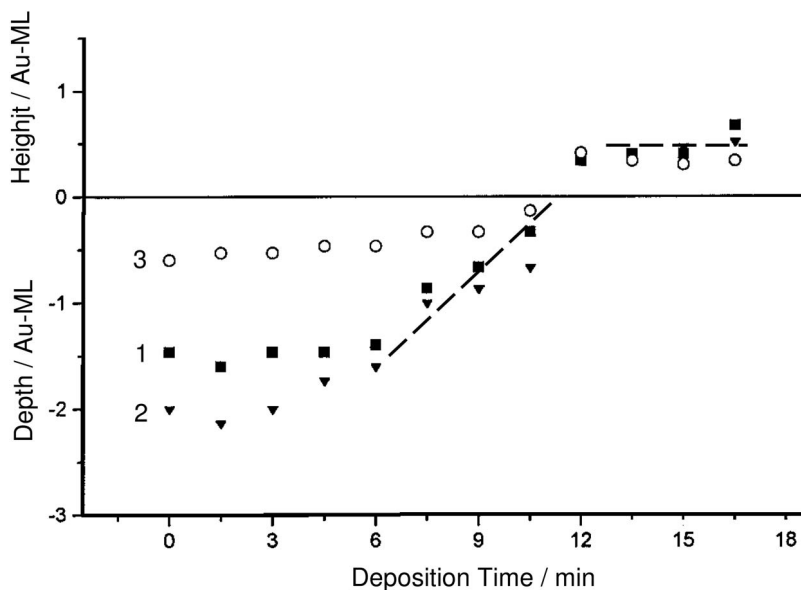


Figure 3.10. Growth of Bi in the three cavities (Fig. 3.9) on Au(111) and in 0.01 M $\text{Bi}(\text{NO}_3)_3 + 0.01$ M HNO_3 as a function of time at $U = +0.15$ V($\text{Bi}^{0/3+}$) [82].

in Au. It needs the stability of condensed UPD layers before 0D cavities can be locally filled and 0D deposits can be generated without masking of overpotential growth of terraces and 3D phases. Only when there is a wide stability region for a dense monolayer as e.g. in the case of Bi between 0 and $+0.19$ V(Bi/BiO^+), can the formation of 2D (terraces) and 3D (bulk) phases be avoided.

3.8

Conclusions

Low-dimensional metal systems on interfaces are of crucial importance for nanotechnology. Localized metal nanostructures of less than 10 nm width can be reproducibly formed by electrochemical approaches. Most of these use stochastic bottom-up techniques such as the deposition of nanowires along steps or hollow channels, of controlled metal nuclei, but top-down, lithographically and electrochemical *in situ* scanning probe microscopy (SPM) techniques are also used. In this context, mainly the combination of a top-down electron beam structuring of self-assembled monolayer templates and the top-down SPM template surface cavities generation, both followed by bottom-up growth of nanometer-sized zero-dimensional (0D) metal dots are discussed.

Acknowledgment

The author would like to thank the German Science Foundation (Deutsche Forschungsgemeinschaft, DFG, Bonn, Germany) for financial support (project “Grundlagen der elektrochemischen Nanotechnologie”), and R. Schuster and G. Ertl (Fritz-Haber-Institute of the Max-Planck-Society, Berlin, Germany) for the generous access to their STM equipment. He gratefully acknowledges the fruitful experimental collaboration with T. Solomun and A. Goelzhaeuser with collaborators, and intensive invaluable discussions with W. J. Lorenz, W. Schindler, and G. Staikov.

References

- 1 *Chemistry at the Beginning of the Third Millennium: Molecular Design, Supramolecules, Nanotechnology and Beyond*, L. FABBRIZZI, A. POGGI (Eds.), Springer, Berlin, Heidelberg, New York, 2000.
- 2 *Electrochemical Nanotechnology – In situ Local Probe Techniques at Electrochemical Interfaces*, W. J. LORENZ, W. PLIETH (Eds.), Wiley-VCH, Weinheim, 1998.
- 3 *Imaging of Surfaces and Interfaces – Frontiers in Electrochemistry*, Vol. 5, P. ROSS, J. LIPKOWSKI (Eds.), Wiley-VCH, Weinheim, 1999.
- 4 *Scaling down in Electrochemistry: Electrochemical Micro- and Nanosystem Technology*, J. W. SCHULTZE, G. STAIKOV (Eds.), Elsevier, Amsterdam 2001.
- 5 *Electrochemical Microsystem Technologies*, J. W. SCHULTZE, T. OSAKA, M. DATTA (Eds.), New Trends in Electrochemical Technology, Vol. 2, Taylor & Francis, London and New York, 2002.
- 6 *Electrochemical Processing of Nanomaterials Vision*, J. W. SCHULTZE, T. OSAKA (Eds.), *Electrochemistry* 2004, Vol. 72.
- 7 J. W. SCHULTZE, A. HEIDELBERG, C. ROSENKRANZ, T. SCHAPERS, G. STAIKOV, *Electrochim. Acta*, 2005, 51, 775.
- 8 E. BUDEVSKI, G. STAIKOV, W. J. LORENZ, *Electrochemical Phase Formation and Growth – An Introduction to the Initial Stages of Metal Deposition*, VCH, Weinheim, 1996.
- 9 G. STAIKOV, W. J. LORENZ, in *Electrochemical Nanotechnology – In situ Local Probe Techniques at Electrochemical Interfaces*, W. J. LORENZ, W. PLIETH (Eds.), Wiley-VCH, Weinheim, 1998, p. 13.
- 10 G. STAIKOV, W. J. LORENZ, E. BUDEVSKI, in *Imaging of Surfaces and Interfaces – Frontiers in Electrochemistry*, Vol. 5, P. ROSS, J. LIPKOWSKI (Eds.), Wiley-VCH, Weinheim, 1999, p. 1.
- 11 R. M. PENNER, C. R. MARTIN, *Anal. Chem.*, 1987, 59, 2625.
- 12 T. M. WHITNEY, J. S. JIANG, P. C. SEARSON, C. L. CHIEN, *Science*, 1993, 261, 1316.
- 13 W. KAUTEK, S. REETZ, S. PENTZIEN, *Electrochim. Acta*, 1995, 40, 1461.
- 14 C. R. MARTIN, D. T. MITCHELL, in *Electroanalytical Chemistry*, Vol. 21, A. J. BARD, I. RUBINSTEIN (Eds.), Marcel Dekker, New York, 1999, p. 1.
- 15 W. SCHWARZACHER, O. I. KASYUTICH, P. R. EVANS, M. G. DARBYSHIRE, GE YI, V. M. FEDOSYUK, F. ROUSSEAU, E. CAMBRIL, D. DECANNINI, *J. Magn. Mater.*, 1999, 198–199, 185.
- 16 GE YI, W. SCHWARZACHER, *Appl. Phys. Lett.*, 1999, 74, 1746.
- 17 M. CHEN, P. C. SEARSON, C. L. CHIEN, *J. Appl. Phys.*, 2003, 93, 8253.
- 18 M. E. TOIMIL MOLARES, V. BUSCHMANN, D. DOBREV, R.

- NEUMANN, R. SCHOLZ, I. U. SCHUCHERT, J. VETTER, *Adv. Mater.*, **2001**, *13*, 62.
- 19 M. E. TOIMIL MOLARES, N. GHTANKO, T. W. CORNELIUS, D. DOBREV, I. ENCULESCU, R. H. BLICK, R. NEUMANN, *Nanotechnology*, **2004**, *15*, S1.
- 20 T. W. CORNELIUS, J. BRÖTZ, N. GHTANKO, D. DOBREV, G. MIEHE, R. NEUMANN, M. E. TOIMIL MOLARES, *Nanotechnology*, **2005**, *16*, S246.
- 21 N. LI, X. LI, X. YIN, W. WANG, S. QIU, *Solid State Commun.*, **2004**, *132*, 841
- 22 C. Y. HAN, Z. L. XIAO, H. H. WANG, G. A. WILLING, U. GEISER, U. WELP, W. K. KWOK, S. D. BADER, G. W. CRABTREE, *Plating Surf. Finish.*, **2004**, *91*, 40–45.
- 23 H. LUO, X. CHEN, P. ZHOU, H. SHI, D. XUE, *J. Electrochem. Soc.*, **2004**, *151*, C567.
- 24 G. JI, S. TANG, W. CHEN, B. GU, Y. DU, *Solid State Commun.*, **2004**, *132*, 289.
- 25 M. P. ZACH, K. H. NG, R. G. PENNER, *Science*, **2000**, *290*, 2120.
- 26 M. A. RAMPI, O. J. A. SCHUELLER, G. M. WHITESIDES, *Appl. Phys. Lett.*, **1998**, *72*, 1781.
- 27 R. E. HOLMLIN, R. HAAG, M. L. CHABINYC, R. F. ISMAGILOV, A. E. COHEN, A. TERFORT, M. A. RAMPI, G. M. WHITESIDES, *J. Am. Chem. Soc.*, **2001**, *123*, 5075.
- 28 A. ULMAN, *Chem. Rev.*, **1996**, *96*, 1533.
- 29 H. O. FINKLEA, *Electroanal. Chem.*, **1996**, *19*, 109.
- 30 Y. N. XIA, J. A. ROGERS, K. E. PAUL, G. M. WHITESIDES, *Chem. Rev.*, **1999**, *99*, 1823.
- 31 Y. N. XIA, G. M. WHITESIDES, *Angew. Chem. Int. Ed. Engl.*, **1998**, *37*, 551.
- 32 O. SKLYAR, T. H. TREUTLER, N. VLACHOPOULOS, G. WITTSTOCK, *Surf. Sci.*, **2005**, *597*, 181.
- 33 M. J. LERCEL, G. F. REDINBO, H. G. CRAIGHEAD, C. W. SHEEN, D. L. ALLARA, *Appl. Phys. Lett.*, **1994**, *65*, 974.
- 34 R. D. PINER, J. ZHU, F. XU, S. H. HONG, C. A. MIRKIN, *Science*, **1999**, *283*, 661.
- 35 M. J. LERCEL, H. G. CRAIGHEAD, A. N. PARIKH, K. SESHADRI, D. L. ALLARA, *Appl. Phys. Lett.*, **1996**, *68*, 1504.
- 36 C. K. HARNETT, K. M. SATYALAKSHMI, H. G. CRAIGHEAD, *Appl. Phys. Lett.*, **2000**, *76*, 2466.
- 37 W. J. DRESSICK, M. S. CHEN, S. L. BRANDOW, K. W. RHEE, L. M. SHIREY, F. K. PERKINS, *Appl. Phys. Lett.*, **2001**, *78*, 676.
- 38 A. GÖLZHÄUSER, W. ECK, W. GEYER, V. STADLER, T. WEIMANN, P. HINZE, M. GRUNZE, *Adv. Mater.*, **2001**, *13*, 806.
- 39 W. GEYER, V. STADLER, W. ECK, A. GÖLZHÄUSER, M. GRUNZE, M. SAUER, T. WEIMANN, P. HINZE, *J. Vac. Sci. Technol. B*, **2001**, *19*, 2732.
- 40 C. DAVID, H. U. MÜLLER, B. VÖLKELE, M. GRUNZE, *Microelectron. Eng.*, **1996**, *30*, 57.
- 41 T. FELGENHAUER, C. YAN, W. GEYER, H. T. RONG, A. GÖLZHÄUSER, M. BUCK, *Appl. Phys. Lett.*, **2001**, *79*, 3323.
- 42 W. GEYER, V. STADLER, W. ECK, M. ZHARNIKOV, A. GÖLZHÄUSER, M. GRUNZE, *Appl. Phys. Lett.*, **1999**, *75*, 2401.
- 43 A. GÖLZHÄUSER, W. GEYER, V. STADLER, W. ECK, M. GRUNZE, K. EDINGER, T. WEIMANN, P. HINZE, *J. Vac. Sci. Technol. B*, **2000**, *18*, 3414.
- 44 J. A. M. SONDAG-HUETHORST, L. G. J. FOKKINK, *Langmuir*, **1992**, *8*, 2560.
- 45 J. A. M. SONDAG-HUETHORST, H. R. J. VAN HELLEPUTTE, L. G. J. FOKKINK, *Appl. Phys. Lett.*, **1994**, *64*, 285.
- 46 G. KALTENPOTH, B. VÖLKELE, C. T. NOTTBOHM, A. GÖLZHÄUSER, M. BUCK, *J. Vac. Sci. Technol. B*, **2002**, *20*, 2734.
- 47 J. A. BECKER, R. SCHAEFER, R. FESTAG, W. RULAND, J. H. WENDORFF, J. PEBLER, S. A. QUAISER, W. HELBIG, M. T. REETZ, *J. Chem. Phys.*, **1995**, *103*, 2520.
- 48 S. PADOVANI, I. CHADO, F. SCHEURER, J. P. BUCHER, *Phys. Rev. B*, **1999**, *59*, 11887.
- 49 J. P. WANG, S. N. PIRAMANAYAGAM, C. H. HEE, L. HUANG, S. I. PANG, S. K. CHOW, X. SHI, T. C. CHONG, *J. Appl. Phys.*, **2002**, *91*, 7694.

- 50 R. MOREL, L. B. STEREN, A. BARTHELEMY, F. PARENT, A. FERT, A. MASSON, B. BELLAMY, *Surf. Rev. Lett.*, **1996**, *3*, 1065.
- 51 D. WANG, J. M. DAUGHTON, D. REED, W. D. WANG, J.-Q. WANG, *IEEE Trans. Magn.*, **2000**, *36*, 2802.
- 52 B. VÖLKELE, G. KALTENPOTH, M. HANDREA, M. SAHRE, C. T. NOTTBOHM, A. KÜLLER, A. PAUL, W. KAUTEK, W. ECK, A. GÖLZHÄUSER, *Surf. Sci.*, **2005**, *597*, 32.
- 53 S. COYLE, M. C. NETTI, J. J. BAUMBERG, M. A. GHANEM, P. R. BIRKIN, P. N. BARTLETT, D. M. WHITTAKER, *Phys. Rev. Lett.*, **2001**, *87*, 176801.
- 54 M. A. GHANEM, P. N. BARTLETT, P. DE GROOT, A. ZHUKOV, *Electrochem. Commun.*, **2004**, *6*, 447.
- 55 S. DIELUWEIT, D. PUM, U. B. SLEYTR, *Supramol. Sci.*, **1998**, *5*, 15.
- 56 S. DIELUWEIT, D. PUM, U. B. SLEYTR, W. KAUTEK, *Mater. Sci. Eng. C*, **2005**, *25*, 727.
- 57 D. M. KOLB, F. C. SIMEONE, *Electrochim. Acta*, **2005**, *50*, 2989.
- 58 W. LI, J. A. VIRTANEN, R. M. PENNER, *J. Phys. Chem.*, **1992**, *96*, 6529.
- 59 R. M. NYFFENEGGER, R. M. PENNER, *Chem. Rev.*, **1997**, *97*, 1195.
- 60 R. ULLMANN, T. WILL, D. M. KOLB, *Chem. Phys. Lett.*, **1993**, *209*, 238.
- 61 D. M. KOLB, R. ULLMANN, T. WILL, *Science*, **1997**, *275*, 1097.
- 62 D. M. KOLB, R. ULLMANN, J. C. ZIEGLER, *Electrochim. Acta*, **1998**, *43*, 2751.
- 63 G. E. ENGELMANN, J. ZIEGLER, D. M. KOLB, *Surf. Sci. Lett.*, **1998**, *401*, L420.
- 64 U. LANDMAN, W. D. LUEDTKE, N. A. BRUNHAM, R. J. COLTON, *Science*, **1990**, *248*, 454.
- 65 J. C. ZIEGLER, G. E. ENGELMANN, D. M. KOLB, *Z. Phys. Chem.*, **1999**, *208*, 151.
- 66 D. M. KOLB, *Angew. Chem. Int. Ed.*, **2001**, *40*, 1162.
- 67 Y. ZHANG, S. MAUPAI, P. SCHMUKI, *Surf. Sci.*, **2004**, *551*, L33.
- 68 S. MAUPAI, A. S. DAKKOURI, P. SCHMUKI, *Surf. Sci.*, **2005**, *597*, 20.
- 69 W. LI, J. A. VIRTANEN, R. M. PENNER, *Appl. Phys. Lett.*, **1992**, *60*, 1181.
- 70 W. LI, G. S. HSIAO, D. HARRIS, R. M. NYFFENEGGER, J. A. VIRTANEN, R. M. PENNER, *J. Phys. Chem.*, **1996**, *100*, 20103.
- 71 J. R. LAGRAFF, A. A. GEWIRTH, *J. Phys. Chem.*, **1994**, *98*, 11246.
- 72 J. R. LAGRAFF, A. A. GEWIRTH, *J. Phys. Chem.*, **1995**, *99*, 10009.
- 73 M. PETRI, D. M. KOLB, *Phys. Chem. Chem. Phys.*, **2002**, *4*, 1211.
- 74 R. T. POETZSCHKE, A. FROESE, W. WIESBECK, G. STAIKOV, W. J. LORENZ, *Proc. – Electrochem. Soc.*, **1997**, *96(19)*, 21.
- 75 D. HOFMANN, W. SCHINDLER, J. KIRSCHNER, *Appl. Phys. Lett.*, **1998**, *73*, 3279.
- 76 R. T. PÖTZSCHKE, G. STAIKOV, W. J. LORENZ, W. WIESBECK, *J. Electrochem. Soc.*, **1999**, *146*, 141.
- 77 W. SCHINDLER, D. HOFMANN, J. KIRSCHNER, *J. Appl. Phys.*, **2000**, *87*, 7007.
- 78 W. SCHINDLER, D. HOFMANN, J. KIRSCHNER, *J. Electrochem. Soc.*, **2001**, *148*, C124.
- 79 K. TERABE, T. NAKAYAMA, T. HASEGAWA, M. AONO, *J. Appl. Phys.*, **2002**, *91*, 10110.
- 80 R. SCHUSTER, V. KIRCHNER, X. H. XIA, A. M. BITTNER, G. ERTL, *Phys. Rev. Lett.*, **1998**, *80*, 5599.
- 81 X. H. XIA, R. SCHUSTER, V. KIRSCHNER, G. ERTL, *J. Electroanal. Chem.* **1999**, *461*, 102.
- 82 S. WIRTH, M. FIELD, D. D. AWSCHALOM, S. VON MOLNAR, *Phys. Rev. B*, **1998**, *57*, R14028.
- 83 S. WIRTH, S. VON MOLNAR, M. FIELD, D. D. AWSCHALOM, *J. Appl. Phys.*, **1999**, *85*, 5249.
- 84 T. SOLOMUN, W. KAUTEK, *Electrochim. Acta*, **2001**, *47*, 679.
- 85 H. SATO, H. KOBAYASHI, H. KUDO, T. IZUMI, T. HOMMA, in *Electrochemical Processing of Nanomaterials Vision*, J. W. SCHULTZE, T. OSAKA (Eds.), *Electrochemistry 2004*, Vol. 72, p. 424
- 86 S. GARCIA, D. SALINAS, C. MAYER, E. SCHMIDT, G. STAIKOV, W. J. LORENZ, *Electrochim. Acta*, **1998**, *43*, 3007.
- 87 C. G. SANCHEZ, E. P. M. LEIVA, *J. Electroanal. Chem.*, **1998**, *458*, 183.
- 88 M. C. GIMENEZ, M. G. DEL POPOLO,

- E. P. M. LEIVA, *Electrochim. Acta*, **1999**, 45, 699.
- 87 A. M. BITTNER, J. WINTTERLIN, G. ERTL, *J. Electroanal. Chem.*, **1995**, 388, 225.
- 88 C. H. CHEN, A. A. GEWIRTH, *J. Am. Chem. Soc.*, **1992**, 114, 5439.
- 89 C. H. CHEN, K. D. KEPLER, A. A. GEWIRTH, B. M. OEKO, J. WANG, *J. Phys. Chem.*, **1993**, 97, 7290.
- 90 B. K. NIECE, A. A. GEWIRTH, *Langmuir*, **1996**, 12, 4909.
- 91 A. A. GEWIRTH, B. K. NIECE, in *Electrochemical Nanotechnology – In situ Local Probe Techniques at Electrochemical Interfaces*, W. J. LORENZ, W. PLIETH (Eds.), Wiley-VCH, Weinheim, **1998**, p. 113.
- 92 E. BAUER, J. H. VAN DER MERWE, *Phys. Rev. B*, **1986**, 33, 3657.
- 93 F. SILVA, M. J. SOTTOMAYOR, A. MARTINS, *Electrochim. Acta*, **1994**, 39, 491.
- 94 A. HAMELIN, J. LECOEUR, *Surf. Sci.*, **1976**, 57, 771.
- 95 D. M. KOLB, J. SCHNEIDER, *Electrochim. Acta*, **1986**, 31, 929.
- 96 A. HAMELIN, *J. Electroanal. Chem.*, **1995**, 386, 1.
- 97 T. VITANOV, A. POPOV, E. S. SEVASTYANOV, *J. Electroanal. Chem.*, **1982**, 142, 1.

4

Nanoscale Electrocrystallization of Metals and Semiconductors from Ionic Liquids

Walter Freyland, Chitradurga L. Aravinda, and Ditimar Borissov

4.1

Introduction

For an understanding of metal deposition mechanisms at the electrified electrode/electrolyte interface the following elementary steps have to be considered – see also Refs. [1–3]:

1. reduction of metal ions at the interface resulting in formation of adatoms;
2. diffusion of adatoms at the interface;
3. formation of critical nuclei;
4. growth of 2D or 3D structures at undersaturation (UPD) or supersaturation (OPD) conditions.

In all these steps interaction with the electrolyte plays an important role. For example, in step 1 the solvation energy of the ions and the adsorption energy of the adatoms depend on the interaction with the electrolyte, whereas the nucleation and growth kinetics and the growth morphology are determined by the interfacial free energies. So the question arises as to what extent different electrolytes, such as aqueous media in comparison with molten salts or room temperature ionic liquids, affect the electrocrystallization of metals, alloys or semiconductors.

Beginning in the late 1980s, *in situ* STM imaging under defined electrochemical conditions and with lateral atomic resolution has been achieved [4–8]. In the following decade numerous investigations on electrochemical phase formation and nanotechnology were performed employing electrochemical *in situ* SPM techniques – see e.g. Refs. [9–12]. In most of these studies aqueous electrolytes were used. However, due to the decomposition potential of water of ~ 1.2 V electrodeposition from this electrolyte is limited to a few metallic elements. In addition, hydrogen evolution can influence the electrodeposition and STM imaging. In order to overcome these limitations we have started in the Karlsruhe Institute electrochemical (EC) STM studies employing ionic liquid electrolytes [13]. They offer the specific advantage of larger electrochemical windows which enables the electrocrystallization of a large range of metals, including transition, rare earth and light metals,

alloys, and elemental and compound semiconductors. A few examples are presented in the following together with a brief introduction to some basic electrochemical properties of ionic liquids and a short description of the EC-STM experiments in these melts.

4.2

Some Electrochemical and Interfacial Characteristics of Ionic Liquids (ILs)

The former interest in molten salt chemistry and electrochemistry has, in recent years, moved towards room temperature ionic liquids (ILs). This is motivated by some unique properties of ILs such as low melting points, extremely low vapor pressures in pure ILs – for example, for $[\text{BMIm}]^+ \text{PF}_6^-$ we observed a partial pressure $< 10^{-6}$ mbar even at ~ 400 K – and a high solubility for a wide range of organic and inorganic compounds. These characteristics explain their increasing use for novel chemical synthesis and first industrial applications [14]. For a recent review on the synthesis, purification and physicochemical properties of ILs we refer to the book by Wasserscheid and Welton [15]. It also contains a section on the electrochemical properties of ILs by Trulove and Manz.

In this chapter we restrict discussion to a few bulk and interfacial electrochemical properties of those ILs which we have employed in our nanoscale electrodeposition studies. These are essentially imidazolium based ILs, i.e. 1-butyl-3-methylimidazolium chloride, $[\text{BMIm}]^+ \text{Cl}^-$, 1-butyl-3-methylimidazolium hexafluorophosphate, $[\text{BMIm}]^+ \text{PF}_6^-$, and their acidic mixtures with AlCl_3 (organic chloride < 50 mol%). When selecting an IL for an electrodeposition experiment, the key question concerns the electrochemical stability or the electrochemical potential window which can be determined by cyclic voltammetry. An example is shown in Fig. 4.1 for $[\text{BMIm}]^+ \text{PF}_6^-$ at different temperatures on a Au(111) working electrode.

It seems that the electrochemical stability of this liquid is strongly temperature dependent. However, it is well known that the electrochemical window, the difference between the anodic and cathodic potential limits, is very sensitive to impurities, in particular, water. Addition of 1% water may reduce the electrochemical window of this type of IL by ~ 0.5 V [16]. In chloroaluminate melts water will react to produce HCl, whereas in melts containing e.g. PF_6^- anions HF is found, see also Ref. [15]. For the example presented in Fig. 4.1 the apparent window of $[\text{BMIm}]^+ \text{PF}_6^-$ is ~ 2.5 V at room temperature, which is roughly 1.5 V less than the literature value of the pure melt [15]. So impurities play an important role.

For a microscopic understanding of the different steps of electrocrystallization knowledge of the interfacial characteristics of ILs is important. Computer simulations of the liquid/vapor interface show no segregation of cations and anions in the surface plane. For imidazolium-based ILs it is found that the cations are oriented with their planes perpendicular to the surface and their dipoles in the surface plane [17]. Across the liquid/vapor interface the surface potential drops by ~ 1 V [18]. Recent measurements of the surface dipole moment density of $[\text{BMIm}]^+ \text{Cl}^-$ and $[\text{BMIm}]^+ \text{PF}_6^-$ are consistent with the predicted surface potential drop [19].

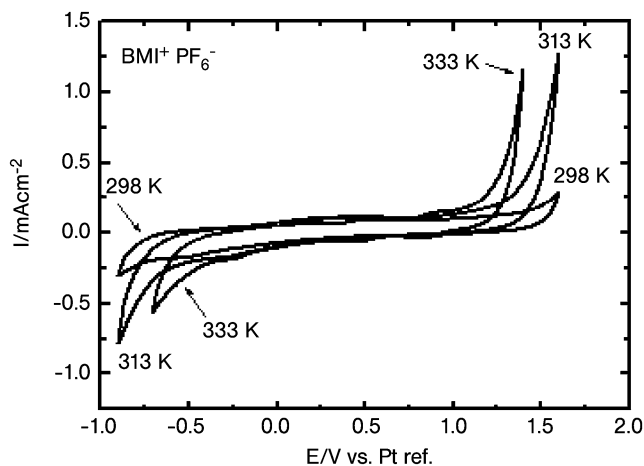


Figure 4.1. Electrochemical potential window of $[\text{BmIm}]^+ \text{PF}_6^-$ at different temperatures determined by cyclic voltammetry, see text (unpublished results).

Anion adsorption and formation of ordered anion adlayers has been intensively studied at the electrified metal/aqueous electrolyte interface, see e.g. Ref. 20. It can have a strong impact on the initial steps of electrocrystallization. This phenomenon of anion adsorption is also important in studies with ionic liquid electrolytes. In an $\text{AlCl}_3^- \text{BmImCl}$ melt a superstructure of AlCl_4^- anions adsorbed on $\text{Au}(111)$ has been observed by high resolution STM images with lattice constants of $a = 8.3 \pm 0.5 \text{ \AA}$ and $b = 9.8 \pm 0.5 \text{ \AA}$ [21]. Similar observations were made for PF_6^- containing melts [21].

4.3

Variable Temperature Electrochemical SPM Technique for Studies with Ionic Liquids

In situ electrochemical STM studies are now widely performed with commercial and homemade instruments. In most cases an open electrochemical cell is used and measurements are conducted under ambient conditions. In addition, the scanner housing and tip holder are not specifically sealed, so that corrosive volatile impurities from the electrolyte can attack the piezo contacts and the scanner electronics. For our EC-STM experiments with ionic liquids we have constructed a new set-up which is shown schematically in Fig. 4.2.

In principle, the electrochemical cell is connected with the scanner by a vacuum-tight super flexible stainless steel bellow. The cell is mounted on a quartz plate to reduce heat losses. The coarse vertical displacement of this quartz plate is realized by three micrometer screws driven by stepping motors which are controlled by the z-piezo of the scanner. The connection of the tip holder with the scanner is sealed with silicon paste or a silicon O-ring to reduce gas exchange with the interior of the

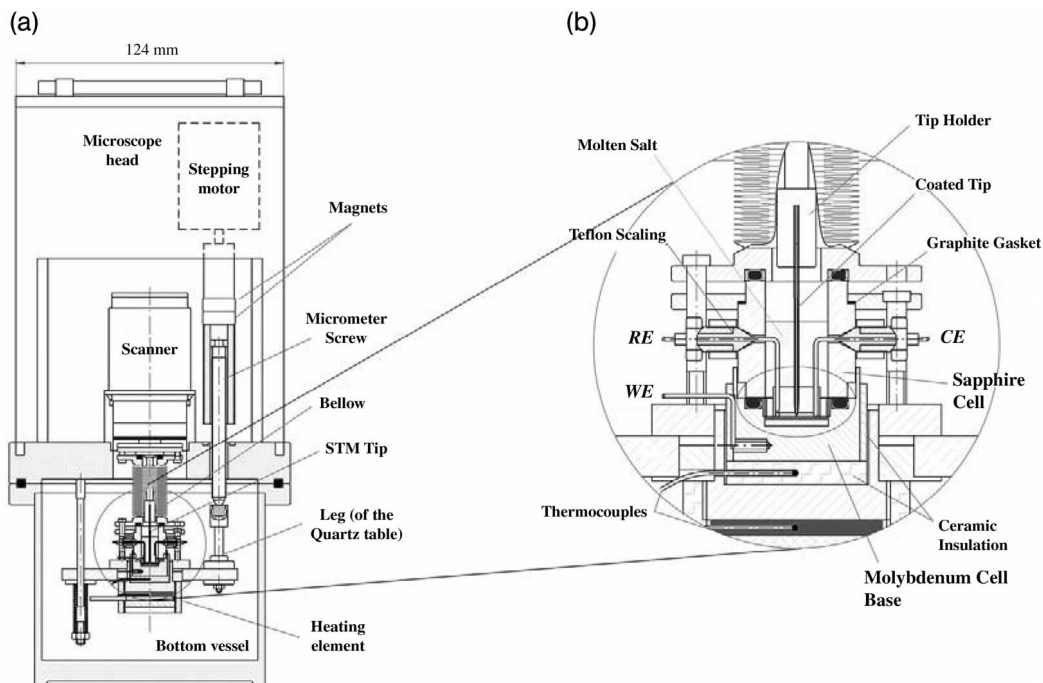


Figure 4.2. Construction of a high temperature electrochemical tunneling microscope (a) and detailed drawing of the piezo scanner and electrochemical cell sealing (b). (From Ref. [22], with permission of the American Institute of Physics.)

scanner. A BN-heating element is used to vary the temperature of the electrochemical cell. The body of the electrochemical cell is made of a cylindrical sapphire ring which is sealed to the respective working electrode at the bottom. Reference and counter electrode are sealed to the sapphire cylinder as shown in Fig. 4.2. This construction has been tested at different temperatures up to 500 K [22] and has been used in the studies reported in Section 4.4.2. Measurements at room temperature have been performed with a simpler, but similar construction made from Teflon, not employing the bellow sealing. For measurements at room temperature electrochemically etched Pt and W STM tips which were coated with epoxide to reduce the effect of Faraday currents have been used. At elevated temperatures insulation of the tips by borsilicate glass proved to be necessary.

4.4

Underpotential Deposition of Metals: Phase Formation and Transitions

At the electrochemical interface, nanostructures of reduced dimension such as 1D nanowires or 2D ultrathin films can be deposited at underpotential, $\Delta E > 0$, or undersaturation, $\Delta\mu < 0$, conditions. They are defined by the following relation:

$$\Delta\mu = \mu_{\text{Me}^{z+}} - \mu_{\text{Me},D} = -zF(E - E_{\text{Me}/\text{Me}^{z+}}) = -zF\Delta E \quad (4.1)$$

Here $\mu_{\text{Me}^{z+}}$ is the chemical potential of metal ions in the electrolyte and $\mu_{\text{Me},D}$ that of metal in the low-dimensional structure of dimension D ; E denotes the actual electrode potential, whereas $E_{\text{Me}/\text{Me}^{z+}}$ is the Nernst equilibrium potential of bulk metal taken as reference with the activity $a_{\text{Me},D=3} \equiv 1$. Accordingly, overpotential deposition of 3D bulk structures occurs for $\Delta E < 0$. The equilibrium potentials of the low-dimensional structures decrease with increasing D . So the stability of these structures and their transformation are controlled by the electrode potential E – for further details see Refs. [2, 23].

Employing the step edge decoration method we succeeded in the electrocrystallization of nanowires of a transition metal, titanium, on highly oriented pyrolytic graphite (HOPG) from an ionic liquid [24]. For space reasons, this cannot be further described here. Instead, we focus in the following on 2D electrochemical phase formation.

4.4.1

Ag on Au(111): Aqueous versus Ionic Liquid Electrolytes

Underpotential deposition of foreign metals on metal substrates from ionic liquids is of fundamental interest to clarify electrocrystallization at the electrode/ionic liquid interface which is not yet fully understood. As an example of UPD phenomena in ionic liquids at room temperature, Ag on Au(111) has been selected, on the one hand, because of the negligibly small lattice misfit, and on the other hand, because Ag UPD has been extensively studied in aqueous solutions [25–28]. In contrast to aqueous electrolytes, Ag UPD on a single crystal Au(111)-surface in $\text{AlCl}_3\text{-BMIImCl}$ is significantly different [21, 29]. A typical cyclic voltammogram (CV) in 1 mM $\text{Ag}_2\text{SO}_4 + 0.1 \text{ M H}_2\text{SO}_4$ at a sweep rate of 30 mV s^{-1} is presented in Fig. 4.3(a).

Ag UPD in the aqueous electrolyte is characterized by two sharp voltammetric reduction peaks occurring at 520 mV (UPD I) and 25 mV (UPD II), whereas in the ionic liquid they appear at 410 mV and 110 mV, see Fig. 4.3(b). However, in the last case UPD I is split into two peaks at 410 mV (C3) and 230 mV (C4) indicating two distinct surface processes. Process C2 corresponds to anion adsorption, see Section 4.2.

Corresponding $Q(E)$ isotherms of Ag on Au(111) measured by the loop technique (see e.g. Ref. 2) in aqueous and ionic electrolytes are plotted in Fig. 4.3(c) and (d), respectively. The isotherms clearly indicate that the surface coverage associated with UPD I in ionic liquid is higher than in aqueous solutions. However, in both cases formation of one densely packed monolayer is found on approaching the Nernst potential which is associated with a charge density of $222 \mu\text{C cm}^{-2}$.

In the UPD I of Ag on Au(111) in the aqueous electrolyte atomically resolved *in situ* STM images at 500 mV show a (3×3) adlayer of Ag (Fig. 4.4), whereas on changing the potential to 20 mV, a phase transition from the more open (3×3) structure to a densely packed (1×1) structure of Ag on Au(111) occurs, see also Ref. 21. A high resolution image of UPD I reveals individual silver adatoms packed

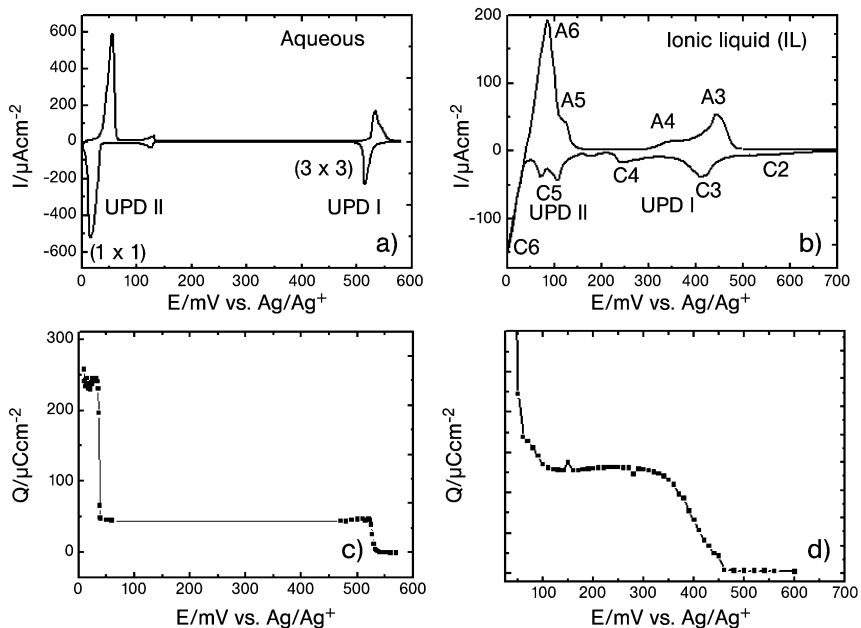


Figure 4.3. Cyclic voltammogram recorded on a single crystal Au(111) surface in (a) 1 mM $\text{Ag}_2\text{SO}_4 + 0.1 \text{ M H}_2\text{SO}_4$ at a sweep rate of 30 mV s^{-1} , (b) 2 mM AgCl in 58:42 mole ratio of AlCl_3 : BMImCl at a sweep rate of 50 mV s^{-1} and $Q(E)$ isotherms in (c) aqueous and (d) ionic liquid.

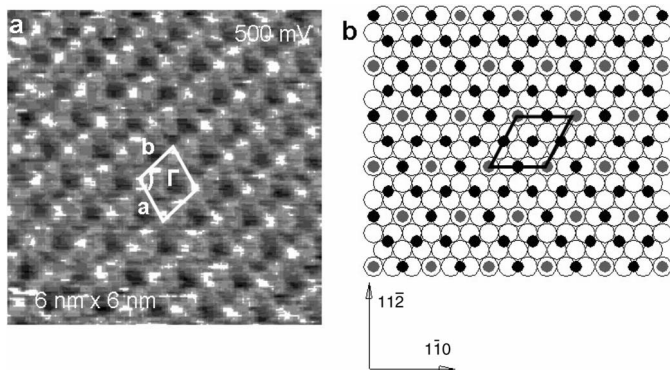


Figure 4.4. (a) Atomically resolved STM image of a $6 \text{ nm} \times 6 \text{ nm}$ scan of the Ag adlayer on Au(111) at 500 mV in aqueous solution. The modulation of height in the $\langle 11\bar{2} \rangle$ direction is a result of alternating adatoms in atop and 2-fold bridge sites; (b) schematic representation of (3×3) structure of Ag on Au(111). Note that filled gray small circles represent Ag adatoms at atop sites, whereas the black ones represent Ag adatoms at bridging sites.

into an ordered adlayer exhibiting a spacing of $a = 8.3 \pm 0.5 \text{ \AA}$ and $b = 8.2 \pm 0.2 \text{ \AA}$ between the adjacent adatoms that have the same contrast and an angle of $\Gamma = 110 \pm 5^\circ$. The interatomic distances suggest a (3×3) superlattice, although the angle in the unit cell deviates a little bit. A schematic representation of the adlayer with the (3×3) structure on Au(111) is given in Fig. 4.4(b) in which the open circles represent Au(111) surface atoms whereas the filled gray ones are Ag adatoms at atop sites and the filled black ones are Ag adatoms at bridge sites. The model clearly shows that silver atoms take both atop and 2-fold bridge sites. Interestingly, the pattern of alternating higher and lower rows is exactly what is seen in the STM image (Fig. 4.4(a)). The modulation of height in the $\langle 1\bar{1}0 \rangle$ direction is less pronounced than that in the $\langle 11\bar{2} \rangle$ direction.

In the ionic liquid, Ag UPD I exhibits two CV peaks at 410 mV and 230 mV. Atomically resolved images in this potential region show the coexistence of two different 2D Ag phases – patches of an ordered structure (their domain boundaries are indicated with a dashed line, see Fig. 4.5(a)) and a disordered phase. An atomically resolved STM image of the ordered phase is depicted in Fig. 4.5(b). In this instance the image reveals a well ordered structure of the silver monolayer yielding a superlattice of $a = 4.4 \pm 0.6 \text{ \AA}$, $b = 5.5 \pm 0.5 \text{ \AA}$ and $\Gamma = 58 \pm 3^\circ$. This indicates that the silver adlayer in the ordered domains has a packing comparable to that of a close packed $(\sqrt{3} \times \sqrt{3})R30^\circ$ structure.

Sweeping the potential further in the negative direction to 200 mV (on the left side with respect to the C4 peak) induces new structural changes. The disordered phase is converted into the $(\sqrt{3} \times \sqrt{3})R30^\circ$ structure resulting in a smoothing of the surface. We interpret this observation (see C4 peak in the CV) as a result of a potential-induced order/disorder transition [21]. Interestingly, stepping back the

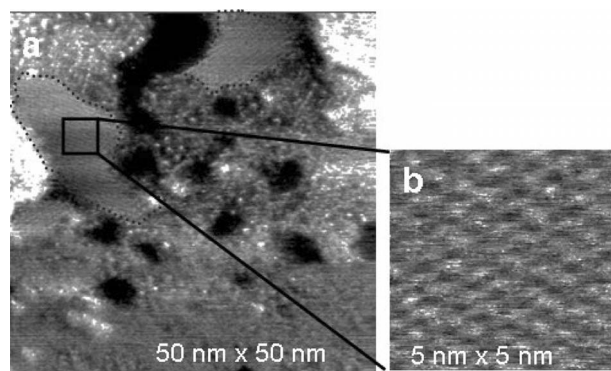


Figure 4.5. *In situ* STM images of the Ag adlayer on Au(111) in AlCl₃:BMImCl at 300 mV; (a) dashed lines show domain boundaries of the ordered Ag phase, (b) high-resolution STM image of the ordered Ag phase with superlattice constants of $a = 4.4 \pm 0.6 \text{ \AA}$, $b = 5.5 \pm 0.5 \text{ \AA}$ and $\Gamma = 58 \pm 3^\circ$.

potential to 400 mV induces the reverse transition from ordered to disordered structures. These observations give evidence that the process of Ag UPD on Au(111) in BMImCl + AlCl₃ undergoes a completely different scenario in comparison with that in aqueous solutions.

4.4.2

Zn on Au(111): Spinodal Decomposition and Surface Alloying

When discussing 2D and 3D phase formation, nucleation and growth phenomena are usually considered. In this case mass transport is governed by normal diffusion, i.e. down the concentration gradient. However, if slow processes like alloy formation and corresponding spinodal decomposition are involved, a thermodynamically modified diffusion process may dominate, whereby concentration fluctuations lead to a flux in the direction up the concentration gradient. This mechanism, which is quite different from that of conventional nucleation and growth, was first described by Cahn and Hilliard [30, 31] in their theory of spinodal decomposition and was successfully applied to explain the spinodal structures of 3D systems like Zn–Al alloys [31]. These are characterized by highly connective structures, sometimes also called labyrinth or wormlike structures. In recent years, a few examples of 2D labyrinth structures have been reported, including the homoepitaxial growth of Ag on Ag(100) and Cu on Cu(100) [32], and the electrochemical dissolution of Au atoms at a Au(111) surface [33]. In all these cases a typical length scale of the spinodal structures of ~ 5 nm is observed. In the following we focus on the electrodeposition of Zn on Au(111) and show that, due to surface alloying in this system, 2D phase formation and dissolution is governed by spinodal decomposition and structures.

Figure 4.6 shows the cyclic voltammogram of the UPD and OPD processes of Zn on Au(111) from the ionic liquid AlCl₃–BMImCl (58:42) + 1 mM Zn(II). In the UPD range below 500 mV vs. Zn/Zn(II) three reduction waves C₁, C₂, and C₃ are indicated, which we assign to the formation of three successive ZnAu and Zn monolayers, respectively. Stripping of the ZnAu surface alloy layers is denoted by the peaks C₁' and C₂'. In the OPD region near the reduction peak at -80 mV vs. Zn/Zn(II) layer-by-layer growth occurs [34] which is followed towards more negative potentials by Al–Zn codeposition. The UPD phase formation has been studied by *in situ* STM imaging which is demonstrated in Fig. 4.6(b)–(d) by a few selected pictures. In the first UPD process island formation sets in around 250 mV. On reducing the potential to 200 mV and increasing the coverage on Au(111) labyrinth or wormlike structures become visible (Fig. 4.6(c)). Before the second UPD process starts an almost complete monolayer with a few defects covers the Au(111) terraces (Fig. 4.6(d)). A similar growth mechanism has been observed by STM imaging during growth of the second and third monolayer, see Ref. [34]. From the height profiles we found that the thickness of the first monolayer is slightly reduced, with a value of 2.2 ± 0.2 Å, whereas the height of the subsequent layers, including those in the bulk, achieved a constant value of 2.4 ± 0.2 Å. On dissolution of the Zn on Au(111) deposits, i.e. jumping the potential for example from -50 to 750 mV, clear

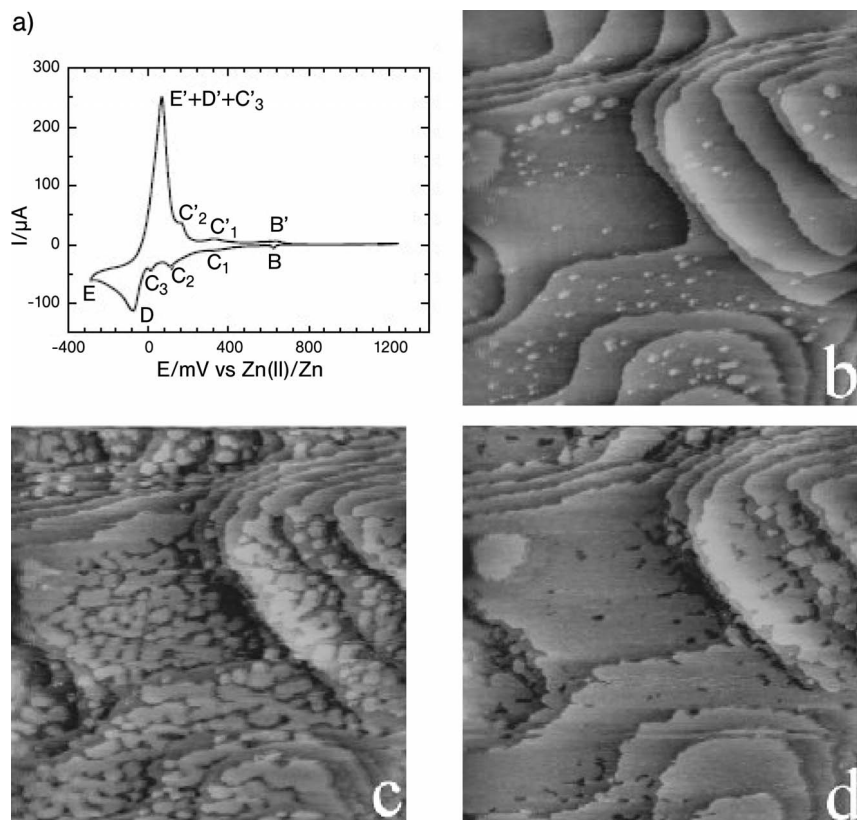


Figure 4.6. First UPD process of Zn on Au(111) in $\text{AlCl}_3\text{-BMImCl}$ (58:42) + 1 mM Zn(II). (a) Cyclic voltammogram of the UPD and OPD processes recorded at a scan rate of 5 mV s^{-1} . (b)–(d) EC-STM images ($110 \times 110 \text{ nm}^2$) at different potentials ((b) 250 mV, (c) 200 mV, (d) 160 mV) taken at time intervals of ~ 5 min. ($E_{\text{tip}} = 100 \text{ mV}$, $I_{\text{tun}} = 5 \text{ nA}$, scan rate 3.3 Hz; from Ref. [34], with permission of the Royal Society of Chemistry.

labyrinth structures evolve with time and finally, after about 1 to 2 h, the Au(111) surface is recovered, containing holes of 1 to 2 ML depth if only UPD films are dissolved, see Fig. 4.7. These holes heal after several hours whereby the respective Au islands disappear – see the white spots in the STM images of Fig. 4.7. This change in the surface structure on electrochemical dissolution has the signature of spinodal decomposition of a surface alloy phase.

In order to gain insight into the kinetics of the UPD surface alloying we have evaluated the average surface coverage θ of the spinodal structures as a function of time for different deposition potentials by analysing the STM images with a proper software program [35]. At constant potential, an exponential time dependence is found:

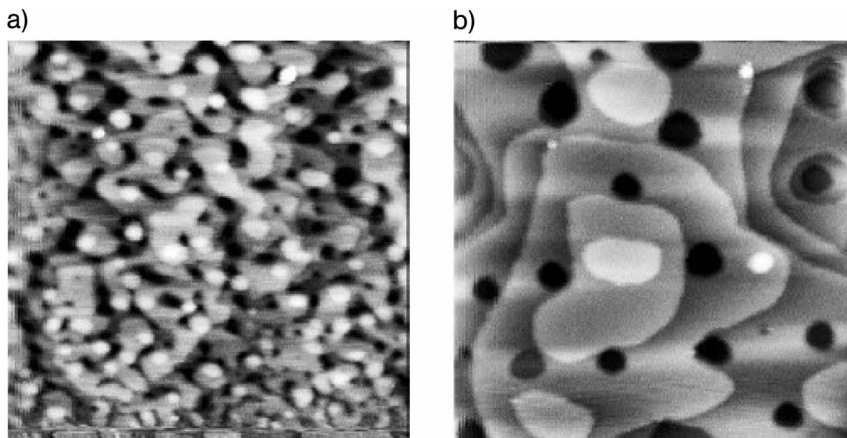


Figure 4.7. Evolution of labyrinth structure during electrochemical dissolution of Zn–Au alloy layers on Au(111). STM images ($129 \times 129 \text{ nm}^2$) after a potential jump from -50 to 750 mV at 3 min (a) and 90 min (b) after the jump. (STM parameters as in Fig. 4.6, taken from Ref. [35], with permission of the American Institute of Physics.)

$$\theta = 1 - \exp(-kt) \quad (4.2)$$

This is shown in Fig. 4.8 for measurements at a constant potential of 200 mV and at two different temperatures. From these data we determine a rate constant of $k = (1.6 \pm 0.2) \times 10^{-3} \text{ s}^{-1}$ at room temperature and estimate an activation energy of $\sim 100 \text{ meV}$ [35]. The rate law and the slow kinetics are consistent with a surface alloying reaction, whereby adsorbed Zn atoms are incorporated into the topmost layers of the Au(111) lattice. A similar model has been suggested for Pb UPD on

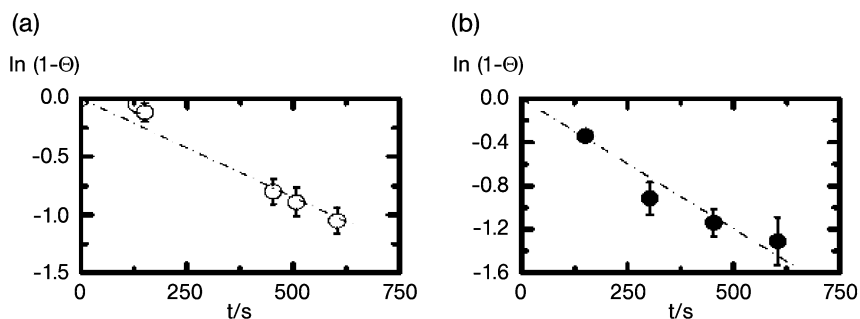


Figure 4.8. Logarithmic plot of average coverage θ vs. time t as determined from the STM images of first monolayer formation at 200 mV ; (a) 298 K , (b) 323 K (taken from Ref. [35] with permission of the American Institute of Physics).

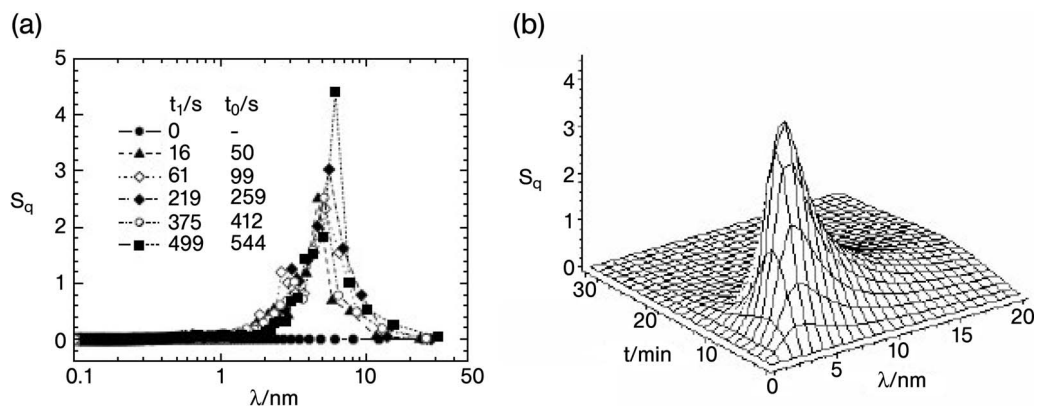


Figure 4.9. Evolution of the surface structure factor, S_q , with time t and wavelength λ of the labyrinth structure of Zn UPD on Au(111) at 200 mV; (a) STM results at 323 K, (b) model calculations (taken from Ref. [35], with permission of the American Institute of Physics).

Ag(111) and similar results for k and the activation energy have been obtained by voltammetric measurements [36].

A 2D hydrodynamic model has been developed to describe the kinetics and the structural evolution of the spinodal decomposition reaction – for details see Ref. 35. Here, we focus on the time evolution of the characteristic length scale and compare the results of the continuum model with experimental STM data, Fig. 4.9. In both cases, the spectral density or the structure factor, S_q , peaks at a wavelength of $\sim 5-6$ nm, which defines the characteristic length scale of the surface structure. As for the time evolution of S_q , the model calculations and the experimental results are in good qualitative agreement.

In conclusion, both the electrochemical STM results and the continuum model calculations of 2D phase formation of Zn on Au(111) show that this system is governed by surface alloying. Phase separation of a Zn-rich and a Zn–Au alloy phase is controlled by two-dimensional spinodal decomposition with characteristic labyrinth structures of a length scale of ~ 5 nm.

4.5

Overpotential Deposition of Metals, Alloys and Semiconductors

4.5.1

Co–Al, Ni–Al and Ti–Al Alloy Deposition

Electrocrystallization of Ni and Co at the Au(111)/chloroaluminate melt interface has been studied by conventional electrochemical and *in situ* EC-STM measurements in both the UPD and OPD range [37, 38]. In addition, the M–Al (M = Ni,

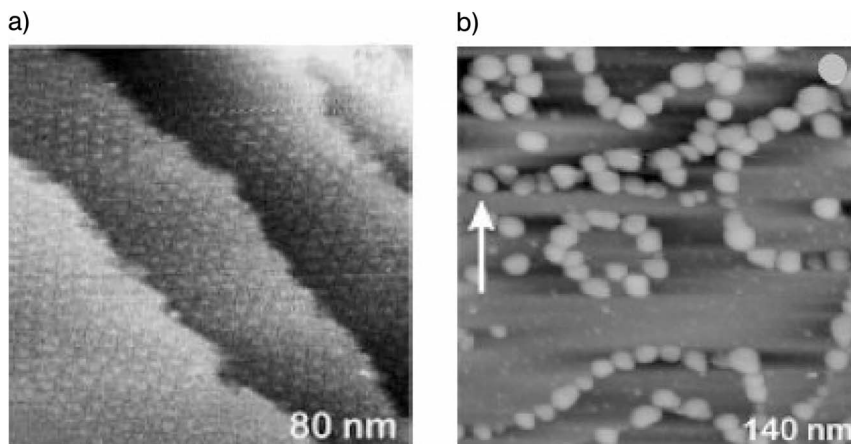


Figure 4.10. UPD and OPD of Ni from the ionic liquid $\text{AlCl}_3\text{-BMIImCl}$ on $\text{Au}(111)$; (a) STM image of the Moiré pattern of the UPD Ni monolayer deposited at 0.1 V vs. $\text{Ni}/\text{Ni}(\text{II})$; (b) OPD step edge decoration by 3D Ni clusters on $\text{Au}(111)$ at -0.2 V vs. $\text{Ni}/\text{Ni}(\text{II})$ ($I_{\text{tun}} = 3$ nA, $E_{\text{tip}} = 0.2$ V; taken from Ref. [37] with permission of the Electrochemical Society).

Co, Ti) codeposition has been investigated and the formation of 3D alloy clusters has been analyzed by *in situ* scanning tunneling spectroscopy (STS) with nanometer resolution [37–39]. Here, we briefly summarize some of the main results on 2D and 3D phase formation of the pure metals and compare them with STM observations made in electrodeposition from aqueous electrolytes. Afterwards we give a brief description of alloy formation as studied by STS spectra.

In the UPD range Ni forms a complete monolayer on $\text{Au}(111)$ which is evidenced by the STM image of a Moiré pattern in Fig. 4.10. A superstructure with a nearest neighbour distance of 23 ± 1 Å is observed at a potential of 0.1 V vs. $\text{Ni}/\text{Ni}(\text{II})$ which can be explained by the incommensurability between the adsorbed Ni monolayer ($d = 2.49$ Å) and the lattice distance of the Au substrate ($d = 2.885$ Å). Integration of simultaneously measured current transients yields a charge of $530 \mu\text{C cm}^{-2}$ which corresponds to 0.9 monolayers [37]. In contrast to Ni UPD, Co and Al do not exhibit the formation of a coherent monolayer [38, 39]. Instead 2D islands with a narrow size distribution form. During anodic dissolution of these islands holes of ~ 2 Å depth appear in the Au substrate which is indicative of surface alloying. This is not observed in the case of Ni.

In the OPD range, nucleation of 3D Ni clusters occurs almost exclusively along the monoatomic step edges of the $\text{Au}(111)$ terraces, see Fig. 4.10. With time these clusters grow and reach columnar shapes. This growth mode is not seen in Co OPD. The UPD and OPD characteristics observed on electrocrystallization from the ionic liquid very much resemble the observations made in aqueous electrolytes [40, 41].

STM investigations of M–Al codeposition have been performed at various deposition potentials between the limits of pure M and pure Al deposition. For the morphology of the 3D alloy clusters the following trend has been observed. Whereas the M-rich clusters reach a grain size of ~ 10 nm, this is clearly reduced with decreasing potential and increasing Al content of the M–Al deposits and approaches a value of 2–3 nm for the Al-rich clusters. To characterize these alloy clusters further we have analyzed them by local current–voltage measurements (I – U curves) which is a special modification of the STS technique, see Ref. 42. It enables a correlation of surface topography with the local electronic structure. In principle, the STM tip is held at a constant distance z (~ 5 – 10 Å) above a specific cluster and the bias voltage U is ramped linearly over a time interval of ~ 200 μ s. Assuming that the electron density of states of sample and tip is constant, the tunneling current, I_{tun} , is approximately given by [42]:

$$I_{\text{tun}} = \text{const } x \int_0^U \exp(-\alpha z(\phi - eV)^{1/2}) dV \quad (4.3)$$

Here $\alpha = 2\hbar^{-1}(2m)^{1/2} = 1.025 \text{ eV}^{-1/2} \text{ \AA}^{-1}$ and ϕ is the effective tunneling barrier height which is related to the work function of the sample and the tip and thus depends on the composition of the alloy clusters. The integral in Eq. (4.3) depends strongly on ϕ and for small ϕ increases exponentially with U . Figure 4.11 shows ϕ -values evaluated according to Eq. (4.3) from I – U curves taken for $\text{Co}_x\text{Al}_{1-x}$ clusters at different deposition potentials in the ionic liquid [38]. Included in Fig. 4.11 are measurements of the alloy composition by different electrochemical methods [43].

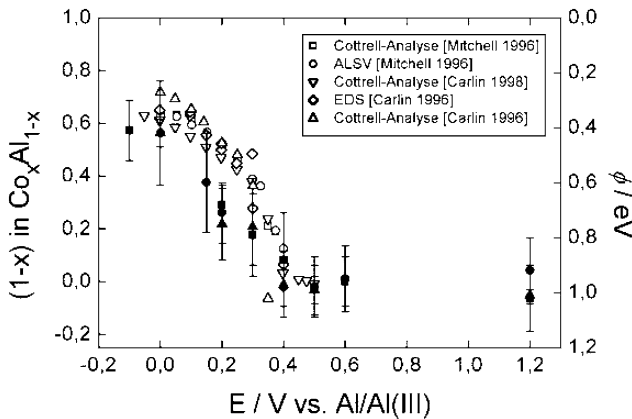


Figure 4.11. Variation of the composition of $\text{Co}_x\text{Al}_{1-x}$ alloy clusters deposited from ionic liquids; left scale, open symbols: results from various electrochemical methods 43, right scale, full symbols: variation of the effective tunneling barrier ϕ from STS measurements as a function of the potential E (taken from Ref. [38] with permission of the American Chemical Society).

Comparing these data sets it becomes clear that the variation of ϕ as a function of potential E probes the change in the alloy cluster compositions with high spatial resolution in the nanometer range.

4.5.2

Nanoscale Growth of Al–Sb Compound Semiconductors

Studies on the electrochemical growth of compound semiconductor nanostructures are rather rare, with the exception of chalcogenide systems [44]. An important reason for this is that most compound semiconductors cannot be deposited from aqueous electrolytes. The III–V group compound semiconductors in general and Sb-based semiconductors in particular are finding immense importance for use as barrier materials in high speed electronics and long-wavelength optoelectronic devices [45]. Focusing here on the nanoscale electrodeposition of compound semiconductors we give an example of electrochemical growth of the compound semiconductor Al_xSb_y from an ionic liquid $\text{AlCl}_3\text{-BMImCl}$ containing Sb^{3+} [46].

The redox processes in the cyclic voltammogram of the melt $\text{AlCl}_3\text{-BMImCl}$ containing 1 mM Sb^{3+} indicate the reduction of Sb^{3+} at -270 mV vs. Al/Al^{3+} and at more cathodic potential, codeposition of Al. A signature due to AlSb deposition is also seen [47]. To gain more insight into the electrodeposition process, STM experiments have been performed in two different potential regions, first, the UPD of Sb and, secondly, the OPD of $\text{Al}_x\text{Sb}_{1-x}$ nanoclusters. Upon changing the potential into the Sb deposition range, 6–16 nm wide and up to ~ 45 nm long 2D nanostructures appear all over the $\text{Au}(111)$ substrate surface (Fig. 4.12). The height of the nanostructures is 2.7 ± 0.2 Å, as expected for a monolayer of Sb. An atomically resolved STM image of the 2D stripes reveals a highly ordered structure of the Sb $\sqrt{7} \times \sqrt{7}$ superlattice having quasi-hexagonal symmetry with interatomic distances of 7.6 ± 0.2 Å and 7.8 ± 0.2 Å (Fig. 4.12(b)). At a potential of -1 V vs. Al/Al^{3+} 3D

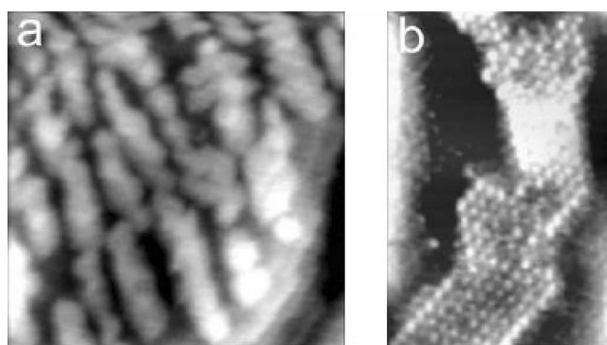


Figure 4.12. (a) STM image (100×100 nm²) showing the UPD of Sb 2D nanostructures at 100 mV vs. Al/Al^{3+} on $\text{Au}(111)$ and (b) 13 nm \times 20 nm high resolution STM image of a Sb nanostructure with $\sqrt{7} \times \sqrt{7}$ superlattice. $E_{\text{tip}} = -50$ mV, $I_{\text{tun}} = 1$ nA.

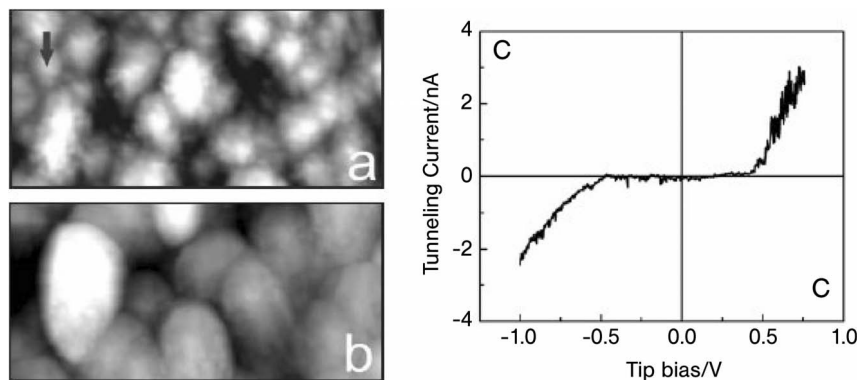


Figure 4.13. Representative *in situ* STM images ($200 \times 100 \text{ nm}^2$) showing the 3D growth of $\text{Al}_x\text{Sb}_{1-x}$ nanoclusters with time; (a) after 3 min (arrow indicates the tip position for STS measurement) and (b) after 20 min. $E = -1 \text{ V}$, $E_{\text{tip}} = -0.7 \text{ V}$, $I_{\text{tunn}} = 1 \text{ nA}$. (c) A typical $I-U$ tunneling spectrum for $\text{Al}_x\text{Sb}_{1-x}$ cluster. $I_{\text{tunn}} = 20 \text{ nA}$.

clusters of $\text{Al}_x\text{Sb}_{1-x}$ appear (Fig. 4.13(a)) and continue to grow with time to form narrowly size dispersed clusters exhibiting a height of $\sim 6 \text{ nm}$ and a width of $\sim 50 \text{ nm}$ (Fig. 4.13(b)). It is apparent from the *in situ* $I-U$ tunneling spectrum (Fig. 4.13(c)) obtained by positioning the tip just above the $\text{Al}_x\text{Sb}_{1-x}$ cluster of interest (see the tip position in Fig. 4.13(a)) that the cluster exhibits semiconductor behavior. The band gap is found to be $\sim 1 \text{ eV}$ which is clearly smaller than the bulk value for the indirect-gap semiconductor AlSb i.e. $\sim 1.6 \text{ eV}$ [48]. The difference may be due to a size effect of the cluster studied and, in addition, deviations from stoichiometry, which results in a relatively high doping of the cluster. The present ECSTM study shows the potential of electrochemical methods to deposit semiconductor nanostructures from an ionic liquid. The method also looks very promising for deposition of various Sb-based compound semiconductor nanostructures containing two or more elements such as InSb, GaSb, AlInSb and GaInAlSb.

4.6

Concluding Remarks

The examples presented in this chapter demonstrate that electrocrystallization studies at the ionic liquid/solid interface can be performed with *in situ* scanning probe techniques. Although ionic liquids, in general, possess relatively high conductivities, STM imaging with atomic resolution can be achieved. Simultaneously, the electronic characteristics of nanostructures are obtained by *in situ* STS measurements. This information is of fundamental interest for elucidation of the electrocrystallization mechanisms, but is also important for applications in nanotechnology. With these tools the microscopic and electronic structure of functional

nanostructures can be probed and manipulated during formation and growth. In comparison with other methods like vapor deposition under UHV conditions, electrodeposition has specific advantages: (i) it occurs near equilibrium conditions; (ii) dimensionality and growth of nanostructures can be controlled by simple variation of the electrode potential.

Considering electrocrystallization of a material from different electrolytes, distinctions in the interatomic interactions and the interfacial energies have to be taken into account. This is particularly apparent for underpotential deposition, as shown here for the example of Ag on Au(111). Different anion adsorption structures and binding influence the 2D phase formation. For a better understanding of these phenomena further investigations of the electrified solid/ionic liquid interface are needed. Aiming at new materials for nanotechnology – we have considered here the examples of transition metal alloys and compound semiconductors – future developments by electrodeposition will focus on ionic liquids. They have large electrochemical potential windows and the process can be conducted under ambient conditions.

Acknowledgment

Financial support of this work by the Center of Functional Nanostructures, DFG, at the University of Karlsruhe and, in part, by Fonds der Chemischen Industrie is gratefully acknowledged. The assistance of D. Rohmert-Hug in the preparation of the manuscript has been invaluable.

References

- 1 H. FISCHER, *Elektrolytische Abscheidung und Elektrokristallisation von Metallen*, Springer-Verlag, Berlin, 1954.
- 2 E. BUDEVSKI, G. STAIKOV, W. J. LORENZ, *Electrochemical Phase Formation and Growth*, VCH, Weinheim, 1996.
- 3 R. GREEF et al, Southampton Electrochemistry Group, *Instrumental Methods in Electrochemistry*, Ellis Horwood, New York, 1990.
- 4 O. MAGNUSSEN, J. HOTLOS, R. NICHOLS, D. M. KOLB, R. J. BEHM, *Phys. Rev. Lett.* **1990**, *64*, 2929.
- 5 S. MANNE, P. K. HANSMA, J. MASSIE, B. V. ELINGS, A. A. GWIRTH, *Science* **1991**, *251*, 183.
- 6 T. HACHIYA, H. HONBO, K. ITAYA, *J. Electroanal. Chem.* **1991**, *315*, 275.
- 7 N. J. TAO, J. PAN, Y. LI, P. J. ODEN, J. A. DE ROSE, S. M. LINDSAY, *Surf. Sci. Lett.* **1992**, *271*, L338.
- 8 W. OBRETEOV, M. HÖPFNER, W. J. LORENZ, E. BUDEVSKI, G. STAIKOV, H. SIEGENTHALER, *Surf. Sci.* **1992**, *271*, 191.
- 9 J. LIPKOWSKI and P. N. ROSS, Eds., *Structure of Electrified Interfaces*, VCH, Weinheim, 1993.
- 10 W. J. LORENZ, W. PLIETH (Eds.), *Electrochemical Nanotechnology*, Wiley-VCH, Weinheim, 1998.
- 11 G. HODES (Ed.), *Electrochemistry of Nanomaterials*, Wiley-VCH, Weinheim, 2001.
- 12 K. WANDELT, S. THURGATE (Eds.), *Solid-Liquid Interfaces*, Springer-Verlag, Berlin, 2003.

- 13 F. ENDRES, W. FREYLAND, *J. Phys. Chem.* **1998**, *102*, 10229.
- 14 M. FREEMANTLE, *Chem. Eng. News* **2003**, *89*, 9; K. R. SEDDON, *Nature Materials* **2003**, *2*, 363.
- 15 P. WASSERSCHIED, T. WELTON (Eds.), *Ionic Liquids in Synthesis*, Wiley-VCH, Weinheim, **2003**.
- 16 U. SCHRÖDER et al., *New J. Chem.* **2000**, *24*, 1009.
- 17 R. M. LYNDEN-BELL, *Mol. Phys.* **2003**, *101*, 2625.
- 18 R. M. LYNDEN-BELL, M. DEL POPOLO, *Phys. Chem. Chem. Phys.* **2006**, *8*, 949.
- 19 V. HALKA, R. TSEKOV, W. FREYLAND, *J. Phys. Condens. Matter* **2005**, *17*, S 3325.
- 20 O. M. MAGNUSSEN, *Chem. Rev.* **2002**, *102*, 679.
- 21 D. BORISSOV, C. L. ARAVINDA, W. FREYLAND, *J. Phys. Chem. B* **2005**, *109*, 11606. GE-BO PAN, W. FREYLAND, *Chem. Phys. Letters* **2006**, *427*, 96.
- 22 A. SHKURANKOV, F. ENDRES, W. FREYLAND, *Rev. Sci. Instrum.* **2002**, *73*, 102.
- 23 W. J. LORENZ, G. STAIKOV, W. SCHINDLER, W. WIESBECK, *J. Electrochem. Soc.* **2002**, *149*, K47.
- 24 I. MUKHOPADHYAY, W. FREYLAND, *Langmuir* **2003**, *19*, 1951.
- 25 K. ITAYA, *Nanotechnology* **1992**, *3*, 185.
- 26 M. J. ESPLANDIN, M. A. SCHNEEWEISS, D. KOLB, *Phys. Chem. Chem. Phys.* **1999**, *1*, 4847.
- 27 P. MROZEK, Y. SUNG, A. WIECKOWSKI, *Surf. Sci.* **1995**, *335*, 44.
- 28 C. H. CHEN, S. M. VESEKY, A. A. GEWIRTH, *J. Am. Chem. Soc.* **1992**, *114*, 451.
- 29 C. A. ZELL, F. ENDRES, W. FREYLAND, *Phys. Chem. Chem. Phys.* **1999**, *1*, 697.
- 30 J. W. CAHN, J. E. HILLIARD, *J. Chem. Phys.* **1959**, *31*, 688.
- 31 J. W. CAHN, *Trans. Metall. Soc. AIME* **1968**, *242*, 166.
- 32 W. W. PAI, J. F. WENDELKEN, C. R. STOLDT, P. A. THIEL, J. W. EVANS, D. J. LIU, *Phys. Rev. Lett.* **2001**, *86*, 3088.
- 33 R. SCHUSTER, D. THRON, M. BINETTI, X. XIA, G. ERTL, *Phys. Rev. Lett.* **2003**, *91*, 066101-1.
- 34 J. DOGEL, W. FREYLAND, *Phys. Chem. Chem. Phys.* **2003**, *5*, 2484.
- 35 J. DOGEL, R. TSEKOV, W. FREYLAND, *J. Chem. Phys.* **2005**, *122*, 094703-1.
- 36 A. POPOV, N. DIMITROV, D. KASHCHIEV, T. VITRANOV, E. BUDEVSKI, *Electrochim. Acta* **1989**, *34*, 269.
- 37 C. A. ZELL, W. FREYLAND, *Proc. Electrochem. Soc., Int. Symp. Molten Salts XIII* **2002**, 660.
- 38 C. A. ZELL, W. FREYLAND, *Langmuir* **2003**, *19*, 7445.
- 39 C. L. ARAVINDA, I. MUKHOPADHYAY, W. FREYLAND, *Phys. Chem. Chem. Phys.* **2004**, *6*, 5225.
- 40 S. MORIN, A. LACKENWITZER, F. A. MÖLLER, O. M. MAGNUSSEN, R. J. BEHM, *J. Electrochem. Soc.* **1990**, *146*, 1013.
- 41 F. A. MÖLLER, J. KINTRUP, A. LACHENWITZER, O. M. MAGNUSSEN, R. J. BEHM, *Phys. Rev. B* **1997**, *56*, 12506.
- 42 R. J. HAMERS, D. F. PADOWITZ, in *Scanning Probe Microscopy and Spectroscopy*, D. A. BONNELL (Ed.), Wiley-VCH, New York, **2001**, 2nd edn., p. 59.
- 43 R. T. CARLIN, P. C. TRULOVE, H. C. DELONG, *J. Electrochem. Soc.* **1996**, *143*, 2747.
- 44 J. L. STICKNEY, *Adv. Electrochem. Sci. Eng.* **2001**, *7*, 1.
- 45 H. BAAZIZ, C. CHARIFI, N. BOUARISSA, *Mater. Chem. Phys.* **2001**, *68*, 197.
- 46 C. L. ARAVINDA, W. FREYLAND, *Chem. Comm.* **2006**, *16*, 1703.
- 47 M. H. YANG, I. W. SUN, *J. Appl. Electrochem.* **2003**, *33*, 1077.
- 48 S. M. SZE, *Physics of Semiconductor Devices*, Wiley Interscience, New York, 1981, 2nd edn., pp. 848–849.

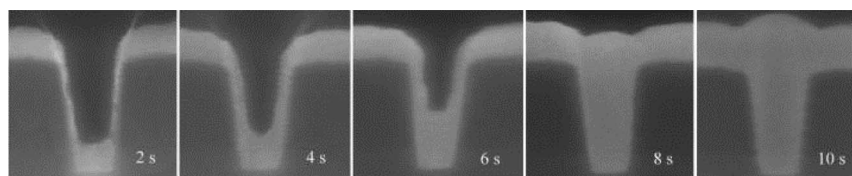
5 Superconformal Film Growth

Thomas P. Moffat, Daniel Wheeler, and Daniel Josell

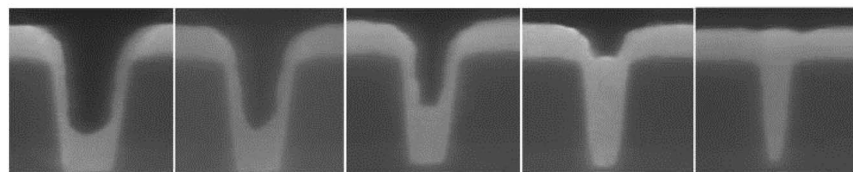
5.1 Introduction

Superconformal film growth is a technologically important deposition process for reducing the roughness of a substrate surface without the occlusion of voids within the deposit. One particularly important example is the superconformal copper electrodeposition process that underlies fabrication of state-of-the-art submicrometer Cu metallizations of silicon microelectronic devices [1, 2] as well as the fabrication of much larger metallizations of vias in printed circuit boards [3] and 3D wafer stacks [4]; this includes filling of features with dimensions ranging from 40 nm to 80 μm , a span of over three orders of magnitude. The growth dynamics are closely associated with smoothing phenomena that have been empirically associated with certain electrolyte additives known as brighteners and levelers. The additives cause local inhibition and/or acceleration of the deposition rate and are often used in combination. Under optimized conditions the additives provide stabilization of smooth planar growth fronts and yield void-free filling of non-planar features such as grooves, trenches and vias. An example of the remarkable deposition behavior associated with a subset of superconformal filling processes called “superfilling” is given in Fig. 5.1 where growth as a function of electrodeposition time and feature aspect ratio reveals preferential metal deposition at the bottom surface of the filling trenches; the preferential deposition continues even after the feature is fully filled, resulting in bump formation above the filled feature.

An understanding of superconformal film growth requires evaluation of both the impact of additive adsorption on the kinetics of metal deposition and the effect of area change on the coverage of the respective adsorbates [2]. Accurate prediction of superfilling processes in particular can be obtained by quantitatively applying these principles to adsorbed accelerating additive, whereby (i) the metal growth velocity is proportional to the local accelerator or catalyst surface coverage and (ii) the catalyst remains segregated at the metal/electrolyte interface during metal deposition (i.e., it is a surfactant). For growth on non-planar geometries, postulation of these two behaviors alone leads to catalyst enrichment on advancing concave surfaces and dilation on convex sections that, in combination, can give rise to distinct



100 nm
Bottom-up filling as a function of time



100 nm
Bottom-up filling as a function of aspect ratio

Figure 5.1. Bottom-up superfilling of submicrometer trenches by copper electrodeposition from an electrolyte containing PEG-SPS-Cl (taken from Ref. [5]).

bottom-up filling of submicrometer features. These enrichment and dilation processes become increasingly important at smaller (optical) length scales since the change in catalyst coverage of a growing surface for a given deposition rate is proportional to the change in the local electrode area. Quantitatively, the effect of area change on the coverage of a given surfactant, θ_i can be expressed in terms of the local curvature κ and growth velocity v normal to the surface

$$\frac{d\theta_i}{dt} = -\frac{1}{\text{Area}} \frac{d(\text{Area})}{dt} \theta_i = \kappa v \theta_i \quad (5.1)$$

Positive κ corresponds to a concave interface such as the bottom of a trench while $\kappa = 0$ defines a planar surface. If the surface is saturated with two different species, adsorbate–adsorbate lateral interactions must be evaluated. In the limiting case of one species being more strongly bound to the surface, the reduction in area that accompanies metal deposition on a saturated concave surface results in expulsion of the more weakly bound species. In contrast, movement of a convex surface simply opens up new surface sites for additive adsorption from solution.

The effect of area change on adsorbate coverage was well recognized in classical dropping mercury electrode studies of surfactant-based charge transfer inhibition [6] and is likewise a central element in studies of adsorption on Langmuir–Blodgett troughs [7]. The impact of area change on adsorbate dynamics and metal electrodeposition on solid electrodes was first recognized over 35 years ago by Schulz-Harder and his work is detailed elsewhere [8, 9] More recently, the curvature enhanced adsorbate coverage mechanism (CEAC) [2, 10–13] was identified

as the key process underlying bottom-up superfilling of trenches and vias; the concept was further developed both experimentally and theoretically for copper electrodeposition [2, 14–37] and then extended to silver [19, 38–41] and gold [42, 43] electrodeposition as well as copper chemical vapor deposition [45]. In all these systems bottom-up superfilling of trenches and vias is associated with selective enrichment on concave sections of an adsorbate that is catalytic towards the metal deposition reaction. Often, this catalyst takes the form of a species that disrupts the formation of a blocking film that otherwise inhibits the metal deposition process. In these cases the filling process involves the convolution of area change with competitive adsorption between a blocking versus an accelerating adsorbate species. Alternatively, the filling process can be simplified by derivatizing the surface with the accelerating species prior to metal deposition [2, 17, 18, 23, 31, 40, 42]. This reduces the problem to tracking the effect of area change on catalyst coverage and its effect on shape evolution without having to consider the details associated with adsorption from the liquid or gas phase media.

This chapter will outline the utility of electroanalytical and surface analytical methods for identifying and characterizing electrolytes capable of yielding superconformal electrodeposition. An understanding of competitive adsorption between adsorbates that catalyze and inhibit the metal deposition reaction is a key aspect. The kinetics of additive adsorption and its effect on the metal deposition rate on planar electrodes are used in combination with the curvature enhanced adsorbate mechanism (CEAC) to predict electrode shape change during deposition in trenches and vias. The CEAC derived stabilization of the growth of smooth flat films using first order perturbation analysis [24] as well as numerical analysis of the response to extremely small amplitude perturbations [25] will also be reviewed. No attempt will be made to comprehensively review the relevant literature (the interested reader may wish to consider Ref. [45]), rather our intent is to highlight a selection of exciting results that deal with the filling of micro- and nanometer scale features along with a methodology for identifying and characterizing other superfilling chemistries.

5.2

Competitive Adsorption: Inhibition versus Acceleration

Superfilling electrolytes are characterized by the rapid adsorption of an inhibiting species that is subsequently challenged by a more strongly binding accelerator species that displaces the inhibitor or blocking agent from the interface. Under suitable conditions this competition gives rise to hysteretic voltammetry, rising chronoamperometry, and depolarizing chronopotentiometry [2, 14, 15, 23, 26, 28, 32]. Prototypical examples for copper superfilling electrolytes are shown in Fig. 5.2. Importantly, these analytical signatures yield the kinetics required for identifying and characterizing the propensity of the given electrolyte to yield superconformal deposition when used within CEAC-based models of feature filling [2]. In the present example, the blocking agent is a coadsorbate structure of PEG and Cl. The catalyst

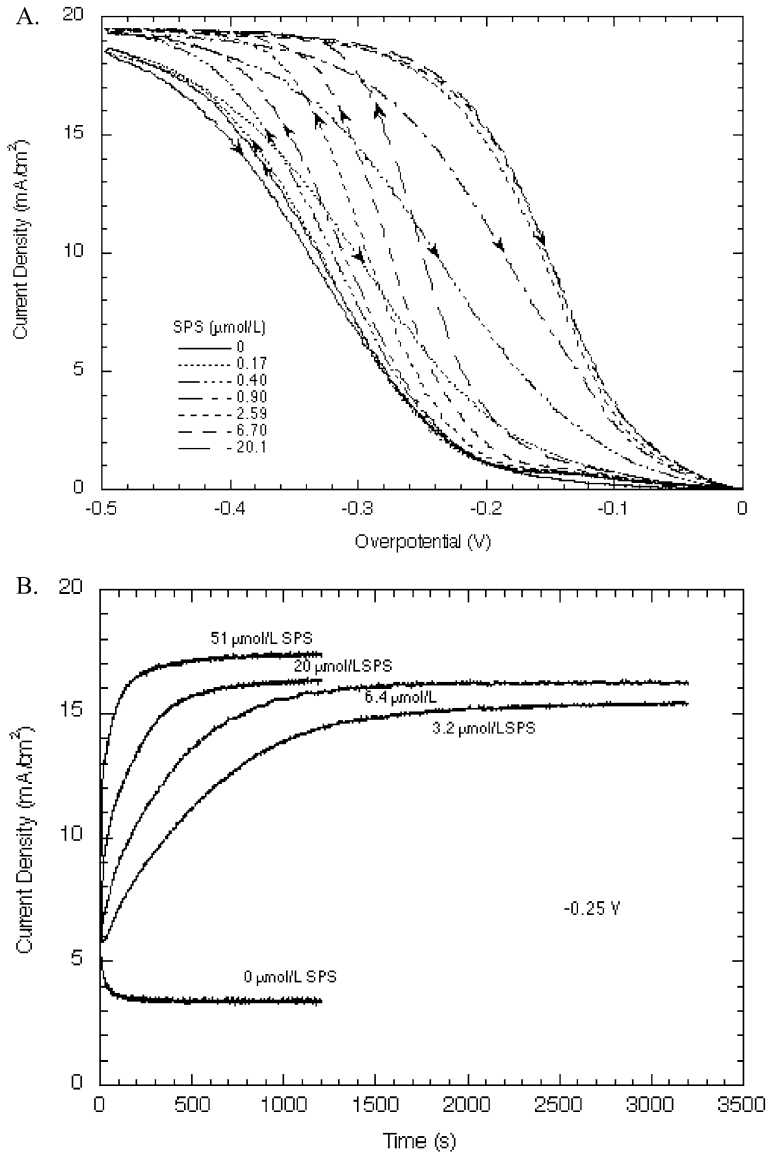


Figure 5.2. (a) Hysteretic voltammetric curves are obtained when the accelerator (SPS) is added to the inhibiting PEG-Cl electrolyte. For the given sweep rate the response on the return sweep is effectively saturated beyond 2.59 mmol L⁻¹ SPS. (b) Rising current transients are observed in the PEG-Cl-SPS electrolyte due to activation of the PEG-Cl inhibited electrodes induced by SPS

adsorption. Qualitatively the transients correspond to following a vertical trajectory across the hysteretic voltammetry curves. In contrast to the single curve for saturated current that characterizes the return sweeps of the voltammetric data shown in (a), the steady-state chronoamperometric current is a function of the SPS concentration (taken from Refs. [2, 23]).

or accelerator is sulfonate-terminated disulfide or thiol. The thiol/disulfide interaction with Cu is greater than that of the inhibiting PEG layer and acts to tether the charged SO_3^- terminal group to the interface. The SO_3^- is responsible for the ability of the molecule to float on the surface and helps displace and prevent the reformation of the blocking PEG layer. Chloride is a required coadsorbate for both the suppressor and accelerator. However, since halide is plentiful in the electrolyte, the needs of the respective coadsorbates are readily met. In other systems, such as silver and gold electrodeposition, the base electrolyte itself contains species such as cyanide complexes that form adlayers that block the metal deposition reaction. Accelerators such as SeCN^- [38–40] and Pb^{2+} [42, 43], for Ag and Au deposition, respectively, disrupt the inhibiting complex adlayers leading to acceleration of the deposition rate. The one to one correspondence between catalyst coverage and acceleration of the deposition rate was demonstrated by comparing chronoamperometric response with XPS measurements of SeCN-coverage as a function of time during silver deposition as shown in Fig. 5.3.

Interestingly, the superfilling process has also been demonstrated for chemical vapor deposition of copper using iodine as a catalyst for the reduction of Cu β -diketonate precursors [44]. This reinforces a key element of the CEAC mechanism outlined above, namely that it is not dependent on some idiosyncrasy of a given

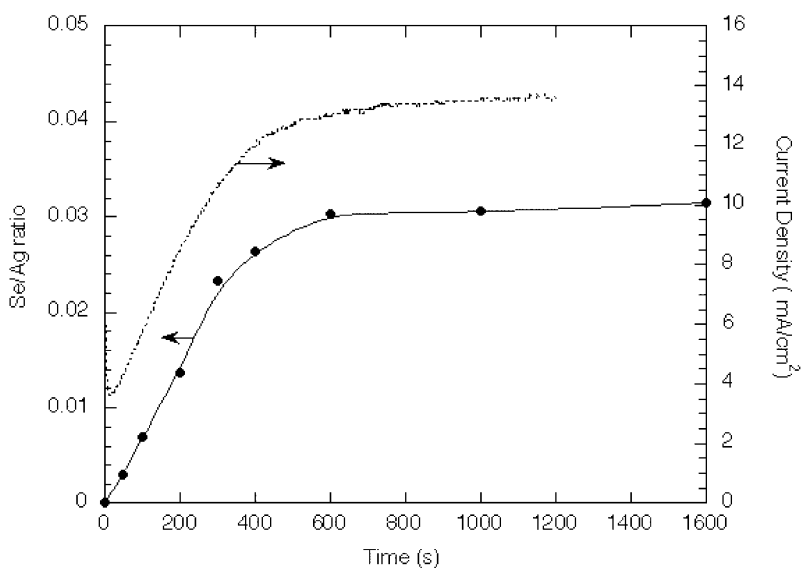


Figure 5.3. The correlation between acceleration of the silver deposition rate during chronoamperometry and the accumulation of a selenocyanate catalyst on the surface as assessed by X-ray photoelectron spectroscopy of samples removed after various deposition times is apparent for deposition at an overpotential of -0.35 V. The XPS data are delineated as solid circles with the line being only a guide to the eye (taken from Ref. [38]).

chemical system or model. Rather, the superfilling process is possible for any deposition process that is controlled by the kinetics of a chemical reaction that can be catalyzed by a surfactant species.

5.3

Quantifying the Impact of Competitive Adsorption on Metal Deposition Kinetics

A simple quantitative description [2] of the competitive adsorption dynamics begins by considering the surface to be saturated with a combination of suppressing θ_{Supp} and/or accelerating θ_{Accel} species

$$\theta_{\text{Supp}} + \theta_{\text{Accel}} = 1 \quad (5.2)$$

Because the concentration of the catalytic species, C_{Accel} , in these electrolytes is often significantly smaller than the concentration of the inhibiting species, C_{Supp} , the surface of a freshly immersed specimen can be assumed to be saturated with the inhibiting species [2, 23]. Furthermore, in the case of copper deposition the PEG suppressor is enriched at the air/water interface [46] and the kinetics of disulfide accumulation, $k_{\text{Accel}}^{\text{ads}}$, are known to be relatively slow (at least for potentials near the open circuit value) compared to that of the suppressor, $k_{\text{Supp}}^{\text{ads}}$

$$k_{\text{Supp}}^{\text{ads}} C_{\text{Supp}} \gg k_{\text{Accel}}^{\text{ads}} C_{\text{Accel}} \quad (5.3)$$

Based on the combination of these factors the initial surface condition can be specified as saturated, or dominated, by inhibitor adsorption. Alternatively, in some systems such as silver cyanide, the base system itself is inhibiting so that, by default, evolution involves simply tracking the accelerator coverage.

In CEAC models, the growth velocity or current density, i , on a given surface is obtained by adding the current densities for surfaces saturated with the accelerating and inhibiting adsorbates weighted by the area fractions that are accelerated and inhibited, θ_i and $(1 - \theta_i)$, respectively. The current densities for the adsorbate saturated surfaces are typically expressed as potential dependent rate constants, k_i , given by a Butler–Volmer expression. The current density as a whole is presumed proportional to the local concentration of the metal cations at the surface C_{Me^+} as determined by diffusion, the long time behavior being constrained by the development of a hydrodynamic boundary layer. Taken together, these considerations yield an expression for the deposition current of the form

$$i = \frac{C_{\text{Me}^+}}{C_{\text{Me}^+}^\infty} nF [k_{\text{Supp}}(1 - \theta_{\text{Accel}}) + k_{\text{Accel}}\theta_{\text{Accel}}] \quad (5.4)$$

Interface motion is expressed as velocity v normal to the surface using Faraday's law $v = i\Omega/nF$ with Ω the molar volume of the deposited metal and n the charge of the metal ion in the electrolyte. The approximation given in Eq. (5.2) enables at-

attention to be focused on either the evolution of the catalyst or inhibitor; herein the former is developed.

The surface coverage of the accelerator is influenced by at least three different processes: (i) area change, (ii) adsorption from the electrolyte and (iii) desorption into the electrolyte or consumption by burial in the growing solid. Adding expressions for the latter two effects to the area change term already described in Eq. (5.1) yields the more general expression

$$\frac{d\theta_{\text{Accel}}}{dt} = \kappa v \theta_{\text{Accel}} + C_{\text{Accel}} k_{\text{Accel}}^{\text{ads}} (1 - \theta_{\text{Accel}}) - k_{\text{Accel}}^{\text{des}} (\theta_{\text{Accel}})^q \quad (5.5)$$

As in Eq. (5.1) the first term is the fundamental term of the CEAC formalism, ensuring mass conservation of an adsorbate that remains segregated on a surface of curvature κ during metal deposition at velocity v . The second term assumes accelerator accumulation from the electrolyte is proportional to the accelerator concentration at the metal/electrolyte interface C_{Accel} , the fraction of surface sites available $1 - \theta_{\text{Accel}}$ and the apparent rate constant $k_{\text{Accel}}^{\text{ads}}$. The rate constant associated with the Langmuir adsorption term is not a fundamental one since adsorption of the accelerator is convoluted with desorption of the inhibitor. In the case of copper electrodeposition from the PEG-Cl-SPS system the rate constant for SPS adsorption, $k_{\text{Accel}}^{\text{ads}}$ is potential dependent, the rate increasing exponentially with overpotential η according to

$$k_{\text{Accel}}^{\text{ads}} = k_o \exp\left(-\frac{\alpha_{\text{ads}} F \eta}{RT}\right) \quad (5.6)$$

The symmetry of the activation barrier, α_{ads} , and the pre-exponential term, k_o , have been determined by fitting experimental cyclic voltammetry curves (i.e., Fig. 5.2(a)) on planar substrates over a range of SPS concentrations [2]. The potential dependence may arise from a number of possible sources including the dynamics of halide ordering, Cu^+ activity, and/or the dynamics associated with PEG adsorption, desorption and/or reorganization. In other systems such as Ag deposition the rate constant for accelerator adsorption does not appear to be a function of potential, at least in the first approximation [38, 39].

The final term in the accelerator evolution Eq. (5.5) quantifies the deactivation of the accelerator species by either incorporation into the growing solid or desorption of the molecule or some fragment back into the electrolyte. The expression for the reaction order and rate constant can take on a variety of forms depending on the details of the system [2, 43]. In the case of Cu plating from the PEG-Cl-SPS electrolyte, the rate constant is potential dependent, taking the form of an asymmetric gaussian function of overpotential [2]. Such consumption kinetics are most readily determined by examining the deactivation of a catalyst derivatized electrode during metal deposition in the presence of the other additives, e.g. monitoring the quenching of the rate of Cu deposition on SPS derivatized electrodes during plating in a PEG-Cl containing electrolyte as shown in Fig. 5.4. The partition coeffi-

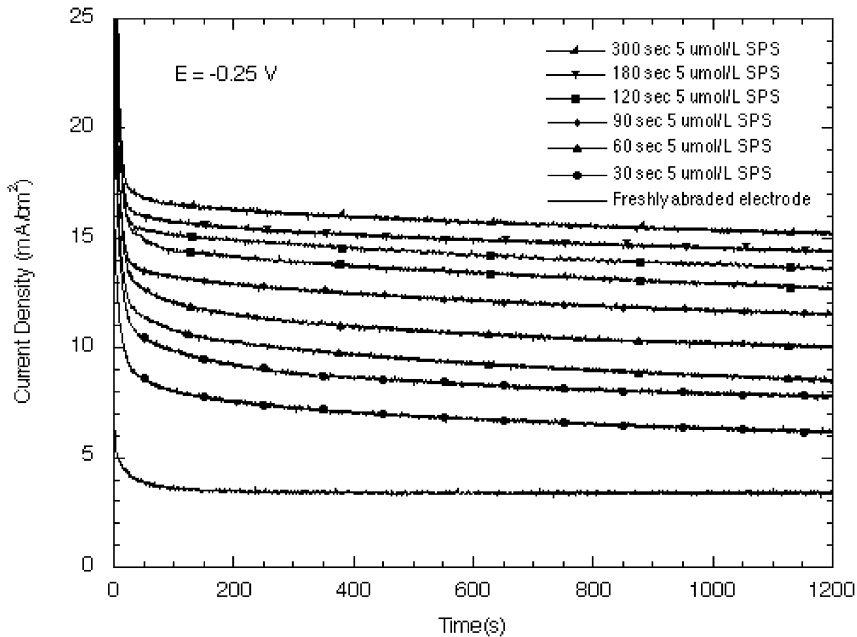


Figure 5.4. Chronoamperometry reveals the magnitude and duration of catalysis obtained on accelerator derivatized electrodes during copper deposition from an electrolyte containing the PEG-Cl inhibitors (taken from Ref. [23]). The derivatization conditions are specified in the legend.

cient so determined may vary from sustained surfactant activity to rapid compound formation, depending on the system in question. This approach to assessing additive consumption has received limited attention in spite of its evident connection to the microstructural refinement that often accompanies electrodeposition in the presence of additives.

Because the area change term in Eq. (5.5) does not contribute to additive evolution during deposition on smooth planar electrodes, conventional electroanalytical measurements on such electrodes, such as are shown in Fig. 5.2, can be used to quantify all the kinetic factors contained in the equation. During deposition on non-planar, e.g. lithographically patterned, surfaces the area change term can dominate the local response of a surface once an appropriate amount of catalyst has accumulated. The resulting increase in accelerator coverage at the bottoms of concave features leads to bottom-up filling that is an essential step in Damascene processing.

Full evaluation of the kinetic model demands a complete mass balance for all specified additives combined with determination of the impact of individual additives on the metal deposition rate [2]. In the simplest case the exchange current density and transfer coefficient for metal deposition need to be obtained for surfaces saturated with the inhibiting and accelerating species respectively. Detailed

descriptions of this procedure are available for electrodeposition of copper [2], silver [38, 39] and gold [43].

5.4 Feature Filling

Experimental studies of Cu trench and via filling reveal a sequence of shape transitions that accompany bottom-up superfilling; CEAC models predict all of these transitions using only the kinetics from the studies on planar substrates. Initially there can be an “incubation period” of near conformal growth as the catalyst begins to accumulate at the interface. The incubation period is followed by the onset of significant enrichment of the catalyst on the lower concave corners due to their high curvature (rapid area decrease), which leads to the accelerated deposition visible at these locations in Fig. 5.5. Qualitatively this corresponds to the transition point where coverage changes due to the reduction of interfacial area outweigh those associated with adsorption from the electrolyte or consumption into the solid. In the absence of significant lateral surface diffusion of the accelerator, the growth fronts propagate away from the corners in directions midway between the horizontal bottom surface and near-vertical sidewalls. In higher aspect ratio features the two advancing corners meet to form a V-notch groove centered on the feature midline; the evolution of this groove is visible in Fig. 5.6 in the two larger features. Enrichment at the vertex of the groove due to the high curvature there leads to the formation of another growth front that rapidly advances upward. When this front reaches the top of the triangular region of the groove new corners

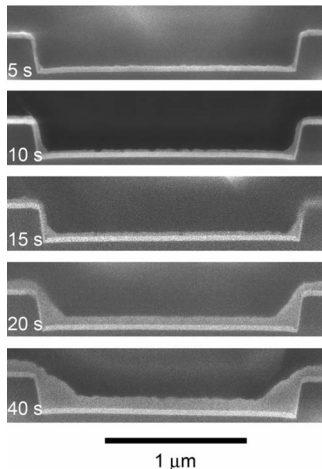


Figure 5.5. Cross-sectional SEM images of copper electrodeposited in wide trenches showing the growth fronts propagating from the lower corners as a function of deposition time (taken from Ref. [47]).

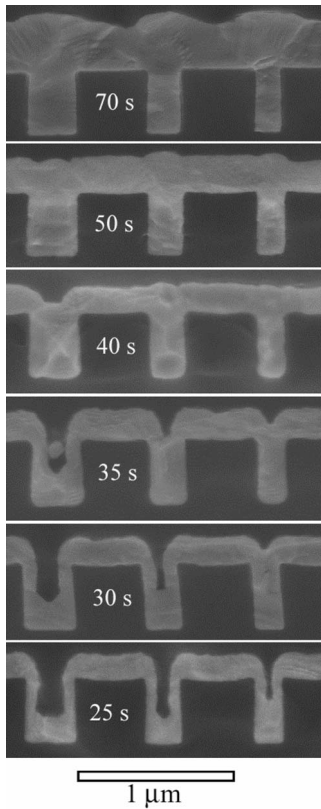


Figure 5.6. SEM images of shape evolution in filling trenches during copper deposition from PEG-Cl-SPS electrolyte at -0.25 V. The trench widths are 350 nm, 250 nm, 200 nm from left to right.

develop, at a shallower angle because of the higher adsorbate coverages on the bottom surface, and another enrichment cycle occurs with the bottom surface continuing to accelerate as more catalyst is transferred to it from the slower moving sidewalls. Subtle oscillations in the profile of the bottom surface, between the flat and shallow V-notch bottom surfaces accompany the continual translation of catalyst from the sidewalls to the bottom surface. The positive feedback cycle thus established leads to increasing differential catalyst coverage between the bottom surface and the sidewalls that results in accelerated bottom-up filling. Close examination of the filling of the two smaller features shown in Fig. 5.6, reveals the rapid bottom-up motion of the catalyst enriched bottom surface while more limited motion of the sidewalls occurs. Finally, when the advancing bottom surface reaches the mouth of the trench the accelerated growth velocity due to its higher catalyst coverage results in formation of a bump above the feature. Significantly, the inception of bump formation is accompanied by a change from concave to convex curva-

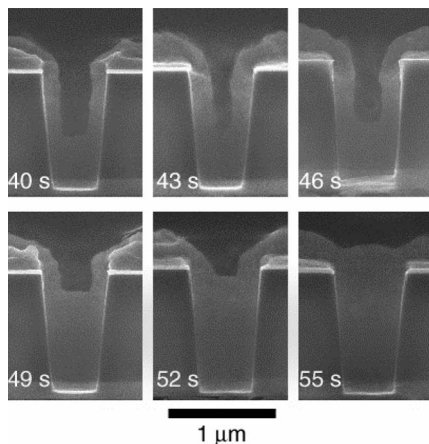


Figure 5.7. Vias cross-sectioned after silver deposition at an overpotential of -0.485 V in a $\text{KAg}(\text{CN})_2\text{-KCN-KSeCN}$ electrolyte. Deposition times are indicated. The first 30 s involved conformal growth (incubation period) that was followed by the onset of SeCN^- accelerator induced bottom-up filling that is captured at 3 s intervals (taken from Ref. [19]).

ture, so that the subsequent bump growth is accompanied by area expansion that gradually decreases the local coverage and the growth velocity on the bump back toward the values in the field.

Feature filling in an electrolyte for Ag superfill exhibits a similar sequence of events that is essentially the same as that observed during Cu superfilling. The incubation period, accelerating bottom-up deposition and overfill bump formation are evident in the via filling pictured in Fig. 5.7. In this case the incubation period lasts over 30 s, the bottom-up filling dynamic subsequently filling the remaining volume of the via in less than 10 s.

Perhaps the most unambiguous demonstration of the role of the CEAC mechanism in trench superfilling is provided by a two-step process that involves derivatization of a patterned copper seed layer with a submonolayer quantity of catalyst followed by copper plating in a catalyst-free electrolyte that contains PEG-Cl [2, 17]. The various shape transitions that accompany trench filling for two different derivatization conditions are shown with the corresponding CEAC-based simulations in Fig. 5.8. The experiments demonstrate that superconformal filling of submicrometer features can be derived from the evolution of a submonolayer quantity of a surface-confined catalyst, without the possibility of significant transport and/or homogeneous chemistry effects within the electrolyte. Filling proceeds through shape transitions that are identical to those just described for filling in an electrolyte containing the catalyst. The generality of the superconformal CEAC growth mode is further demonstrated by the observation of similar shape transitions during Ag deposition in SeCN^- -catalyzed trenches [40] as well as iodine-catalyzed Cu

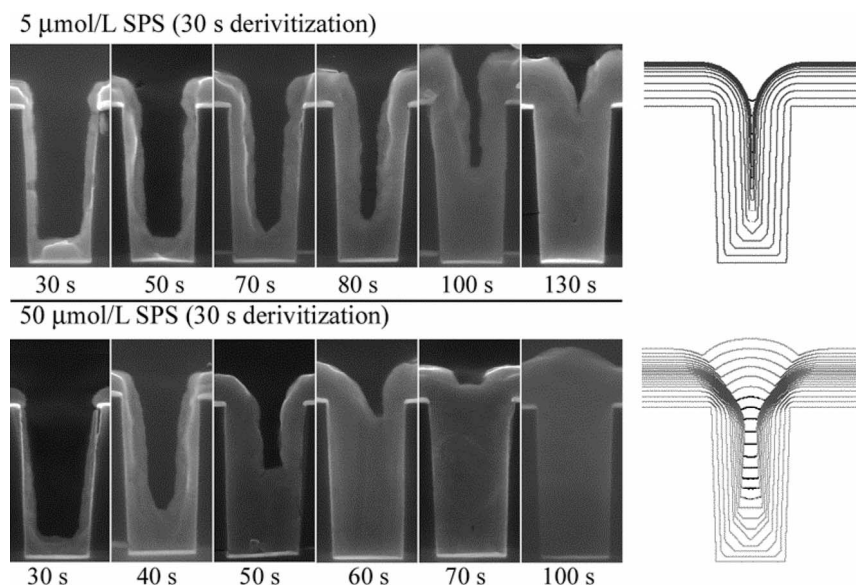


Figure 5.8. Superfilling of trenches pretreated with catalyst prior to copper plating for the indicated times in a PEG-Cl electrolyte at an overpotential of -0.25 V. Filling for two different SPS pretreatments is shown along with the corresponding filling simulations; the gray scale of the contour lines corresponds to catalyst coverage. Darker lines indicate a higher catalyst coverage. The specimens were derivitized in solution containing the indicated concentrations of SPS accelerator dissolved in $1.8 \text{ mol L}^{-1} \text{ H}_2\text{SO}_4$.

CVD in trenches and vias [44]. Significantly, catalyzed substrates offer the practical advantage of bypassing the incubation period and, thereby, increasing the aspect ratio of features that can be filled for a given chemistry. The derivitization approach may also offer improved process control for systems with unstable accelerator chemistry.

5.5

Shape Change Simulations

Quantitative prediction of feature filling, as well as the more general simulation of morphological evolution, requires a shape change algorithm to implement the kinetic descriptions of the effect of adsorbates on metal deposition. A variety of schemes have been employed for these shape change algorithms with the most accurate keeping track of the interface position, additive coverage, and the concentration fields in the electrolyte consistent with the appropriate adsorption and deposition boundary conditions.

The first generation description invoked a string model to track interface position and catalyst coverage while depletion effects within the trench were ignored [10]; later versions of this model accounted for average depletion of reactants across the boundary layer between the planar field and the bulk electrolyte [2]. In the case of Cu deposition two different initial conditions were explored: (i) uniform, nonzero catalyst coverage at $t = 0$, corresponding to catalyst derivatization, followed by plating in an electrolyte containing PEG-Cl [2, 17] (Fig. 5.8) and (ii) catalyst adsorption via Langmuir kinetics during Cu plating, corresponding to electrodeposition in an electrolyte containing SPS-PEG-Cl [2, 10] (Fig. 5.6). Superfilling in both trench and via geometries, including the impact of sidewall tilt, was modeled [2]. The simulations predicted all the shape transitions observed in experimental superfilling, i.e., incubation period of near-conformal growth, formation and rapid advance of 45° inclined segments from the bottom corners, their intersection and the formation of a nearly flat bottom surface, rapid bottom-up filling and, finally, bump formation (when the bottom surface reached the top of the trench before the sidewalls could impinge) [2, 10]. The agreement between the geometries of predicted and experimental trench filling for the case of derivatized substrates is evident in Fig. 5.8. A similar comparison in Fig. 5.9 for deposition in PEG-Cl-SPS

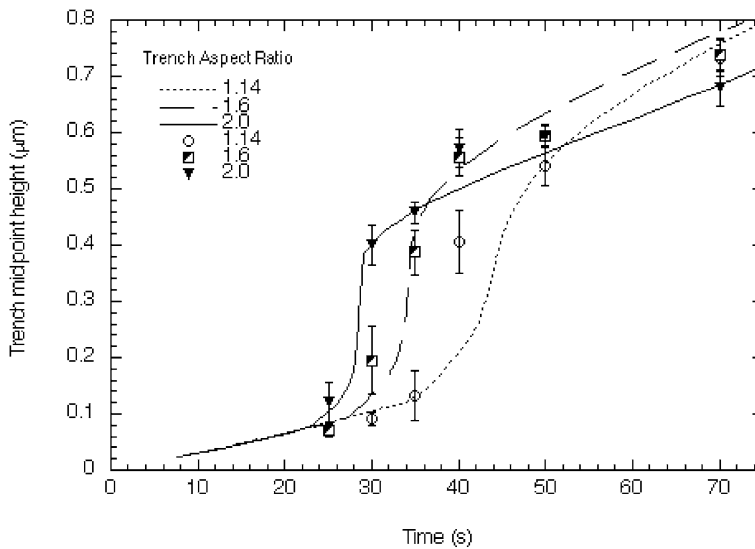


Figure 5.9. Trench-filling experiments compared with shape-change simulations by tracking the interface height on the trench centerline as a function of deposition time. The initial slope corresponds to conformal growth. It is followed by accelerated bottom-up filling, after a time that depends on the

trench width, and then by gradual deceleration as the bottom surface escapes the trench and curvature inversion associated with overflow bump formation starts to decrease the accelerator coverage. The symbols correspond to experimental results obtained from the images shown in Fig. 5.6.

electrolyte demonstrates agreement in time as well as geometry; predicted heights of the growth fronts along the mid-lines of the trenches as functions of time agree well with the symbols marking the heights obtained from the images in Fig. 5.6. Such simulations are also able to accurately predict fill versus fail conditions as a function of feature size, overpotential, and trench aspect ratio.

A second generation model coupled the level set method for interface tracking with a finite difference scheme allowing tracking of the evolving adsorbate coverage on the moving interface as well as evaluation of all relevant concentrations throughout the electrolyte [13]. In the case of optimal superfilling, the shape transitions predicted using this full solution were qualitatively indistinguishable from those predicted by the approximate string model; this agreement occurs because the evolution of feature filling in these cases is dominated by the area change term, which is implemented without approximation in both numerical models [10, 13]. Simulation where features fail to fill differ only in that the level set construct yields voiding due to depletion of metal ion concentration within the trench while the string model indicates seam formation due to side wall impingement. Several of these simulation codes are now available in the public domain (<http://www.nist.ctcms.gov/fipy/>) [48].

In parallel with the numerical implementations of CEAC-based models, several analytical CEAC-based treatments for trench and via filling have also been developed [12, 16, 19, 22]. The simplest of these models assumes that accelerator adsorbed on the trench or via sidewall area eliminated by the upward moving bottom surface is immediately and uniformly redistributed across the bottom surface predicting observed bottom-up acceleration through positive feedback [12, 16]. If the bottom surface reaches the top of the original feature before sidewall impingement, the feature is said to be successfully filled. The solutions provide a reasonably accurate description of the shape profiles observed prior to bump formation during optimized bottom-up trench filling, although, because of the assumptions employed, the constructs inherently fail to describe profiles for sub-optimal feature filling as well as bump formation after successful bottom-up filling. Be that as it may, the models permits rapid exploration of the parameter space associated with optimal superfilling compared to the more accurate, but more computationally intensive, shape evolution codes.

More recently, an exact algebraic solution for the incubation period of bottom-up filling has been described for the case when catalyst is preadsorbed and negligible consumption occurs during subsequent metal deposition [22]. Importantly, this analytical solution provides a metric for evaluating the accuracy of numerical implementations of all CEAC models.

Recent CEAC modeling has shifted toward understanding efforts to control the bumps formed by “momentum” plating (elimination of the bumps is desired because they hamper subsequent steps in Cu Damascene processing). A variety of schemes have been explored for quenching the activity of the catalyst-enriched bottom surface once it reaches the free surface [49]. The use of an additional additive to selectively deactivate the catalyst has been explored both experimentally and theoretically [49–51]; for Cu deposition in particular, cationic surfactants (LEV)

have been shown to deactivate the accelerating anionic sulfonate-terminated thiol or disulfide catalyst in the PEG-Cl-SPS-LEV system [50, 51]. A generalized version of the CEAC mechanism was shown to quantitatively describe the impact of this competition during deposition on planar and patterned electrodes [50]. Significantly, the modeling showed that when the leveling species had surfactant qualities so that it was subject to the CEAC enrichment process on advancing concave surfaces, it was able to counteract enrichment of the catalyst at those locations. As in the case of bottom-up superfilling, the impact of area change on the coverage of the surfactant leveler was able to far outweigh coverage variations arising from the convolution of the specimen geometry and the Laplacian flux field as used in traditional diffusion–adsorption–consumption leveling constructs.

In summary, a variety of models incorporating the CEAC mechanism have been shown to be effective tools for predicting and optimizing trench and via superfilling and controlling bump formation. Importantly, the most complete shape evolution models permit modeling of deposition on and within arbitrary surface profiles.

5.6

Stability Analysis

Another general aspect of morphological evolution during film growth is the stability of a planar interface against growth of small amplitude perturbations. Interestingly, the same CEAC mechanism that underlies superfilling of patterned features also impacts the stability of such planar surfaces. In one study of the PEG-Cl-SPS Cu plating system, the stability of a planar surface against growth of an infinitesimal amplitude sinusoidal height perturbation was examined as a function of catalyst (SPS) concentration and growth potential [24]. The evaluation used a first order perturbation analysis of the CEAC formalism under steady-state conditions determined from the known SPS accumulation and consumption kinetics. As shown in Fig. 5.10, for deposition at an overpotential of -0.3 V (circles) substantial stabilization is provided by a catalyst concentration of $0.1 \mu\text{mol L}^{-1}$ (10^{-10} mole cm^{-3}) SPS; in this case planarity is maintained for perturbation wavelengths ($\lambda_{\text{crit}} = 2\pi/\omega_{\text{crit}}$) up to $210 \mu\text{m}$, a value that exceeds the boundary layer thickness used in the analysis. The system is sharply destabilized (λ_{crit} decreases) when the catalyst concentration falls below $0.1 \mu\text{mol L}^{-1}$. Under these conditions the critical wavelength λ_{crit} falls to the value of $4.5 \mu\text{m}$ associated with capillary stabilization alone; the steady-state coverage of catalyst on the surface for these electrolyte concentrations is simply too low to have a significant effect. The critical wavelength also decreases, although more gradually, with increase in catalyst concentration; a critical wavelength of $6 \mu\text{m}$ is predicted for a catalyst concentration of $100 \mu\text{mol L}^{-1}$ (10^{-7} mole cm^{-3}). It should be noted, however, that this destabilization is due to the increasing gradient of Cu^{2+} associated with the higher metal deposition rates at higher steady-state adsorbate coverages. Similarly, the critical wavelength in-

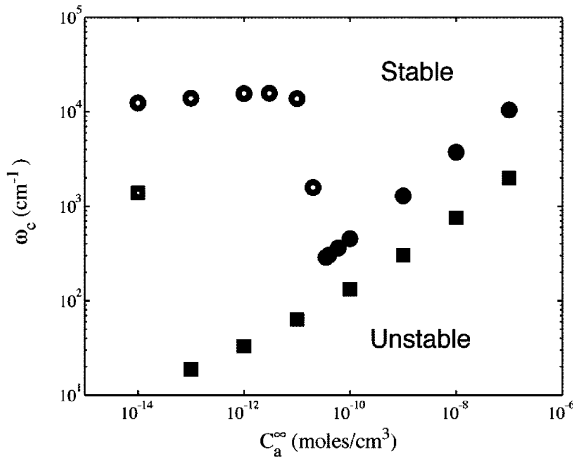


Figure 5.10. The dependence of the critical wavenumber on the concentration of the accelerator SPS during copper electrodeposition in the PEG-Cl-SPS system. A sine wave perturbation to the surface height will decay if its wavenumber satisfies $\omega > \omega_{crit}$. The stable range is increased by two orders of magnitude in the presence of sufficient catalyst. Stability

was assessed for two different overpotentials, -0.3 V (circles) and -0.2 V (squares). The closed symbols correspond to the boundary between real (monotonic) decay and growth modes while the open symbols correspond to the boundary between complex (oscillatory) decay and growth modes (taken from Ref. [24]).

creases (deposition is stabilized) with decreasing overpotential because of the decreased Cu^{2+} gradient at the lower deposition rate.

While a quantitative comparison remains to be done, the predictions do confirm the optical observation of substantial surface stabilization during film growth in Cu superfilling electrolytes. Significantly, the first order perturbation analysis predicts only capillary stabilization during deposition on a surface with preadsorbed catalyst in a catalyst-free electrolyte (the result is obtained by taking certain limits). The model is therefore unable to explain experimental observation of optical quality smoothing during substantial deposition on derivatized substrates.

The origin of the sustained brightening during growth on catalyst derivatized Cu electrodes was investigated by numerical analysis [25]. The results showed that surfaces with fixed total coverage of a catalyst develop oscillating perturbations of amplitude (and catalyst coverage) with finite, but extremely small, amplitudes. Thus, consistent with the predictions of the linear stability analysis, the system is unstable. At the same time, because the oscillations remain extremely small in amplitude for all times, there is no significant roughening, and the surface remains essentially smooth and bright, consistent with experimental observations. The long term “stability” of the oscillating perturbations is demonstrated for a particular growth condition in Fig. 5.11 by the convergence of the amplitudes of perturbations that were initiated with a range of amplitudes to the intermediate, steady-state value.

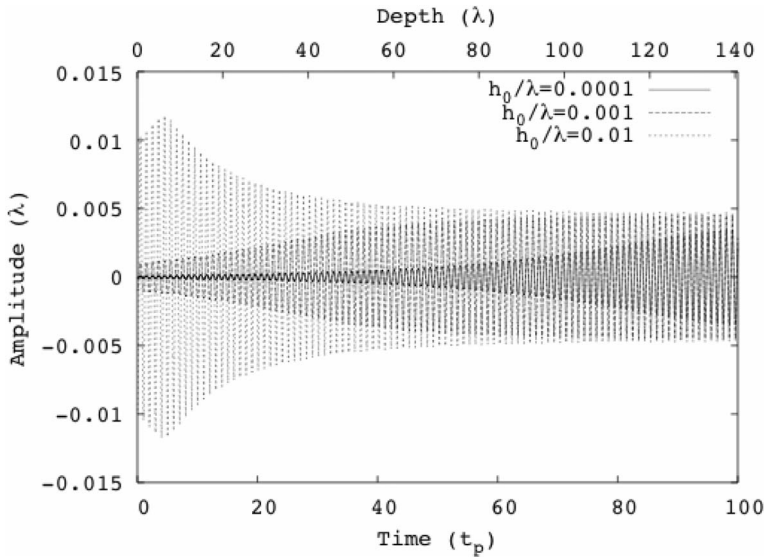


Figure 5.11. Evolution over time of the amplitudes of spatially periodic perturbations is shown for a surface with preadsorbed, conserved catalyst. The oscillatory behavior of the perturbations is evident for initial perturbation amplitudes 0.01, 0.001 and 0.0001 (scaled by the perturbation wavelength λ); time is scaled by the oscillatory period t_p , which is the same for the three results. The convergence of all three curves to the same, small amplitude envelope at long times explains the “stabilization” of derivatized surfaces against substantial (visible) roughening [25].

5.7

Conclusions and Outlook

The impact of electrode area change on adsorbate coverage and its consequent impact on the local metal deposition kinetics is central to understanding morphological evolution during electrodeposition in the presence of additives. The CEAC model highlights the ability of such area change to generate significant variation of adsorbate coverage that cannot be generated by the concentration gradients that arise from traditional diffusion–adsorption–consumption leveling models. The important technical enterprise of superfilling submicrometer features has provided an excellent vehicle for demonstrating and validating the predictions of these CEAC-based models. As feature dimensions continue to shrink into the nanometer length scale, the importance of the area change effects embodied in the CEAC mechanism can only be expected to increase.

To date CEAC derived superconformal film growth has been demonstrated for electrodeposition of Cu, Ag and Au and chemical vapor deposition of Cu. Experiments are underway probing its extension to the deposition of thin films and par-

ticles involving other elemental and alloy systems as well as composites; the salient requirement is to identify surfactant species that substantially mediate the rate of metal deposition. From an even broader perspective the CEAC mechanism might also impact the dynamics and morphological evolution of precipitation reactions such as those involved in biomineralization.

Electrode derivatization represents a powerful tool for identifying catalysts and inhibitors for CEAC applications as well as for developing a quantitative understanding of the influence and fate of individual electrolyte additives during metal deposition. Derivatization experiments have helped to elucidate the influence of monolayer chemistries on metal deposition as well as their central role in successful filling of recessed submicrometer surface features. Future studies of the impact of defined adsorbate structures on material deposition kinetics promise to further illuminate the role of additives in both morphological and microstructural development.

References

- 1 P. C. ANDRICACOS, C. UZOH, J. O. DUKOVIC, J. HORRANS, H. DELIGIANNI, *IBM J. Res. Dev.*, **42**, 567 (1998).
- 2 T. P. MOFFAT, D. WHEELER, M. D. EDELSTEIN, D. JOSELL, *IBM J. Res. Dev.*, **49**, 19 (2005).
- 3 M. LEFEBVRE, G. ALLARDYCE, M. SEITA, H. TSUCHIDA, M. KUSAKA, S. HAYASHI, *Circuit World*, **29**, 9 (2003).
- 4 J. J. SUN, K. KONDO, T. OKAMURA, S. J. OH, M. TOMISAKA, H. YONEMURA, M. HOSHINO, K. TAKAHASHI, *J. Electrochem. Soc.*, **150**, G355 (2003).
- 5 T. P. MOFFAT, D. WHEELER, D. JOSELL, *Interface*, **13**, 4, 46 (2004).
- 6 A. J. BARD, L. R. FAULKNER, *Electrochemical Methods*, Ch. 12, J. Wiley & Sons, New York (1980), and references therein.
- 7 A. W. ADAMSON, *Physical Chemistry of Surfaces*, J. Wiley & Sons, New York (1976).
- 8 J. SCHULZ-HARDER, Dissertation, Ein neuer Mechanismus des Einflusses von Badzusätzen auf die Stromdichteverteilung bei der Metallabscheidung auf rauen Kathoden und seine experimentelle Begründung, Technischen Universität Berlin, (1971).
- 9 J. OSTERWALD, J. SCHULZ-HARDER, *Galvanotechnik*, **66**, 360 (1975).
- 10 T. P. MOFFAT, D. WHEELER, W. H. HUBER, D. JOSELL, *Electrochem. Solid-State Lett.*, **4**, C26 (2001).
- 11 A. C. WEST, S. MAYER, J. REID, *Electrochem. Solid-State Lett.*, **4**, C50 (2001).
- 12 D. JOSELL, D. WHEELER, W. H. HUBER, J. E. BONEVICH, T. P. MOFFAT, *J. Electrochem. Soc.*, **148**, C767 (2001).
- 13 D. WHEELER, D. JOSELL, T. P. MOFFAT, *J. Electrochem. Soc.*, **150**, C302 (2003); D. JOSELL, D. WHEELER, T. P. MOFFAT, *Phys. Rev. Lett.*, **87**, 016102 (2001).
- 14 T. P. MOFFAT, J. E. BONEVICH, W. H. HUBER, A. STANISHEVSKY, D. R. KELLY, G. R. STAFFORD, D. JOSELL, *J. Electrochem. Soc.*, **147**, 4524 (2000).
- 15 J. REID, *Jpn. J. Appl. Phys.*, **40**, 4B, 2650 (2001).
- 16 D. JOSELL, D. WHEELER, T. P. MOFFAT, *Electrochem. Solid-State Lett.*, **5**, C49 (2002).
- 17 T. P. MOFFAT, D. WHEELER, C. WITT, D. JOSELL, *Electrochem. Solid-State Lett.*, **5**, C110 (2002).
- 18 S. K. CHO, S.-K. KIM, J. J. KIM, *J. Electrochem. Soc.*, **152**, C330 (2005).
- 19 D. JOSELL, B. BAKER, C. WITT, D. WHEELER, T. P. MOFFAT, *J. Electrochem. Soc.*, **149**, C637 (2002).
- 20 T. P. MOFFAT, B. BAKER, D. WHEELER, D. JOSELL, *Electrochem. Solid-State Lett.*, **6**, C59 (2003).

- 21 L. T. KOH, G. Z. YOU, C. Y. LI, P. D. FOO, *Microelectronics J.*, **33**, 229 (2002).
- 22 D. JOSELL, T. P. MOFFAT, D. WHEELER, *J. Electrochem. Soc.*, **151**, C19 (2004).
- 23 T. P. MOFFAT, D. WHEELER, D. JOSELL, *J. Electrochem. Soc.*, **151**, C262 (2004).
- 24 G. B. MCFADDEN, S. R. CORIELL, T. P. MOFFAT, D. JOSELL, D. WHEELER, W. SCHWARTZACHER, J. MALLETT, *J. Electrochem. Soc.*, **150**, C591 (2003).
- 25 D. WHEELER, T. P. MOFFAT, G. B. MCFADDEN, S. CORIELL, D. JOSELL, *J. Electrochem. Soc.*, **151**, C538 (2004).
- 26 J. REID, C. GLACK, S. J. HEARNE, *Electrochem. Solid State Lett.*, **6**, C26 (2003).
- 27 P. M. VEREECKEN, R. A. BINSTED, H. DELIGIANNI, P. C. ANDRICACOS, *IBM J. Res. Dev.*, **42**, 3 (2005).
- 28 M. TAN, J. HARB, *J. Electrochem. Soc.*, **150**, C420 (2003).
- 29 B. M. BASOL, *J. Electrochem. Soc.*, **151**, C765 (2004).
- 30 S.-K. KIM, J. J. KIM, *Electrochem. Solid-State Lett.*, **7**, C98 (2004).
- 31 W. P. DOW, M. Y. YEN, *Electrochem. Solid State Lett.*, **8**, C161 (2005).
- 32 W.-P. DOW, M.-Y. YEN, W.-B. LIN, S.-W. HO, *J. Electrochem. Soc.*, **152**, C769 (2005).
- 33 Y. CAO, P. TAEPHAISITPHONGSE, R. CHALUPA, A. WEST, *J. Electrochem. Soc.*, **148**, C466 (2001).
- 34 P. TAEPHAISITPHONGSE, Y. CAO, A. C. WEST, *J. Electrochem. Soc.*, **148**, C492 (2001).
- 35 K. R. HEBERT, S. ADHIKARI, J. E. HOUSER, *J. Electrochem. Soc.*, **152**, C324 (2005).
- 36 Z. V. FENG, X. LI, A. A. GEWIRTH, *J. Phys. Chem. B*, **107**, 9415 (2003).
- 37 M. WALKER, L. J. RICHTER, T. P. MOFFAT, *J. Electrochem. Soc.*, **153**, C403 (2005).
- 38 T. P. MOFFAT, B. BAKER, D. WHEELER, J. E. BONEVICH, M. EDELSTEIN, D. R. KELLY, L. GAN, G. R. STAFFORD, P. J. CHEN, W. F. EGELHOFF, D. JOSELL, *J. Electrochem. Soc.*, **149**, C423 (2002).
- 39 B. C. BAKER, M. FREEMAN, B. MELNICK, D. WHEELER, D. JOSELL, T. P. MOFFAT, *J. Electrochem. Soc.*, **150**, C61 (2003).
- 40 B. C. BAKER, C. WITT, D. WHEELER, D. JOSELL, T. P. MOFFAT, *Electrochem. Solid-State Lett.*, **6**, C67 (2003).
- 41 E. J. AHN, J. J. KIM, *Electrochem. Solid-State Lett.*, **7**, C118 (2004).
- 42 D. JOSELL, C. R. BEAUCHAMP, D. R. KELLEY, C. A. WITT, T. P. MOFFAT, *Electrochem. Solid-State Lett.*, **8**, C54 (2005).
- 43 D. JOSELL, D. WHEELER, T. P. MOFFAT, *J. Electrochem. Soc.*, **153**, C11 (2006).
- 44 D. JOSELL, S. KIM, D. WHEELER, T. P. MOFFAT, S. G. PYO, *J. Electrochem. Soc.*, **150**, C368 (2003) and references therein.
- 45 T. P. MOFFAT, D. WHEELER, D. JOSELL, Superconformal Film Growth, in *Advances in Electrochemistry and Electrochemical Engineering*, R. ALKIRE, D. M. KOLB, P. ROSS, J. LIPKOWSKI (Eds.), Wiley-VCH, Weinheim, in press.
- 46 M. WINTERHALTER, H. BURNER, S. MARZINKA, R. BENZ, J. J. KASIANOWICZ, *Biophys. J.*, **69**, 1372 (1995).
- 47 D. JOSELL, C. WITT, T. P. MOFFAT, *Electrochem. Solid-State Lett.*, **9**, C41 (2006).
- 48 D. WHEELER, J. GUYER, J. A. WARREN, FiPy: A Finite Volume PDE Solver Using Python; <http://www.ctcms.nist.gov/fipy/>
- 49 J. REID, E. WEBB, J. SUKAMTO, Y. TAKADA, T. ARCHER, in *Electrochemical Processing in ULSI and MEMS*, H. DELIGIANNI, S. T. MEYER, T. P. MOFFAT, G. R. STAFFORD (Eds.), PV 2004-17, p. 184, The Electrochemical Society Proceedings Series, Pennington, NJ (2005).
- 50 T. P. MOFFAT, D. WHEELER, S.-K. KIM, D. JOSELL, *J. Electrochem. Soc.*, **153**, C127 (2006).
- 51 S.-K. KIM, D. JOSELL, T. P. MOFFAT, *J. Electrochem. Soc.*, **153**, C616 (2006).

II

Preparation and Properties of Nanostructures

6

Localized Electrocrystallization of Metals by STM Tip Nanoelectrodes

Werner Schindler and Philipp Hugelmann

6.1

Electrochemistry in Nanoscale Dimensions

Electrochemical processes proceed on atomic or molecular scales, however, they have traditionally been studied with integral techniques like cyclic voltammetry, impedance spectroscopy or potential pulse. The development of laterally resolved imaging of solid/liquid interfaces by scanning tunneling microscopy (STM) 20 years ago [1–3] has stimulated rapid progress in various fields of electrochemistry. The availability of this technique, allowing imaging of surfaces *in situ* in the electrolyte with a lateral resolution of subnanometers, resulted, for example, in a rapid increase in the understanding of delocalized electrochemical metal deposition processes [4], underpotential deposition (UPD) of metals [5], reconstruction [6] or adsorption [7] phenomena at solid/liquid interfaces. Although the STM imaging process is laterally, in part atomically resolved, the studied processes or reactions have been usually controlled by the working electrode, i.e. the substrate, potential and thus applied over the whole electrode surface simultaneously.

Many studies have revealed that electrochemical nucleation and growth processes are determined by specific substrate properties [4]. Preferred nucleation occurs at substrate inhomogeneities like step edges or kink sites. The formation of one-dimensional (1D) and two-dimensional (2D) structures could be resolved in cyclic voltammetry for example during Pb deposition on Ag (111) in the undersaturation regime with respect to bulk Pb deposition [4, 8]. Zero-dimensional (0D) nuclei can be formed at even higher potentials in the undersaturation regime [9]. The equilibrium potential of low-dimensional structures is usually more positive than the corresponding equilibrium potential of 3D bulk structures [10]. An application of these features is, for example, the growth of nanowires at step edges of HOPG [11–13]. Large substrate areas can be covered by delocalized electrodeposition at the same time, but the achievable structures depend on the actual surface inhomogeneities. These may be distributed randomly across a surface unless a regular structure of nucleation sites has been established before electrodeposition.

Electrochemical nanoelectrodes provide the possibility to change or to measure ion concentrations locally [14–16]. When combined with a piezo scanner their lat-

eral position can be precisely controlled and arbitrarily adjusted with high accuracy and resolution. This allows a local modification of electrochemical conditions at substrate surfaces, and allows one to perform a local electrochemistry with a lateral resolution in the nanometer range, and to apply locally resolved *in situ* measurements [17, 18]. The scanning electrochemical microscope (SECM) [19, 20] utilizes electrochemical nanoelectrodes to study electrochemical processes, at present, however, with a lateral resolution of hundreds of nanometers rather than a few nanometers [21, 22]. Alternatively, nanoelectrodes can be represented by STM tips which provide the tip apex shape required for a lateral resolution in the lower nanometer range.

So far, however, STM tips have been mainly used as sensors for the tunneling current during STM imaging of surfaces at solid/liquid interfaces at potential control of both substrate and STM tip. Since a STM tip current I_{tip} consists, at sufficiently small distance (gap width) between the tip apex and the substrate surface, of both tunneling current I_{tunnel} and electrochemical (Faraday) currents I_{EC} , STM tips are usually isolated with wax or lacquers leaving only a small tip apex surface exposed to the electrolyte [23–25]. This ensures that at appropriate tip potentials almost the whole tip current results from electron tunneling between substrate surface and tip apex, and electrochemical (Faraday) currents are sufficiently low. It is obvious that STM imaging works better the lower the level of Faraday currents at the particular STM tip potential. For the purpose of STM imaging, the electrochemically most inactive tip surface is the most desirable surface, because it shows the lowest Faraday currents, and $I_{\text{tip}} \approx I_{\text{tunnel}}$ is realized to the best extent.

In parallel to detailed investigations of electrodeposition processes at extended surfaces with nanometer resolution, STM has also been used for local modification of solid/liquid interfaces on the nanometer scale. The advantage of STM over other methods in this field of surface modification is its high lateral resolution in the sub-ångstrom regime. Various techniques have been tried to prepare nanostructures with the STM tip on substrate surfaces utilizing mechanical, electrochemical or other interactions between the STM tip apex and the substrate surface underneath [26–40]. All the techniques utilized interactions between the tip and the substrate surface at tunneling distance, that is at distances of typically 0.5 nm. A consequence of such small distances is the practically unavoidable problem of making mechanical and hence, simultaneously, electrical contact between STM tip and substrate surface during the nanostructuring process. This disturbs the potentials of the tip or/and the substrate surface, resulting in undefined electrochemical conditions. Therefore, a clear separation of mechanisms for the nanostructuring process is difficult to achieve, although it would be crucial for defining the basic physical mechanisms involved in the nanostructure formation.

6.2

Jump-to-Contact Metal Deposition

A major achievement in the field of nanostructuring at solid/liquid interfaces has been the “jump-to-contact” deposition of metal clusters with diameters of several

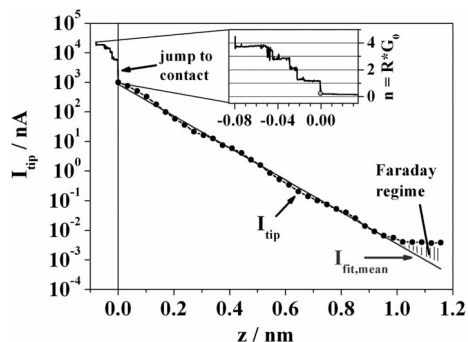


Figure 6.1. *In situ* measurement of the tunneling current – distance characteristic at a Au (111) surface using a Au STM tip, starting from the regime of the formation of quantized conductance channels at tip currents of several μA to the regime of Faraday tip currents below 10 pA [41, 42]. The complete data set has been superposed from three different measurements in different overlapping current ranges, using different tip current converter modules for the measurements. This has been necessary to achieve the required signal to noise ratio. The

zero point of the distance scale has been defined by the point of jump-to-contact. Black dots: Current–distance curve measured with a tip movement of 6.7 nm s^{-1} ; gray line: fit of a straight line to the data, considering only current values between 50 pA and 1000 nA and neglecting the obvious modulation in the data [41, 42]. $E_{\text{WE}} = 240\text{ mV}$ for $z > 0$, 175.5 mV for $z < 0$, $E_{\text{tip}} = 340\text{ mV}$ for $z > 0$, 240 mV for $z < 0$, $U_{\text{bias}} = E_{\text{tip}} - E_{\text{WE}} = 100\text{ mV}$ for $z > 0$, 64.5 mV for $z < 0$. Electrolyte: 0.02 M HClO_4 . Potentials are quoted with respect to SHE.

nanometers by Kolb and coworkers [32–38]. This technique utilizes a permanent electrodeposition of metal from the electrolyte onto the STM tip at low overpotentials, a defined approach of the tip towards the substrate surface until jump-to-contact occurs between tip apex and substrate surface and, upon jump-to-contact, a retraction of the tip, which leaves, under certain conditions, a small metal cluster on the surface.

The jump-to-contact effect is illustrated in Fig. 6.1. The tunneling current between the STM tip and the substrate surface increases almost exponentially with decreasing gap width between the tip apex and the substrate surface, until quantized conductance channels of atomic size are formed between them [41, 42]. Then, the tip current jumps to a finite value

$$I_{\text{tip}} = U_{\text{bias}} \cdot nG_0, \quad \text{with } G_0 = (12906\ \Omega)^{-1} \text{ and } n = 1, 2, 3, \dots \quad (6.1)$$

This current results from electron transport through quantized conductance channels rather than from electron tunneling across the tunneling gap between the STM tip apex and the substrate surface.

The low overpotential at the STM tip, usually a Pt/Ir tip, guarantees its permanent coverage by the desired metal, for example Cu. Thus, a nanoelectrode is established which consists of the particular metal dissolved in the electrolyte. As has been found by Kolb and coworkers, only those metal/substrate systems which are known to show underpotential deposition (UPD) behavior form clusters using this

technique [34]. Different metal/substrate systems have been reported to result in monoatomically high islands, or even holes in the substrate surface when atoms jump from the substrate to the STM tip apex [35]. Hence, it has not been possible to deposit metal clusters on silicon surfaces [36] which show a weak metal/substrate interaction. Although there is a mechanical contact formed during the approach of the STM tip towards the substrate surface, the procedure can be reproducibly applied to produce large arrays of clusters [37, 38]. The interaction between the tip and the substrate surface can be varied by the approach parameters of the tip, as found experimentally and calculated theoretically [39]. With an appropriate approach routine of the tip, the interaction between tip and substrate surface is kept sufficiently small and the clusters can be electrochemically dissolved, leaving behind a smooth substrate surface [40]. This suggests that the jump-to-contact deposition of metal clusters may not necessarily result in alloying and site exchange processes between substrate and metal cluster.

6.3

Scanning Electrochemical Microscope

The scanning electrochemical microscope (SECM) developed by Bard and co-workers [19, 20] utilizes solely electrochemical processes for imaging of surfaces, and can be used to study locally electrochemical processes occurring either at the substrate underneath the SECM tip, or at the tip, or in the electrolyte in the gap between the substrate and the tip. There is no mechanical interaction between the tip and the substrate surface involved in the measurements since the distance between them is of the order of a micrometer. Usually, a glass capillary or a flat metal tip electrode encapsulated by a non-conductive isolation with a thickness of multiples of the metal tip electrode diameter are used to probe the substrate surface (Fig. 6.2(a)). The achievable lateral resolution is typically in the micrometer range due to (i) the metal tip electrode diameter, which is variable but hard to downsize below 100 nm, and (ii) the diffusion behavior of the electroactive species in the gap between the substrate and the tip electrode, which is of the order of micrometers rather than nanometers [21, 22]. Such geometry (Fig. 6.2 (a)) results in diffusion profiles of micrometer width at the position of the tip electrode, even if there is a point source at the substrate. It is difficult to approach a SECM tip closer to the substrate than a micrometer since ultraflat substrate surfaces and a perfectly parallel orientation of substrate and tip surfaces would be required to avoid mechanical contact.

6.4

STM Tip Electrochemical Nanoelectrodes

The configuration of the substrate surface and the STM tip (Fig. 6.2(b)) does not form a parallel plane geometry as in the case of the SECM. Figure 6.2 shows both

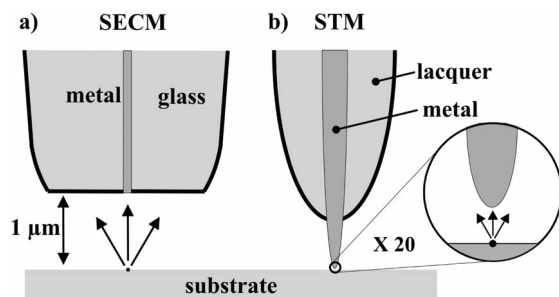


Figure 6.2. Schematic picture of the tip–substrate geometry in SECM (a) and in STM (b). Both schematics are drawn to a comparable scale. The arrows indicate hemispherical diffusion from a small area on the substrate underneath the STM tip.

geometries drawn to the same scale. It is evident that the influence of a sharp STM tip on the diffusion of electroactive species is much less than the influence of a SECM tip on the diffusion to and from the substrate underneath the respective tip. Thus, this geometry would be favorable from the point of view of electrochemistry and for the study of charge transfer processes. On the other hand, the theoretical description of diffusion processes requires the consideration of non-planar, hemispherical diffusion to/from the STM tip, and consideration of the whole unisolated area of the tip exposed to the electrolyte, which contributes to the electrochemical tip current. This requires the detailed shape of the STM tip to be known.

When a STM tip is positioned above a substrate surface at a distance ≥ 10 nm, the electrochemical double layers of both substrate and tip are well separated. At ion concentrations of 10^{-3} to 10^{-1} M, as typically used for electrochemical experiments, the thickness of the electrochemical double layer ranges from less than 1 nm to a few nm [43]. The electrochemical processes in such a geometry are mainly determined by the potentials of the two working electrodes, i.e. STM tip and substrate, and by diffusion processes of ions in the electrolyte between the two electrodes. Migration effects need not be considered since the potentials across the solid/liquid interfaces at the electrodes drop across the corresponding electrochemical double layers.

The STM tip can be used either as a local sensor for electrolyte constituents with a spacial resolution of 10^{-15} cm³, or as a nanoscale generator electrode which can release tip material locally into or collect ions locally from the electrolyte surrounding the tip. The first technique has been developed by Meier and Stimming [16, 44] and can be successfully applied for example in investigations of catalytic activity at nanoscale clusters. The second technique, localized electrodeposition, has been developed by Hofmann and Schindler [14, 15]. This technique allows solely electrochemical deposition of single metal clusters on both metal [14, 15] and semiconducting [45] substrates, independent of whether the metal/substrate interaction is strong or weak, which is difficult to achieve with techniques utilizing different mechanisms, as for example the jump-to-contact mechanism [34–36].

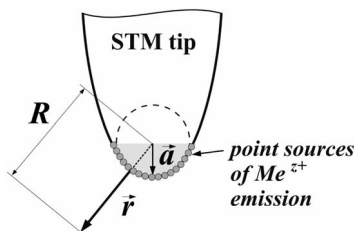


Figure 6.3. Geometry for the calculation of the metal ion (Me^{z+}) concentration around a STM tip upon dissolution from the STM tip. a denotes the diameter of the STM tip apex, r and R are the distances from the tip apex surface and tip apex center, respectively. The diffusion profile is calculated by integration of point sources across the surface of the hemisphere, as indicated in the graph. (Reprinted from Ref. [15] with permission.)

6.5

Metal Deposition by STM Tip Electrochemical Nanoelectrodes

The localized metal deposition process will be discussed for the example of an electrochemical nanoelectrode, realized by a STM tip. Diffusion processes in the electrolyte volume around the tip and in the gap between the substrate surface and the tip, or around a nanostructure on a substrate surface, determine the ion transport to or from the tip or substrate surface underneath the tip, respectively.

This configuration can be modelled by assuming the STM tip apex to be a hemisphere with radius a (Fig. 6.3), neglecting in a first approach the other tip areas exposed to the electrolyte, which is reasonable since these do not contribute much to the ion diffusion to the substrate area opposite to the tip apex, as is evident from Fig. 6.2(b). Then, the diffusion equation for metal (Me) ions dissolving from the STM tip can be solved. The concentration of Me^{z+} at a particular distance R from the center of the tip apex hemisphere and at time t_0 is given by [15]:

$$C(R, t_0) = \frac{aj_{\text{Me}^{z+}}}{eR\sqrt{\pi D}} \times \int_0^{t_0} \frac{1}{\sqrt{t}} \left\{ \exp\left(-\frac{(R-a)^2}{4Dt}\right) - \exp\left(-\frac{R^2+a^2}{4Dt}\right) \right\} dt + c_0 \quad (6.2)$$

The bulk concentration of Me^{z+} in the electrolyte is c_0 , typical diffusion constants for ions in diluted aqueous electrolytes are $D \approx 10^{-5} \text{ cm}^2 \text{ s}^{-1}$ [46].

Equation (6.2) is plotted in Fig. 6.4 versus time for the case of Co as metal, and for two distances $r = R - a$ of 5 and 40 nm. The total tip surface area exposed to the electrolyte, i.e. the Co nanoelectrode area, is $S_{\text{tip}} \approx 10 \mu\text{m}^2$, the Co^{2+} dissolution, i.e. emission, current from the STM tip is 520 nA. Thus, the Co^{2+} emission current density is $j_{\text{Co}^{2+}} = 5.2 \text{ A cm}^{-2}$. The bulk Co^{2+} concentration in the electrolyte is assumed to be $c_0 (r = \infty) = 1 \text{ mM}$. At a constant Co^{2+} dissolution current density of 5.2 A cm^{-2} the Co^{2+} concentrations at different distances to the STM tip surface are $c_1 (r = 5 \text{ nm}) \approx 23 \text{ mM}$ and $c_2 (r = 40 \text{ nm}) \approx 13 \text{ mM}$.

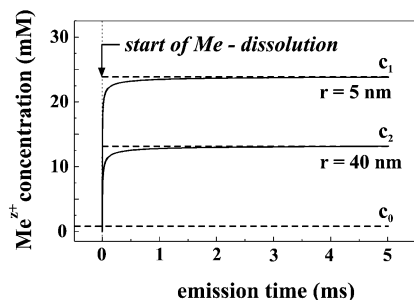


Figure 6.4. Calculated time dependence of the metal ion (Me^{z+}) diffusion profile for different distances $r = 5$ nm and $r = 40$ nm from the STM tip apex surface upon initiation of the metal ion dissolution from the STM tip at $t = 0$, using Eq. (6.2). The particular example here is Co^{2+} . $j_{\text{Me}^{z+}} = 5.2 \text{ A cm}^{-2}$, $S_{\text{tip}} = 10 \mu\text{m}^2$, bulk electrolyte ion concentration c_0 ($r = \infty$) = 1 mM. (Reprinted from Ref. [15] with permission.)

The possible enhancement of ion concentration is important for the supersaturation which can be achieved. In the presented example this is a factor of between 13 and 23, depending on the distance r . According to Eq. (6.2) this enhancement is proportional to the emission current density $j_{\text{Me}^{z+}}$. The concentration profile formed around the STM tip is stationary and needs approximately 100–200 μs after initiation of metal dissolution from the tip electrode at $t = 0$ to build up (Fig. 6.4). There are stationary equiconcentration surfaces formed in the electrolyte around the STM tip at particular distances r from the hemispherical tip surface, each corresponding to a particular ion concentration. This is indicated by the lines around the STM tip in Fig. 6.5. The dashed lines in Fig. 6.5 are extrapolations of the calculated curves around the hemispherical STM tip apex.

So far, solely the individual STM tip or nanoelectrode has been considered. However, ions dissolved from the nanoelectrode will, for example, be deposited onto a substrate surface underneath. Therefore, it is important to consider the ion concentrations in a plane underneath the tip and at a particular distance r . This is shown in Fig. 6.5 for two cases: $r = 5$ nm (a) and $r = 40$ nm (b). Supposing that the substrate does not influence the ion diffusion process, the intersection points of the substrate surface with the equiconcentration surfaces around the tip define equiconcentration circles on the substrate surface. Figure 6.5 shows this in one dimension. The substrate acts as a sink for the metal ions during electrodeposition at sufficient supersaturation, and no backward diffusion into the electrolyte occurs assuming a sticking coefficient of 1 for the metal ions. Using the Nernst equation, Nernst potentials can be calculated from the corresponding ion concentration values at the substrate surface. The difference ΔNP of these calculated potentials and the Nernst potential of a 1 mM Co^{2+} electrolyte is shown in Fig. 6.5 for two distances 5 and 40 nm between the STM tip apex and the substrate surface. The Nernst potential variation ΔNP is at a maximum on the tip axis and decreases with increasing distance from the axis, as plotted in Fig. 6.5. Typical values for

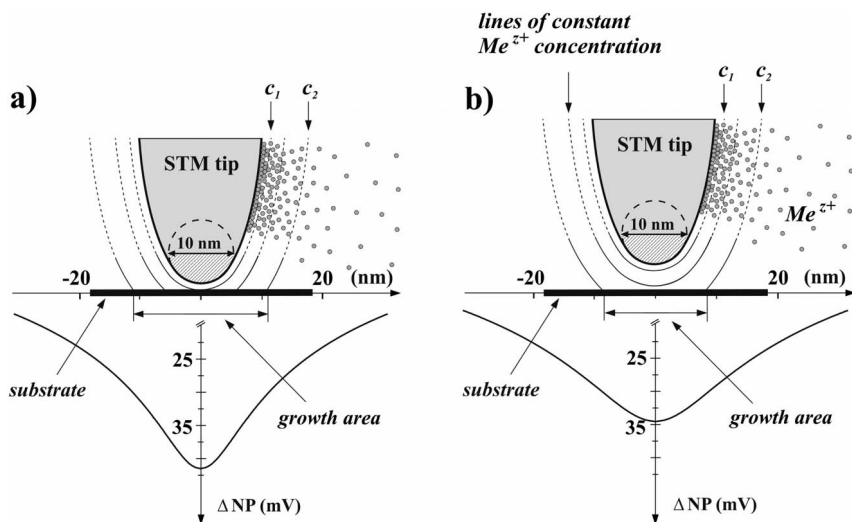


Figure 6.5. Calculated stationary concentration profiles (equiconcentration surfaces) around a STM tip assuming hemispherical diffusion from the STM tip apex. The dependence of the growth area where electrochemical nucleation and growth occurs is shown for two tip-substrate distances (a) $\Delta z = 5$ nm and (b) $\Delta z = 40$ nm. $j_{\text{Me}^{z+}} = 5.2 \text{ A cm}^{-2}$, $S_{\text{tip}} = 10 \text{ }\mu\text{m}^2$, c_2 denotes the particular Me^{z+} concentration which results at a substrate surface underneath the STM tip in an effective Nernst potential equal to E_{WE} . Nucleation is initiated within the growth area where the effective Nernst potential exceeds E_{WE} .

ΔNP in the described example and at the respective parameters for emission current density and distance between tip and substrate are around 30 mV.

This local variation of the metal ion concentration around the STM tip can be exploited to control supersaturation conditions in the volume around the tip, and in particular at the surface of a substrate underneath the tip. Since STM tips can be easily positioned above any substrate surface, the metal deposition onto a substrate surface can be controlled laterally resolved by adjusting a particular stationary metal ion concentration in the volume around the tip. Thus, this technique provides the possibility of controlling the metal deposition process precisely by the metal ion concentration rather than by adjusting the electrode potential, which is the same in all substrate surface areas. Examples of this technique are given in Section 6.8.

6.6

Metal Dissolution by STM Tip Electrochemical Nanoelectrodes

The reverse process, the generation of undersaturation conditions around the STM tip can be correspondingly achieved by applying an appropriate potential to the tip where ions are electrodeposited in bursts from the electrolyte onto the tip. The ion

concentration around the tip is lowered, and at a constant metal deposition current $j_{\text{Me}^{z+}}$ a stationary depletion profile of metal ions is generated around the tip. There applies a similar equation for ion diffusion from the electrolyte to the hemispherical tip apex surface as for the case of dissolution from a hemispherical tip surface:

$$C(R, t_0) = c_0 - \frac{a}{2eR\sqrt{\pi D}} \times \int_0^{t_0} \frac{j_{\text{Me}^{z+}}}{\sqrt{t}} \left\{ \exp\left(-\frac{(R-a)^2}{4Dt}\right) - \exp\left(-\frac{R^2+a^2}{4Dt}\right) \right\} dt \quad (6.3)$$

During dissolution from the STM tip apex surface, which case was described in Section 6.5, a constant metal ion current density $j_{\text{Me}^{z+}}$ was assumed. In the case of electrodeposition this assumption may not be valid in most cases. The important difference is that $j_{\text{Me}^{z+}}$ is here diffusion limited and determined by the ion concentration c_0 in the bulk electrolyte. The ion concentration at the surface of the tip apex hemisphere cannot drop below zero, even at high overpotentials applied at the tip electrode. Therefore, $j_{\text{Me}^{z+}}$ cannot be maintained at arbitrary high values. The diffusion limited current density $j_{\text{Me}^{z+},\text{lim}}$ for electrodeposition of Me^{z+} onto a hemisphere with radius a is rather given by [47]:

$$j_{\text{Me}^{z+},\text{lim}} = \frac{zF\sqrt{D}c_0}{\sqrt{\pi t}} + \frac{zFDc_0}{a} \quad (6.4)$$

Then, $j_{\text{Me}^{z+}}$ in Eq. (6.3) can be replaced by the time-dependent diffusion limited current density $j_{\text{Me}^{z+},\text{lim}}$ (Eq. (6.4)) and the concentration $C(R, t_0)$ can be numerically calculated:

$$C(R, t_0) = c_0 \times \left(\begin{aligned} &1 - \frac{F\sqrt{D}}{2eR\sqrt{\pi}} \times \int_0^{t_0} \frac{1}{\sqrt{t}} \left\{ \exp\left(-\frac{(R-a)^2}{4Dt}\right) - \exp\left(-\frac{R^2+a^2}{4Dt}\right) \right\} dt \\ &- \frac{aF}{2eR\pi} \times \int_0^{t_0} \frac{1}{t} \left\{ \exp\left(-\frac{(R-a)^2}{4Dt}\right) - \exp\left(-\frac{R^2+a^2}{4Dt}\right) \right\} dt \end{aligned} \right) \quad (6.5)$$

The resulting time dependence of the ion depletion profile during the electrodeposition in bursts of ions onto the STM tip is shown in Fig. 6.6 for a bulk concentration of 1 mM, the same concentration as assumed for the simulation of the dissolution process from the tip in Section 6.5. As for the electrochemical dissolution from a STM tip nanoelectrode a stationary concentration profile is built up within approximately 100 μs . In contrast to the dissolution process, the variation of the concentration is smaller for the electrodeposition process onto the tip since the deposition current is diffusion limited and cannot achieve any arbitrary value. The lower limit for the ion concentration at the tip surface is zero and, thus, the concentration variation cannot be higher than the bulk electrolyte concentration. This is seen more clearly in simulations showing the lateral variation of the depletion profile at the position of a substrate surface (Fig. 6.7), calculated under the same

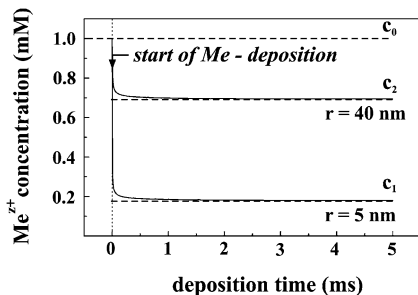


Figure 6.6. Calculated time dependence of the metal ion (Me^{z+}) diffusion profile for different distances $r = 5$ nm and $r = 40$ nm from the STM tip apex surface upon initiation of the metal ion deposition onto the STM tip at $t = 0$, using Eq. (6.5). $j_{\text{Me}^{z+}}$ has been set to the diffusion limited current, bulk electrolyte ion concentration c_0 ($r = \infty$) = 1 mM.

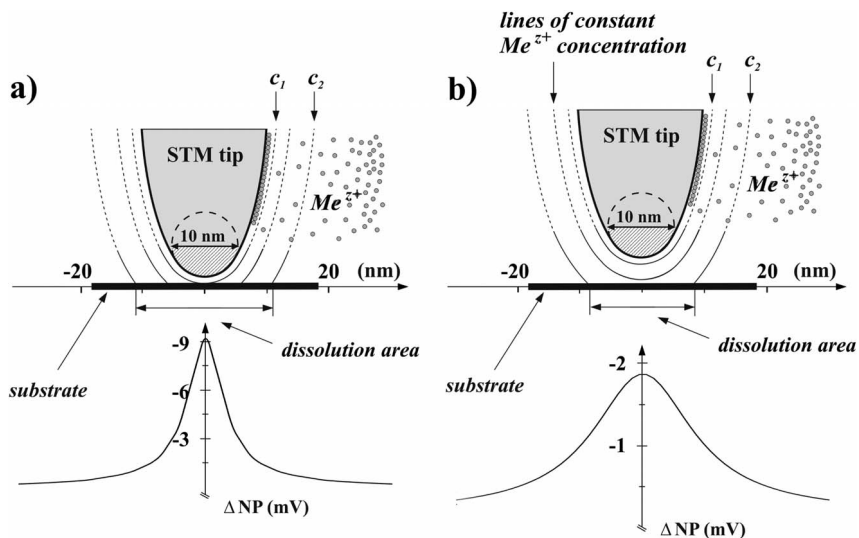


Figure 6.7. Calculated stationary concentration profiles (equiconcentration surfaces) around a STM tip assuming hemispherical diffusion to the STM tip apex. The dependence of the dissolution area where metal is dissolved from the substrate surface is shown for two tip-substrate distances (a) $\Delta z = 5$ nm and (b) $\Delta z = 40$ nm. $j_{\text{Me}^{z+}}$ has been set to the diffusion limited current, c_2 denotes the particular Me^{z+} concentration which results in an effective Nernst potential equal to E_{WE} . Dissolution is initiated within the dissolution area where the effective Nernst potential is lower than E_{WE} .

assumptions as Fig. 6.5 for the case of the electrochemical dissolution from the tip. The lateral variation of the Nernst potential ΔN_P with respect to the Nernst potential of the 1 mM bulk electrolyte across a substrate surface is shown in Fig. 6.7. It results in a dissolution area on a substrate surface underneath the tip where the local Nernst potential becomes lower than the adjusted substrate potential E_{WE} . Compared to the reverse process shown in Fig. 6.5 smaller absolute values for ΔN_P are calculated. Although the maximum variation is $\Delta N_P \approx -9$ mV, the effect may be utilized for surface modification using appropriate bipotentiostatic instrumentation to provide the required stability. In contrast to the nucleation area on substrate surfaces in the dissolution process of metal from the STM tip electrode as shown in Fig. 6.5, the dissolution area on substrate surfaces in the electrodeposition process onto the tip is significantly smaller.

Similar effects of a partial dissolution of surfaces underneath scanning STM tips have been reported previously [48, 49] and may be explained by the described process, although the situation during STM imaging is quite different since the electrochemical double layers of the tip and the substrate surface overlap due to the small gap width of approximately 0.5 nm. In this case, the overlapping electrochemical double layers result in a modification of the potential in the tunneling gap, which may play a major role in the dissolution processes during STM imaging.

6.7

The Importance of Nanoelectrode Tip Shape and Surface Quality

It is obvious that the shape and surface quality of the STM tip apex is of great importance for successful application of STM tip nanoelectrodes. At present, the detailed shape and the surface morphology of electrochemically etched tips, as usually used in STM experiments at solid/liquid interfaces, is rather irreproducible, although a variety of tip etching procedures have been published throughout the past two decades [50–52]. This fact can be deduced from numerous studies of electrochemically etched STM tips by scanning electron microscopy (SEM) [53]. Additionally, the surface of electrochemically etched STM tips is, in part, electrochemically inactive due to etching residuals on the surface, unwanted adsorbates, and oxidized areas of the surface.

This general feature of electrochemically etched tips is usually not considered to be a problem if such tips are used exclusively for STM imaging. At first glance, the detailed shape and electrochemical quality of the tip seems to be completely irrelevant for STM imaging of surfaces, because STM imaging assumes the whole tip current measured to be the tunneling current between the two closest adjacent atoms of tip apex and substrate surface forming the tunneling gap. This assumption is valid as long as Faradaic processes resulting from the tip surface area exposed to the electrolyte add only marginally to the STM tip current. The STM tip surface area is minimized by isolating the tip with either Apiezon wax or electrophoretic lacquers, and Faradaic currents are minimized by carefully deoxygenating

the electrolyte to minimize oxygen reduction reactions and by keeping the potential of the tip in the double layer regime of the tip electrode. An electrochemically inactive tip surface even helps to achieve the goal of minimization of the electrochemically active tip surface area.

When extended atomically flat surfaces are imaged by blunt STM tips high resolution images can still be obtained [54]. Difficulties arise when surfaces with a larger height variation are imaged at high lateral resolution. A prominent example is supported clusters with diameters in the lower nanometer range and heights of several atomic layers. STM images of such clusters usually do not show the expected individual atomic layers and step edges [32–38, 55], but rather a hemispherical shape which results from the convolution of the real shape of the cluster with the actual geometry of the tip apex [54, 56]. Unfortunately, this convolution changes both the diameter and height of the scanned object, which results in a complicated interpretation of the corresponding STM images.

Severe problems arise, however, when electrochemically etched tips are used for more advanced purposes such as all techniques using the tip for initiation or detection of electrochemical processes on a nanometer scale, that is using the tip as a nanoelectrode or as a high resolution electrochemical sensor probe. Such purposes require a well-defined tip shape and an electrochemically clean tip surface which is usually not the case for electrochemically etched STM tips.

In order to combine the requirements for STM imaging, a very small diameter of the tip apex for high lateral resolution, with the requirements for electrochemistry at the STM tip, namely a well-defined geometrical shape and electrochemically clean surface area of the tip exposed to the electrolyte, the tip preparation can be substantially improved by applying a field emission/sputtering process subsequent to the electrochemical etching step [57]. Although the mechanisms of electron field emission and sputtering by ionized ions have been known for almost 50 years [58–60], this technique has not been applied routinely for the preparation of STM tips. The basic idea is that the diameter of a metal tip can be precisely determined by the voltage for field emission of electrons. This correlation can be exploited to precisely determine the diameter of a tip from its field emission voltage. Figure 6.8 shows this correlation for various tips prepared with this technique. It is worth mentioning that STM tips can be produced from nearly any metal wire, in particular from Au which is often assumed not to be suitable for the formation of stable and sharp STM tips.

Such STM tips with a defined geometrical shape can be modelled, in a first approximation, as a sphere of certain diameter, which is typically of the order of 5 to 30 nm. Transmission electron microscopy (TEM) images as shown in Fig. 6.9 prove the validity of such an assumption.

An example demonstrating the deposition and dissolution of metal from such a defined STM tip surface area is shown in Fig. 6.10. The arrows indicate small contributions of underpotential deposition and dissolution (UPD) from the (111) facets of the polycrystalline Au STM tip surface.

Thus, these STM tips can be used for both STM imaging and localized electrochemistry at the tip.

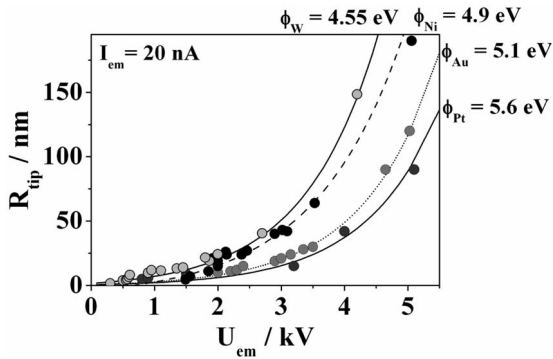


Figure 6.8. STM tips prepared in ultrahigh vacuum by a field emission/sputtering technique. The emission voltage for field emission in ultrahigh vacuum is a direct measure of the diameter $2 \times R_{\text{tip}}$ of the STM tip apex. The curves show data at an emission current of 20 nA for Au, W, Ni, and Pt STM tips. The tip apex diameters have been determined by electron microscopy.

6.8 Localized Electrodeposition of Single Metal Nanostructures

Electrodeposition of a metal onto a substrate is achieved at supersaturation conditions. As mentioned above, these can be realized either by applying an appropriate overpotential to a substrate surface, or by increasing the ion concentration without changing the electrode potential. Whereas the first possibility is often applied in nucleation and growth, the latter option is used much less. It requires the release of metal ions from a generator electrode, and control of the ion concentration

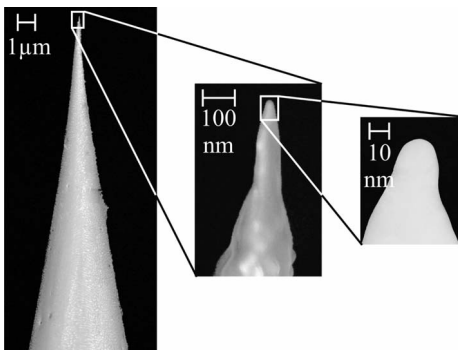


Figure 6.9. Scanning and transmission electron images of Au STM tips, as prepared with the combined field emission/sputtering technique. The diameter of the STM tip apex is approximately 20 nm.

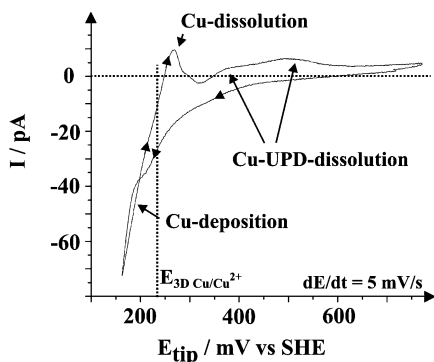


Figure 6.10. Cyclic voltammetry of sputter-prepared Au STM tips showing the electrodeposition and dissolution of Cu. Despite the polycrystalline surface of the STM tip there is indication of a small contribution of underpotential deposition (UPD) phenomena on Au (111) facets of the STM tip surface. Potentials are quoted with respect to SHE.

in front of the substrate surface, which is not as easy as controlling the electrode potential.

When using a STM tip as a nanoelectrode, there exists a well-defined geometry and a well-defined distance between tip and substrate surface. Under such conditions, the tip nanoelectrode can be used as a generator electrode for metal ions, and the ion concentration profile in the electrolyte shows radial symmetry around the tip axis, as explained in Section 6.5. Such experimental conditions can be calculated theoretically, and result in supersaturation conditions at the substrate surface within a certain circular growth area underneath the tip. In order to examine the cluster formation process in full detail, well-defined substrate surfaces have been used as shown exemplarily for Au (111) in Fig. 6.11.

As can be seen from Fig. 6.5, which assumes an ideal hemispherical generator electrode, the diameter of the growth area where nucleation occurs on the substrate surface is determined by the diffusion profile of ions emitted from the generator electrode. Nucleation occurs in that particular area where the increased ion concentration results in a Nernst potential which exceeds the preadjusted working electrode (substrate) potential. There may be various Nernst potentials for the formation of zero-dimensional nuclei (0D-Nernst potential), two-dimensional growth (2D-Nernst potential), and three-dimensional growth of clusters (3D-Nernst potential) [4, 10].

According to the hemispherical ion diffusion from the hemispherical STM tip apex shape, the size of the growth area becomes less the larger the distance between tip and substrate surface. Therefore, the tip must be adjusted to distances in the range of several tens of nanometers, which is easy to achieve.

In order to achieve a sufficient supersaturation in a small substrate area underneath the STM tip, a special potential routine must be applied at the tip (Fig. 6.12).

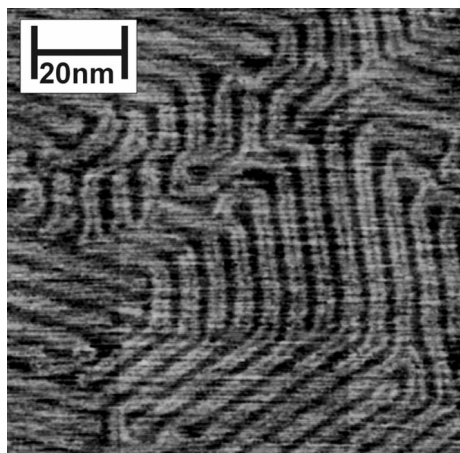


Figure 6.11. Unfiltered *in situ* STM image of a reconstructed Au (111) surface in 0.02 M HClO_4 as used in the electrodeposition experiments. $E_{\text{WE}} = 240$ mV, $E_{\text{tip}} = 340$ mV, $I_{\text{tunnel}} = 5$ nA. Potentials are quoted with respect to SHE. (Reprinted from Ref. [61] with permission.)

In a first step, the Au tip is covered with a layer of metal (Me), which is deposited from the electrolyte around the tip, and a nanoelectrode is formed. The second step consists of a burst-like dissolution of this metal from the tip resulting in a concentration profile of metal ions around the tip. At a correspondingly adjusted substrate potential E_{WE} the increase in the Me^{z+} concentration results in sufficient supersaturation to initiate nucleation and subsequent growth of a cluster on a particular small substrate surface area, i.e. growth area, underneath the tip. The predeposited charge Q_{cat} can be released from the tip either in a single step, or in multiple steps for the deposition of sequences of clusters.

The major parameters determining the diameter of the growing metal cluster, i.e. the growth area, are (i) emission current density $j_{\text{Me}^{z+}}$, (ii) the STM tip–substrate distance Δz , (iii) the substrate potential E_{WE} , and (iv) the STM tip apex diameter [15, 17].

The growth area is determined by the stationary concentration profile which depends on the emission current density $j_{\text{Me}^{z+}}$, according to Eq. (6.2). The equiconcentration surfaces and their intersection points with the substrate surface, as plotted in Fig. 6.5, are shifted outwards when $j_{\text{Me}^{z+}}$ increases, resulting in a larger diameter of the growth area. The influence of the tip–substrate distance can also be understood from Fig. 6.5. The intersection points of the equiconcentration surfaces with the substrate surface, as plotted in Fig. 6.5, move inward towards the STM tip axis, when the tip–substrate distance is increased. The experimental verification is shown in Fig. 6.13. The upper two clusters have been deposited at $\Delta z = 15$ nm, the two lower clusters at $\Delta z = 10$ nm. Whereas all clusters show the same height, the diameter varies, as predicted from Fig. 6.5.

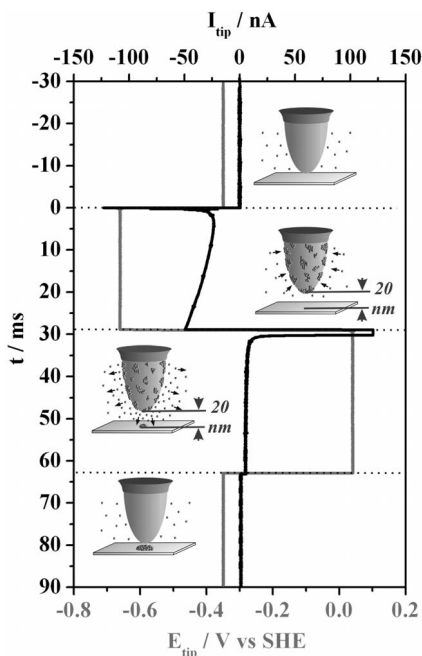


Figure 6.12. Potential transient as applied at the STM tip, and current transient as measured at the tip upon application of the potential routine during the deposition procedure. In a first step, metal is deposited electrochemically from the electrolyte onto the STM tip. The deposited charge is Q_{cat} . Localized electrodeposition is achieved in a subsequent step by a burst-like dissolution of metal ions from the STM tip, resulting in the generation of supersaturation conditions at the substrate surface underneath the tip. Q_{cat} can be released either in a single step or in multiple steps. Potentials are quoted with respect to SHE.

The height of the clusters depends on the total charge emitted from the nanoelectrode, that is the STM tip. At a constant emission current density $j_{\text{Me}^{z+}}$ the height increases with increasing emission time, supposed that the adjusted tip–substrate distance Δz remains almost constant during the cluster deposition process. Figure 6.14 shows the increase in the cluster height with the predeposited charge Q_{cat} when Q_{cat} is fully released from the tip in a single step.

An example of a single Co cluster which is three atomic layers high, deposited onto a reconstructed Au (111) surface is shown in Fig. 6.15. The deposit–substrate interaction between Co and Au (111) is relatively weak, although not as weak as the interaction of metal deposits and semiconducting surfaces. A Pb cluster deposited onto n-Si (111):H is shown in Fig. 6.16. The sequence of STM images before and after deposition, as well as after subsequent dissolution of the Pb cluster from n-Si (111):H demonstrates that clusters deposited by localized electrodeposition can be electrochemically dissolved on increasing the substrate potential (Fig. 6.16(c)).

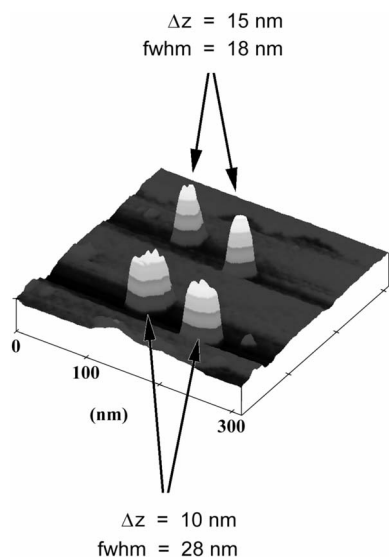


Figure 6.13. STM image showing the dependence of the cluster diameter on the distance Δz between the STM tip and substrate surface during the deposition procedure. Upper row: $\Delta z = 15$ nm during deposition; lower row: $\Delta z = 10$ nm during deposition; $Q_{\text{cat}} = 800$ pC which has been fully dissolved during the burst-like dissolution from the STM tip; $E_{\text{WE}} = -540$ mV;

the fwhm of the clusters grown with $\Delta z = 15$ nm is 18 ± 1 nm, with $\Delta z = 10$ nm it is 28 ± 1 nm, as determined from the STM image. Each gray scale value corresponds to a height of 1 nm. The lower baselines of the STM scans across the clusters, compared to the substrate surface, are a scan artefact. Potentials are quoted with respect to SHE. (Reprinted from Ref. [15] with permission.)

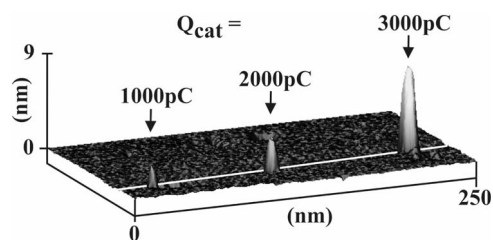


Figure 6.14. STM image showing the dependence of the cluster height on the predeposited charge Q_{cat} when fully released from the STM tip nanoelectrode during the burst-like dissolution step. Substrate: Au (111), $E_{\text{WE}} = -450$ mV, $\Delta z = 20$ nm, $I_{\text{Co}^{2+}} = 120$ nA during dissolution from the STM tip, electrolyte: 0.25 M $\text{Na}_2\text{SO}_4 + 1$ mM CoSO_4 . Potentials are quoted with respect to SHE.

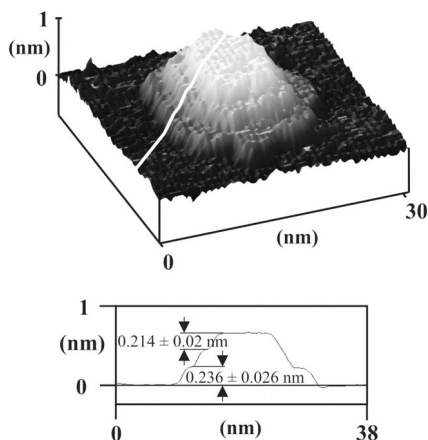


Figure 6.15. STM image of a single Co cluster deposited on Au (111) by localized electrodeposition. The fwhm of the cluster is 15 nm as measured by STM. The cluster shows three atomic layers which form a pyramidal shape. Cluster deposition at $E_{WE} = -460$ mV, $\Delta z = 20$ nm, cathodic predeposited tip charge $Q_{cat} = 1500$ pC which has been fully dissolved during the burst-like dissolution from the STM tip.

STM image measured at $I_{tunnel} = 916$ pA. The step heights are mean values which have been derived from a series of measurements across different clusters and various line profiles across each cluster, as exemplarily indicated by the line profile shown. Electrolyte: 0.25 M $\text{Na}_2\text{SO}_4 + 1$ mM CoSO_4 . Potentials are quoted with respect to SHE. (Reprinted from Ref. [45] with permission.)

In all experiments Au STM tips have been used because, when properly prepared, they combine the features of sharp STM tips and electrochemically “clean” nanoelectrodes.

6.9 Summary and Outlook

Localized electrodeposition and dissolution processes allow local modification of substrate surfaces in the range of a few nanometers by solely electrochemical means. These electrochemical processes are nondestructive to the underlying substrate surface, and allow the most gentle preparation of nanostructures. The solid/liquid interface provides the unique feature that undersaturation and supersaturation conditions can be precisely adjusted by varying either the electrode potential or the ion concentration. The latter can be achieved with high accuracy using STM tips as electrochemical nanoelectrodes. Nanostructures can be deposited at substrate surface sites which are actively defined by the position of the STM tip.

Calculation of the stationary accumulation or depletion of ions around a STM tip nanoelectrode at appropriate potentials and the corresponding calculation of local

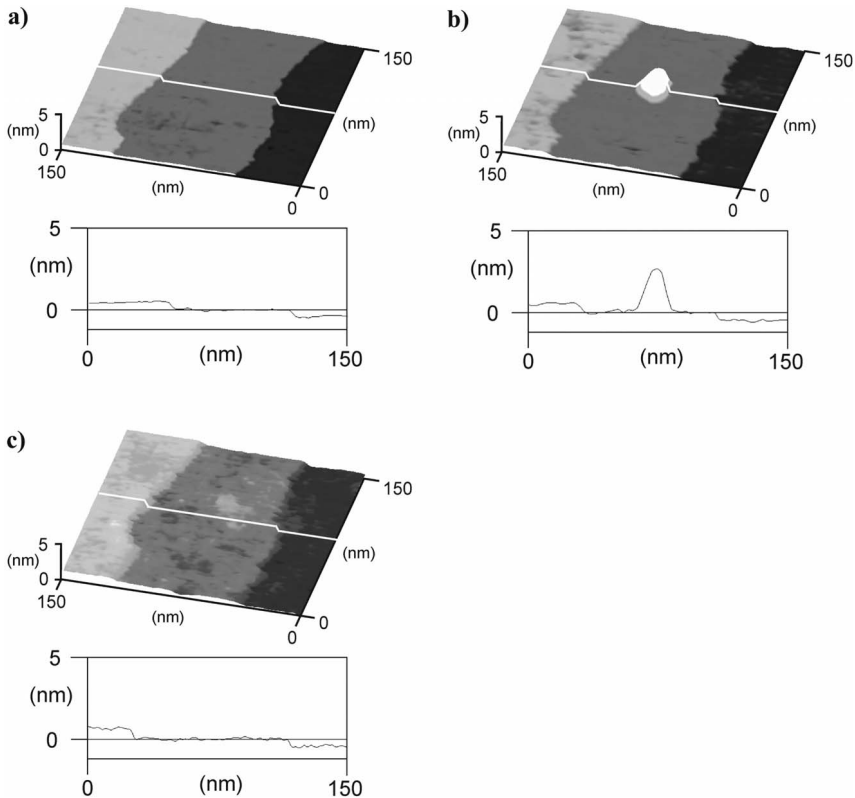


Figure 6.16. Localized electrodeposited Pb cluster on n-Si (111):H. (a) Bare n-Si (111):H surface before cluster deposition; (b) same n-Si (111):H surface after deposition of a Pb cluster; (c) same n-Si (111):H surface upon a change of the substrate potential E_{WE} resulting in dissolution of the Pb cluster. Electrolyte: 0.1 M HClO_4 + 1 mM $\text{Pb}(\text{ClO}_4)_2$. Imaging conditions: $E_{WE} = -240$ mV, $E_{tip} = +640$ mV, $I_{tip} = 200$ pA. Cluster

deposition parameters: $E_{WE} = -240$ mV, cathodic predeposited tip charge $Q_{cat} = 2000$ pC which has been fully dissolved during the burst-like dissolution from the STM tip, Pb^{2+} ion current during the burst-like dissolution from the STM tip $I_{\text{Pb}^{2+}} = 120$ nA, tip-substrate distance during cluster deposition $\Delta z = 20$ nm. Potentials are quoted with respect to the SHE. (Reprinted from Ref. [17] with permission.)

changes in metal/metal ion equilibrium potentials at a surface underneath the STM tip electrode document that STM tip nanoelectrodes allow reproducible application in nanostructure formation at solid/liquid interfaces.

The presented examples of localized electrodeposition of Co clusters on Au (111) or of Pb clusters on n-Si (111):H surfaces show the potential of STM based *in situ* techniques at solid/liquid interfaces in the fields of nanophysics and nanoelectrochemistry.

Acknowledgments

The initial part of the work is the PhD thesis of Detlef Hofmann carried out at the Max-Planck-Institut für Mikrostrukturphysik, Halle, Germany, the remainder was carried out at the Universität Karlsruhe. Experimental support has been provided by Jürgen Kirschner, Max-Planck-Institut für Mikrostrukturphysik. Financial support by the Deutsche Forschungsgemeinschaft under contracts Schi 492/1 and 2 is greatly appreciated.

References

- 1 R. CHRISTOPH, H. SIEGENTHALER, H. ROHRER, H. WIESE, *Electrochim. Acta* **1989**, *34*, 1011.
- 2 K. ITAYA, E. TOMITA, *Surf. Sci.* **1988**, *201*, L501.
- 3 J. WIECHERS, T. TWOMEY, D. M. KOLB, R. J. BEHM, *J. Electroanal. Chem.* **1988**, *248*, 451.
- 4 E. BUDEVSKI, G. STAIKOV, W. J. LORENZ, *Electrochemical Phase Formation and Growth*, VCH, Weinheim, Germany, **1996**.
- 5 O. M. MAGNUSSEN, J. HOTLOS, R. J. NICHOLS, D. M. KOLB, R. J. BEHM, *Phys. Rev. Lett.* **1990**, *64*, 2929.
- 6 D. M. KOLB, *Prog. Surf. Sci.* **1996**, *51*, 109.
- 7 M. WILMS, P. BROEKMANN, C. STUHLMANN, K. WANDELT, *Surf. Sci.* **1998**, *416*, 121.
- 8 G. STAIKOV, K. JÜTTNER, W. J. LORENZ, E. BUDEVSKI, *Electrochim. Acta* **1978**, *23*, 319.
- 9 G. STAIKOV, W. J. LORENZ, E. BUDEVSKI, in *Imaging of Surfaces and Interfaces* (Frontiers of Electrochemistry, Vol. 5), J. LIPKOWSKI, P. N. ROSS (Eds.), Wiley-VCH, Weinheim, **1999**.
- 10 W. J. LORENZ, G. STAIKOV, W. SCHINDLER, W. WIESBECK, *J. Electrochem. Soc.* **2002**, *149*, K47.
- 11 E. C. WALTER, B. J. MURRAY, F. FAVIER, G. KALTENPOTH, M. GRUNZE, R. M. PENNER, *J. Phys. Chem. B* **2002**, *106*, 11407.
- 12 E. C. WALTER, M. P. ZACH, F. FAVIER, B. J. MURRAY, K. INAZU, J. C. HEMMINGER, R. M. PENNER, *Chem. Phys. Chem.* **2003**, *4*, 131.
- 13 H. X. HE, S. BOUSSAAD, B. Q. XU, C. Z. LI, N. J. TAO, *J. Electroanal. Chem.* **2002**, *522*, 167.
- 14 D. HOFMANN, W. SCHINDLER, J. KIRSCHNER, *Appl. Phys. Lett.* **1998**, *73*, 3279.
- 15 W. SCHINDLER, D. HOFMANN, J. KIRSCHNER, *J. Electrochem. Soc.* **2001**, *148*, C124.
- 16 J. MEIER, K. A. FRIEDRICH, U. STIMMING, *Faraday Discuss.* **2002**, *121*, 365.
- 17 M. HUGELMANN, P. HUGELMANN, W. J. LORENZ, W. SCHINDLER, *Surf. Sci.* **2005**, *597*, 156.
- 18 W. SCHINDLER, M. HUGELMANN, P. HUGELMANN, *Electrochim. Acta* **2005**, *50*, 3077.
- 19 A. J. BARD, F. R. F. FAN, J. KWAK, *Anal. Chem.* **1988**, *61*, 132.
- 20 A. J. BARD, *Scanning Electrochemical Microscopy*, Taylor & Francis, Oxford, **2001**.
- 21 F. M. BOLDT, N. BALTES, K. BORGHARDT, J. HEINZE, *Surf. Sci.* **2005**, *597*, 51.
- 22 O. SKLYAR, T. H. TREUTLER, N. VLACHOPOULOS, G. WITTSTOCK, *Surf. Sci.* **2005**, *597*, 181.
- 23 M. J. HEBEN, M. M. DOVEK, N. S. LEWIS, R. M. PENNER, *J. Microsc.* **1988**, *152*, 651.
- 24 L. A. NAGAHARA, T. THUNDAT, S. M. LINDSAY, *Rev. Sci. Instrum.* **1989**, *60*, 3128.
- 25 A. A. GEWIRTH, D. H. CRASTON, A. J. BARD, *J. Electroanal. Chem.* **1989**, *261*, 477.
- 26 W. LI, J. A. VIRTANEN, R. M. PENNER, *Appl. Phys. Lett.* **1992**, *60*, 1181.

- 27 W. LI, J. A. VIRTANEN, R. M. PENNER, *J. Phys. Chem.* **1996**, *96*, 6529.
- 28 W. LI, G. S. HSIAO, D. HARRIS, R. M. NYFFENEGGER, J. A. VIRTANEN, R. M. PENNER, *J. Phys. Chem.* **1996**, *100*, 20103.
- 29 R. SCHUSTER, V. KIRCHNER, X. H. XIA, A. M. BITTNER, G. ERTL, *Phys. Rev. Lett.* **1998**, *80*, 5599.
- 30 Y. ZHANG, S. MAUPAI, P. SCHMUKI, *Surf. Sci.* **2004**, *551*, L33.
- 31 R. T. PÖTZSCHKE, G. STAIKOV, W. J. LORENZ, W. WIESBECK, *J. Electrochem. Soc.* **1999**, *146*, 141.
- 32 R. ULLMANN, T. WILL, D. M. KOLB, *Chem. Phys. Lett.* **1993**, *209*, 238.
- 33 D. M. KOLB, R. ULLMANN, T. WILL, *Science* **1997**, *275*, 1097.
- 34 D. M. KOLB, R. ULLMANN, J. C. ZIEGLER, *Electrochim. Acta* **1998**, *43*, 2751.
- 35 D. M. KOLB, G. E. ENGELMANN, J. C. ZIEGLER, *Solid State Ionics* **2000**, *131*, 69.
- 36 J. C. ZIEGLER, Dissertation, Universität Ulm, **2000**.
- 37 J. C. ZIEGLER, G. E. ENGELMANN, D. M. KOLB, *Z. Phys. Chem.* **1999**, *208*, 151.
- 38 G. E. ENGELMANN, J. C. ZIEGLER, D. M. KOLB, *Surf. Sci. Lett.* **1998**, *401*, L420.
- 39 M. G. DEL POLPOLO, E. P. M. LEIVA, M. MARISCAL, W. SCHMICKLER, *Surf. Sci.* **2005**, *597*, 133.
- 40 D. M. KOLB, G. E. ENGELMANN, J. C. ZIEGLER, *Angew. Chem. Int. Ed.* **2000**, *39*, 1123.
- 41 M. HUGELMANN, W. SCHINDLER, *Surf. Sci. Lett.* **2003**, *541*, L643.
- 42 M. HUGELMANN, W. SCHINDLER, *J. Electrochem. Soc.* **2004**, *151*, E97.
- 43 C. H. HAMANN, W. VIELSTICH, *Elektrochemie I*, VCH, Weinheim, **1985**.
- 44 M. EIKERLING, J. MEIER, U. STIMMING, *Z. Phys. Chem.* **2003**, *217*, 395.
- 45 W. SCHINDLER, P. HUGELMANN, M. HUGELMANN, F. X. KÄRTNER, *J. Electroanal. Chem.* **2002**, *522*, 49.
- 46 P. VANYSEK, in *CRC Handbook of Chemistry and Physics*, D. R. LIDE, H. P. R. FREDERIKSE (Eds.), CRC Press, Boca Raton, FL, **1993**.
- 47 A. J. BARD, L. R. FAULKNER, *Electrochemical Methods*, 2nd edn., Wiley, Hoboken, NJ, **2001**.
- 48 Z.-X. XIE, D. M. KOLB, *J. Electroanal. Chem.* **2000**, *481*, 177.
- 49 S. G. GARCÍA, D. R. SALINAS, C. E. MAYER, W. J. LORENZ, G. STAIKOV, *Electrochim. Acta* **2003**, *48*, 1279.
- 50 A. J. MELMED, *J. Vac. Sci. Technol. B* **1991**, *9*, 601.
- 51 M. C. BAYKUL, *Mater. Sci. Eng. B* **2000**, *74*, 229.
- 52 M. KLEIN, G. SCHWITZGEBEL, *Rev. Sci. Instrum.* **1997**, *68*, 3099.
- 53 P. HUGELMANN, personal communication, **2000**.
- 54 W. SCHINDLER, in *Scanning Probe Techniques for Materials Characterization at Nanometer Scale*, (Proc. *Electrochem. Soc.* **2003**, 2003-27), W. SCHWARZACHER, G. ZANGARI (Eds.), The Electrochemical Society, Pennington, **2003**, p. 615.
- 55 S. MAUPAI, A. S. DAKKOURI, M. STRATMANN, P. SCHMUKI, *J. Electrochem. Soc.* **2003**, *150*, C111.
- 56 N. BREUER, U. STIMMING, R. VOGEL, *Electrochim. Acta* **1995**, *40*, 1401.
- 57 P. HUGELMANN, W. SCHINDLER, submitted.
- 58 R. GOMER, *Field Emission and Field Ionization*, Harvard University Press, Cambridge, MA, **1961**.
- 59 E. W. MÜLLER, T. T. TSONG, *Field Ion Microscopy*, Elsevier, New York, **1969**.
- 60 K. M. BOWKETT, D. A. SMITH, *Field-Ion-Microscopy*, Elsevier, Amsterdam, Netherlands, **1970**.
- 61 P. HUGELMANN, W. SCHINDLER, *J. Phys. Chem. B* **2005**, *109*, 6262.

7

Fabrication of Ordered Anodic Nanoporous Alumina Layers and their Application to Nanotechnology

Hidetaka Asoh and Sachiko Ono

7.1 Introduction

Nanomaterials not only have potential technological applications in various fields but also are of fundamental interest in that the properties of a material can change in this regime of transition between the bulk and atomic/molecular scales. Since the 1990s, there has been growing interest in the fabrication of nanostructures in many fields: surface/interface chemistry, electrochemistry, colloidal chemistry, polymer science, biochemistry, zeolite and clay chemistry, scanning probe microscopy (SPM), and others. Above all, nanomaterials with ordered pores of dimensions ranging from the submicrometer to nanometer range have generated considerable interest in both basic research and commercial applications because of the application of a host or a template to the fabrication of nanodevices [1–6].

Porous-type anodic oxide film, so-called anodic porous alumina, which is formed by the anodization of Al, is a typical self-ordered nanoporous material. It is often called a nanochannel or nanohole structure, depending on the dimensions of the porous-type anodic oxide film. This porous material has thus far been widely applied as a key material in the fabrication of several types of device [7–31], because of its potential applications based on a unique solid geometry and its so-called honeycomb structure on the nanometer scale, as shown in Fig. 7.1.

From the many morphological studies of anodic porous alumina, it is known that the anodic oxide film on Al consists of two regions: a thick outer region of porous-type oxide and a thin inner region of barrier-type oxide lying adjacent to the metal. In 1953, Keller, Hunter and Robinson reported on the structural features of porous alumina film determined by electron microscopy, and were the first to propose a geometrical cell model [32]. Moreover, they suggested that cell dimensions, such as pore and cell diameters and barrier layer thickness, depend primarily on formation voltage, and they increase linearly with voltage. Later, some researchers showed similar lines of evidence supporting their findings concerning the cell dimensions of the anodic films [33]. For the general background of the growth mechanism of anodic films prior to the 1990s, see Refs. [32–35].

We will now focus on the applied aspects of anodic porous alumina. Over the past several decades, although studies have been carried out on the protection or

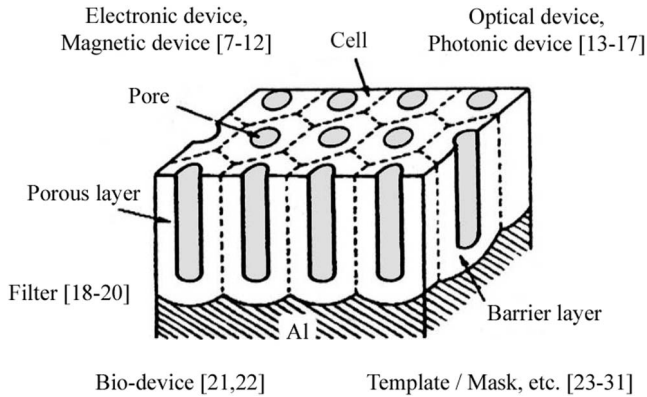


Figure 7.1. Application fields of anodic porous alumina.

design of Al surfaces owing to commercial application, little attention has been given to the regularity of the self-organized cell structure in anodic porous alumina. In 1995, Masuda and Fukuda reported for the first time that pore configurations with long-range ordering were formed in anodic porous alumina under optimized anodization conditions [36]. Since then, there has been renewed interest in anodic porous alumina, particularly in its applications in several types of device with the application of ordered nanostructures, as shown in Fig. 7.1. Therefore, many studies have been carried out on the improvement in the regularity of the pore arrangement, the control of the size and position of the pores, and the fabrication of sophisticated structures with two-dimensional (2D) or three-dimensional (3D) periodicity. At the same time, the application of anodic porous alumina to a host or template structure has been studied.

In this chapter, we describe state-of-the-art anodic porous alumina films. The period under review will be from approximately 1995 to the present day. Above all, we focus on our results on the fabrication of various nanomaterials, as described below. In addition, we discuss the possible applications of these nanoporous alumina layers.

7.2

Self-ordered Anodic Porous Alumina

7.2.1

Introduction

Commercially available anodic porous alumina, for example Anodisc [37], has insufficient pore arrangement, as usually found in anodic porous films formed on Al without extra pretexturing. Therefore, such porous alumina is not suitable for device application in which a strictly ordered array of pores without defects is required. Masuda and Fukuda first reported that the long-range ordering of the pore

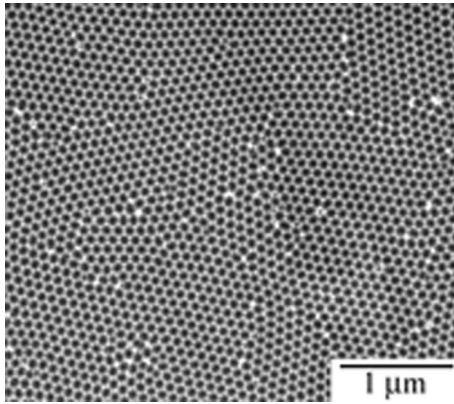


Figure 7.2. SEM image of typical self-ordered cell structure of anodic porous alumina obtained in oxalic acid at 40 V for 6 h at 20 °C. SEM observation was conducted at the oxide/substrate interface after removing the anodic film.

arrangement of anodic porous alumina could be obtained under optimized anodization conditions for oxalic acid [36]. In addition, they suggested that the ordered porous film formed by two-step anodization could be applicable to templates for the fabrication of novel optical devices. Then, they obtained self-ordered anodic porous alumina in three types of electrolyte at individually specified self-ordering voltages, i.e., sulfuric acid at 25 V [38], oxalic acid at 40 V [36] and phosphoric acid at 195 V [39], giving 63 nm, 100 nm and 500 nm pore intervals, respectively. They reported that the self-ordering of the pore arrangement proceeds through the rearrangement of the cell configuration, which changes gradually from a random configuration in the initial stage of anodization to an ordered configuration after the steady-state growth of the oxide layer. In particular, the self-ordering of the pore arrangement is strongly dependent on the formation voltage, which is specific for each electrolyte.

A typical scanning electron microscopy (SEM) image of the self-ordered cell structure of anodic porous alumina is shown in Fig. 7.2. The self-ordered cell arrangement shows a domain structure at the boundary at which imperfections in the arrangement accumulated. The size of the domain is dependent on cell size, and the number of cells existing in each domain is roughly the same as that in the case of self-ordered anodic porous alumina. Similar results have also been reported by other groups [40–45].

7.2.2

Controlling Factor of Self-ordering of Pore Arrangement in Anodic Porous Alumina

To expand the application field of anodic porous alumina, the fabrication of ordered porous alumina with arbitrary pore intervals or the clarification of the mechanism for the self-ordering of pore arrangement was required. Jessensky et al. [42] and Li et al. [43] suggested the correlation between the mechanical stress caused by

the volume expansion of oxide films and the self-ordering of pore arrangement. In accordance with their reports, the self-organized arrangement of neighboring pores in hexagonal arrays can be explained by the repulsive interaction between the pores. However, definite information was lacking to fully explain such an arrangement. To our knowledge, the mechanism of the self-ordering of pore arrangement has not yet been fully confirmed.

Ono and coworkers investigated the self-ordering behavior of anodic porous alumina formed in three major acid electrolytes (sulfuric acid, oxalic acid, and phosphoric acid) by focusing on current density during oxide growth and the effect of the ratio of pore diameter to cell diameter. To put it more concretely, the ratio is controlled by the electric field strength at the barrier layer of porous alumina during anodizing, as reported previously by Ono and coworkers [46–49]. Namely, the ratios of the cell diameter d_{cell} to the pore diameter d_{pore} obtained at different voltages in different electrolytes have a linear relationship with the log of current density. In accordance with the classical theory of ionic conduction at a high field strength for an anodic barrier film grown on various metals [50, 51], the film thickness of each metal is inversely proportional to the logarithm of the ionic current when each film is formed at the same voltage. Thus, it is indicated that the log of current density $\log i$ is proportional to the electric field strength E , i.e., the formation voltage/film thickness ratio at the barrier layer [52]. Therefore, we have tried to prove the correlation between electric field strength and self-ordering behavior. The confirmation of the controlling factor for the self-ordering of pore arrangement can be helpful for the fabrication of a new self-ordering film by applying the proposed mechanism.

7.2.3

Typical Current–Time Transients at Constant Voltages

Figure 7.3 shows current–time (I – t) transients during constant-voltage anodizing in sulfuric acid solution as a typical case [53]. This type of stable I – t curve is usu-

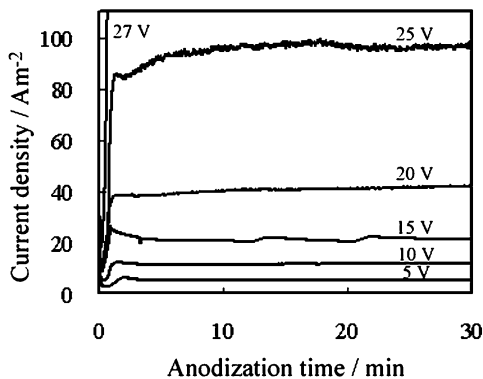


Figure 7.3. Current–time curves of anodizing in 0.3 mol dm^{-3} sulfuric acid at $20 \text{ }^\circ\text{C}$ in the voltage range from 5 to 27 V [53].

ally obtained when stable porous film growth occurs. With increasing formation voltage, the current density increased. When the formation voltage exceeded the self-ordering voltage, i.e., at 27 V, a high current accompanied by intense gas evolution over the entire surface was observed. In this unstable case, there was no film growth over the entire specimen surface. In the case of oxalic acid solution, a similar phenomenon of a high current appeared at 45 V. As revealed by the intense gas evolution, electronic current caused by the electric breakdown at the barrier layer is preferential to ionic current.

7.2.4

Change in the Porosity of Anodic Alumina with Increasing Formation Voltage

Figure 7.4 shows the changes in steady-state current density (a) and the porosity of anodic films (b) with formation voltage [53, 54]. Here, to estimate the porosity of anodic porous alumina, voltage–time curves were measured during the re-anodizing of the porous alumina specimens in a neutral solution, as described in detail in Ref. [53]. This method for porosity measurement is well established and is called the “pore-filling” technique [55, 56].

The current density increased exponentially for the three types of electrolyte when the voltage increased to a value close to the individual self-ordering volt-

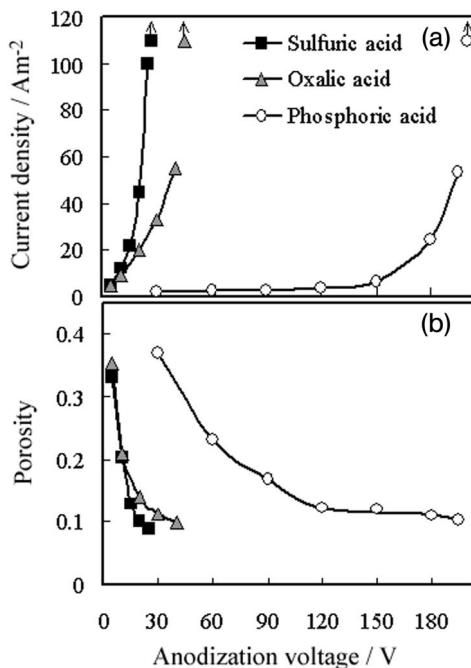


Figure 7.4. Changes in steady-state current density (a) and porosity (b) of anodic films with formation voltage measured in three electrolytes [53].

age, i.e., sulfuric acid 25 V, oxalic acid 40 V and phosphoric acid 195 V. The self-ordering voltage is strongly dependent on the pH of each electrolyte, namely, the oxide dissolution ability. At a voltage higher than the individually specified self-ordering voltage, an extremely high current was observed in the three electrolytes. Thus, it is apparent that self-ordering occurs at a voltage just under the critical voltage which induces an extremely high current and prevents uniform film growth. The high-field theory suggests that the log of current density has a linear relationship with electric field strength. Ono et al. reported previously that the theory was applicable to porous film growth and confirmed the linear relationship between the log of current density and the ratio of the pore diameter d_{pore} to the cell diameter d_{cell} [49]. This suggests that the $d_{\text{pore}}/d_{\text{cell}}$ ratio is controlled by the electric field strength E at the barrier layer and that the ratio decreases with increasing E . Therefore, it is assumed that self-ordering proceeds in the film with a low $d_{\text{pore}}/d_{\text{cell}}$ ratio formed under a high electric field. As shown in Fig. 7.4(b), the porosity of each anodic film decreased markedly and converged to approximately 0.1 (regardless of the electrolyte), which corresponded to a $d_{\text{pore}}/d_{\text{cell}}$ ratio of approximately 0.3, when the voltage approached the individual self-ordering voltage accompanying the exponential current increase.

For comparison of the three types of electrolyte, formation voltage was normalized to self-ordering voltage. As shown in Fig. 7.5, porosity was plotted against the ratio of the formation voltage V_f to the self-ordering voltage V_s . The three lines corresponding to the three different electrolytes decreased in almost the same manner, regardless of electrolyte type and V_f . The minimum porosity of the films obtained just under the critical voltage of the extremely high current appears to be 0.1. This indicates an important fact: that self-ordering can be attained when, with increasing electric field strength, the $d_{\text{pore}}/d_{\text{cell}}$ ratio approaches 0.3, regardless of the electrolyte type and V_f itself. Thus, the mechanism of self-ordering is assumed to be closely related to the high electric field strength at the barrier layer during anodic film growth, rather than to the individual V_s itself.

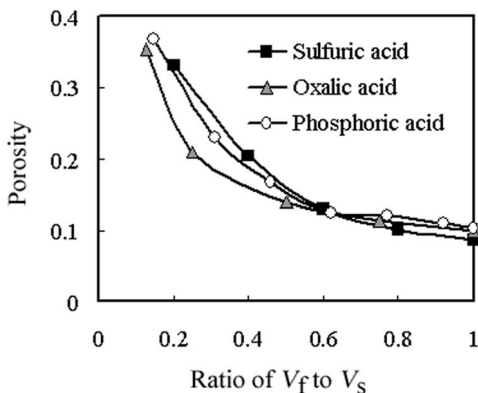


Figure 7.5. Porosity plotted as function of ratio of formation voltage V_f to self-ordering voltage V_s [53].

In 2002, Nielsch et al. reported that the three types of self-ordered porous alumina all gave a porosity of 0.1 [57]. They explained that the porosity of approximately 0.1, which was produced as a balance of the formation and dissolution of anodic oxide, was morphologically most stable from the viewpoint of mechanical stress. They also claimed that 0.1 was a transitional and optimum porosity value for self-ordering. However, we have shown clearly that the porosity value of 0.1 for porous alumina was the optimum and also the minimum value.

7.2.5

Typical Self-ordering Behavior

When the anodizing voltage was three quarters of the established self-ordering voltage, i.e., 30 V in oxalic acid, the cell size was not uniform, as clearly shown in Fig. 7.6(a). This implies that irregular film growth proceeds under a low current density, i.e., a low electric field. Homogeneity of cell size could be attained and domains of self-ordered cell arrays in the same direction appeared when the anodizing voltage was increased to 40 V, just under the critical voltage of the extremely high current (Fig. 7.6(b)). To verify the effects of formation voltage and film thick-

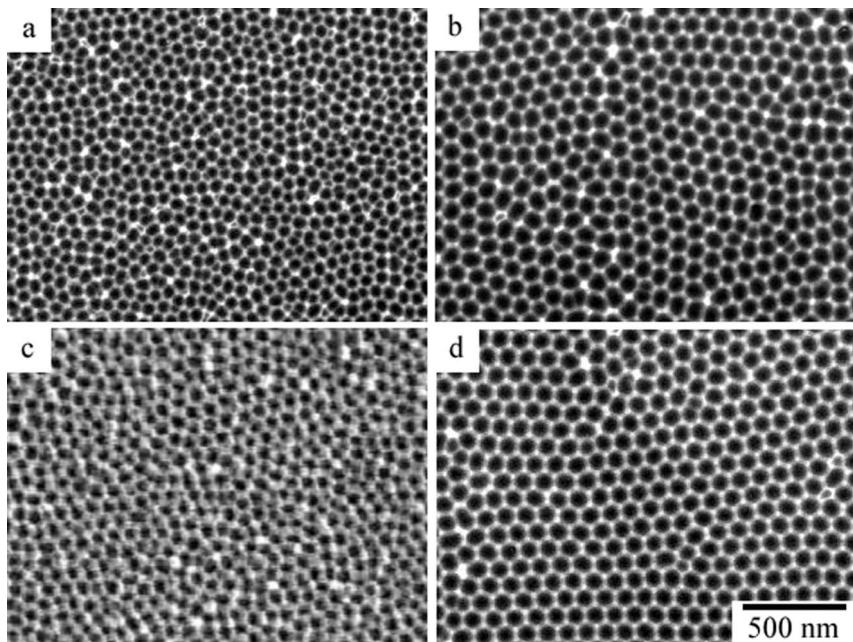


Figure 7.6. SEM images of metal/oxide interface after removal of porous alumina formed in 0.3 mol dm^{-3} oxalic acid at 20°C showing the dependence of cell arrangement on formation voltage and anodizing time. (a) 30 V for 1 h, (b) 40 V for 1 h, (c) 30 V for 1 h 40 min, and (d) 40 V for 6 h [53].

ness on the self-ordering, an anodic film was formed at 30 V for a corresponding time to consume electricity equivalent to that consumed at 40 V for 1 h, namely, 1 h 40 min. As shown in Fig. 7.6(c), the cell homogeneity of the anodic film formed at 30 V for prolonged time was somewhat improved, but it was apparently inferior to that associated with 40 V even though the film thicknesses were similar. Thus, the necessity of a high current density during anodization for the self-ordering of cell arrangement besides film thickness was clarified. The size of the domain continuously increased with increasing anodizing time up to 6 h as shown in Fig. 7.6(d), suggesting the need for long-term electrolysis to organize the cell arrangement and to form the resulting thick porous layer. Similar self-ordering results were also observed in the films formed in sulfuric acid solution and phosphoric acid solution [53].

7.2.6

High-current-density/High-electric-field Anodization

The self-ordering of the pore arrangement of anodic porous alumina can be achieved at the maximum voltage required to induce high-current-density anodization while preventing “burning”, that is, an extremely high current flow concentrated at local points leading to local film thickening or electric breakdown over the entire surface accompanied by vigorous gas evolution [58]. Such a maximum voltage was identical to the previously established self-ordering voltage.

A comparison between the $I-t$ curve measured during burning and that during stable anodizing at 195 V in phosphoric acid solution is shown in Fig. 7.7. With a rapid current increase, local thickening of the film was detected. Figure 7.8(a) shows an SEM image of a burnt area indicating a protrusion of thickened anodic

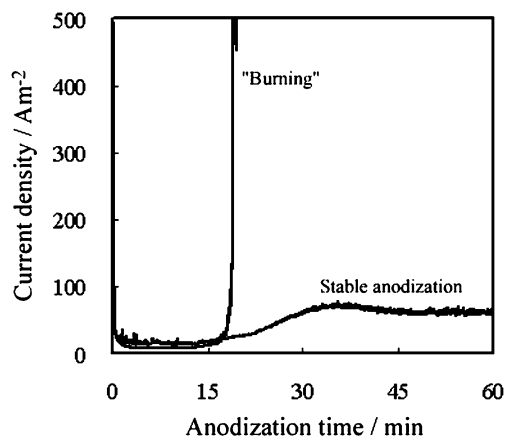


Figure 7.7. Comparison between current–time curve measured at burning and that at stable anodization at 195 V in 0.2 mol dm^{-3} phosphoric acid at $0\text{--}5 \text{ }^\circ\text{C}$ [53].

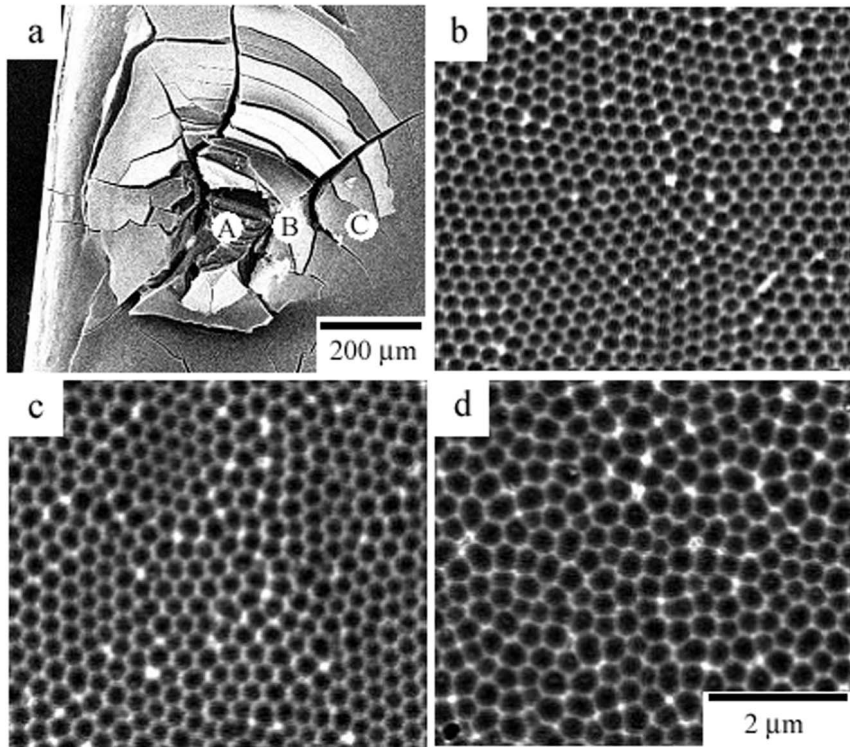


Figure 7.8. (a) SEM image of burnt protrusion of thickened anodic film with large number of cracks. The protrusion is divided into three regions: (A) center, (B) intermediate and (C) outer. (b)–(d) SEM images of substrate surfaces of the three regions corresponding to A, B and C in (a) after removal of anodic films [53].

film with a large number of cracks. The protrusion is divided into three regions: (A) center, (B) intermediate and (C) outer regions. The substrate surface images of the corresponding regions after the removal of the anodic films are also shown in Fig. 7.8(b)–(d). Apparently, the regularity of the cell arrangement is higher in the center region than that in the outer region. Because the current density seems to be higher at the center, the regularity of cell arrangement could be further improved. Thus, it is suggested again that the condition of high current density, i.e., a high electric field, is the most important factor that determines the self-ordering of the pore arrangement. In addition, the cell size is smaller when the regularity of the cell arrangement is higher. Compared with the ratio of cell size to applied voltage of 2.5 (nm/V) observed for the standard anodic porous films [47, 59], the ratios obtained here are all low. Therefore, it can be said that cell size is affected by the electric field strength E and decreases with increasing E at the same voltage. This finding is similar to that observed for barrier layer thickness [52]. As described in

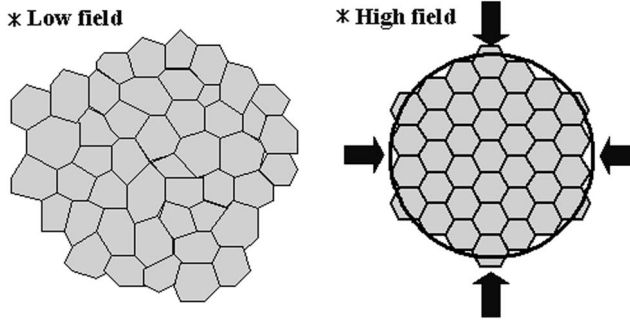


Figure 7.9. Schematic representation of self-organization of cell arrangement at high current density, i.e., high electric field [60].

detail in Ref. [58], the cell size at the exact center spot of the protruded area made by burning, where the high current density was most concentrated, was extremely small. This implies the importance of current density in the self-ordering of porous alumina, regardless of the specific self-ordering voltage itself. Thus, it is suggested that the condition inducing film growth under a high current density, namely, a high electric field strength, is the key factor determining the self-ordering of porous alumina rather than the self-ordering voltage itself. Schematic representation of self-organization under a high electric field is shown in Fig. 7.9.

7.2.7

New Self-ordering Conditions

With the above background, we have studied the self-ordering conditions of anodic porous alumina grown in solutions of various organic acids such as citric acid [53], malonic acid [60] and tartaric acid [60], and confirmed new self-ordering conditions in such organic acid electrolytes using the previously suggested mechanism of anodization at a barrier layer. In these acid electrolytes, a relatively large cell is available upon application of a high anodization voltage due to their low acidity. These organic acids are all carboxylic acids, as is oxalic acid.

In 2004, Shingubara et al. [61] reported on the formation of self-ordering porous anodic alumina in a mixture of sulfuric acid and oxalic acid at a voltage between 25 and 40 V. However, little information is available on porous alumina formed at voltages between 40 and 195 V, and higher than 200 V. Thus, we advanced our preliminary work while considering high-electric-field anodization conditions and found newly self-ordering conditions in concentrated phosphoric acid solutions in the voltage range from 160 to 195 V [62] and in a mixture of sulfuric acid and malonic acid solutions in the voltage range from 25 to 195 V [63]. The details of these anodization conditions will be published elsewhere. In 2005, Chu et al. reported that self-ordered porous alumina could be obtained in sulfuric acid solutions under a high electric field of 40–70 V and 1600–2000 A m⁻², which is much higher than

* JES: *J. Electrochem. Soc.*, ESL: *Electrochem. Solid-State Lett.*,
AM: *Adv. Mater.*, EA: *Electrochimica Acta*, JJAP: *Jpn. J. Appl. Phys.*

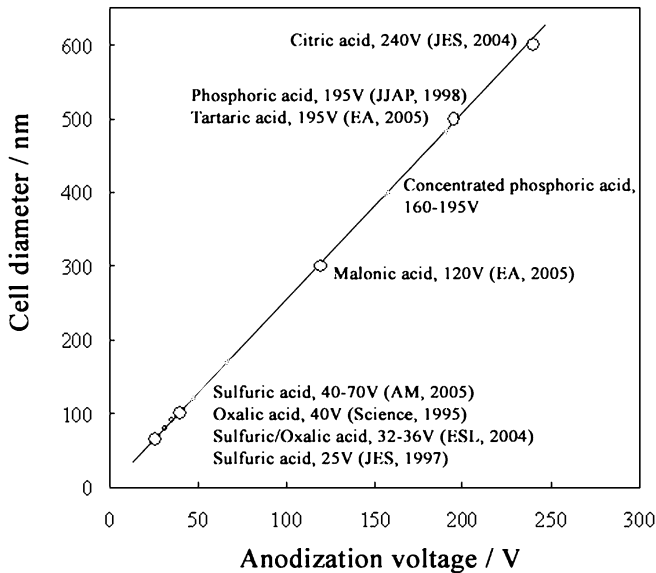


Figure 7.10. Summary of results of self-ordering voltages and corresponding cell diameters reported to date.

that obtained by ordinary anodization (<27 V, <200 A m⁻²) [64]. This report is consistent with our hypothesis, in which a high current density, namely, a high electric field strength, is the key controlling factor for the self-ordering of anodic porous alumina.

The self-ordering voltages reported to date and the corresponding cell diameters are summarized in Fig. 7.10. In addition to the conventional self-ordering conditions formed in sulfuric, oxalic and phosphoric acid solutions, new self-ordering conditions that have been realized recently are shown. Further research on the self-ordering of anodic porous alumina would clarify the association of the mechanism for the self-ordering of pore arrangement and the anodization at a high electric field.

7.3

Ideally Ordered Anodic Porous Alumina

7.3.1

Two-step Anodization

The defect-free area of naturally occurring ordering is limited to a size of several μm^2 and appears in a domain structure where the defects are concentrated on the

boundary between domains. Therefore, it is difficult to achieve an ordered pore array of a single domain because the domains do not combine regularly with each other in the self-ordering process. Two-step anodization proposed by Masuda et al. is a promising technique for preparing an ideally ordered porous structure with straight channels over a large area [36, 132]. Since 1995, this technique has been commonly used to fabricate various nanomaterials. In this process, first anodization is carried out at a constant voltage for a long period of more than 10 h. The regularity of the pore arrangement can be improved by longer anodization [36]. After removal of the alumina layer, an array of shallow concave features is obtained on the Al substrate. Then, a second anodization is performed for a short period under the same conditions as for the first anodization. As a result, each concave area can act as an initiation site for pore generation and guide the growth of channels. Namely, a porous alumina membrane with a straight channel can be obtained easily.

However, there has been no study that has tried to clarify the pore nucleation and growth of porous alumina in the case of two-step anodization by detailed observation. Thus we examined the pore growth mechanism more closely by transmission electron microscopy (TEM). Figure 7.11 shows the TEM images of the stripped anodic film formed at different stages. The first anodization was carried out in 0.3 mol dm^{-3} oxalic acid at 40 V for 6 h. After removal of the alumina layer, the specimens were re-anodized at each stage. In the initial stage of film growth, which corresponds to the decreasing part of the $I-t$ transient, the locally thicker barrier film develops above the edge of the concave area formed on Al (Fig. 7.11(a)). With further anodization, plural fine pores develop at the center of the concave area (Fig. 7.11(b)). In the steady state, a close-packed array of hexagonal cells, each containing a straight pore at the center of hexagonal cells, was observed (Fig. 7.11(c)). These results indicate that the development of the ordered pores was controlled by the pattern of the shallow concave areas on the Al substrate, and an almost ideally ordered porous structure can be obtained without special texturing, such as standard lithography. A basic principle of pore nucleation and growth of

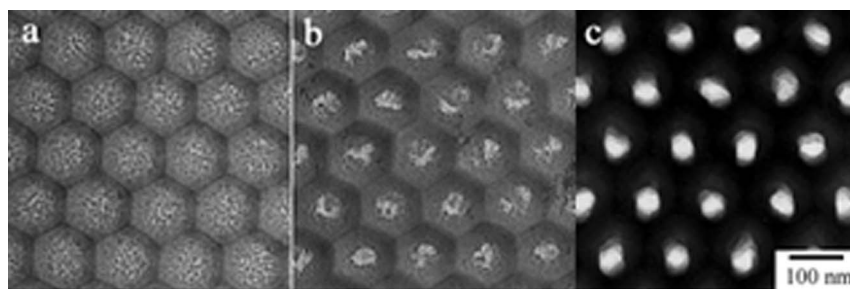


Figure 7.11. TEM images of stripped films formed in 0.3 mol dm^{-3} oxalic acid solution at 30°C at 40 V for time t : (a) $t = 3 \text{ s}$, (b) $t = 17 \text{ s}$, and (c) $t = 58 \text{ s}$. First anodization was conducted under the same conditions for 6 h.

anodic porous alumina in the initial stage of anodization is similar to the case of the imprinting process we describe below.

7.3.2

Fabrication of Ideally Ordered Anodic Porous Alumina

Concerning the fabrication of a single-domain pore configuration in a 2D plane, in 1997 Masuda et al. [65] and then in 2001 Asoh and coworkers [66, 67] reported that ideally ordered anodic porous alumina could be obtained by employing an imprinting process for an Al substrate. In 2002, Masuda et al. fabricated a similar nanopore array structure in anodic porous alumina based on nanoindentation using SPM [68]. Several groups have also reported similar results concerning the fabrication of a single-domain configuration of highly ordered pores using an imprinting process [69], electron-beam lithography [70], the focused ion beam technique [71, 72], the grating embossing technique [73], holographic lithography [74], and SPM lithography [75]. Recently, the fabrication of highly ordered anodic alumina using a combination process involving colloidal crystal templating and subsequent anodization has also been reported [76, 77].

In these fabrication techniques, the shallow concave areas formed on an Al substrate can serve as initiation sites for pore nucleation, thereby guiding the growth of the porous structure. As for the background of the growth mechanism of ideally ordered anodic porous alumina with hexagonal cells, see Refs. [65–67]. Here, we describe the results for anodic porous alumina with square cells formed by the imprinting process.

7.3.3

Square Cell Arrangement

Tiling of a 2D plane with equilateral polygons is limited to three cases: tiling with regular triangles, with squares, and with regular hexagons, as shown in Fig. 7.12. In anodic porous alumina, a cell pattern can be generated by a polygon, the boundary of which is the perpendicular bisector of two adjacent pores [78]. In the case of self-ordered anodic porous alumina, Voronoi cells are hexagonal in shape on average, in a triangular lattice, that is, they have a hexagonal close-packed arrangement. This is because the triangular lattice is the most probable to achieve the closest packing of uniformly sized cylindrical cells and has the most stable configuration. However, it was expected that the shape of cells could be controlled as other than ordinary hexagonal cells by changing the initiation patterns based on the tiling through the close packing of equilateral cells.

In 2001, Masuda et al. reported the fabrication of ideally ordered anodic porous alumina with square or triangular cells based on the 2D tiling theory [79]. The most important concept of this approach is that the arrangement of nuclei (shallow concave areas) in a 2D plane determines the shape of the obtained cells as a result of the closely packed tiling. The obtained new types of porous structure with square and triangular openings, which never occur in nature, have consid-

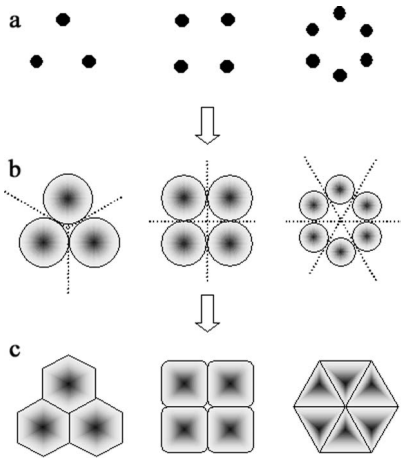


Figure 7.12. Cell development in anodic porous alumina based on Voronoi tessellation. (a) initiation sites, (b) growth of cells, and (c) three types of ideally ordered cell configuration.

erable potential for a variety of applications as a template for the fabrication of nanostructures.

At the same time, we have investigated the pore nucleation and growth of anodic porous alumina with hexagonal or square cells by observing the film structure in the initial stage of anodization. In such a study, it was confirmed that the initiation sites of the square lattice pattern as shown in Fig. 7.13, which is different from the

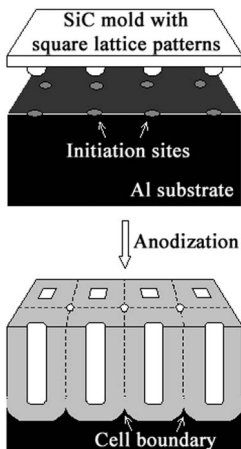


Figure 7.13. Schematic of fabrication process for anodic porous alumina with square cells [81].

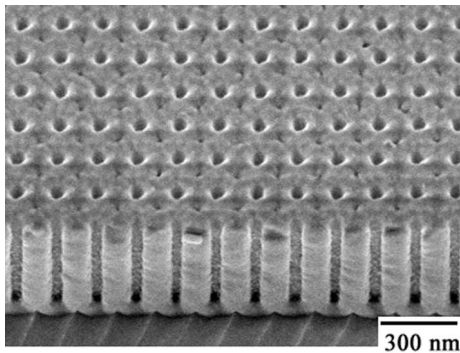


Figure 7.14. Cross-sectional view of ordered anodic porous alumina with square cells. Anodization was conducted in 0.3 mol dm^{-3} oxalic acid solution at 30°C at 60 V for 60 s [81].

normal hexagonal cell arrangement, markedly control the growth process of a porous structure [80, 81].

7.3.4

Detailed Observation of Square Cells

Figure 7.14 shows a SEM image of a cross-sectional view of the pore array structure with a square lattice pattern. The anodized specimen was bent into a V-shape, producing cracks in the oxide film. The growth of straight parallel channels perpendicular to the substrate can be observed only in the pre-textured area. In addition, it can be confirmed from the surface morphology that the surroundings of each hole were thick and ordered small pores were located at the center of the four nearest holes, that is, the fourfold point of the cell junction. These small pores were formed to compensate the closest packing of a two-dimensional space by circular cells in the initial stage of film growth. This compensation is similar to previous results [69, 82, 83].

Figure 7.15 shows the TEM images of the stripped anodic film formed at different stages. In the initial stage of film growth, which corresponds to the decreasing part of the $I-t$ transient, a locally thicker barrier film develops above the edge of the concave area formed on Al as well as under the concave area (Fig. 7.15(a)). With further anodization, a nearly square cell develops around the initiation site (Fig. 7.15(b) and (c)). Each initiation site was considered to be the center of cell growth, with growth occurring radially at almost equal rates from all sites. When the contact of two adjacent cells was accomplished, the expansion of cells was stopped and boundary lines were formed. Finally, ideal square cells were established by the time that the current reached the final steady state. A steady-state cell structure is formed by a close-packed array of square cells, each containing a pore with a square opening at the center (Fig. 7.15(d)). The shape of the pores changed from circular to square during anodization without additional etching, and was different

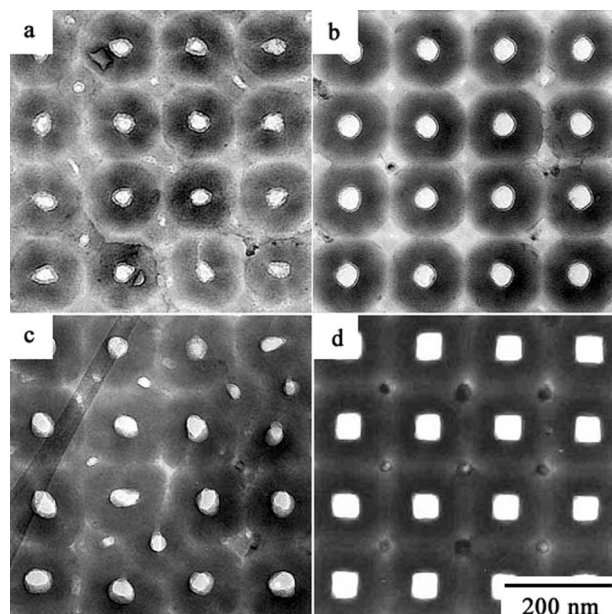


Figure 7.15. TEM images of stripped films formed in 0.3 mol dm^{-3} oxalic acid solution at 30°C at 60 V for time t : (a) $t = 2 \text{ s}$, (b) $t = 6 \text{ s}$, (c) $t = 17 \text{ s}$, and (d) $t = 30 \text{ s}$ [80].

from those observed at the top surface of the films at the corresponding stage. This indicates that the shape of pores near the cell base is square, while the shape of those near the outer surface is circular.

A TEM image of an ultramicrotomed cross section showed voids or incorporation of unoxidized Al into the oxide film at the fourfold point of the cell junction [81]. The height of the protrusions of the Al substrate at the cell junction was considerably larger than that of protrusions formed in naturally occurring anodic porous alumina with hexagonal cells [41, 84, 85]. These specific features were thought to be caused by the inhomogeneous distribution of current at the square pore base. In addition, this inhomogeneous distribution of current at the square pore base causes not only the incorporation of unoxidized Al into the oxide film but also the generation of voids, accompanied by the breakdown of the barrier layer or gas evolution in protrusions of the Al substrate [86–88]. The formation mechanism of anodic porous alumina with a square cell structure will also give helpful information on self-ordering in naturally occurring anodic porous alumina with uniformly sized hexagonal cells. In addition to the fundamental study of pore nucleation and cell structure growth, there is interest in applications in novel devices. Namely, shape- and size-controlled anodic porous alumina is a useful material as a template for the fabrication of designed structures on the nanometer scale. For example, the synthesis of diamond cylinders or carbon nanotubes with a triangular

or square cross section using a porous alumina template has been demonstrated by Yanagishita et al. [89, 90].

7.4

Anodic Porous Alumina with 3D Periodicity

7.4.1

Modulation of Channel Structure

Several studies have been carried out on the modulation of the channel structure in the direction of film thickness. For the preparation of such structures, the periodic modulation of the channel diameter in the direction of film thickness, which can be achieved by varying the formation voltage during anodization, is a promising process [34, 91]. In fact, the synthesis of Y-junction carbon nanotubes using a porous alumina template has been demonstrated by J. Li et al. [92]. We have also proposed the fabrication process for the 3D designed anodic porous alumina having different pore diameters in the direction of pore depth using heat treatment, subsequent dissolution treatment and multi-anodization [93]. Against this background, a new fabrication process for porous alumina with a more ordered 2D cell configuration and more sophisticated 3D geometries has been thought to be necessary for the achievement of various functional applications.

7.4.2

2D/3D Composite Porous Alumina

3D porous materials that are formed using spherical colloidal particles as templates have attracted considerable attention in recent years because of their potential for applications in unique optical devices such as photonic crystals [6, 94–99]. Using an inverse opal structure, which could be produced only in the voids between the particles, it has been possible to fabricate various types of porous material using different matrix materials. One of the notable features of colloidal crystal templating is its simplicity in comparison with conventional lithography techniques.

In 2005, we proposed a novel approach to the fabrication of the 2D/3D composite porous alumina structure, which is based on a combination of a templating process of colloidal crystals and subsequent multistep anodization [100]. Novel composite porous materials with controlled morphologies may overcome some of the limitations of the 2D bulk channel structure. An important advantage of the process proposed here is that it is possible to connect the structures with different dimensional characteristics by applying additional anodization. Figure 7.16 shows a schematic of the templating process and typical 2D/3D composite porous alumina structures. For further details of the experimental process, see Ref. [100]. The anodized specimens were bent into a V-shape, producing cracks in the oxide film. These composite structures consisted of an outer inverse opal structure and

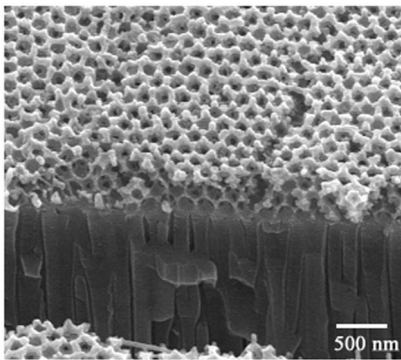
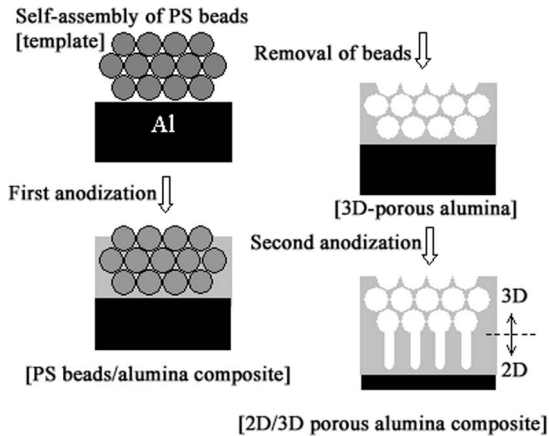


Figure 7.16. Schematic of templating process and cross-sectional SEM image of anodized Al with 2D/3D composite structures. The PS bead used as template was 204 nm in diameter [100].

an inner parallel channel array structure formed on an Al substrate. On the basis of this image, it was confirmed that the 2D channel array structure could be produced only underneath the outer 3D porous structure. As shown in Fig. 7.16, polystyrene (PS) beads of 204 nm diameter were used as templates. The periodicity of the pores of the outer inverse opal alumina was almost in agreement with that of the underlying straight parallel channels on which anodization was conducted under a constant voltage of 80 V to adjust the channel interval to approximately 200 nm. Therefore, the growth of straight parallel channels perpendicular to the substrate could be observed underneath each hollow space.

Figure 7.17 demonstrates the ordered pore configuration with a 200 nm interval in the inner 2D porous alumina. To clearly show the arrangement of 2D pore arrays, the outer 3D porous alumina was removed prior to additional anodization. This result indicates that the hemispherical scalloped pattern of the bottom layer in inverse opal alumina can initiate pore development and can guide the growth

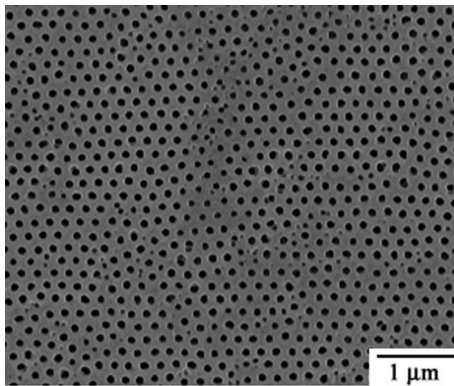


Figure 7.17. SEM image of surface of inner 2D channel array structure. To facilitate the observation, pore-widening treatment was carried out in 5 wt% phosphoric acid at 30 °C for 60 min [100].

of the channel in the film thickness direction, as discussed in the previous section. This fabrication process using the scalloped pattern formed on an Al substrate is somewhat similar to that used in our previous work, which involves the imprinting process using molds [65–67]. However, this proposed method has an advantage in that it can be used for large-area patterning using a simple electrochemical process with a high throughput and a low cost without special tools, including molds for imprinting.

7.5

Application of Nanoporous Alumina to a Mask for Fabrication of Nanostructures

7.5.1

Nanopatterning: Conventional Lithography vs. Natural Lithography

One of the most significant issues in the development of nanotechnology in both basic research and commercial applications is the fabrication of semiconductor materials with ordered nanostructures, because of their potential applications in various devices, such as quantum electronic devices, photoelectronic devices, functional electrodes, bioreactors, and data storage devices. The techniques commonly used in fabricating these functional devices with nanometer dimensions are conventional lithographic technologies: top-down patterning techniques using optical, electron, or X-ray beams. Although these techniques have many advantages, they are not suited for large-scale patterning with feature sizes of sub-100 nm due to the limit of their resolution and low throughput. Therefore, a novel patterning process that can be used easily and efficiently is required. Recently, many nanolithographic methods have been developed to overcome these drawbacks. For example, nanoimprint lithography [101] and SPM lithography [102–104] are typical methods

which can be used to fabricate an ordered pattern with a high resolution in the nanometer range. However, these processes have still not been popularized as general methods because of the necessity for special tools, including molds for imprinting or SPM equipment. For further details of new techniques for nanopatterning, see the review Ref. [105].

In terms of simple and inexpensive methods, natural lithography [106], which is based on a self-organization process, has recently attracted considerable attention as a key fabrication method owing to its relative simplicity and low cost. Several studies have been reported on the nanopatterning of semiconductors using self-assembled colloidal particles [107–111] or self-ordered anodic porous alumina. In particular, anodic porous alumina has attracted considerable interest as a promising candidate for a host or template structure to fabricate various nanodevices. Moreover, the formation of anodic porous alumina using an evaporated or sputtered film of Al on various substrates has been extensively studied, because the resulting porous structure can be directly used as a host or a template to fabricate nanodevices [112–130].

7.5.2

Anodization of Al on a Si Substrate

In recent years, to apply anodic porous alumina to the template structure for the patterning of metal and semiconductor surfaces, the formation of anodic porous alumina using evaporated or sputtered films of Al on various substrates including semiconductor [112–128] and conductive oxide materials (e.g., indium tin oxide ITO) [129, 130] has been widely studied. In this process, the resulting porous structure can be used directly as a host or a template to fabricate nanoscale devices, including its use as an etch mask to transfer a closely packed hexagonal array of pores into various substrates. However, detailed observation of the structural transformation at the $\text{Al}_2\text{O}_3/\text{Al}/$ underlying substrate interface has not been carried out thus far.

To clarify the structural transformation of interface structures during anodization, we studied the anodization behavior of Al films sputtered on a Si substrate using oxalic acid solution, a commonly used solution for anodization [131]. Figure 7.18 shows the current density transient for anodizing the Al film sputtered on the Si substrate. During the first constant-current stage up to point a, the anodization of Al on the Si substrate was in progress. Then the current decreased suddenly and a visible change in the color of the $\text{Al}_2\text{O}_3/\text{Al}/\text{Si}$ structure was observed (point b). This period implies that the Al film sputtered on the Si substrate was consumed gradually at the Si surface and changed to a transparent oxide film. When the Al film was consumed completely, the current reached a minimum value (point c). Further anodization results in a subsequent sharp increase in current (point d), implying the localized anodization of the underlying Si substrate. After showing the first sharp peak of current, a second broad peak was observed. This indicates that the Si substrate was anodized over the entire area of the specimen following the destruction of the porous film by extensive gas evolution.

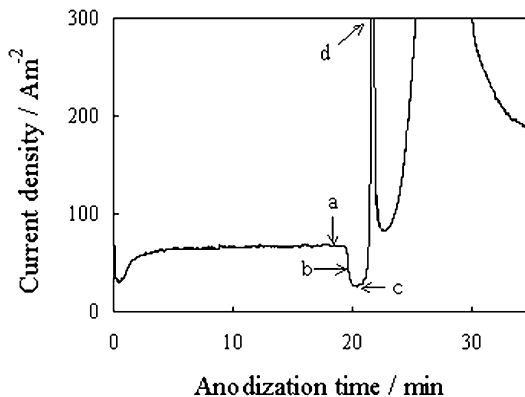


Figure 7.18. Current–time curve for anodization of aluminum film sputtered on Si in 0.3 mol dm^{-3} oxalic acid at 20°C at 40 V. Arrows mark the average anodization times for observation of images in Fig. 7.19(a)–(d) [131].

The transformation of the nanostructure of anodic porous alumina grown on the Si substrate was comparable to the current transient during anodic alumina film formation. After removing the anodic alumina film, the geometric pattern that remained on the Si substrate was observed by SEM, as shown in Fig. 7.19(a)–(d). When the Al film remained on the Si substrate, the self-ordered scalloped pattern of the Al film was confirmed, as shown in Fig. 7.19(a). This pattern was in good agreement with the hemispherical barrier layer of the porous film. The interval between the scallops, that is, the size of the cells, was approximately 100 nm, corresponding to a formation voltage of 40 V. As the barrier layer of the porous film reached the Si surface, isolated Al dots were observed at the cell junction, as shown in Fig. 7.19(b). With further anodization, the Al film was consumed completely as observed in the flat Si substrate, as shown in Fig. 7.19(c). With overanodization, convex features, which were suggested to be silicon oxide, were observed at the center of each cell, as shown in Fig. 7.19(d). These convex features were arranged hexagonally over the entire area of the specimen corresponding to the cell configuration of anodic porous alumina.

These results indicate that porous alumina directly formed on a Si substrate can act as a mask for the localized anodization of the underlying Si substrate without additional through-hole treatment of the barrier layer, namely, silicon oxide can be produced only in the conductive area between the barrier layer of a porous film and a Si surface. Although several studies have been carried out on pattern transfer using through-hole alumina as a mask for dry processes (e.g., reactive ion etching [115, 116], ion milling [118], vacuum evaporation [118, 132], reactive beam etching [133], and fast atom beam etching [134]), there have been few studies that attempted to apply the as-anodized oxide film as a mask for pattern transfer into various substrates without additional through-hole treatment. Recently, Chen et al.

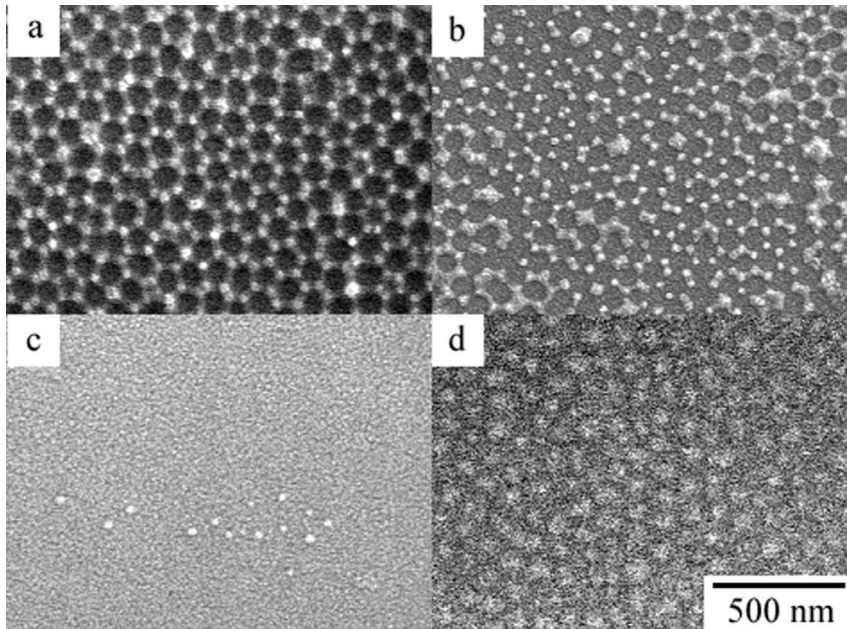


Figure 7.19. SEM images of Si surface after removal of anodic porous alumina, corresponding to marked points in Fig. 7.18 [131].

have reported that nanodot arrays of titanium oxide can be prepared from TiN/Al films on a Si substrate by the localized anodization of a TiN layer using anodic alumina as a mask [135, 136]. Their result indicates that the formation of oxide nanodot arrays, which are formed using alumina as a mask for the localized anodization of the underlying substrate, can be achieved even in the case of using an underlying layer other than a Si substrate. In brief, the localized anodization of the underlying substrate through the barrier layer of anodic alumina can be regarded as a flexible and reproducible patterning technique.

In addition, the formation mechanism of the silicon oxide pattern on the Si substrate based on localized anodization is similar to that induced by lithography techniques using a conductive probe in SPM [137–140]. In the case of SPM lithography using anodization, when a negative bias is applied to the tip, a local anodization process is carried out on the Si surface under moist air between the tip and the sample. As a result, the growth of silicon oxide can be observed at the locally scanned area. Although there are many advantages of using SPM lithography, improvements in the lithographic speed and area over which fabrication can be performed are necessary for the realization of industrial applications. On the other hand, our proposed method based on the self-organization process has the advantage of possible use for large-area patterning in one step. In principle, there is no limitation to the patterned area, because it is unnecessary to use a special operating system such as a piezoelectric scanner.

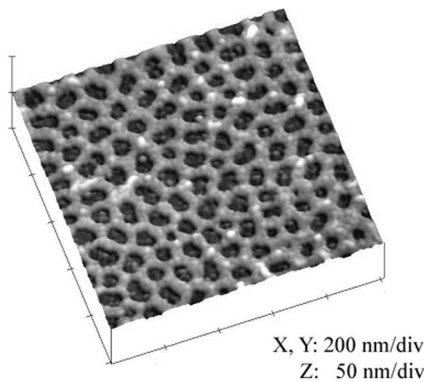


Figure 7.20. AFM image of Si nanohole array fabricated by selective removal of silicon oxide in HF [142].

7.5.3

Natural Lithography of Si Surfaces Using Anodic Porous Alumina as a Mask

To examine the pattern transfer of anodic porous alumina onto the Si substrate, the anodized specimen was immersed in hydrofluoric acid (HF) solution to remove silicon oxide at the center of each cell. With chemical etching in HF solution, the selective removal of silicon oxide from the Si substrate was easily realized by utilizing the difference in chemical reactivity between Si and silicon oxide for HF treatment [131]. After removing silicon oxide by wet chemical etching in 47 wt% HF for 90 s, the shallow concave pattern of the Si substrate was observed by atomic force microscopy (AFM), as shown in Fig. 7.20. The anodization was stopped immediately at the minimum current, point c in Fig. 7.18. The diameter and depth of the concave features were 60–80 nm and ~10 nm, respectively. The arrangement and shape of this concave pattern were similar to those of the porous pattern of the upper anodic porous alumina. Namely, the transfer of the nanoporous pattern of anodic alumina into the Si substrate could be achieved by removing silicon oxide, which was produced by the anodic oxidation of the local part of the Si substrate underneath the barrier layer corresponding to the pore base, as shown schematically in Fig. 7.21.

The periodicity of hole arrays in a Si substrate is basically determined by the pore interval of the upper anodic porous alumina, which is known to be strongly dependent on anodization conditions, such as the types of electrolyte and formation voltage. Namely, the dimensions of the resultant nanopattern can be adjusted easily by controlling anodization conditions. In fact, nanohole arrays with a 60 nm hole periodicity were fabricated on a Si substrate by anodizing an aluminum film in sulfuric acid at 25 V and subsequent chemical etching in HF. More detailed results concerning the reduction of the dimensions of the nanopattern are reported in Ref. [141].

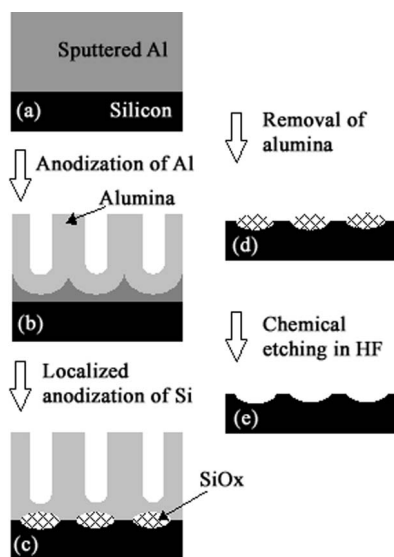


Figure 7.21. Schematic of patterning process by localized anodization of Si: (a) aluminum film sputtered on Si substrate; (b), (c) transformation of anodic porous alumina grown on Si substrate during anodization; (d) silicon oxide nanodot arrays formed after removal of alumina film; (e) nanohole arrays formed on Si after chemical etching in HF [141].

On the basis of the presented patterning mechanism, various modifications and structuring of a Si substrate can be achieved by chemical [142] or electrochemical etching [143] and electrochemical deposition of metals [144]. The details of the procedure have been published elsewhere [142–144].

7.6 Summary

In this chapter we have focused our interest mainly on the fabrication of ordered anodic nanoporous alumina and its application. As already mentioned above, the most characteristic feature of this material has been emphasized with the extremely unique geometrical structure formed by self-organization of each cell. The regularity and periodicity of pore arrays in anodic porous alumina is basically determined by anodization conditions, such as the type of electrolyte and anodization voltage. Therefore, the clarification of the mechanism for self-ordering of pore arrangement will continue to expand the field of application of anodic porous alumina. In addition, some of the recent applications discussed herein have an advantage in that they can be used for large-area patterning using a simple electro-

chemical process with a high throughput and low cost, that cannot be achieved with conventional lithographic techniques.

As regards new types of porous oxide film other than porous alumina, some groups have recently reported that a variety of metals such as Ti [145, 146], W [147, 148], Sn [149], Zr [150, 151], Nb [152], Hf [153], and Ta [154], have been found to form self-organized porous structures under optimized anodization conditions. We are now studying the formation of porous niobium oxide, porous tantalum oxide and porous tin oxide with a thick porous layer on the micrometer scale, with the expectation that these oxide films can be used for catalysts and chemical-sensing applications [155, 156]. Such similar work will be very useful for the development of new functional materials. In addition to the device applications, there is strong interest in the fundamental study of the self-organized porous oxide films formed by anodization. Lastly, we are convinced that the porous materials and various fabrication techniques described here will be applied increasingly in many research fields that require ordered surface morphology or periodic porous structure on the nanometer scale in the near future.

Acknowledgments

Parts of this work were financially supported by a Grant-in-Aid for Scientific Research from the Japan Society for the Promotion of Science and the Light Metal Education Foundation of Japan. Thanks are also due to the “High-Tech Research Center” Project for Private Universities: matching fund subsidy from the Ministry of Education, Culture, Sports, Science and Technology.

References

- 1 G. D. STUCKY, J. E. M. DOUGALL, *Science*, **247**, 669 (1990).
- 2 R. J. TONUCCI, B. L. JUSTUS, A. J. CAMPILLO, C. E. FORD, *Science*, **258**, 783 (1992).
- 3 J. S. BECK, J. C. VARTULI, W. J. ROTH, M. E. LEONOWICZ, C. T. KRESGE, K. D. SCHMITT, C. T.-W. CHU, D. H. OLSON, E. W. SHEPPARD, S. B. MCCULLEN, J. B. HIGGINS, J. L. SCHLENKER, *J. Am. Chem. Soc.*, **114**, 10834 (1992).
- 4 T. M. WHITNEY, J. S. JIANG, P. C. SEARSON, C. L. CHIEN, *Science*, **261**, 1316 (1993).
- 5 C. R. MARTIN, *Science*, **266**, 1961 (1994).
- 6 Y. XIA, B. GATES, Y. YIN, Y. LU, *Adv. Mater.*, **12**, 693 (2000).
- 7 S. KAWAI, R. UEDA, *J. Electrochem. Soc.*, **122**, 32 (1975).
- 8 H. DAIMON, O. KITAKAMI, O. INAGOYA, A. SAKEMOTO, *Jpn. J. Appl. Phys.*, **30**, 282 (1991).
- 9 D. AL-MAWLAWI, N. COOMBS, M. MOSKOVITS, *J. Appl. Phys.*, **70**, 4421 (1991).
- 10 C. A. HUBER, T. E. HUBER, M. SADOQI, J. A. LUBIN, S. MANALI, C. B. PRATER, *Science*, **263**, 800 (1994).
- 11 M. ZHENG, L. MENON, H. ZENG, Y. LIU, S. BANDYOPADHYAY, R. D. KIRBY, D. J. SELLMYER, *Phys. Rev. B*, **62**, 12 282 (2000).
- 12 K. NIELSCH, R. B. WEHRSPHON, J. BARTHEL, J. KIRSCHNER, U. GÖSELE, S. F. FISCHER, H. KRONMÜLLER, *Appl. Phys. Lett.*, **79**, 1360 (2001).

- 13 M. SAITO, M. KIRIHARA, T. TANIGUCHI, M. MIYAGI, *Appl. Phys. Lett.*, **55**, 607–609 (1989).
- 14 C. K. PRESTON, M. MOSKOVITS, *J. Phys. Chem.*, **97**, 8495–8503 (1993).
- 15 Y. DU, W. L. CAI, C. M. MO, J. CHEN, L. D. ZHANG, X. G. ZHU, *Appl. Phys. Lett.*, **74**, 2951–2953 (1999).
- 16 H. MASUDA, M. OHYA, H. ASOH, M. NAKAO, M. NOHTOMI, T. TAMAMURA, *Jpn. J. Appl. Phys.*, **38**, L1403 (1999).
- 17 Y. LI, G. W. MENG, L. D. ZHANG, F. PHILLIPP, *Appl. Phys. Lett.*, **76**, 2011–2013 (2000).
- 18 K. ITAYA, S. SUGAWARA, K. ARAI, S. SAITO, *J. Chem. Eng. Jpn.*, **17**, 514 (1984).
- 19 M. KONNO, M. SHINDO, S. SUGAWARA, S. SAITO, *J. Membrane Sci.*, **37**, 193 (1988).
- 20 S. K. DALVIE, R. E. BALTUS, *J. Membrane Sci.*, **71**, 247 (1992).
- 21 T. SANO, N. IGUCHI, K. IIDA, T. SAKAMOTO, M. BABA, H. KAWAURA, *Appl. Phys. Lett.*, **83**, 4438 (2003).
- 22 F. MATSUMOTO, K. NISHIO, T. MIYASAKA, H. MASUDA, *Jpn. J. Appl. Phys.*, **43**, L640 (2004).
- 23 H. MASUDA, K. NISHIO, N. BABA, *Thin Solid Films*, **223**, 1 (1993).
- 24 D. AL-MAWLAWI, C. Z. LIU, M. MOSKOVITS, *J. Mater. Res.*, **9**, 1014 (1994).
- 25 T. KYOTANI, L. TSAI, A. TOMITA, *Chem. Mater.*, **8**, 2109 (1996).
- 26 D. ROUTKEVITCH, T. BIGIONI, M. MOSKOVITS, J. M. XU, *J. Phys. Chem.*, **100**, 14037 (1996).
- 27 P. HOYER, K. NISHIO, H. MASUDA, *Thin Solid Films*, **286**, 88 (1996).
- 28 J. LIANG, H. CHIK, A. YIN, J. XU, *J. Appl. Phys.*, **91**, 2544 (2002).
- 29 M. S. SANDER, A. L. PRIETO, R. GRONSKY, T. SANDS, A. M. STACY, *Adv. Mater.*, **14**, 665 (2002).
- 30 X. MEI, D. KIM, H. E. RUDA, Q. X. GUO, *Appl. Phys. Lett.*, **81**, 361 (2002).
- 31 S. SHINGUBARA, *J. Nanoparticle Res.*, **5**, 17 (2003).
- 32 F. KELLER, M. S. HUNTER, D. L. ROBINSON, *J. Electrochem. Soc.*, **100**, 411 (1953).
- 33 J. P. O'SULLIVAN, G. C. WOOD, *Proc. R. Soc. London, Ser. A*, **317**, 511 (1970).
- 34 J. W. DIGGLE, T. C. DOWNIE, C. W. GOULDING, *Chem. Rev.*, **69**, 365 (1969).
- 35 C. BAILEY, G. C. WOOD, *Trans. Inst. Metal Finish.*, **52**, 187 (1974).
- 36 H. MASUDA, K. FUKUDA, *Science*, **268**, 1466 (1995).
- 37 Anodisc from Whatman International Ltd., Maidstone, England.
- 38 H. MASUDA, F. HASEGAWA, S. ONO, *J. Electrochem. Soc.*, **144**, L127 (1997).
- 39 H. MASUDA, K. YADA, A. OSAKA, *Jpn. J. Appl. Phys.*, **37**, L1340 (1998).
- 40 S. SHINGUBARA, O. OKINO, H. SAKAUE, T. TAKAHAGI, *Jpn. J. Appl. Phys.*, **36**, 7791 (1997).
- 41 F. LI, L. ZHANG, R. M. METZGER, *Chem. Mater.*, **10**, 2470 (1998).
- 42 O. JESSENSKY, F. MÜLLER, U. GÖSELE, *Appl. Phys. Lett.*, **72**, 1173 (1998).
- 43 A. P. LI, F. MÜLLER, A. BIRNER, K. NIELSCH, U. GÖSELE, *J. Appl. Phys.*, **84**, 6023 (1998).
- 44 O. JESSENSKY, F. MÜLLER, U. GÖSELE, *J. Electrochem. Soc.*, **145**, 3735 (1998).
- 45 A. P. LI, F. MÜLLER, A. BIRNER, K. NIELSCH, U. GÖSELE, *J. Vac. Sci. Technol. A*, **17**, 1428 (1999).
- 46 S. ONO, N. BABA, N. MASUKO, *Kinzoku Hyomen Gijyutsu.*, **42**, 133 (1991).
- 47 S. ONO, N. MASUKO, *Corros. Sci.*, **33**, 503 (1992).
- 48 S. ONO, T. OSAKA, N. MASUKO, *Denki Kagaku oyobi Kogyo Butsuri Kagaku*, **64**, 1005 (1996).
- 49 S. ONO, K. TAKEDA, N. MASUKO, in *Proceedings of the Second International Symposium on Al Surface Science Technology*, H. TERRY (Ed.), p. 398, University of Manchester, Manchester (2000).
- 50 N. CABRERA, N. F. MOTT, *Rep. Prog. Phys.*, **12**, 163 (1948).
- 51 C. J. DELL'OCA, L. YOUNG, *J. Electrochem. Soc.*, **117**, 1548 (1970).
- 52 S. ONO, F. MIZUTANI, M. UE, N. MASUKO, in *Corrosion and Corrosion Protection*, J. D. SINCLAIR, R. P. FRANKENTHAL, E. KÁLMÁN (Eds.), PV 2001-22, p. 1129, The Electrochemical Society Proceedings Series, The Electrochemical Society, Pennington, NJ (2001).

- 53 S. ONO, M. SAITO, M. ISHIGURO, H. ASOH, *J. Electrochem. Soc.*, **151**, B473 (2004).
- 54 S. ONO, H. ASOH, M. SAITO, M. ISHIGURO, *Electrochemistry*, **71**, 105 (2003).
- 55 A. DEKKER, A. MIDDELHOEK, *J. Electrochem. Soc.*, **117**, 440 (1970).
- 56 H. TAKAHASHI, M. NAGAYAMA, *Corros. Sci.*, **18**, 911 (1978).
- 57 K. NIELSCH, J. CHOI, K. SCHWIM, R. B. WEHRSPHON, U. GÖSELE, *Nano Lett.*, **2**, 677 (2002).
- 58 S. ONO, M. SAITO, H. ASOH, *Electrochem. Solid-State Lett.*, **7**, B21 (2004).
- 59 S. ONO, N. MASUKO, *Surf. Coat. Technol.*, **169–170**, 139 (2003).
- 60 S. ONO, M. SAITO, H. ASOH, *Electrochim. Acta*, **51**, 827 (2005).
- 61 S. SHINGUBARA, K. MORIMOTO, H. SAKAUE, T. TAKAHAGI, *Electrochem. Solid-State Lett.*, **7**, E15 (2004).
- 62 S. ONO, N. KATO, M. SAITO, H. ASOH, in Pits and Pores III: Formation, Properties, and Significance for Advanced Materials, P. Schmuki, D. J. Lockwood, Y. H. Ogata, M. Seo, H. S. Isaacs (Eds), PV2004-19, p. 34, The Electrochemical Society Proceedings Series, The Electrochemical Society, Pennington, NJ, in press.
- 63 S. TAMURA, H. ASOH, S. ONO, 111th Meeting of Surface Finish Society of Japan, Matsushima, Japan, September 13, 2004, p. 121 (abstracts).
- 64 S. Z. CHU, K. WADA, S. INOUE, M. ISOGAI, A. YASUMORI, *Adv. Mater.*, **17**, 2115 (2005).
- 65 H. MASUDA, H. YAMADA, M. SATOH, H. ASOH, M. NAKAO, T. TAMAMURA, *Appl. Phys. Lett.*, **71**, 2770 (1997).
- 66 H. ASOH, K. NISHIO, M. NAKAO, T. TAMAMURA, H. MASUDA, *J. Electrochem. Soc.*, **148**, B152 (2001).
- 67 H. ASOH, K. NISHIO, M. NAKAO, A. YOKOO, T. TAMAMURA, H. MASUDA, *J. Vac. Sci. Technol. B*, **19**, 569 (2001).
- 68 H. MASUDA, K. KANEZAWA, K. NISHIO, *Chem. Lett.*, **31**, 1218 (2002).
- 69 J. CHOI, K. NIELSCH, M. REICHE, R. B. WEHRSPHON, U. GÖSELE, *J. Vac. Sci. Technol. B*, **21**, 763 (2003).
- 70 A. P. LI, F. MÜLLER and U. GÖSELE, *Electrochem. Solid-State Lett.*, **3**, 131 (2000).
- 71 C.-Y. LIU, A. DATTA and Y.-L. WANG, *Appl. Phys. Lett.*, **78**, 120–122 (2001).
- 72 N.-W. LIU, A. DATTA, C.-Y. LIU, C.-Y. PENG, H.-H. WANG, Y.-L. WANG, *Adv. Mater.*, **17**, 222 (2005).
- 73 I. MIKULSKAS, S. JUODKAZIS, R. TOMASIUNAS, J. G. DUMAS, *Adv. Mater.*, **13**, 1574 (2001).
- 74 Z. SUN, H. K. KIM, *Appl. Phys. Lett.*, **81**, 3458 (2002).
- 75 S. SHINGUBARA, Y. MURAKAMI, K. MORIMOTO, T. TAKAHAGI, *Surf. Sci.*, **532–535**, 317 (2003).
- 76 H. MASUDA, Y. MATSUI, M. YOTSUYA, F. MATSUMOTO, K. NISHIO, *Chem. Lett.*, **33**, 584 (2004).
- 77 S. F.-BIDOZ, V. KITAEV, D. ROUTKEVITCH, I. MANNERS, G. A. OZIN, *Adv. Mater.*, **16**, 2193 (2004).
- 78 J. BROUGHTON, G. A. DAVIES, *J. Membr. Sci.*, **106**, 89 (1995).
- 79 H. MASUDA, H. ASOH, M. WATANABE, K. NISHIO, M. NAKAO, T. TAMAMURA, *Adv. Mater.*, **13**, 189 (2001).
- 80 H. ASOH, S. ONO, T. HIROSE, M. NAKAO, H. MASUDA, *Electrochim. Acta*, **48**, 3171 (2003).
- 81 H. ASOH, S. ONO, T. TOMOHIRO, I. TAKATORI, H. MASUDA, *Jpn. J. Appl. Phys.*, **43**, 6342 (2004).
- 82 H. MASUDA, M. YOTSUYA, M. ASANO, K. NISHIO, M. NAKAO, A. YOKOO, T. TAMAMURA, *Appl. Phys. Lett.*, **78**, 826 (2001).
- 83 H. MASUDA, A. ABE, M. NAKAO, A. YOKOO, T. TAMAMURA, K. NISHIO, *Adv. Mater.*, **15**, 161 (2003).
- 84 L. ZHANG, H. S. CHO, F. LI, R. M. METZGER, W. D. DOYLE, *J. Mater. Sci. Lett.*, **17**, 291 (1998).
- 85 D. ALMAWLAWI, K. A. BOSNICK, A. OSIKA, M. MOSKOVITS, *Adv. Mater.*, **12**, 1252 (2000).
- 86 S. ONO, H. ICHINOSE, N. MASUKO, *J. Electrochem. Soc.*, **138**, 3705 (1991).
- 87 S. ONO, H. ICHINOSE, N. MASUKO, *J. Electrochem. Soc.*, **139**, L80 (1992).
- 88 D. D. MACDONALD, *J. Electrochem. Soc.*, **140**, L27 (1993).
- 89 T. YANAGISHITA, K. NISHIO, M. NAKAO, A. FUJISHIMA, H. MASUDA, *Chem. Lett.*, **31**, 976 (2002).
- 90 T. YANAGISHITA, M. SASAKI, K. NISHIO, H. MASUDA, *Adv. Mater.*, **16**, 429 (2004).

- 91 G. C. WOOD, J. P. O'SULLIVAN, B. VASZKO, *J. Electrochem. Soc.*, **115**, 618 (1968).
- 92 J. LI, C. PAPADOPOULOS, J. XU, *Nature*, **402**, 253 (1999).
- 93 H. ASOH, S. ONO, *ATB Metallurgie*, **43**, 319 (2003).
- 94 B. T. HOLLAND, C. F. BLANFORD, A. STEIN, *Science*, **281**, 538 (1998).
- 95 J. E. G. J. WIJNHOVEN, W. L. VOS, *Science*, **281**, 802 (1998).
- 96 P. V. BRAUN, P. WILTZIUS, *Nature*, **402**, 26 (1999).
- 97 G. SUBRAMANIA, K. CONSTANT, R. BISWAS, M. M. SIGALAS, K.-M. HO, *Appl. Phys. Lett.*, **74**, 3933 (1999).
- 98 A. RICHEL, N. P. JOHNSON, D. W. MCCOMB, *Appl. Phys. Lett.*, **76**, 1816 (2000).
- 99 N. TÊTREVAULT, H. MÍGUEZ, G. A. OZIN, *Adv. Mater.*, **16**, 1471 (2004).
- 100 H. ASOH, S. ONO, *Appl. Phys. Lett.*, **87**, 103102 (2005).
- 101 S. Y. CHOU, P. R. KRAUSS, P. J. RENSTROM, *Science*, **272**, 85 (1996).
- 102 E. S. SNOW, P. M. CAMPBELL, *Science*, **270**, 1639 (1995).
- 103 S. HONG, J. ZHU, C. A. MIRKIN, *Science*, **286**, 523 (1999).
- 104 U. KUNZE, B. KLEHN, *Adv. Mater.*, **11**, 1473 (1999).
- 105 M. GEISSLER, Y. XIA, *Adv. Mater.*, **16**, 1249 (2004).
- 106 H. W. DECKMAN, J. H. DUNSMUIR, *Appl. Phys. Lett.*, **41**, 377 (1982).
- 107 J. C. HUILTEEN, R. P. V. DUYN, *J. Vac. Sci. Technol. A*, **13**, 1553 (1995).
- 108 C. HAGINOYA, M. ISHIBASHI, K. KOIKE, *Appl. Phys. Lett.*, **71**, 2934 (1997).
- 109 K. PIGLMAYER, R. DENK, D. BÄUERLE, *Appl. Phys. Lett.*, **80**, 4693 (2002).
- 110 Y. LU, S. THEPPAKUTTAI, S. C. CHEN, *Appl. Phys. Lett.*, **82**, 4143 (2003).
- 111 K. H. PARK, S. LEE, K. H. KOH, R. LACERDA, K. B. K. TEO, W. I. MILNE, *J. Appl. Phys.*, **97**, 024311 (2005).
- 112 S. GAVRILOV, S. LEMESHKO, V. SHEVYAKOV, V. ROSCHIN, *Nanotechnology*, **10**, 213 (1999).
- 113 S. SHINGUBARA, O. OKINO, Y. SAYAMA, H. SAKAUE, T. TAKAHAGI, *Solid-State Electronics*, **43**, 1143 (1999).
- 114 T. IWASAKI, T. MOTOI, T. DEN, *Appl. Phys. Lett.*, **75**, 2044 (1999).
- 115 D. CROUSE, Y.-H. LO, A. E. MILLER, M. CROUSE, *Appl. Phys. Lett.*, **76**, 49 (2000).
- 116 S. SHINGUBARA, O. OKINO, Y. MURAKAMI, H. SAKAUE, T. TAKAHAGI, *J. Vac. Sci. Technol. B*, **19**, 1901 (2001).
- 117 W. HU, D. GONG, Z. CHEN, L. YUAN, K. SAITO, C. A. GRIMES, P. KICHAMBARE, *Appl. Phys. Lett.*, **79**, 3083 (2001).
- 118 H. MASUDA, K. YASUI, Y. SAKAMOTO, M. NAKAO, T. TAMAMURA, K. NISHIO, *Jpn. J. Appl. Phys.*, **40**, L1267 (2001).
- 119 S. SHINGUBARA, Y. MURAKAMI, H. SAKAUE, T. TAKAHAGI, *Jpn. J. Appl. Phys.*, **41**, L340 (2002).
- 120 A. CAI, H. ZHANG, H. HUA, Z. ZHANG, *Nanotechnology*, **13**, 627 (2002).
- 121 M. T. WU, I. C. LEU, J. H. YEN, M. H. HON, *Electrochem. Solid-State Lett.*, **7**, C61 (2004).
- 122 M. T. WU, I. C. LEU, M. H. HON, *J. Mater. Res.*, **19**, 888 (2004).
- 123 L. PU, Y. SHI, J. M. ZHU, X. M. BAO, R. ZHANG, Y. D. ZHENG, *Chem. Commun.*, (8) 942 (2004).
- 124 N. V. MYUNG, J. LIM, J.-P. FLEURIAL, M. YUN, W. WEST, D. CHOI, *Nanotechnology*, **15**, 833 (2004).
- 125 H. SHIRAKI, Y. KIMURA, H. ISHII, S. ONO, K. ITAYA, M. NIWANO, *Appl. Surf. Sci.*, **237**, 369 (2004).
- 126 F. MÜLLER, A.-D. MÜLLER, S. SCHULZE, M. HIETSCHOLD, *J. Mater. Sci.*, **39**, 3199 (2004).
- 127 M. KOKONOU, A. G. NASSIOPOULOU, K. P. GIANNAKOPOULOS, *Nanotechnology*, **16**, 103 (2005).
- 128 M. TIAN, S. XU, J. WANG, N. KUMAR, E. WERTZ, Q. LI, P. M. CAMPBELL, M. H. W. CHAN, T. E. MALLOW, *Nano Lett.*, **5**, 697 (2005).
- 129 S. Z. CHU, K. WADA, S. INOUE, S. TODOROKI, *J. Electrochem. Soc.*, **149**, B321 (2002).
- 130 S. Z. CHU, K. WADA, S. INOUE, S. TODOROKI, *Chem. Mater.*, **14**, 266 (2002).
- 131 H. ASOH, M. MATSUO, M. YOSHIHAMA, S. ONO, *Appl. Phys. Lett.*, **83**, 4408 (2003).

- 132 H. MASUDA, M. SATOH, *Jpn. J. Appl. Phys.*, **35**, L126 (1996).
- 133 M. NAKAO, S. OKU, T. TAMAMURA, K. YASUI, H. MASUDA, *Jpn. J. Appl. Phys.*, **38**, 1052 (1999).
- 134 Y. KANAMORI, K. HANE, H. SAI, H. YUGAMI, *Appl. Phys. Lett.*, **78**, 142 (2001).
- 135 P.-L. CHEN, C.-T. KUO, T.-G. TSAI, B.-W. WU, C.-C. HSU, F.-M. PAN, *Appl. Phys. Lett.*, **82**, 2796 (2003).
- 136 P.-L. CHEN, C.-T. KUO, F.-M. PAN, T.-G. TSAI, *Appl. Phys. Lett.*, **84**, 3888 (2004).
- 137 E. S. SNOW, P. M. CAMPBELL, P. J. McMARR, *Appl. Phys. Lett.*, **63**, 749 (1993).
- 138 H. SUGIMURA, T. YAMAMOTO, N. NAKAGIRI, M. MIYASHITA, T. ONUKI, *Appl. Phys. Lett.*, **65**, 1569 (1994).
- 139 M. ARA, H. GRAAF, H. TADA, *Appl. Phys. Lett.*, **80**, 2565 (2002).
- 140 M. CAVALLINI, P. MEI, F. BISCARINI, R. GARCIA, *Appl. Phys. Lett.*, **83**, 5286 (2003).
- 141 H. ASOH, A. OIDE, S. ONO, *Appl. Surf. Sci.*, **252**, 1668 (2005).
- 142 A. OIDE, H. ASOH, S. ONO, *Electrochem. Solid-State Lett.*, **8**, G172 (2005).
- 143 H. ASOH, K. SASAKI, S. ONO, *Electrochem. Commun.*, **7**, 953 (2005).
- 144 S. ONO, A. OIDE, H. ASOH, *Electrochimica Acta*, in press (2006).
- 145 D. GONG, C. A. GRIMES, O. K. VARGHESE, W. HU, R. S. SINGH, Z. CHEN, E. C. DICKEY, *J. Mater. Res.*, **16**, 3331 (2001).
- 146 R. BERANEK, H. HILDEBRAND, P. SCHMUKI, *Electrochem. Solid-State Lett.*, **6**, B12 (2003).
- 147 N. MUKHERJEE, M. PAULOSE, O. K. VARGHESE, G. K. MOR, C. A. GRIMES, *J. Mater. Res.*, **18**, 2296 (2003).
- 148 H. TSUCHIYA, J. M. MACAK, I. SIEBER, L. TAVEIRA, A. GHICOV, K. SIRODNA, P. SCHMUKI, *Electrochem. Commun.*, **7**, 295 (2005).
- 149 H.-C. SHIN, J. DONG, M. LIU, *Adv. Mater.*, **16**, 237 (2004).
- 150 H. TSUCHIYA, P. SCHMUKI, *Electrochem. Commun.*, **6**, 1131 (2004).
- 151 W.-J. LEE, W. H. SMYRL, *Electrochem. Solid-State Lett.*, **8**, B7 (2005).
- 152 I. SIEBER, H. HILDEBRAND, A. FRIEDRICH, P. SCHMUKI, *Electrochem. Commun.*, **7**, 97 (2005).
- 153 H. TSUCHIYA, P. SCHMUKI, *Electrochem. Commun.*, **7**, 49 (2005).
- 154 I. V. SIEBER, P. SCHMUKI, *J. Electrochem. Soc.*, **152**, C639 (2005).
- 155 S. ONO, T. NAGASAKA, H. SHIMAZAKI, H. ASOH, in Pits and Pores III: Formation, Properties, and Significance for Advanced Materials, P. SCHMUKI, D. J. LOCKWOOD, Y. H. OGATA, M. SEO, H. S. ISAACS (Eds.), PV2004-19, p. 123, The Electrochemical Society Proceedings Series, The Electrochemical Society, Pennington, NJ, in press.
- 156 S. ONO, H. ASOH, 113th Meeting of Surface Finish Society of Japan, Kawagoe, Japan, March 15, 2006, p. 102 (abstracts).

8

Electrochemical Fabrication of Metal Nanocontacts and Nanogaps

Fang Chen and N. J. Tao

8.1

Introduction

The rapid progress in microelectronics over the past several decades relies critically on miniaturization which has been achieved by carving smaller and smaller features on semiconductor chips. As the conventional semiconductor devices shrink down to the nanometer scale, various nanoscale building blocks such as nanocontacts and carbon nanotubes [1, 2] single organic molecules [3] and even single atoms [4], have been considered as potential alternatives for ever smaller devices. Important tasks on the route towards the ultimate degree of miniaturization are to develop methods to fabricate various nanoscale building blocks, to assemble the building blocks into devices, and to measure the fundamental electron transport properties of the devices.

A number of powerful experimental techniques have become available over the past two decades, including scanning tunneling microscopy (STM) and atomic force microscopy (AFM), and other scanning probe methods. In addition to their well-known capabilities in imaging and spectroscopy, STM and AFM are capable of creating nanoscale structures. For example, Ringger [5] and Staufer [6] used STM as a nanolithographic tool in vacuum. Dagata et al. [7] used a STM tip to induce local oxidation on a silicon substrate in air. Penner et al. [8] and Kolb et al. [9] have pioneered the electrochemical STM method to generate metal, semiconductor and polymer nanostructures. Gimzewski et al. [10] employed an STM tip to study the conductance in atomic-sized contacts and Durig et al. [11] measured the forces of nanoscale contacts using AFM. Both STM and AFM have also been used to measure the conductance of single molecules positioned between the STM or AFM tip and a solid substrate [12–16].

STM and AFM, as well as other scanning probe-related methods, rely on mechanical actuations. Another mechanically actuated technique is mechanically controllable break junction (MCBJ) [17, 18], which is applied to create and study molecular/atomic sized junctions. The basic principle of the MCBJ technique is to break a notched metal wire supported on a substrate into two facing electrodes by bending the substrate. The breakdown process and the separation between the

electrodes can be precisely controlled with a piezoelectric transducer. Although MCBJ does not have the ability to image, it offers far better stability than the STM and AFM. It has been shown that by carefully controlling the very last stage of the breakdown of the metal wire, a single atom contact can be created and held for many hours. Furthermore, by depositing a layer of dithiol molecules onto the metal wire, a molecule junction consisting of a molecule sandwiched between two electrodes via metal–thiolate bonds can be formed [19–21].

The scanning probe and the MCBJ techniques have provided us with important insights into the fundamental properties of nanoscale structures and molecules. However, since they rely on mechanical actuations to achieve controllability and flexibility, they are not compatible with device applications. An alternative way to fabricate nanoscale structures uses electrochemical methods combined with some prefabricated structures as template or with conventional lithographic techniques. For example, by electrochemically depositing metal into various templates, including nanoscale channels within a porous material, step edges on crystal surfaces, and self-assembled molecular structures, metal nanoparticles and nanocontacts with dimensions controlled by the template structures have been fabricated. More detailed information regarding the electrochemical fabrication using these templates can be found in a recent review [22]. Another kind of unique template is the pre-designated pattern electrode, on which a metal film can be electrochemically deposited along the original shape of the electrode. As a result, the spacing between two or three electrodes can be shrunk to a desirable size, which may not be reached by means of conventional microfabrication techniques, such as photolithography, electron beam lithography (EBL), or focus ion beam (FIB) milling. For example, the electrochemical methods can fabricate electrodes separated with a gap of ~ 1 nm which cannot be easily achieved using EBL. Another unique advantage of the electrochemical fabrication methods is the reversibility, i.e., a nanostructure can be dissolved and re-fabricated until the most desirable structure is created.

In this chapter, we mainly focus on electrochemical fabrications of electrodes separated with a molecular scale gap (referred to as nanogaps), and metal nanocontacts (referred to as quantum point contacts or atomic scale contacts). The remainder of this chapter is organized as follows: the electrochemical fabrications of metal nanocontacts are described in Section 2, and electrodes separated with nanoscale gaps in Section 3. In each section, we will start with various electrochemical fabrication methods. We will then discuss some important physical properties of the nanocontacts and nanogaps, and summarize some of the applications and potential applications.

8.2

Electrochemical Fabrication of Metal Nanocontacts

When two metal pieces are brought together, a contact is formed and electron transport through the contact between the two pieces can be studied. If the contact

size is much greater than the mean free path of electrons, which are typically of the order of a few tens of nm at room temperature, the transport is described by classical diffusive scattering. If the contact is reduced to below the mean free path the electron transport through the contact becomes ballistic. Yanson et al. [23] developed a spear–anvil technique to study electron transport in metallic point contacts in which each point contact is formed by bringing a metal needle into contact with a metal surface. This technique was used to create stable contacts with typical resistance ranging from ~ 0.1 to $\sim 10 \Omega$, corresponding to contact diameters between 10 and 100 nm, which were used to demonstrate the ballistic nature of electron transport at low temperature. When the contact diameters are further decreased down to the order of the electron wavelength, which is of the order of a few Å, the conductance of the contact becomes quantized. A comprehensive review of nanocontacts formed by mechanical techniques has been published recently [4]. Here we will mainly focus on electrochemical fabrication of metal nanocontacts.

8.2.1

STM/AFM Assisted Method

STM is a versatile tool to study the topology and electronic properties of conductive surfaces with atomic resolution, and the sharp tip of STM is also suitable to create atomic scale contacts. In the latter application, an atomic scale contact is formed when the tip is pressed into the substrate, during which the conductance between the tip and the substrate is recorded [10]. Just before the tip touches the substrate, a salient change in conduction occurs due to electron tunneling. When a contact is established, the tunneling process is replaced by the ballistic transport mechanism, and the transition from the tunneling regime to ballistic transport is observed as an abrupt jump in the conductance, from which the contact diameter can be estimated. An atomic contact can be also created by pulling out the tip that is in contact with the substrate [24].

Both pressing and pulling tips involve mechanical movement, which makes the nanocontacts unstable. Li and Tao [25, 26] demonstrated an electrochemical method to create atomic contacts using an electrochemical STM setup (Fig. 8.1). In their approach, the STM tip is first held at a fixed distance of 10–150 nm from an Au substrate in a Cu plating solution, and then Cu is selectively electroplated onto the STM tip. When the sharpest part of the growing Cu reaches the substrate, a contact is formed between the tip and the substrate, which is reflected by a sharp increase in the current that flows between the tip and substrate. The width of the nanocontact can be varied reversibly by dissolving or re-depositing Cu via controlling the potentials applied to the tip and substrate. This electrochemical method does not involve mechanical movements, which facilitates the formation of nano-scale contacts with long term stability [26–28].

Schindler et al. [29, 30] used a STM tip to deposit Au clusters onto n-Si(111): H substrates from a gold plating electrolyte, creating Au–silicon contacts at the solid/liquid interface. The contacts showed a Schottky diode behavior with current den-

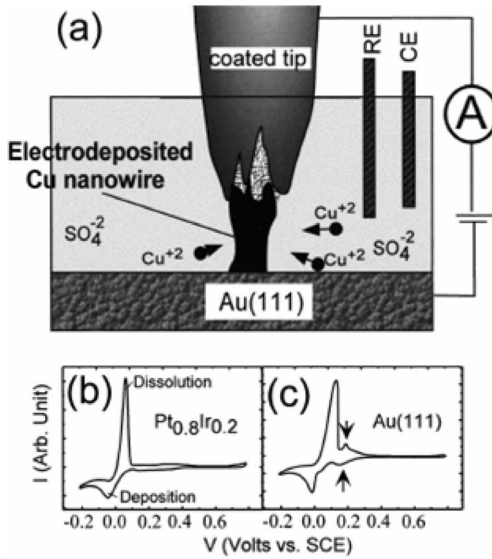


Figure 8.1. (a) Schematic drawing of the experimental setup. (b) and (c) the deposition/dissolution current vs. potential plots for Au substrate and Pt_{0.8}Ir_{0.2} by sweeping the potential linearly at a rate of 50 mV/s. A pair of arrows in (c) point out the underpotential deposition/dissolution in the present conditions. Reprinted with permission from Ref. [25]. © 1998, American Institute of Physics.

sities much higher than expected from thermionic emission. The method allows *in situ* studies of electronic properties at any (semi-) conducting nanostructure at solid/liquid interfaces under well-defined conditions.

Snow et al. [31–33] reported an AFM anodization method to fabricate Al point contacts, where the AFM tip is first used to anodize a 1 μm wide Al thin film into a 40 nm wide by 500 nm long nanowire. The anodization process was similar to conventional electrochemical anodization, except that the AFM tip was used as the cathode and the water bridge due to the capillary effect serves as a faradaic cell. By further anodizing a section of the nanowire, an atomic scale point contact was formed. In order to achieve the high controllability necessary to fabricate atomic sized features, *in situ* electrical measurements were used as feedback to monitor the anodization. In some of the samples, the conductance can be stabilized at the lowest few quantum steps for a long time, which corresponds to the formation of an atomic scale contact.

8.2.2

Electrodeposition on Surface-supported Electrodes

STM and AFM in the above methods are used as nice precision control tools, but they suffer from stability and throughput problems. One way to avoid using STM

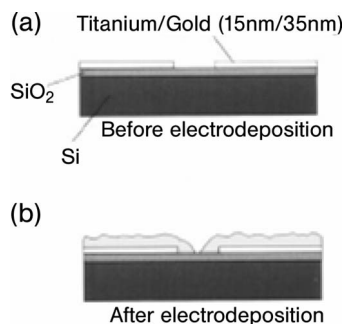


Figure 8.2. (A) The initial electrode pairs with large separation are fabricated by conventional lithography. (B) Metal is electrodeposited onto the electrodes, reducing their separation. V_{dc} controls the electrodeposition rate while V_{ac} is used to monitor the conductance and thus the separation between the electrodes. When deposition is stopped before the electrodes touch, separations on 1 nm scale are obtained reproducibly. Reprinted with permission from Ref. [34]. © 1999, American Institute of Physics.

and AFM is to create atomic scale contacts supported on a solid substrate such as a silicon chip. Typically this method starts with a pair of metal electrodes, which is fabricated by conventional lithographic techniques. The initial separation between the two electrodes varies from a few tens of nm to many μm , depending on the resolution of the lithographic tools. The electrodes are then immersed in an electroplating solution and serve as the working electrodes, on which metal ions are reduced and electrocrystallized to form a metal film (see Fig. 8.2). Consequently, the electrode separation decreases and eventually a small contact is formed between the electrodes. By carefully choosing feedback signals, such as deposition current or growth time, metal contacts with atomic size can be obtained. Using this technique, Morpurgo et al. [34] have observed conductance quantization during the formation of an Au contact. They prepared the initial Au electrodes with EBL, which can control the gap between the electrodes to ~ 50 nm, and then formed an atomic scale contact by depositing metal into the gap. Their results indicated that an extremely low deposition rate is necessary to get well defined nanocontacts. Li et al. [35] reported Cu deposition on EBL fabricated electrodes with the help of a bipotentiostat that can simultaneously control the deposition rate and measure the conductance between the electrodes. In order to adjust the size of the contacts precisely, they used the tunneling current to act as a feedback signal, which is very sensitive to the distance between the electrodes before the metallic atoms form contacts. By stabilizing the tunneling current on various steps using a feedback loop, they have demonstrated stable molecular-scale gaps with sub-ångstrom precision. FIB milling is another powerful tool to define nanometer separated electrodes, which is realized by cleaving metal nanocontacts with a heavy ion beam [36].

Using EBL or FIB, one can fabricate electrodes separated by a few tens of nm, but such a small initial separation is not necessary to construct metal nanocontacts in electrochemical fabrications. A conventional photolithography technique was also used to produce the relatively large electrode pairs with micrometer scale separation. Starting from these micron-scale spaced electrodes, atomic scale contacts can also be formed by electrodeposition, although it is harder to control the electrodeposition processes than with the EBL- and FIB-fabricated electrodes [37–40].

Electrochemical deposition is a convenient method to fabricate metal nanocontacts and to study the various properties of the nanocontacts. A variety of metal nanocontacts have been produced including Au [34, 41], Cu [39], Ag [42], Al [43], Pt [44] and Ni [40, 45, 46]. Nakabayashi et al. fabricated contacts by electrochemically growing a Zn fractal into contact with a Cu ring electrode, where the Zn fractal is synthesized at an immiscible interface between water and 4-methyl-2-pentanone so that it is quasi two-dimensional [47].

8.2.3

Self-terminated Method

The electrodeposition methods described above require sophisticated bipotentiostat or feedback loops to control the fabrication process. A simpler electrochemical method to fabricate metal nanocontacts is the so-called self-terminated method [48, 49]. The basic principle is illustrated in Fig. 8.3. It starts with a pair of electrodes separated by a relatively large gap in an electrolyte. When a bias voltage between the two electrodes, metal atoms are etched off from the anode and deposited onto the cathode. The etching takes place all over the anode surface, but the depo-

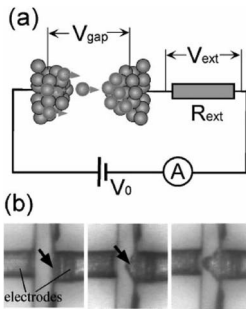


Figure 8.3. (a) Schematic illustration of the setup. Metal atoms etched off the left electrode are guided and deposited onto the right electrode by applying a voltage between the electrodes with an external resistor in series. The gap resistance decreases as the electrode gap shrinks which results in a drop in etching/deposition voltage and eventually terminates the etching/deposition processes. (b) Snapshots of an experiment that started with a pair of 25 μm Cu electrodes separated by a $\sim 20 \mu\text{m}$ gap. Reprinted with permission from Ref. [48]. © 2002, American Institute of Physics.

sition is localized to the sharpest point on the cathode, due to the high electric field and metal ion concentration near the sharpest point. Consequently, the gap narrows and disappears eventually when a point contact is formed between the two electrodes. In order to control the formation of the contact between the electrodes, the etching and deposition processes must be terminated immediately after a desired contact is formed. This self-termination mechanism was introduced by connecting one electrode in series with an external resistor R_{ext} , thus the voltage drop V_{gap} on the gap can be derived by:

$$V_{\text{gap}} = \frac{R_{\text{gap}}}{R_{\text{gap}} + R_{\text{ext}}} V_0 \quad (8.1)$$

where R_{gap} is the resistance between the two electrodes, and V_0 is the applied voltage. Initially $R_{\text{gap}} \gg R_{\text{ext}}$, V_{gap} is $\sim V_0$ according to Eq. (8.1), so the etching and deposition take place at full speed. As the gap narrows by a few nm, electron tunneling across the gap occurs and R_{gap} decreases. This results in a decreasing V_{gap} , or a slowdown in the etching and deposition rates. Eventually, when $R_{\text{gap}} \ll R_{\text{ext}}$, $V_{\text{gap}} \sim 0$, which terminates the etching and deposition. In this work, the final gap width or contact size is determined by R_{ext} . If R_{ext} is greater than $h/2e^2$ ($\sim 13 \text{ K}\Omega$), it terminates with a small tunneling gap between the electrodes. On the other hand, if R_{ext} is smaller than $h/2e^2$, it terminates with an atomic-scale contact between the electrodes. This self-termination method allows one to simultaneously fabricate an array of metal nanocontacts, which are suitable for device and sensor applications (see Section 8.2.7).

8.2.4

Electrochemical Etching

Li et al. demonstrated an electrochemical etching strategy to prepare nanocontacts. In this method, a metal wire supported on a solid substrate with an initial diameter of a few tens of μm is glued onto a glass slide [50]. The glue covers the entire wire except for a small portion that is exposed to electrolyte for electrochemical etching or re-deposition. The exposed portion is less than a few μm so that ionic conduction through the electrolyte is negligible compared to the electronic conduction through the wire. By electrochemical etching, the diameter of the wire is reduced to the atomic scale, at which the conductance becomes quantized. The process can be reversed to increase the diameter by electrochemical deposition. When the conductance is greater than the preset value, etching is activated to reduce the diameter of the wire. While the conductance is smaller than the preset value, deposition is turned on to increase the diameter. By repeating the etching and depositing process, the resultant atomic-scale contacts can last from minutes to days. Further improvement of the stability may be achieved by “coating” the wire with appropriate molecules. The method has been successfully used to fabricate metal contact with conductance quantized at different steps, as well as being applicable to various metals, including Ag, Cu, Pd, Pb and Ni [51, 52]. These experiments in-

indicated that while Cu, Ag, Ni, and Pd can form stable contacts with conductance quantized near $1 G_0$, the conductance quantization of Pb contacts is rather unstable. A nice feature of the approach is that the supporting electrodes can be reused by dissolving away the quantum contacts.

8.2.5

Nanocontacts Prepared Using Nanopores

Elhoussine et al. employed nanopores of track-etched polymer membranes as the templates to deposit magnetic nanocontacts (Ni) [53, 54]. The pore diameters ranged from 60 to 120 nm and pore densities were about $10^8/\text{cm}^2$. The bottom side of the membrane is covered with a thick gold layer by electron beam evaporation, which plays the role of the cathode for nanowire electrodeposition. On the top side, another gold electrode is deposited through a metallic mask. These two conducting layers serve for the resistance measurement of the nanocontact. Generally, there are two different configurations to form stable nanocontacts: in one case, the nanocontact is formed between a growing Ni nanowire and the upper electrodeposited Ni film; in the other case, the nanocontact takes place inside the pore via Ni deposition on the upper Au electrode. As expected for ferromagnetic metals without spin degeneracy, these experiments showed that the conductance of the contacts is quantized in units of e^2/h . This system might be useful for studying ballistic spin transport through electrodeposited nanocontacts and tunneling through controllable magnetic nanogaps.

8.2.6

Solid State Electrochemical Reaction

Compared with conventional electrochemistry, taking place at solid/liquid interface, there is another kind of electrochemical reaction occurring in a solid state electrolyte. Certain sulfides and selenides are good solid electrolytes, exhibiting ion mobilities as high as $10^3 \text{ cm}^2 \text{ V}^{-1} \text{ s}^{-1}$ and good thermal stability. Aono et al. provided a solid electrochemical reaction to form a quantum point contact. They found that a silver nano-protrusion can be formed at the surface of a silver sulfide (Ag_2S) crystal [55, 56]. This substance has a structure that allows positive silver ions to travel like a liquid through a lattice of negative sulfur ions when a certain bias is applied to the two ends. Silver ions can move in the reverse direction by changing the polarity of the bias voltage.

Figure 8.4 depicts the basic principal for making Ag atomic contacts in a switchable manner. STM tips made of silver sulfide are positioned near a conductive sample and loaded with an appropriate amount of positive voltage [57]. This electric field causes positive silver ions to be drawn out of the end of the tip, and a bridge of silver atoms is formed locally (Fig. 8.4(a)). Conversely, loading negative voltage onto the tip causes the silver ions to be drawn back into the sulfur ion lattice, which results in loss of contact between the two electrodes (Fig. 8.4(b)). So growth and shrinkage of the silver contacts are easily controlled by changing the polarity of

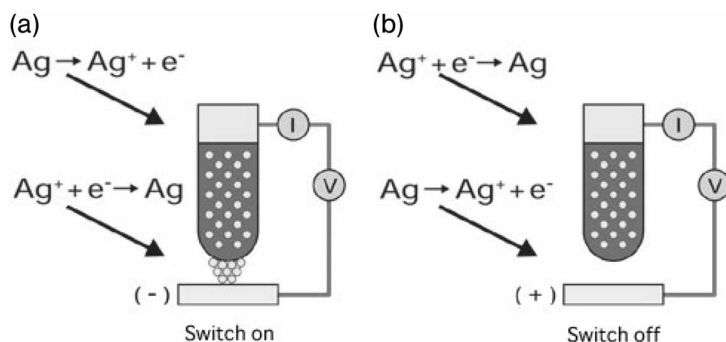


Figure 8.4. The principle of the atomic switch formed from a solid electrochemical reaction. (a) The switch is on when a positive voltage is applied on the Ag/Ag₂S layer supported on the cathode; (b) the switch is off when an opposite bias is added. Reprinted from website: <http://www.riken.jp/engn/r-world/info/release/news/2002/apr/>

the bias voltage applied to the material. The conductance through the device can be as small as one quantum unit of conductance, suggesting that the silver bridge can touch the substrate with just one atom. Besides Ag contacts, a nanometer-scale switch that uses a copper sulfide film was also tried and its performance described [58].

8.2.7

Properties of Metal Nanocontacts

Nanoscale metal contacts possess properties that are different from their bulk counterparts. For example, the electron transport properties cannot be described by the classical theories when the size of the contacts becomes comparable to, or even smaller than, the characteristic length scales, such as electron mean free path (the average distance over which electrons can traverse without experiencing a scattering event) and the de Broglie wavelength of conduction electrons. As a consequence, while a macroscopic gold wire is more conductive than lead by an order of magnitude, a gold atom contact is three times more conductive than a lead atom contact [59]. This kind of “unusual” property can even be observed at room temperature because the energy scales involved in metals are much greater than room temperature thermal energy. Interesting “unusual” properties are not limited to electrical properties. It has been found that the electrical properties of atomic scale contacts are intimately related to their mechanical properties [4]. Researchers around the world have also been exploring the magnetic and chemical properties of these atomic scale contacts. We discuss some of these properties below.

8.2.7.1 Mechanical Properties

Mechanical properties in metal nanocontacts have been widely investigated using STM and MCBJ [60, 61]. For example, it has been found that an atomic scale con-

tact has a mechanical strength of an ideal metal crystal, much greater than that of macroscopic contacts. Agrait et al. have studied Pb contacts at 4.2 K [62] using an STM supplemented by a force sensor. They found that for contact radii between 3 and 13 nm the pressure in the contact during plastic deformation was approximately 1 GPa. Further experiments by the group on Au contacts between 2 and 6 nm in diameter, at 4.2 K [63] and at room temperature [64], and on contacts of a single atom at room temperature [65], showed that the deformation process, either contraction or elongation, proceeds in alternating elastic and yielding stages. Since mechanical stress is concentrated at the narrowest point of a contact, it is natural to assume that plastic deformation will involve mostly the narrowest portion and will also control the electrical conductance. Using this assumption in conjunction with volume conservation, it is possible to estimate the length involved in plastic deformation from the curves of conductance vs. elongation [66]. Stalder et al. concluded that the plastic flow is confined within a region comprising five to six atomic layers (assuming 0.2 nm for the layer spacing) [67].

He et al. [68] studied the effect of molecular adsorption on the mechanical stability of gold nanocontacts. By performing the measurement in electrolytes containing various adsorbates, they were able to control the surface coverage of adsorbates on the nanocontacts by controlling the electrode potential. The length over which a contact can be elongated before losing stability provides important mechanical information about these nanocontacts. Figure 8.5 plots the average elongation length of Au nanocontacts with conductance at the lowest quantum step as a function of potential [69]. In the absence of molecular adsorbates, the elongation length is about 1.2 Å [65, 70], which is largely independent of the potential. When adding adenine, a molecule known to adsorb on gold, the elongation length becomes de-

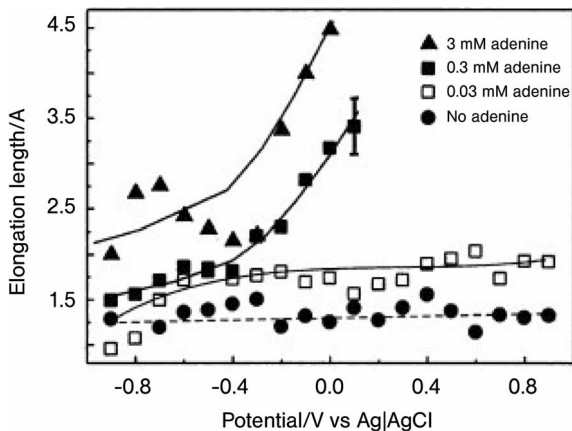


Figure 8.5. Average elongation length of Au nanocontacts with conductance at the lowest quantum step as a function of potential in 0.1 M NaClO₄ containing different amounts of adenine. Reprinted with permission from Ref. [68]. © 2002, Elsevier.

pendent on the potential. At low potentials where adenine does not adsorb onto gold, the elongation is $\sim 1.2 \text{ \AA}$, about the same as that in the absence of adenine. However, on increasing the potential from -0.8 V to 0 V , adenine begins to adsorb onto the Au contacts and the elongation length increases from ~ 1.2 to $\sim 4.5 \text{ \AA}$. The large increase in the elongation length indicates an enhanced stability of the contacts by molecular adsorbates. The strong interactions between the adsorbates and the nanocontacts apparently change the atomic scale configuration of the nanocontacts and thus the mechanical properties.

The temperature effect on the mechanical properties of various metallic atomic contacts has not been studied systematically. For Au contacts no significant difference in the conductance quantization is observed between room temperature and low temperature (e.g., 4.2 K) [64, 65, 71]. However, the contacts are much more stable at low temperatures, which is due in part to the slowing down of diffusion processes and in part to the higher stability of the cryogenic setup.

8.2.7.2 Electron Transport

Macroscopic conductors are characterized by Ohm's law, which establishes that the conductance G of a given sample is directly proportional to its cross sectional area S and inversely proportional to its length L ,

$$G = \sigma S/L \quad (8.2)$$

where σ is the conductivity of the sample. Although conductance is still a useful quantity to describe atomic scale conductors, the above relation is no longer applicable. Atomic scale conductors are a limiting case of mesoscopic systems in which quantum coherence plays a central role in the transport properties. In mesoscopic systems one can identify different transport regimes according to the relative size of various length scales. These scales are, in turn, determined by different scattering mechanisms. One of the important length scales is the phase-coherence length L_ϕ , which measures the distance over which quantum coherence is preserved. Direct calculation of the coherence length from microscopic theories is a difficult task. One can, however, obtain information on L_ϕ indirectly from weak localization experiments [13]. A typical value for Au at $T = 1 \text{ K}$ is around 1 \mu m [72]. The mesoscopic regime is determined by the condition $L < L_\phi$, where L is a typical length scale of the sample. Another important length scale is the elastic mean free path l , which roughly measures the distance between two successive elastic collisions of the electron with static impurities. The regime $L \gg l$ is called diffusive. In a semi-classical picture the electron motion in this regime can be viewed as a random walk of step size l among the impurities. On the other hand, when $L \ll l$ the electron transport becomes ballistic in which case the electron momentum can be assumed to be constant and changes only via scattering with the boundaries of the sample. These two regimes are illustrated in Fig. 8.6 [73].

For an atomic scale contact, the electron transport is not only ballistic but also exhibits quantum behavior because its diameter is comparable to the Fermi

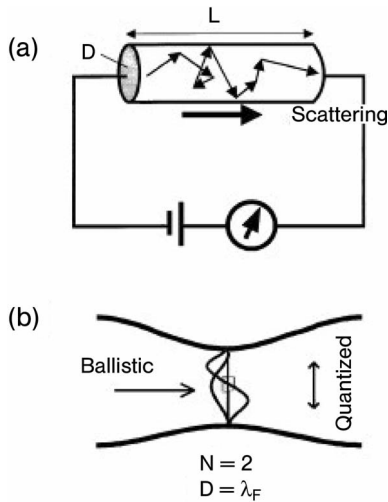


Figure 8.6. Schematic illustration of a diffusive (a) and ballistic (b) conductor. Reprinted with permission from [73]. © 2002, Elsevier.

wavelength, λ_F , of the electrons. The conductance of the system is described by the Landauer formula [74]:

$$G = \frac{2e^2}{h} \sum_{i=1}^N T_i \quad (8.3)$$

where e is the electron charge, h is Planck's constant, N is the number of conduction channels and T_i is the transmission probability of each mode. In an ideal case, T_i is either 0 or 1 and Eq. (8.3) is simplified as $G = NG_0$, where $G_0 = 2e^2/h \sim 1/12.9 \text{ k}\Omega^{-1}$ is the conductance quantum, so the conductance is quantized. This conductance quantization phenomenon was first clearly demonstrated in semiconductor devices containing a two-dimensional electron gas confined in a narrow constriction by the gate voltage, where $\lambda_F \sim 400 \text{ \AA}$ is much larger than the atomic scale [75, 76]. Similar conductance quantization has been observed in three-dimensional metallic contacts created by mechanically breaking a fine metal wire [77] or separating two electrodes in contact [10, 24, 78–80]. Since the wavelength of conduction electrons in a typical metal is only a few \AA , comparable to the size of an atom, a metallic wire with conductance quantized at the lowest steps must be atomically thin. This conclusion was supported by high resolution transmission electron microscopy [81].

8.2.7.3 Electrochemical Properties

Xu et al. measured the quantized conductance changes by modulating the potential of the contacts in an electrolyte. In the regime of double layer charging, the po-

tential modulation induces a conductance modulation with a phase shift of about 180° , but the amplitude depends on the atomic configuration of the wire. A statistical analysis of over 1000 contacts shows that the amplitudes in most contacts with conductance quantized near $1 G_0$ (the thinnest contacts) are about $0.55 G_0 V^{-1}$. The authors attributed the potential-induced conductance modulation to a change in the effective diameters of the contacts, in a fashion similar to the split gate control in the semiconductor quantum wires. A simple model was proposed to explain the phase and the amplitude of the conductance modulation as well as the dependence of the conductance modulation on the diameter of the wire [82, 83].

On the other hand, Xu et al. [83] also studied the potential-induced conductance modulation in electrolytes containing, F^- , Cl^- , Br^- , and I^- . These anions are known to adsorb onto Au electrodes with different strengths [84]. At very negative potentials, the conductance modulations are the same for all the electrolytes, since no substantial anion adsorption takes place. On increasing the potential, however, the induced conductance modulation increases as anions adsorb onto the contact. Figure 8.7 displays that the dependence of the conductance change on the potential correlates well with the adsorption strengths of the anions, in the sequence $F^- < Cl^- < Br^- < I^-$, which is consistent with measurements performed on classical metal films [85–89]. The significant increase in the conductance modulation upon anion adsorption is attributed to the scattering of the conduction electrons in the contact by the adsorbed anions [90, 91]. Because the contact is typically a few atoms long, enough to accommodate only a few ions, the sensitive dependence of the conductance on the adsorption suggests a method to detect a single or a few ions. It has also been observed that the conductance of the atomic scale contacts drops abruptly to a fractional value upon molecular adsorption (Fig. 8.7) [92, 93]. The largest conductance drop occurs for the contacts with conductance at the low-

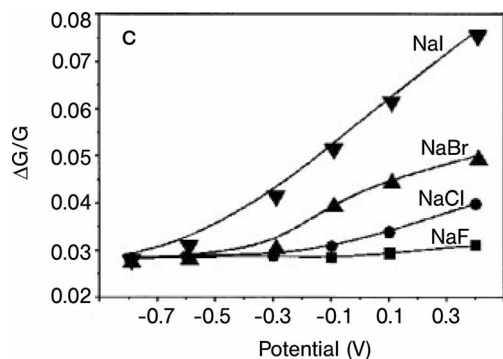


Figure 8.7. The dependence of $\Delta G/G$ on electrochemical potential for nanocontacts with conductance near $1G_0$ in 0.5 M NaF, 0.01 M NaCl + 0.5 M NaF, 0.01 M NaBr + 0.5 M NaF, and 0.01 M NaI + 0.5 M NaF. Reprinted with permission from Ref. [83]. © 2002, American Chemical Society.

est quantum step, and the drop diminishes quickly at higher steps as the quantum ballistic regime is replaced by the classical diffusive regime.

8.2.7.4 Device Properties

Xie et al. [42, 94] reported a gate-controlled atomic quantum switch that opens and closes an electrical circuit reproducibly by controlling the configuration of silver atoms within an atomic scale contact. The only movable parts of the switch are the contacting atoms, which are entirely controlled by an external electrochemical voltage applied to an independent third gate electrode. Figure 8.8(a) demonstrates the control setup and Fig. 8.8(b) a typical switching result. Controlled switching was performed between a quantized, electrically conducting “on state”, exhibiting a conductance of $G_0 = 2e^2/h$ ($\approx 1/12.9$ k Ω) or pre-selectable multiples of this value, and an insulating “off state” [95]. Depending on the properties of the individual contacts, typical on/off ratios between 1000 and more than 3000 were achieved. The switching processes do not occur instantaneously after the control potential is changed, there is a characteristic delay of the order of seconds, depending on contact geometry and ion concentrations. The atomic scale switching process itself, however, occurs on a much shorter time scale.

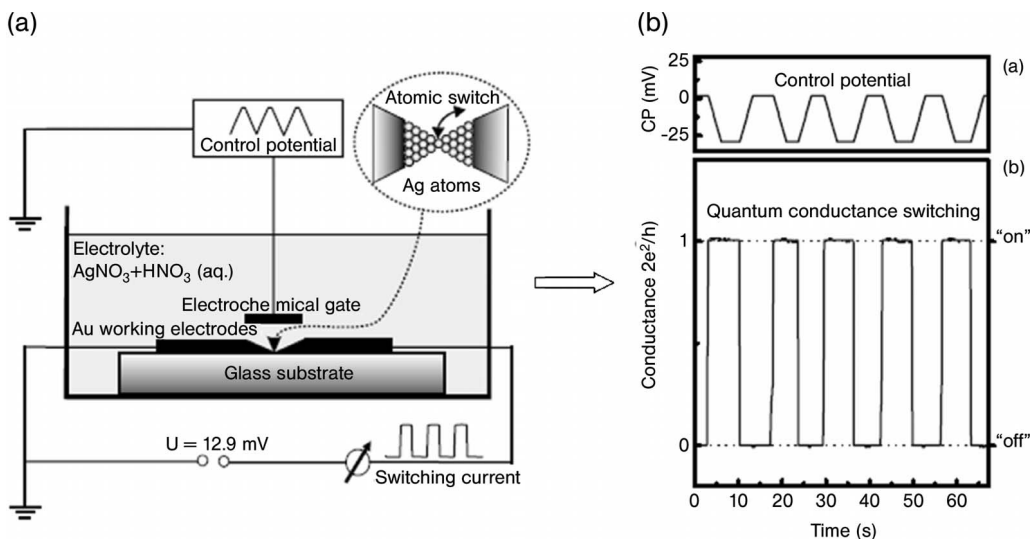


Figure 8.8. (a) Schematic diagram of the experimental setup. (b) Quantum conductance switch controlled by an electrochemical gate. By varying the electrochemical control potential (CP), a digital switching of the quantum point contact between an insulating “off state” and a quantized conducting “on state” at $1 G_0 = 2e^2/h$ is induced. The conductance switches sharply following the changes in electrochemical control potential applied to the reference electrode. Reprinted with permission from Ref. [42]. © 2004, American Physical Society.

Kozicki et al. reported nanoscale memory devices using Se-rich Ge–Se as solid electrolytes [96, 97]. By placing an anode that has oxidizable Ag and an inert cathode (e.g., Ni) in contact with a thin layer of such a material, a device is formed that has an intrinsically high resistance, but which can be switched to a low-resistance state at small voltages via reduction of the silver ions. An opposite bias will bring the device back to the high-resistance state, and this reversible switching effect is the basis of programmable metallization cell technology [98]. In detail, electron beam lithography was used to make sub-100 nm openings in polymethylmethacrylate layers which served as the dielectric between the electrodes. The Ag–Ge–Se [99] electrolyte was created by the photodiffusion of an Ag layer into the Ge–Se base glass [100, 101], and the solid electrolyte film was formed in these via-holes so that their small diameter defined the active switching area between the electrodes. The nanoscale devices write at an applied bias as low as 0.2 V, erase by -0.5 V, and fall from over $10^7 \Omega$ to a low-resistance state (e.g., $10^4 \Omega$ for a $10 \mu\text{A}$ programming current) in less than 100 ns. Cycling appears excellent with projected endurance well beyond 10^{11} cycles. Kozicki et al. also fabricated non-volatile memory based on Ag- or Cu-doped WO_3 , which showed great promise as memory devices. In this case, Cu is the material that is already in use in advanced integrated circuits, and if Cu can be “converted” into embedded memory elements, the cost will be decreased to a quite low level [102, 103].

Aono’s group demonstrated a single-atom memory device using a solid electrochemical reaction [104, 105]. They constructed a crossbar structure using silver sulfide-coated silver wire and platinum wire, in order to easily create switches at the crossing points. When the voltage loaded between the silver and platinum contacts was changed at a high speed, switching was enabled at a frequency of 1 MHz, and this kind of switch is expected to be able to function at 10 GHz in the future. Using this strategy, they have succeeded in achieving four different states, referred to as “0”, “1”, “2”, and “3”, using one terminal, by controlling the degree of contact of a switch. “0” is the off state, in which a switch is detached, “1” is a state in which a switch is connected with one atom, generating slight electrical conductivity, “2” is a state in which a switch is connected with more atoms, generating an electrical conductivity two times higher than that in “1”, and “3” is a state in which a switch is connected with still more atoms, generating an electrical conductivity three times higher than that in “1”. A switch with two terminals can achieve 16 (4×4) different states. Moreover, they also created three types of logical circuits necessary for computer calculations (AND circuit, OR circuit, and NOT circuit) using the above crossbar structure and atomic switches.

8.2.7.5 Magnetic Properties

Equation (8.3) describes the conductance quantization in units of $2e^2/h$, and the factor “2” is due to spin degeneracy. For a ferromagnetic material in which the exchange splitting energy lifts the spin degeneracy, the conductance quantization should be in units of e^2/h . This conductance quantization at integer multiples of $e^2/2h$ has been reported by several groups working on ferromagnetic materials [54, 106, 107].

Another interesting magnetic property in nanocontacts is ballistic magnetoresistance (BMR) which occurs when the spin-flip mean free path is long compared with the magnetic domain-wall width. When a magnetic-domain wall resides in the nanocontact, the electrical resistance changes with the external magnetic field, and the resulting magnetoresistive effect is much larger than giant magnetoresistance (GMR) or tunneling magnetoresistance (TMR). Consequently, BMR has the potential to replace TMR in nonvolatile memory chips and replace GMR in hard-disk read heads [108, 109]. Theoretically, there is so far no consensus on the transport mechanism to explain very large values of BMR. Experimentally, there is large variation in the magnitude of the BMR.

Garcia et al. performed a series of experiments on atomic scale contacts of Fe, Co and Ni, and observed BMR of several hundred percent [110–114]. Their results indicated the trend that the smaller the contact the larger the magnetoresistance response, and these large values of the magnetoresistance were attributed to spin ballistic transport through a magnetic “dead layer” at the contact. Yang et al. studied the magnetoresistance effect of Ni nanocontacts by sweeping an external magnetic field during electrodeposition and etching of nanocontacts [45, 115, 116]. The observed magnetoresistance can be greater than 10% for nanocontacts with conductance values smaller than $50e^2/h$. However, Chopra and Hua reported a 100 000% BMR effect in electrodeposited Ni nanocontacts [117–119].

In addition to Fe, Co and Ni, the magnetoresistance effect has been observed in other materials. For example, Versluijs et al. observed 500% magnetoresistance in magnetite Fe_3O_4 crystallites [120–122]. Yu et al. [123, 124] reported magneto-transport properties in electrochemically fabricated atomic scale gold nanocontacts. At low temperatures, Au nanocontacts exhibit large zero bias anomalies in the differential conductance measurements. They pointed out that the anomalies are consistent with a reduced local density of states in the disordered metal, which may originate from Coulomb interactions in the granular material.

Recently, Chopra et al. [125] measured complete magnetoresistance loops across magnetic quantum point contacts of cobalt that are as small as a single atom. ‘Discrete’ or quantum magnetoresistance loops were observed which were associated with varying transmission probability from the available discrete conductance channels. A remarkable feature of these quantum contacts is the discovery of a rapid oscillatory decay in magnetoresistance with increasing contact size. The results provide an evolutionary trace of spin-dependent transport from a single atom to larger ensembles. This study also rules out the possible magnetostrictive, magnetostatic and magnetomechanical effects that might mimic BMR [40, 126].

8.2.7.6 Sensing Properties

As mentioned before, the conductance of atomic scale contacts is sensitively dependent on molecule adsorption. Therefore, these kinds of nanocontacts may be useful for detecting trace amounts of molecules. Since a metal nanocontact with conductance at the lowest step consists of only a few atoms [81], a microscopic theory that treats the individual atoms and adsorbate molecules seems necessary and the adsorbate scattering is expected to be an important mechanism. Landman

et al. simulated the adsorption of a methyl thiol molecule onto an Au contact made of a chain of four Au atoms between two well-defined electrodes [127]. They found that the molecule binds strongly to the Au atom and becomes a part of the contact. The final conductance of the molecule–Au contact can be even greater than the Au contact. Using a self-consistent scheme, Lang has calculated the conductance through a chain of three Al atoms connected to Jellium electrodes [128]. Substituting one of the Al atoms with a sulfur atom decreases the conductance. The theoretical work mentioned above predicts an adsorbate-induced conductance change, but further theoretical work is needed to explain other experimental observations.

Bogozi et al. [92] studied the changes in the quantized conductance upon adsorption of dopamine, mercaptopropionic acid (MPA), and 2,2'-bipyridine (22BPY) in electrolytes. The conductance decreases as the molecules adsorb onto the nanocontacts, which is attributed to the scattering of the conduction electrons by the adsorbates as the electrons impinge on the surface [91, 129]. The relative conductance change is as large as $\sim 50\%$ for the nanocontacts with conductance quantized at the lowest step, $1 G_0$, but it diminishes at higher conductance steps, where classical diffusive scattering eventually takes over. Figure 8.9 shows the comparative results, from which the highest sensitivity is found with the nanocontacts at low quantum steps, corresponding to a few atoms in thickness. While the thickness-dependent sensitivity is expected from the semi-classical theory as well as the simple surface-to-volume ratio argument, these theories deviate significantly from the experimental data for the thinnest nanocontacts. In addition to the thickness dependence, the adsorbate-induced conductance change depends on the strengths of absorption of the molecules to the nanocontacts. MPA induces the largest change, dopamine the least, and 22BPY is in between, consistent with the relative binding strengths of these three molecules to Cu electrodes. The sensitive dependence of the quantized conductance on molecular adsorption may be used for molecular detection.

Castle et al. [49] employed a self-limiting electrodeposition method to form atomic scale Au contacts with quantized conductance, and measured AC impedance change due to the adsorption of hexadecanethiol (HDT) onto the atom-scale junction. The molecule is a Lewis base and the adsorption onto the atomic scale junction caused a $71 \pm 1\%$ increase in the resistance.

8.3

Electrochemical Fabrication of Metal Nanogaps

The electrochemical deposition method has also been widely used to create metal electrodes with nanometer spacing (referred to as nanogaps or nanoelectrodes) ranging from less than 1 nm to more than 100 nm for different systems, which can be used to connect small molecules or biomolecules, nanoparticles and nanotubes into electrical circuits. Such electrically wired systems can lead to many applications. For example, Javey et al. [130] studied electron transport in single-walled carbon nanotubes with lengths ranging from several microns down to 10 nm.

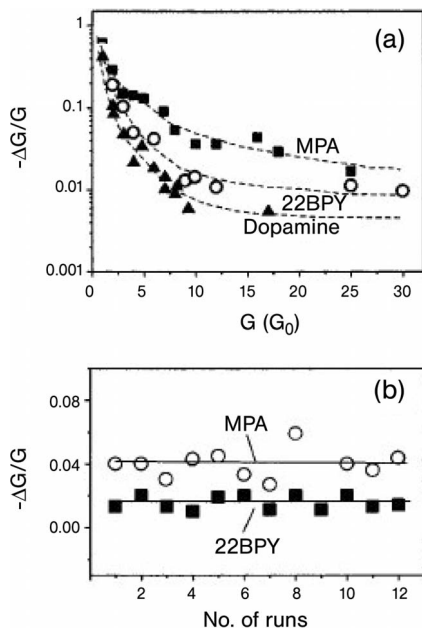


Figure 8.9. (a) Comparison of dopamine-, MPA-, and 22BPY-induced conductance changes in a Cu nanocontact with conductance at various quantum steps. The changes are consistent with the relative binding strengths of the three molecules. Due to the rapid decay in the changes, a logarithmic scale is used. (b) Repeated measurements of MPA- and 22BPY-induced conductance changes in nanocontacts quantized at $10 G_0$. Each data point was obtained from a freshly fabricated nanowire from different chips in order to minimize contamination. Reprinted with permission from Ref. [92]. © 2001, American Chemical Society.

To date, there are many different approaches to the fabrication of electrodes separated with nanogaps. Conventional top-down lithography techniques, such as electron beam lithography, can routinely fabricate electrodes with gaps of a few tens of nm, which is often still too wide for many applications. The MCBJ method [18] mentioned earlier can create gaps of a few nm or less, but the involvement of mechanical actuation is not desirable for many applications. Electromigration is another way to produce nanogaps between electrodes [131, 132]. It works by passing a current through a nanometer scale metal contact. An attractive feature of the technique is the self-termination mechanism because the current drops sharply once a gap is opened anywhere along the contact [133]. The gap size is, however, not controllable after formation since electromigration is not reversible.

The electrochemical method is a versatile approach to the fabrication of electrodes separated by a controllable gap. By electrodepositing metal atoms onto a specific face of electrodes, one can narrow the gap from the micrometer scale

down to a few nm or less. Moreover, the electrodeposition process can be reversed in the electrodisolution mode to etch away unwanted metal atoms from the electrodes back to the electrolyte, thus re-widening the gap until a desired gap width is achieved. The most important feature of the electrochemical method is the possibility to precisely control the gap size with a feedback system. Such signals include the current, resistance, or impedance measured between the electrodes, which can serve as indicators and allow one to monitor the spacing between the electrodes. For example, when the spacing decreases below a couple of nm, electron tunneling between the two electrodes can be used to determine the gap width. There are several different ways to control the electrochemical processes and these are discussed below.

8.3.1

AC-loop Monitoring System

Morpurgo et al. [34] demonstrated an ac-loop monitoring technique to form nanogaps. During the electrodeposition process, they monitored the resistance between two prefabricated electrodes by applying a 4 mV ac bias at 1 Hz using a lock-in amplifier (Fig. 8.10). Three phases of electrodeposition corresponding to different ranges of electrode separation were identified from the time evolution of the resistance. In the first phase, when the electrodes are far apart, the ac monitor current (~ 20 nA) is small and roughly constant. This current is proportional to the immersed surface area of the electrodes (dominated by the surfaces of the counter electrode, gold contact in this case) and results from the ac modulation of the dc deposition current. The second phase is marked by a sudden increase in the monitor current. At this point the electrodes are already very close, less than 5 nm. The additional current observed in this phase is presumably due to direct tunneling between the contacts, enhanced by the screening effect of ions in the gap, which reduces the height of the tunnel barrier. The third phase, when the electrodes fi-

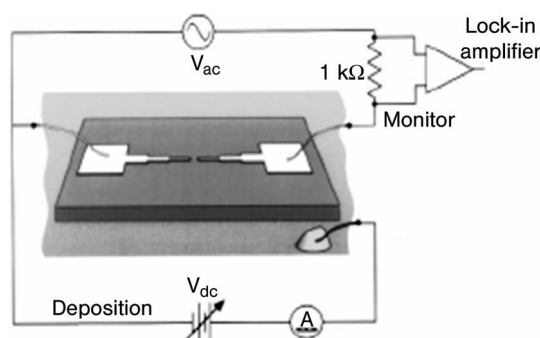


Figure 8.10. A typical ac monitoring system used to control the nanogap width during the electrochemical fabrication. Reprinted with permission from Ref. [34]. © 1999, American Institute of Physics.

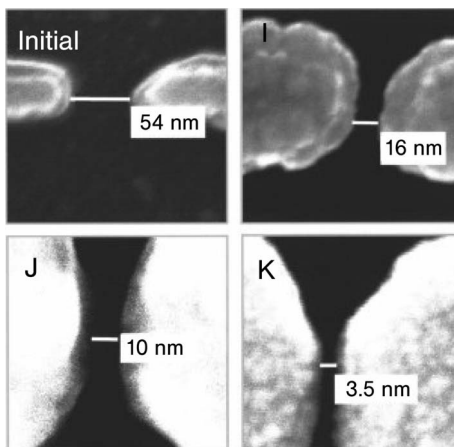


Figure 8.11. Pairs of platinum electrodes with separation between 20 and 3.5 nm after the controlled electrodeposition. Reprinted with permission from Ref. [44]. © 2002, American Institute of Physics.

nally touch, is marked by a sudden jump in the monitor current. During the second phase of electrodeposition, when the electrodes are very close together but not yet touching, the monitor current is extremely sensitive to electrode distance, enabling control of the separation on an atomic scale. Based on this technique, Kervennic et al. [44] have fabricated pairs of platinum electrodes with calibrated separation between 20 and 3.5 nm (Fig. 8.11).

Deshmukh et al. [131] described an electrochemical method to fabricate two electrodes made of dissimilar metals separated by a nanogap. To keep electrodeposition on one of the facing electrodes while making the resistance measurements, the electrode pairs are connected by a 400 μF capacitor. This method enables the fabrication of asymmetric tunnel junctions made of two different metals that exhibit distinct magnetic properties or work functions, which are very difficult to achieve with conventional lithography techniques. Using the method, Kashimura et al. [134] fabricated nanogap electrodes with a gold and platinum finger. They also proposed an electric circuit to form multi-nano electrodes, which offers the potential to develop a variety of molecular devices, since it allows the selection of electrode material, electrode shape, molecular design and method for interfacing between single molecules and electrodes, etc., selective chemisorption.

8.3.2

DC-loop Monitoring System

Tao et al. [35] have developed a method in which a bipotentiostat is used to carry out both electrodeposition and *in situ* monitoring processes. Pairs of Au electrodes with an initial spacing of tens of nm serve as working electrodes 1 and 2 (WE1 and WE2), both of which are kept in negative potential to induce electrodeposition on

them. There exists a small bias difference between WE1 and WE2, usually in the range of tens of mV. By carefully insulating the working electrodes, they can measure the tunneling current from pA to mA, and clearly observed the stepwise variation in the tunneling current during deposition and etching. The stepwise tunneling current originates from the discrete nature of atoms and a series of structural relaxations of the atoms at the electrodes between stable configurations upon deposition and etching. By stabilizing the tunneling current on various steps using a feedback loop, stable molecular-scale gaps, typically, $\sim 0.5 \text{ \AA}$ can be fabricated. This method affords the advantage of making gaps smaller than 1 nm, but is not suitable for larger gaps.

8.3.3

Electric Double Layer as Feedback

Recently, Tian et al. [135] reported a simple chronopotentiometry method where they used the electrical double layer as the feedback signal to control the gap widths ranging from 4.5 nm down to 2 Å (Fig. 8.12). They used one of the initial electrode pairs as the working electrode (WE) and the other as the reference electrode (RE) and monitored the potential difference between WE and RE during the electrodeposition process. Since a constant current is applied between WE and a counter electrode, the potential difference is a fixed value initially when WE and RE are far apart. When the separation between the two electrodes is reduced below the double layer thickness, the potential difference decreases since electrode potential mainly drops across the electrical double layers of the WE and RE electrodes. So, using the potential drop as a feedback, they were able to control the size of the gap over a much greater range than that achieved using tunneling current as a feedback signal [35]. For example, in a diluted electrolyte, the largest gap size

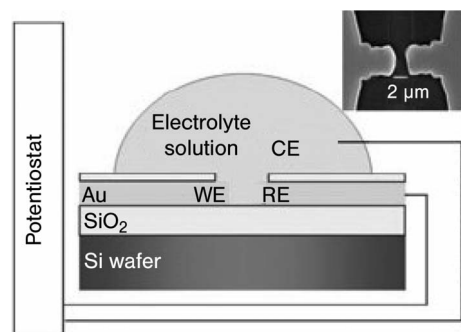


Figure 8.12. Electrochemical setup using electric double layer as feedback to fabricate metallic electrodes with controlled gap widths over a wide range from about 10 nm down to several ångstrom nanogaps. Reprinted with permission from Ref. [135]. © 2005, Wiley-VCH.

accessible for fabrication was found to be as large as 10 nm. The entire process is simple and controllable; enabling rapid fabrication of a wide range of nanogaps without requiring any sophisticated instrumentation or elaborate lithography techniques.

8.3.4

High-frequency Impedance as Feedback

The feedback signal of the above methods normally utilizes a dc or low frequency ac voltage (<10 Hz), in order to minimize the ratio of capacitive reactance to the whole reactance, so the region that the electron can tunnel between electrodes is the gap width people can reach, typically ~ 1 nm. Recently, Chen et al. [38, 136] used a high-frequency impedance as the feedback to control nanogaps over a wider range. In this case, a well designated feedback loop is necessary to monitor the electrodeposition process with different ac amplitudes and frequencies. Through this work, the measured impedance shows distinctive dependence on the ac frequency. At a relatively high frequency (e.g., 3 kHz), the impedance is dominated by capacitive reactance which has been used to fabricate nanogaps of a few tens of nm. This distance is affected by the frequency and the amplitude of the ac signal, and the gap can be further finely tuned to around 1 nm by simply controlling the subsequent deposition time. At low frequency, such as 300 Hz, the impedance is dominated by resistive reactance, reflecting tunneling events between the electrodes. Consequently, the impedance changes significantly only when the gap size is reduced below a few nm. This method can also be used to study the impedance of a confined, nanoscale electrochemical system that is either in equilibrium or in a dynamic state.

8.3.5

Application of Nanogaps

As we have mentioned at the beginning of this section, the most profitable application of metal electrodes separated by nanogaps is to study electron transport in various nanostructures, such as nanoparticles, polymer and even molecular junctions. Below, we provide a brief overview of some of the applications.

One interesting example is conducting polymers. Conducting polymers have attracted much attention in electrochemical synthesis because they can be directly synthesized by electrochemical methods onto metal electrodes and their conductances are tunable by controlling electrochemical parameters [137, 138]. He et al. [139] fabricated nanoelectrodes with a separation as small as nm using an electrodeposition method. They then bridged the small gap with polyaniline. In contrast to the bulk polyaniline, the conductance values of the nanoscale polyaniline junction switch in discrete steps from insulating to conductive phases as a function of the electrode potential. One possible explanation of the discrete conductance steps is individual polymer strands that are successively switched from neutral (insulating) state to oxidized (conducting) state [140]. Using polyaniline nanojunctions

functionalized with peptides, Alvaro et al. [141] demonstrated chemical sensor applications. By choosing different peptide sequences, they detected a trace amount of heavy metal ions in drinking water. The signal transduction mechanism of the sensor is based on the change in the nanojunction conductance as a result of polymer conformational changes induced by the metal-ion chelating peptide.

Recently, Hu et al. [142, 143] demonstrated a successful example of the connection of conjugated polymer molecules between lateral electrodes by chemical bonding. Au nanogap electrodes with gap width ~ 18 nm were generated by combining conventional e-beam lithography and controlled electroplating techniques, then poly(*p*-phenyleneethynylene) derivatives with thiol end groups (TA-PPE) [144] were wired into the electrode pairs monitored with a current–time circuit. As soon as one polymer molecule or one polymer bundle was connected into the circuit, the first current jump was observed in the current signal, and therefore the self-assembly process was stopped by gently removing the polymer solution. In the following measurements, they observed highly periodic and identical stepwise features in current vs. voltage (I – V) curves at room temperature, which were attributed to the opening of different conducting channels that are associated with the unoccupied molecular orbitals of the polymer molecule. Furthermore, Hu et al. investigated the photoresponse and transistor behavior of TA-PPE in self-assembled nanodevices [145]. With photoirradiation on/off, the tunneling junction can be switched on/off quickly as a nanometer-scale photoswitch. With an increase in gate bias, strong conductance oscillation was observed in this self-assembled transistor at the low temperature of 147 K, which is very likely due to single-electron charging oscillations arising from electron tunneling through the device.

Nanoparticles are also a system that has many interesting transport properties and potential device applications. Kervennic et al. [44] fabricated pairs of platinum electrodes with separation between 20 and 3.5 nm using a symmetric electrodeposition setup. By electrostatically capturing Au nanoparticles with different sizes into the nanogaps, they measured the electron transport of the system. The room-temperature resistance of trapped particles typically ranges between 100 M Ω and 10 G Ω , whereas the resistance across the electrodes before trapping is always larger than 100 G Ω . The I – V curves measured on a 5 nm particle exhibit a pronounced nonlinearity, and current suppression was observed at low bias, which is consistent with Coulomb blockade through the cluster. Similarly, Deshmukh et al. [146] have measured the I – V characteristics of 2 nm Au particles at the low temperature of 4.2 K, and the particles were incorporated between Au and Cu electrodes. In this case, Cu was selectively electrodeposited on one of the initial Au electrodes. Their results showed that $\sim 15\%$ of the devices exhibit a Coulomb blockade and the rest exhibit either single-junction tunneling or linear current–voltage characteristics due to tunneling via multiple nanoparticles. Olofsson et al. also studied the charge transport phenomena in self-assembled monolayer modified Au nanoparticles using electrochemically fabricated electrodes [147].

Another application of nanogaps is to measure the charge transport properties in single molecules. Li et al. [148] have used the electrochemically fabricated electrodes to study I – V characteristics in small molecules. They started with a pair of

metal electrodes fabricated with electron beam lithography on a Si substrate. The initial gap between the electrodes is between 20 and 60 nm, which is then reduced to ~ 1 nm by electrodeposition of Au on the electrodes. They then bridged the gap with molecules terminated with thiols to form Au–S bonds between molecules and electrodes. This approach has two major advantages. First, it is highly stable, which allowed them to carefully study the electron transport under different conditions (temperature, magnetic field, etc.). Second, the molecular junctions are supported on an oxidized Si chip, making it possible to study the gate effect on the electron transport of the molecules. Park et al. used self-terminated electrochemical procedures to bridge thiol molecules between prefabricated Pt electrode pairs and measured the temperature-dependent current–voltage characteristic of this molecular junction. In their work, 1,4-benzenedimethanethiol (BDMT) molecules were firstly adsorbed on the surface of Pt electrodes which were fabricated by conventional e-beam lithography; then a dc bias voltage was applied between the two electrodes in an electroplating solution containing 0.1 M K_2PtCl_4 and 0.5 M H_2SO_4 , so that the electrochemical deposition of Pt occurred on the negatively biased electrode. Once the sharpest part of the growing Pt electrode contacted with BDMT molecules adsorbed on the other electrode, they stopped the electrodeposition process and measured the I – V properties of the bridged molecules at different temperature. Their results indicated that the I – V curves are nonlinear and asymmetric over the entire temperature range and the current decreases with decreasing temperature down to 40 K.

However, for most of the electrochemical fabrications to form metal–molecule–metal junctions, the yield of successful molecular junctions is too low to produce a large number of molecular junctions for statistical analysis. More critically, the number of molecules and the binding geometries of the molecules to the Au electrodes are unknown in most cases.

8.4

Summary

This chapter provides an overview of various electrochemical methods for fabricating well defined nanocontacts and nanogaps. Attractive features of the methods are reversibility (via deposition and etching), controllability (via electrode potential) and relatively simple experimental apparatus. Electrochemically fabricated nanocontacts have many fascinating properties, including conductance quantization, BMR behavior and conductance changes due to molecular adsorption. Potential applications of the nanocontacts range from single atom memory devices and hard disk heads to chemical and biosensors. On the other hand, nanogaps are suitable for wiring nanostructures into electrical circuits and thus allowing one to study electron transport in the nanostructures and develop applications based on electrically wired nanostructures.

In spite of the great success, there are still many open questions and remaining challenges. For example, because the length scale of the nanocontacts and nano-

gaps is comparable with the double layer thickness of the electrode/electrolyte interfaces, the applicability of the theories developed for bulk electrodes becomes questionable. Another remaining challenge is the ability to precisely control the gap size over a wide range. For a gap size narrower than a few nm, electron tunneling provides a good feedback signal that can control the gap size down to a single atom. However, long term stability of such a small gap varies from run to run. For larger gap widths, the tunneling current becomes too small to be measured. Although several alternative feedback signals have been used, these signals often depend on the microscopic state of the initial electrodes such as local surface morphology, and electrode geometries that are not easily reproduced by tuning macroscopic parameters.

Acknowledgment

The authors thank NSF, DOE and VW for financial support.

References

- 1 H. W. C. POSTMA, et al., *Science* **293** (2001) 76–79.
- 2 Y. CUI, C. M. LIEBER, *Science* **291** (2001) 851–853.
- 3 A. AVIRAM, M. A. RATNER, *Chem. Phys. Lett.* **29** (1974) 277–283.
- 4 N. AGRAIT, A. L. YEYATI, J. M. VAN RUITENBEEK, *Phys. Rep.* (review section of *Phys. Lett.*) **377** (2003) 81–279.
- 5 M. RINGGER, et al., *Appl. Phys. Lett.* **46** (1985) 832–834.
- 6 U. STAUFER, et al., *Appl. Phys. Lett.* **51** (1987) 244–246.
- 7 J. A. DAGATA, et al., *Appl. Phys. Lett.* **56** (1990) 2001–2003.
- 8 R. M. PENNER, *Scanning Microsc.* **7** (1993) 805–813.
- 9 D. M. KOLB, F. C. SIMEONE, *Electrochim. Acta* **50** (2005) 2989–2996.
- 10 J. K. GIMZEWSKI, R. MOLLER, *Phys. Rev. B* **36** (1987) 1284–1287.
- 11 U. DURIG, O. ZUGER, D. W. POHL, *Phys. Rev. Lett.* **65** (1990) 349–352.
- 12 X. D. CUI, et al., *Science* **294** (2001) 571–574.
- 13 S. DATTA, *Electronic Transport in Mesoscopic Systems*, Cambridge University Press, Cambridge, (1997).
- 14 S. DATTA, et al., *Phys. Rev. Lett.* **79** (1997) 2530–2533.
- 15 S. M. LINDSAY, *Jpn. J. Appl. Phys.* **41** (2002) Part 1, 4867–4870.
- 16 B. Q. XU, N. J. J. TAO, *Science* **301** (2003) 1221–1223.
- 17 J. MORELAND, J. W. EKIN, *J. Appl. Phys.* **58** (1985) 3888–3895.
- 18 C. J. MULLER and R. D. OUBOTER, *J. Appl. Phys.* **77** (1995) 5231–5236.
- 19 M. A. REED, et al., *Science* **278** (1997) 252–254.
- 20 R. M. METZGER, et al., *J. Am. Chem. Soc.* **119** (1997) 10455–10466.
- 21 C. ZHOU, et al., *Appl. Phys. Lett.* **71** (1997) 611–613.
- 22 H. X. HE, N. J. TAO, Electrochemical Fabrication of Metal Nanowires, in *Encyclopedia of Nanoscience and Nanotechnology*, H. S. NAIWA (ed.), American Scientific Publishers, (USA), (2003), pp. 1–18.
- 23 I. K. YANSON, *Zh. Eksp. Teoret. Fiz.* **66** (1974) 1035–1050.
- 24 L. OLESEN, et al., *Phys. Rev. Lett.* **72** (1994) 2251–2254.
- 25 C. Z. LI, N. J. TAO, *Appl. Phys. Lett.* **72** (1998) 894–896.
- 26 N. J. TAO, *J. Chem. Educ.* **82** (2005) 720–726.
- 27 M. KIGUCHI, et al., *Phys. E-Low-Dimensional Systems & Nanostructures* **29** (2005) 530–533.

- 28 C. SHU, et al., *Phys. Rev. Lett.* **84** (2000) 5196–5199.
- 29 M. HUGELMANN, et al., *Surf. Sci.* **597** (2005) 156–172.
- 30 M. HUGELMANN, W. SCHINDLER, *Appl. Phys. Lett.* **85** (2004) 3608–3610.
- 31 E. S. SNOW, P. M. CAMPBELL, D. PARK, *Superlattices Microstruct.* **20** (1996) 545–553.
- 32 E. S. SNOW, P. M. CAMPBELL, *Phys. B* **227** (1996) 279–281.
- 33 P. M. CAMPBELL, E. S. SNOW, P. J. McMARR, *Surf. Sci.* **362** (1996) 870–873.
- 34 A. F. MORPURGO, C. M. MARCUS, D. B. ROBINSON, *Appl. Phys. Lett.* **74** (1999) 2084–2086.
- 35 C. Z. LI, H. X. HE, N. J. TAO, *Appl. Phys. Lett.* **77** (2000) 3995–3997.
- 36 C. Z. LI, et al., *Appl. Phys. Lett.* **76** (2000) 1333–1335.
- 37 B. LIU, et al., *Electrochim. Acta* **50** (2005) 3041–3047.
- 38 F. CHEN, et al., *Appl. Phys. Lett.* **86** (2005) 123105.
- 39 M. W. WU, L. L. SOHN, *IEEE Electron. Device Lett.* **21** (2000) 277–279.
- 40 J. J. MALLETT, et al., *Phys. Rev. B* **70** (2004) 172406.
- 41 A. UMEMO, K. HIRAKAWA, *Appl. Phys. Lett.* **86** (2005) 143103.
- 42 F. Q. XIE, C. OBERMAIR, T. SCHIMMEL, *Solid State Commun.* **132** (2004) 437–442.
- 43 Y. V. KERVENNIC, et al., *Appl. Phys. Lett.* **83** (2003) 3782–3784.
- 44 Y. V. KERVENNIC, et al., *Appl. Phys. Lett.* **80** (2002) 321–323.
- 45 C. S. YANG, et al., *Appl. Phys. Lett.* **84** (2004) 2865–2867.
- 46 O. CESPEDES, et al., *J. Magn. Magn. Mater.* **242** (2002) Part 1, 492–494.
- 47 S. NAKABAYASHI, et al., *Nano Lett.* **1** (2001) 507–510.
- 48 S. BOUSSAAD, N. J. TAO, *Appl. Phys. Lett.* **80** (2002) 2398–2400.
- 49 P. J. CASTLE, P. W. BOHN, *Anal. Chem.* **77** (2005) 243–249.
- 50 C. Z. LI, et al., *Nanotechnology* **10** (1999) 221–223.
- 51 J. Z. LI, et al., *Appl. Phys. Lett.* **81** (2002) 123–125.
- 52 J. Z. LI, et al., *Chem. Commun.* (2001) 2170–2171.
- 53 F. ELHOSSINE, et al., *J. Appl. Phys.* **93** (2003) Part 3, 8567–8569.
- 54 F. ELHOSSINE, et al., *Appl. Phys. Lett.* **81** (2002) 1681–1683.
- 55 K. TERABE, T. NAKAYAMA, N. IYI, M. AONO, *Proc. 9th Int. Conf. on Production Engineering*, Y. FURUKAWA, Y. MORI, T. KATAOKA (Eds.), (1999), pp. 711–716.
- 56 K. TERABE, et al., *J. Appl. Phys.* **91** (2002) 10110–10114.
- 57 K. TERABE, T. HASEGAWA, T. NAKAYAMA, M. AONO, *Riken Rev.* **37** (2001) 7–8.
- 58 T. SAKAMOTO, et al., *Appl. Phys. Lett.* **82** (2003) 3032–3034.
- 59 J. J. RIQUELME, et al., *Europhys. Lett.* **70** (2005) 663–669.
- 60 K. L. JOHNSON, *Contact Mechanics*, Cambridge University Press, Cambridge, (1985).
- 61 E. M. L. L. D. LANDAU, *Theory of Elasticity, Landau and Lifshitz Course of Theoretical Physics*. 3rd edn. Pergamon Press, Oxford, Vol. 7, (1986).
- 62 N. AGRAIT, et al., *Thin Solid Films* **253** (1994) 199–203.
- 63 N. AGRAIT, G. RUBIO, S. VIEIRA, *Phys. Rev. Lett.* **74** (1995) 3995–3998.
- 64 N. AGRAIT, G. RUBIO, S. VIEIRA, *Langmuir* **12** (1996) 4505–4509.
- 65 G. RUBIO, N. AGRAIT, S. VIEIRA, *Phys. Rev. Lett.* **76** (1996) 2302–2305.
- 66 C. UNTIEDT, et al., *Phys. Rev. B* **56** (1997) 2154–2160.
- 67 A. STALDER, U. DURIG, *J. Vacuum Sci. Technol. B* **14** (1996) 1259–1263.
- 68 H. X. HE, et al., *J. Electroanal. Chem.* **522** (2002) 26–32.
- 69 N. J. TAO, J. A. DEROSE, S. M. LINDSAY, *J. Phys. Chem.* **97** (1993) 910–919.
- 70 J. L. COSTAKRAMER, et al., *Phys. Rev. B* **55** (1997) 5416–5424.
- 71 G. RUBIO-BOLLINGER, et al., *Phys. Rev. Lett.* **8702** (2001) 026101.
- 72 S. WASHBURN, Resistance fluctuations in small samples: be careful when playing with Ohm's law, in *Quantum Coherence in Mesoscopic Systems*, B. KRAMER (Ed.), Plenum Press, New York, (1991) pp. 341–367.

- 73 H. X. HE, et al., *J. Electroanal. Chem.* **522** (2002) 167–172.
- 74 R. LANDAUER, *IBM J. Res. Devel.* **1** (1957) 223–231.
- 75 D. A. WHARAM, et al., *J. Phys. C-Solid State Phys.* **21** (1988) L209–L214.
- 76 B. J. VANWEEES, et al., *Phys. Rev. Lett.* **60** (1988) 848–850.
- 77 J. M. KRANS, et al., *Nature* **375** (1995) 767–769.
- 78 J. I. PASCUAL, et al., *Phys. Rev. Lett.* **71** (1993) 1852–1855.
- 79 J. L. COSTAKRAMER, et al., *Surf. Sci.* **342** (1995) L1144–L1149.
- 80 H. YASUDA and A. SAKAI, *Phys. Rev. B* **56** (1997) 1069–1072.
- 81 H. OHNISHI, Y. KONDO, K. TAKAYANAGI, *Nature* **395** (1998) 780–783.
- 82 B. Q. XU, et al., *Electrochim. Acta* **48** (2003) 3085–3091.
- 83 B. Q. XU, H. X. HE, N. J. TAO, *J. Am. Chem. Soc.* **124** (2002) 13568–13575.
- 84 J. LIPKOWSKI, et al., *Electrochim. Acta* **43** (1998) 2875–2888.
- 85 G. A. FRIED, Y. M. ZHANG, P. W. BOHN, *Thin Solid Films* **401** (2001) 171–178.
- 86 R. I. TUCCERI, D. POSADAS, *J. Electroanal. Chem.* **283** (1990) 159–166.
- 87 R. I. TUCCERI, D. POSADAS, *J. Electroanal. Chem.* **270** (1989) 415–419.
- 88 R. I. TUCCERI, D. POSADAS, *J. Electroanal. Chem.* **191** (1985) 387–399.
- 89 H. WINKES, D. SCHUMACHER, A. OTTO, *Surf. Sci.* **400** (1998) 44–53.
- 90 R. G. TOBIN, *Surf. Sci.* **502** (2002) 374–387.
- 91 B. N. J. PERSSON, *J. Chem. Phys.* **98** (1993) 1659–1672.
- 92 A. BOGOZI, et al., *J. Am. Chem. Soc.* **123** (2001) 4585–4590.
- 93 C. Z. LI, H. SHA, N. J. TAO, *Phys. Rev. B* **58** (1998) 6775–6778.
- 94 F. Q. XIE, et al., *Phys. Rev. Lett.* **93** (2004) 128303.
- 95 D. P. E. SMITH, *Science* **269** (1995) 371–373.
- 96 M. I. MITKOVA, M. N. KOZICKI, J. P. ABEROUE, *J. Non-Cryst. Solids* **326** (2003) 425–429.
- 97 M. N. KOZICKI, M. PARK, M. MITKOVA, *IEEE Trans. Nanotechnol.* **4** (2005) 331–338.
- 98 M. N. KOZICKI, et al., *Superlattices Microstruct.* **34** (2003) 459–465.
- 99 M. MITKOVA, M. N. KOZICKI, *J. Non-Cryst. Solids* **299** (2002) Part B, 1023–1027.
- 100 M. MITKOVA, et al., *J. Non-Cryst. Solids* **338–40** (2004) 552–556.
- 101 M. MITKOVA, et al., *Thin Solid Films* **449** (2004) 248–253.
- 102 G. C. KOZICKI, M. BALAKRISHNAN, M. PARK, M. MITKOVA, Non-Volatile Memory Based on Solid Electrolytes, in *Proceedings of the 2004 Non-Volatile Memory Technology Symposium*, (2004), pp. 10–17.
- 103 N. E. GILBERT, C. GOPALAN, M. N. KOZICKI, *Solid-State Electron.* **49** (2005) 1813–1819.
- 104 K. TERABE, et al., *Nature* **433** (2005) 47–50.
- 105 J. VAN RUITENBEEK, *Nature* **433** (2005) 21–22.
- 106 H. OSHIMA, K. MIYANO, *Appl. Phys. Lett.* **73** (1998) 2203–2205.
- 107 T. ONO, et al., *Appl. Phys. Lett.* **75** (1999) 1622–1624.
- 108 G. A. PRINZ, *Science* **282** (1998) 1660–1663.
- 109 E. Y. TSYMBAL, D. G. PETTIFOR, Perspectives of giant magnetoresistance, *Solid State Phys.* (2001), 113–237.
- 110 N. GARCIA, et al., *Appl. Phys. Lett.* **79** (2001) 4550–4552.
- 111 N. GARCIA, M. MUNOZ, Y. W. ZHAO, *Phys. Rev. Lett.* **82** (1999) 2923–2926.
- 112 N. GARCIA, M. MUNOZ, Y. W. ZHAO, *Appl. Phys. Lett.* **76** (2000) 2586–2587.
- 113 N. GARCIA, G. G. QIANG, I. G. SAVEDIEV, *Appl. Phys. Lett.* **80** (2002) 1785–1787.
- 114 N. GARCIA, et al., *Phys. Rev. Lett.* **85** (2000) 3053–3056.
- 115 C. S. YANG, et al., *J. Magn. Magn. Mater.* **286** (2005) 186–190.
- 116 C. S. YANG, et al., *J. Phys.-Condens. Matter* **14** (2002) L765–L771.
- 117 H. D. CHOPRA, S. Z. HUA, *Phys. Rev. B* **66** (2002) 020403.

- 118 S. Z. HUA, H. D. CHOPRA, *Phys. Rev. B* **67** (2003) 060401.
- 119 M. R. SULLIVAN, et al., *Phys. Rev. B* **71** (2005) 024412.
- 120 J. M. D. COEY, J. J. VERSLUIJS, M. VENKATESAN, *J. Phys. D-Appl. Phys.* **35** (2002) 2457–2466.
- 121 J. J. VERSLUIJS, J. M. D. COEY, *J. Magn. Mater.* **226** (2001) Part 1, 688–689.
- 122 J. J. VERSLUIJS, M. A. BARI, J. M. D. COEY, *Phys. Rev. Lett.* **8702** (2001) 026601.
- 123 L. H. YU, D. NATELSON, *Phys. Rev. B* **68** (2003) 113407.
- 124 L. H. YU, D. NATELSON, *Appl. Phys. Lett.* **82** (2003) 2332–2334.
- 125 H. D. CHOPRA, et al., *Nature Mater.* **4** (2005) 832–837.
- 126 W. F. EGELHOFF, et al., *J. Appl. Phys.* **95** (2004) Part 2, 7554–7559.
- 127 H. HAKKINEN, R. N. BARNETT, U. LANDMAN, *J. Phys. Chem. B* **103** (1999) 8814–8816.
- 128 N. D. LANG, *Phys. Rev. B* **52** (1995) 5335–5342.
- 129 H. ISHIDA, *Phys. Rev. B* **52** (1995) 10819–10822.
- 130 A. JAVEY, et al., *Phys. Rev. Lett.* **92** (2004) 106804.
- 131 J. PARK, et al., *Nature* **417** (2002) 722–725.
- 132 W. J. LIANG, et al., *Nature* **417** (2002) 725–729.
- 133 H. PARK, et al., *Appl. Phys. Lett.* **75** (1999) 301–303.
- 134 Y. KASHIMURA, et al., *Thin Solid Films* **438** (2003) 317–321.
- 135 M. L. TIAN, et al., *Nano Lett.* **3** (2003) 919–923.
- 136 Q. QING, et al., *Angew. Chem. Int. Ed.* **44** (2005) 7771–7775.
- 137 H. S. WHITE, G. P. KITTLESEN, M. S. WRIGHTON, *J. Am. Chem. Soc.* **106** (1984) 5375–5377.
- 138 E. T. T. JONES, O. M. CHYAN, M. S. WRIGHTON, *J. Am. Chem. Soc.* **109** (1987) 5526–5528.
- 139 H. X. HE, et al., *J. Am. Chem. Soc.* **123** (2001) 7730–7731.
- 140 H. X. HE, et al., *Phys. Rev. B* **68** (2003) 045302.
- 141 A. D. AGUILAR, et al., *Appl. Phys. Lett.* **87** (2005) 193108.
- 142 W. P. HU, et al., *Phys. Rev. Lett.* **96** (2006) 027801.
- 143 W. P. HU, et al., *Appl. Phys. Lett.* **85** (2004) 115–117.
- 144 W. P. HU, et al., *Phys. Rev. B* **69** (2004) 165207.
- 145 W. P. HU, et al., *J. Am. Chem. Soc.* **127** (2005) 2804–2805.
- 146 M. M. DESHMUKH, et al., *Nano Lett.* **3** (2003) 1383–1385.
- 147 L. G. M. OLOFSSON, et al., *J. Low Temp. Phys.* **118** (2000) 343–353.
- 148 X. L. LI, et al., *Surf. Sci.* **573** (2004) 1–10.

9 Nanowires by Electrochemical Step Edge Decoration (ESED)

Reginald M. Penner

9.1 Introduction

In 1999, Michael Zach demonstrated that MoO_2 , an electronically conductive oxide, could be selectively electrodeposited at the step edges present on a graphite electrode. When this electrodeposition was continued for several hundred seconds, electrically continuous MoO_2 nanowires were formed along the step edges on the graphite surface and these nanowires could be more than 100 μm in length [1]. Zach's observations marked the beginning of the development by this research group of a new family of methods for preparing nanowires based on the electrocrystallization of materials at the step edges present on the basal plane of highly oriented pyrolytic graphite (HOPG) electrodes [2, 3]. Collectively, we term these methods electrochemical step edge decoration or ESED.

ESED can be implemented in three different modes to produce nanowires. The most straightforward approach, effective for many metals and metal oxides (Table 9.1), is simply to electrodeposit the material of interest directly at step edges [1, 4–8]. For compounds, such as CdSe and Bi_2Te_3 , direct electrodeposition fails to produce the required stoichiometry, and instead, cyclic electrodeposition/stripping protocols have been developed to produce nanowires possessing the correct composition [9, 10]. The third method involves the formation by ESED of nanowires of a precursor material that is subsequently reacted with a second gas phase reactant at elevated temperature to produce nanowires of the desired compound. This “electrochemical/chemical” approach was originally applied to the synthesis of semiconductor nanoparticles [11–15] but recently we have adapted it to the synthesis of nanowires composed of the compounds CdS (from cadmium metal using H_2S) [16] and MoS_2 (from MoO_2 using H_2S) [17, 18] as well as the metal molybdenum (also from MoO_2 but using H_2) [1, 8]. A final nuance is the possibility of reducing the diameters of nanowires by electrooxidation. Electrooxidation has been employed to “etch” nanowires of antimony, gold and Bi_2Te_3 , reducing the diameter of these nanowires from more than 100 nm to less than 50 nm [5]. In this chapter, we review progress in the area of ESED nanowire synthesis, describing each of these ESED methods in greater detail.

Table 9.1. Summary of nanowire syntheses by electrochemical step edge decoration.

Material	ESED Method	Wire diameter (nm)	Functional properties evaluated	Ref(s).
Mo	E/C ^[a]	1000–15	electrical	1, 8
MoO ₂	direct	1250–20	none	1, 8
MnO ₂	direct	150–40	none	19
Pd	direct	500–50	electrical, hydrogen sensing	4, 6
Ag	direct	1000–200	electrical, ammonia sensing	20, 21
Pt, Cu	direct	750–60	electrical	2, 7
Ag _x O	direct	1100–700	electrical, ammonia sensing	22
Au	direct + EO ^[b]	300–50	none	5, 7
Sb	direct + EO	300–30	none	5
Bi ₂ Te ₃	cyclic ED/S ^[c] + EO	300–30	electrical, thermoelectric power generation	5, 10
CdSe	cyclic ED/S	300–30	photoluminescence	9
CdS	E/C	116–550	photoluminescence, photoconductivity	16
MoS ₂	E/C	800–50 (w) × 3–100 (h)	optical absorbance	17, 18
SiO ₂	CVD ^[d]	80 (w) × 20–40 (h)	none	23

^aE/C = electrochemical/chemical. ^bEO = electrooxidation. ^cED/S = electrodeposition/stripping. ^dSiO₂ “nanowires” were obtained by reacting SiCl₄ vapor with water physisorbed at step edges on the HOPG basal plane. This synthesis is a chemical, not electrochemical, process.

9.2

General Considerations

Based on our experience with ESED over a period of more than 6 years, the localization of electrodeposition at step edges is only possible at HOPG and other layered materials such as MoS₂. We have been unsuccessful, for example, at achieving step edge decoration at hydrogen-terminated silicon electrode surfaces, in spite of the fact that H-Si(111) exhibits a very low surface free energy, very much like that of HOPG. What makes HOPG unique? The answer seems to be that step edges on HOPG behave like linear nanoelectrodes – lines along which electron transfer to solution-phase redox species is catalyzed. This idea is at least 15 years old, since the electrocatalytic nature of step edges on graphite was recognized and

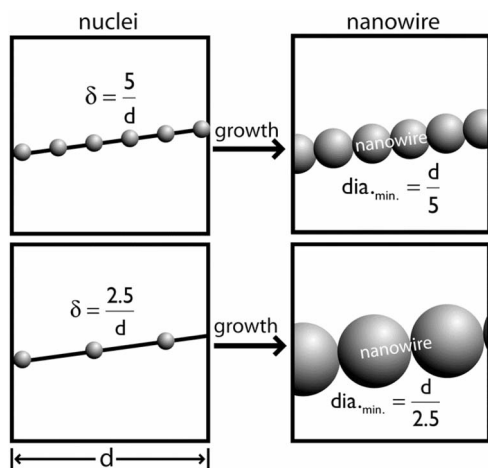


Figure 9.1. Reciprocal relationship between the nucleation density, δ , and the minimum nanowire diameter, $\text{dia}_{\text{min.}}$ for nanowires prepared by ESED.

investigated by McCreary and coworkers [19–21] who demonstrated a clear correlation between the presence of lattice defects on graphite surfaces and the rate of electron transfer to solution-phase redox species.

Irrespective of the material that is electrodeposited, the formation of nanowires by ESED occurs in two steps: First, nanoparticles are nucleated on step edges and terraces of the HOPG surface, and second, these nanoparticles are grown until they coalesce into electrically continuous nanowires. This mechanism produces polycrystalline nanowires with a distinctive morphology in which grains of the deposited material, each derived from a nanoscopic nucleus, are arrayed in a line along the axis of each nanowire, as shown in Fig. 9.1. A second implication of this mechanism, also shown in Fig. 9.1, is that the minimum nanowire diameter, $\text{dia}_{\text{min.}}$, is inversely proportional to the density of nuclei present on the step edges, δ . Since an objective of nanowire growth is often to obtain the smallest possible nanowires, within the context of the ESED method this objective translates into a requirement for the highest possible δ values.

A clear trend has become apparent as we have attempted to prepare nanowires from a variety of different electrodeposited materials. We find that δ increases as the heterogeneous electron transfer rate constant for the deposition reaction becomes smaller. In other words, reactions that are kinetically slow, such as the electrodeposition of MoO_2 from MoO_4^{2-} , produce a high nucleation density at step edges ($\delta > 20 \mu\text{m}^{-1}$) and readily form nanowires, whereas reactions that are kinetically facile, such as silver ion reduction, tend to produce a low nucleation density ($\delta < 5 \mu\text{m}^{-1}$). The products of these fast electron transfer reactions are the most challenging from which to obtain nanowires using the ESED method. This correlation is qualitative since reliable rate constants for many of the reactions we have

investigated have not been measured, but it is useful to ask what is its origin? One possible explanation is the following: A large δ is promoted by the application of a large overpotential, but nucleation is also inhibited in the vicinity of growing nuclei by the formation, around each growing nucleus, of a diffusion layer that is depleted of reactant. Since this nucleation “self inhibition” requires rapid, diffusion-controlled growth it is reduced or eliminated in cases where the kinetic barriers slow the growth of nuclei and eliminate the diffusion layers around growing nuclei (in the limit of kinetically controlled growth, no concentration polarization is present). Conversely, nucleation “self-inhibition” occurs efficiently, and is very difficult to eliminate, for deposition reactions that are kinetically facile.

9.3

Direct Nanowire Electrodeposition

Step edge localized growth on HOPG surfaces is most easily achieved for the electrodeposition of electronically conductive metal oxides such as MoO₂ [1, 8], Cu₂O [3] or MnO₂ [22]. For these materials, ESED is implemented by applying a single, small amplitude potentiostatic pulse lasting several hundred seconds and the degree of step edge selectivity is directly related to the electrodeposition overpotential, η_{dep} , of this pulse. This effect is shown in Fig. 9.2 for the electrodeposition of MoO₂ according to the reaction:



At an applied potential of just -0.70 V vs. SCE, nearly perfect step edge selectivity is observed for the deposition of MoO₂ (Fig. 9.2C) with virtually no electrodeposition observed away from step edges on the terraces of this surface. As this potential is made progressively more negative (Fig. 9.2D–E), an increasing number of particles are seen on these terraces until at the most negative potential of -2.2 V (Fig. 9.2F), step edges can hardly be distinguished from terraces. In practice, the value of η_{dep} employed for nanowire growth is a compromise.

Another characteristic of the ESED experiment is the observation of a pseudo-constant deposition current during nanowire growth (Fig. 9.2B). This constant current permits the derivation of an equation governing the time dependence of nanowire growth:

$$r(t) = \sqrt{\frac{2i_{\text{dep}}t_{\text{dep}}V_{\text{m}}}{\pi nFl}} \quad (9.2)$$

where i_{dep} is the deposition current density, t_{dep} is the deposition duration, V_{m} is the molar volume of the deposited material ($19.8 \text{ cm}^3 \text{ mol}^{-1}$ for MoO₂), n is the number of electrons transferred, and l is the total length of nanowires on the graphite surface. Equation (9.2) predicts that growing nanowires become smoother,

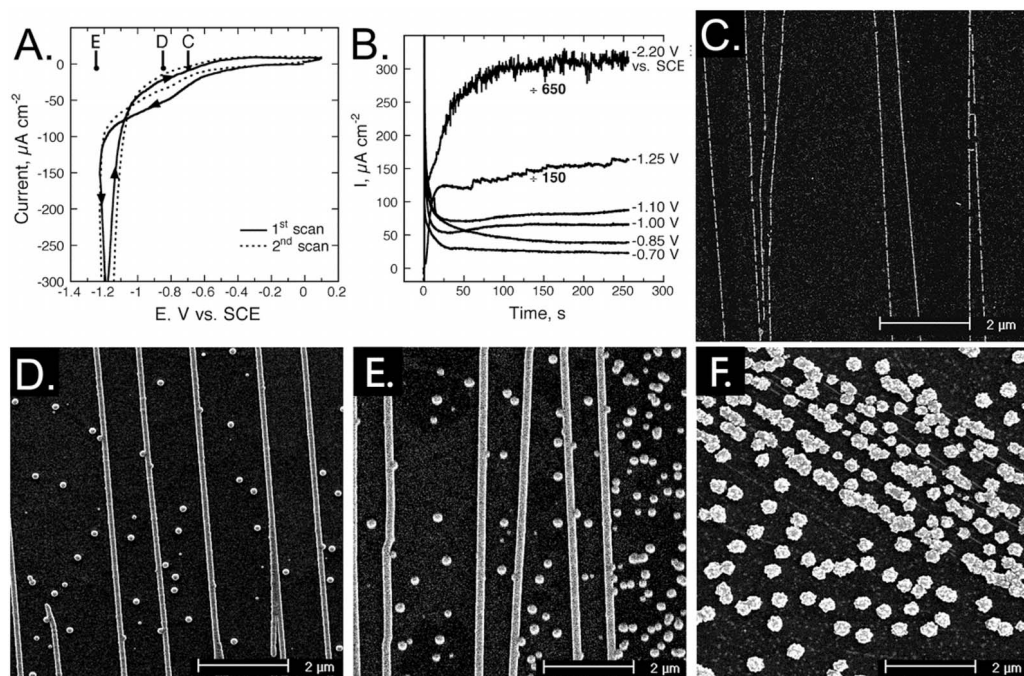


Figure 9.2. (A) Cyclic voltammogram at 20 mV s^{-1} for an HOPG working electrode in an aqueous plating solution containing $1 \text{ mM Na}_2\text{MoO}_4$, 1.0 M NaCl , $1.0 \text{ M NH}_4\text{Cl}$ and adjusted to pH 8.5 with the addition of aqueous NH_3 . (B) Current versus time for the electrodeposition of MoO_2 from the plating solution described in (A). (C to F) Scanning electron microscope (SEM) images of

graphite surfaces after the electrodeposition of MoO_2 for 256 s (or 1024 s in (C) only). The plating solution in these experiments was $7 \text{ mM Na}_2\text{MoO}_4$, 1.0 M NaCl , $1.0 \text{ M NH}_4\text{Cl}$, pH 8.5. The deposition potential becomes progressively more negative in these six experiments as follows: -0.70 V vs. SCE (C), -0.85 V (D), -1.1 V (E), and -2.2 V (F). After Ref. [8].

and this effect is shown in the calculation of Fig. 9.3A which shows the time evolution of the mean nanowire radius, $\langle r \rangle$, and the standard deviation of the radius, σ_r , for a nanowire consisting of a linear ensemble of 20 nm nanoparticles. Wire diameter distributions (Fig. 9.3B) become narrower as a function of growth time as a consequence of these “convergent” growth kinetics.

Nanowires composed of metals, including antimony, copper, silver, gold, platinum, and palladium have also been obtained by this direct deposition ESED technique (Table 9.1). However, the deposition algorithm in this case is more complex than for metal oxides, involving the application of three successive voltage pulses as shown in Fig. 9.4.

Copper nanowires produced using this procedure are shown in the scanning electron micrographs of Fig. 9.5. In these images, the distinctive grain structure alluded to in Fig. 9.1 is readily apparent.

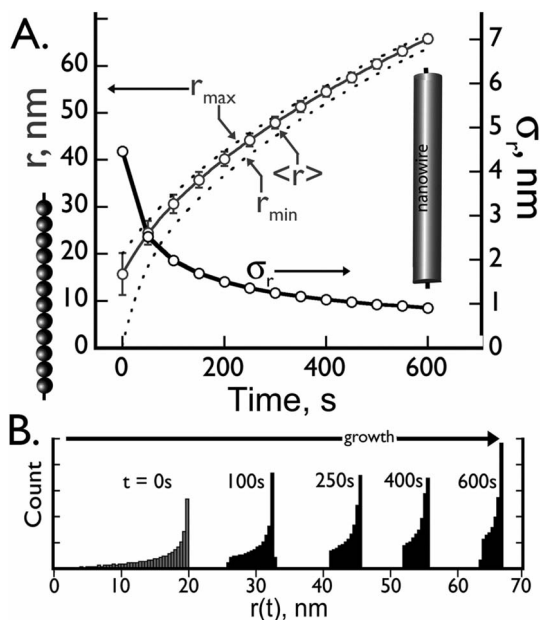


Figure 9.3. (A) Calculated mean nanowire radius, $\langle r \rangle$, and radius distribution, versus time calculated using Eq. (9.1) starting with a nanowire consisting of hemispherical silver particles with a radius of 20 nm. Other parameters used in this calculation were the following: $i_{dep} = 1 \times 10^{-9} \text{ A cm}^{-2}$, $V_m = 10.26 \text{ cm}^3 \text{ mol}^{-1}$, $l = 1 \text{ cm}$. Dotted lines show increase in radius for largest (r_{max}) and smallest (r_{min}) wire segments. The standard deviation of the radius, σ_r , versus time is plotted as labelled. (B) Histogram of wire radii shown at several times during the deposition. After Ref. [5].

9.4

Compound Nanowires by Cyclic Electrodeposition/Stripping

Compounds are difficult to electrodeposit potentiostatically from solutions containing two or more precursor species because it is difficult to locate a potential corresponding to the correct stoichiometry. An additional complication is the possibility that compound formation from electrodeposited precursors can be incomplete. One strategy that circumvents both of these issues is cyclic electrodeposition/stripping. In a cyclic electrodeposition/stripping experiment, the compound of interest is electrodeposited together with excesses of one or more reactants in a forward scan, say, to negative potentials. These excess reactants are then electrochemically removed (“stripped”) during a subsequent positive-going scan leaving the compound of interest. By repeating this electrodeposition/stripping scan sequence, Sailor and coworkers [23] demonstrated that highly stoichiometric CdSe films could be synthesized. We have adapted the Sailor strategy to the synthesis of nanowires composed of two different compounds: Bi_2Te_3 , a material of interest for thermoelectric applications [10], and CdSe, a direct-gap semiconductor [9].

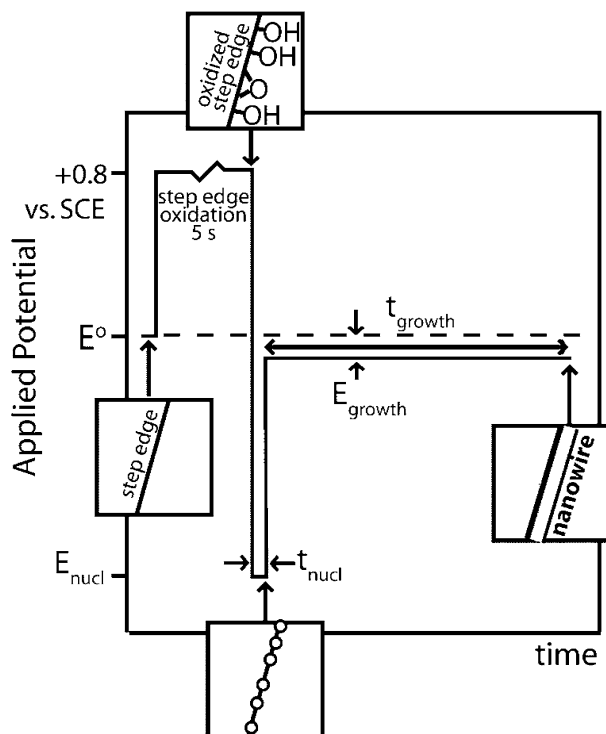


Figure 9.4. Potential program required for “direct” ESED of metal nanowires. Step 1, $+0.80\text{ V vs. SCE} \times 5\text{ s}$ causes the selective oxidation of step edges. Step 2, $(-1.0\text{ V vs. } E_{rev} \times 5\text{--}50\text{ ms})$ nucleates metal nanoparticles at step edges. Step 3, $(-20) - (-150)\text{ mV vs. } E_{rev}$ results in growth of nanoparticles without further nucleation.

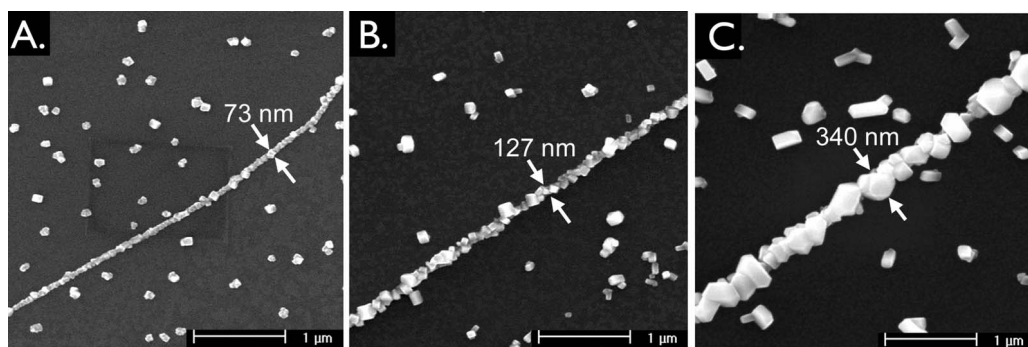


Figure 9.5. Scanning electron micrographs of copper nanowires. These nanowires were electrodeposited from an $2.0\text{ mM CuSO}_4 \cdot 5\text{H}_2\text{O}$, $0.1\text{ M Na}_2\text{SO}_4$ using $E_{nucl} = -800\text{ mV}_{SCE}$ and $E_{grow} = -5\text{ mV}_{SCE}$. The growth times employed in each experiment were: A, 120 s; B, 600 s; C, 2700 s. After Ref. [7].

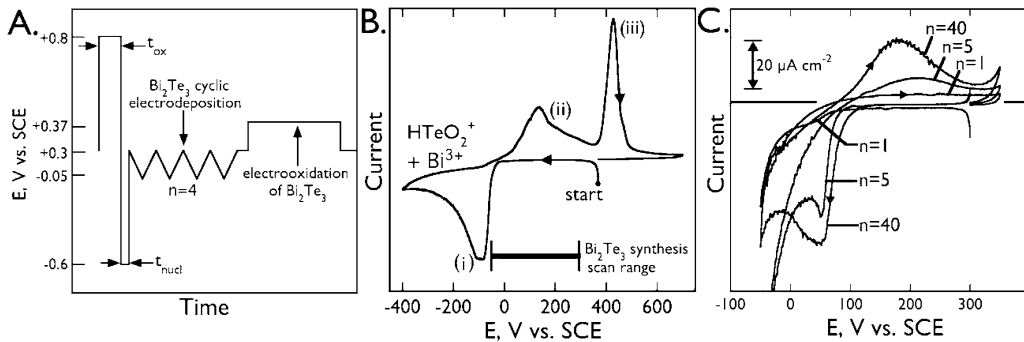
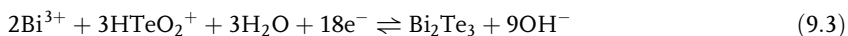


Figure 9.6. (A) Potential program used for the synthesis and electrooxidation of Bi₂Te₃ nanowires on HOPG electrodes. The electrodeposition of Bi₂Te₃ nanowires involves three steps: 1. Potentiostatic oxidation of step edges on the HOPG surface at $E_{ox} = 0.80$ V vs. SCE for a time, $t_{ox} = 5$ s. 2. Potentiostatic nucleation of Bi₂Te₃ at $E_{nucl} = -0.6$ V for $t_{nucl} = 5$ ms. 3. Cyclic electrodeposition of stoichiometric Bi₂Te₃ involving n potential cycles at 20 mV s^{-1}

of $E_{(+)}$ (+0.30 V) and a negative limit of $E_{(-)}$ (-0.05 V). Electrooxidation at +0.37 V to reduce the nanowire diameter adds a fourth step. (B) Cyclic voltammograms at 20 mV s^{-1} for an HOPG electrode in contact with 1.5 mM Bi(NO₃)₃ and 1.0 mM TeO₂ in 1 M HNO₃. (C) CVs acquired during the growth of Bi₂Te₃ nanowires using cyclic electrodeposition/stripping. The CV is shown at scans 1, 5 and 40 as indicated. After Ref. [10].

In the case of Bi₂Te₃ [10], a negative-going “forward” voltammetric scan to -400 mV (peak (i), Fig. 9.6B) deposits both Bi₂Te₃ and excess bismuth. On the return scan, excess bismuth is selectively removed (at peak (ii)), but the positive limit of this scan remains on the negative side of peak (iii) which involves the oxidation of Bi₂Te₃.

The net synthesis reaction is:



The synthesis by electrodeposition/stripping of CdSe nanowires is analogous to this, involving the electrodeposition of cadmium-rich CdSe nanowires [9], and the subsequent stripping of cadmium. Nanowires of these two materials are shown in Fig. 9.7. A high degree of wire diameter control is obtained in these experiments using the number of E/S cycles as shown there.

9.5

Electrochemical/Chemical Synthesis of Nanowires

Some materials cannot be prepared directly using electrodeposition. Two examples are MoS₂ and molybdenum metal. Nanowires of these two materials can neverthe-

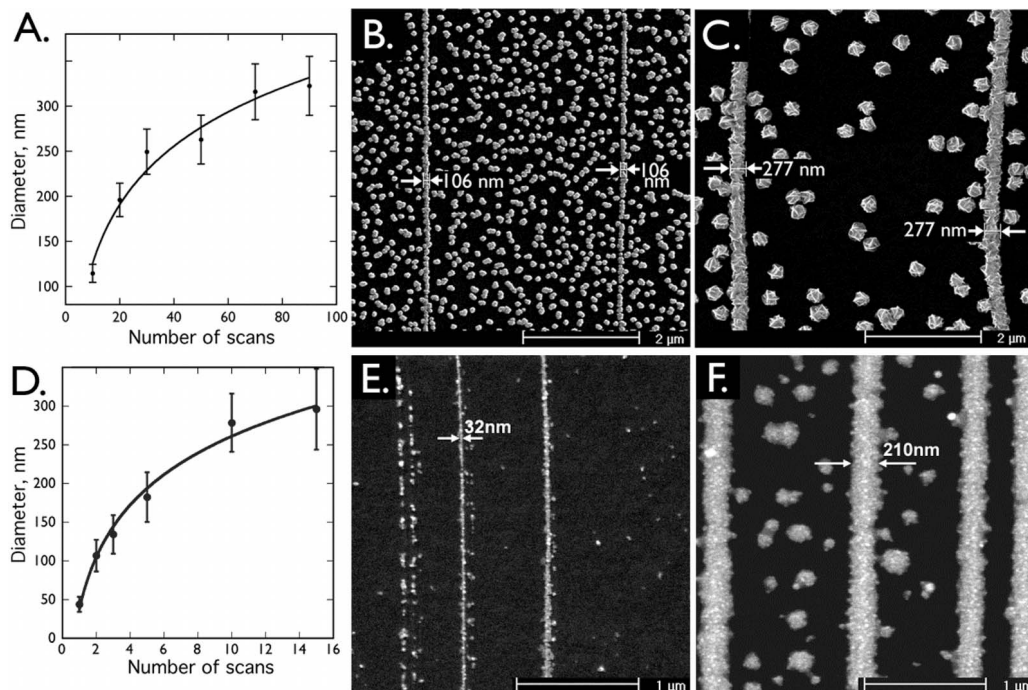


Figure 9.7. (A), (D) – Diameter versus number of electrodeposition/ stripping scans for the synthesis of Bi₂Te₃ nanowires (A) and CdSe nanowires (D). (B), (C) – Scanning electron micrographs of Bi₂Te₃ nanowires prepared using the conditions specified in Fig. 9.6 using 10 (E) and 50 (F) E/S cycles. (E), (F) – Scanning electron micrographs of CdSe nanowires synthesized by scanning at 20 mV s⁻¹ between -1.0 V and 0.8 V in aqueous 100 mM CdSO₄ and 1 mM SeO₂ aqueous solution, pH = 2.7 for 1 cycle (E) and 5 cycles (F). After Refs. [10] and [9].

less be obtained by electrodepositing nanowires of a precursor material (MoO₂ in both cases), and then reacting these nanowires at elevated temperature with a gas-phase species producing the desired product (H₂ in the case of molybdenum metal, and H₂S in the case of MoS₂) [1, 8, 17, 18]. This strategy, called electrochemical/chemical synthesis [3, 15], significantly expands the palette of materials that can be rendered as nanowires using the ESED method. The conversion from precursor to product can cause dramatic morphological changes in the nanowires, as illustrated for MoS₂ in Fig. 9.8. In this case, nanowires of MoO₂ were electro-deposited as shown in Fig. 9.2. These nanowires were then exposed to H₂S at 700 °C in order to effect the conversion according to the reaction:



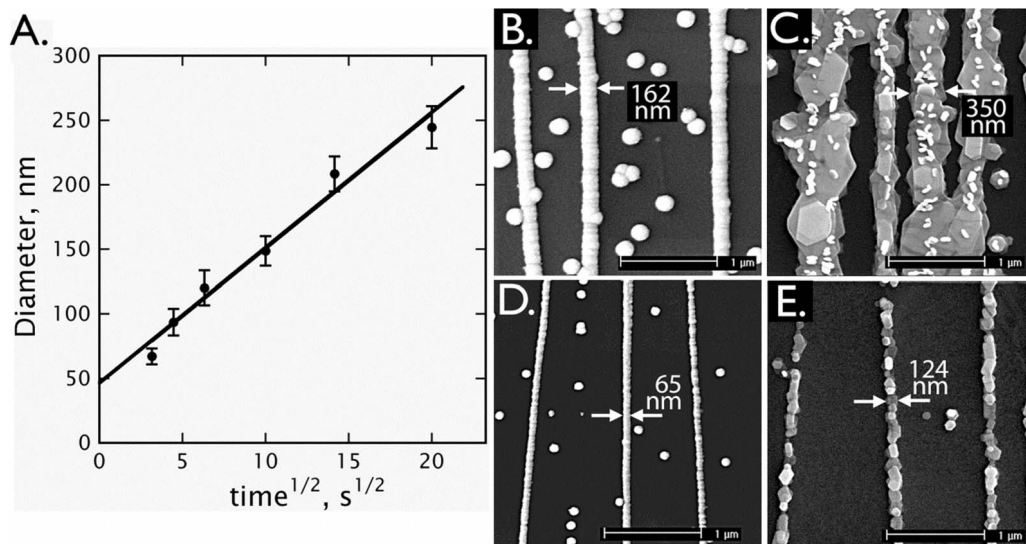


Figure 9.8. (A) Diameter of MoO_x nanowires as measured by SEM plotted as a function of the square root of the deposition time. Error bars indicate $\pm 1\sigma$ in the diameter distribution. (B), (D): SEM images of MoO_x nanowires prepared for deposition times of 400 s (B) and 5 s (D). (C), (E): MoS₂ nanowires obtained from the nanowires shown in (B) and (D) by heating in H₂S at 700 °C for 84 h. After Ref. [18].

MoS₂ is a layered material in which covalently bound S–Mo–S layers are disposed in van der Waals contact with one another. As the conversion from MoO₂ to MoS₂ proceeds, these nanowires flatten and increase in width as MoS₂ layers are formed in van der Waals contact with the graphite surface (Fig. 9.8). The resulting MoS₂ nanowires can be as thin as 7 nm, corresponding to 12 MoS₂ layers [18].

9.6 Nanowire “Thinning” by Electrooxidation

A weakness of the ESED method is that nanowires with a diameter smaller than 80 nm are rarely obtained. As already discussed in Fig. 9.1, this minimum diameter is directly related to the maximum density of nuclei that can be formed along step edges. This correlation immediately suggests that a strategy for obtaining smaller nanowires is to increase the nucleation density, and we are working towards methods for accomplishing this objective but definitive results for this approach have not yet been obtained. A second strategy is to grow larger nanowires using the ESED method, and then to reduce the diameter of these either by chemical etching or by electrochemical oxidation. We have recently succeeded in applying this “electrooxidation” approach for nanowires of the materials antimony, gold, and Bi₂Te₃ [5].

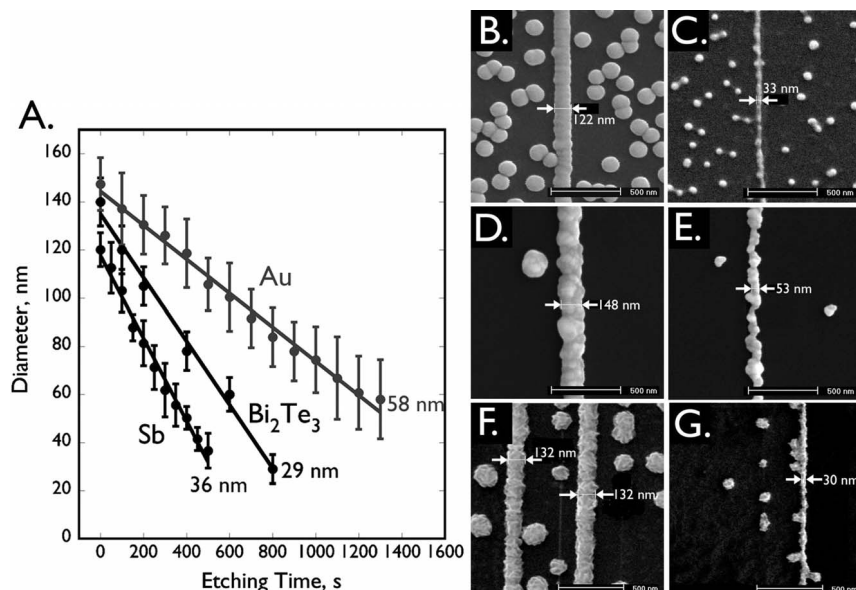


Figure 9.9. (A) Plots of mean nanowire diameter, $\langle \text{dia.} \rangle$, versus t_{ox} for gold, antimony, and Bi_2Te_3 . Each data point plotted represents a separate nanowire growth experiment involving, for a particular material, nucleation and growth under identical conditions, followed by electrooxidation for various "etching times". (B), (C) – Antimony nanowires before (B) and after (C) electrooxidation for 500 s. (D), (E) – Gold nanowires before (D) and after (E) electrooxidation for 1300 s, and (F), (G) – Bismuth telluride nanowires before (F) and after (G) electrooxidation for 800 s. After Ref. [5].

This approach was successful only when the electrooxidation process was carried out under conditions approximating kinetic control of the oxidation reaction. In this limit, data like that shown in Fig. 9.9 was obtained. Specifically, wire diameter versus time plots were linear, in accordance with the equation [5]:

$$r(t) = r_{o2} - \frac{j_{\text{ox}} t_{\text{ox}} V_m}{nF} \quad (9.5)$$

where r_{o2} is the initial radius of a nanowire subjected to oxidation and J_{ox} and t_{ox} , are the oxidation current density and duration, respectively. The derivation of Eq. (9.5) assumes that etching occurs by a kinetically controlled process. Electrooxidation permitted nanowires with an initial diameter of 100–150 nm to be reduced to a minimum diameter of 30 nm in the case of Bi_2Te_3 and antimony, and 50 nm in the case of gold. When a higher rate of electrooxidation was employed, nanowires decomposed promptly into linear particle ensembles along step edges, indicating that the rate of the nanowire narrowing, dr/dt was highest at constrictions in these nanowires [5].

9.7

Summary

Electrochemical step edge decoration is a method by which ensembles of nanowires can be prepared on HOPG electrode surfaces. These nanowires are polycrystalline and are organized into dense arrays containing many hundreds of wires. These are two of the principle disadvantages of the ESED technique. On the other hand, these nanowires can be extremely long ($<100\ \mu\text{m}$) and are often narrowly dispersed in term of the diameter distribution, and have a diameter that can be adjusted over a wide range, down to 30 nm for several materials in recent experiments. Moreover, ESED can be applied to the synthesis of a wide variety of materials, extending even to some materials that are inaccessible by electrodeposition.

ESED will continue to command our attention only if we are able to solve two vexing problems: First, methods like electrooxidation must be developed that permit the synthesis of “quantum wires” in the sub-10 nm diameter range. The properties of such nanowires can be expected to be significantly diameter-dependent, a fascinating regime that we have hardly broached in our synthesis efforts up until now. Second, a means must be discovered for “patterning” step edges on surfaces. Ideally, such a method would permit the synthesis by ESED of single nanowires, or even the design of nanowire-based circuits. In our laboratory, we are endeavoring to solve these two problems.

Acknowledgments

Many talented students and postdoctoral students have contributed to the development of ESED including Michael Zach, Erich Walter, Fred Favier (CNRS Montpellier, France), Ben Murray, Erik Menke, Qiguang Li, and Michael Thompson. Also crucial to the success of this research has been a collaboration with Professor J. C. Hemminger and his students Matt Brown and John Newberg at UCI. We are grateful for funding of this research by the National Science Foundation (grants DMR-0405477 and CHE-0111557) and by the petroleum Research Fund administered by the American Chemical Society (grant 40714-AC5). We are also grateful for many donations of HOPG from Dr. Arthur Moore, formally of GE Advanced Ceramics. HOPG for other work was supplied by a grant from the EU Commission FP6 NMP-3 project 505457-1 ULTRA-1D.

References

- 1 M. P. ZACH, K. H. NG, R. M. PENNER, *Science* **2000**, *290*, 2120–2123.
- 2 E. C. WALTER, M. P. ZACH, F. FAVIER, B. J. MURRAY, K. INAZU, J. C. HEMMINGER, R. M. PENNER, *Chemphyschem* **2003**, *4*, 131–138.
- 3 R. M. PENNER, *J. Phys. Chem. B* **2002**, *106*, 3339–3353.
- 4 F. FAVIER, E. C. WALTER, M. P. ZACH, T. BENTER, R. M. PENNER, *Science* **2001**, *293*, 2227–2231.
- 5 M. A. THOMPSON, E. J. MENKE, C. C. MARTENS, R. M. PENNER,

- J. Phys. Chem. B* **2006**, *110*, 36–41.
- 6 E. C. WALTER, F. FAVIER, R. M. PENNER, *Anal. Chem.* **2002**, *74*, 1546–1553.
- 7 E. C. WALTER, B. J. MURRAY, F. FAVIER, G. KALTENPOTH, M. GRUNZE, R. M. PENNER, *J. Phys. Chem. B* **2002**, *106*, 11407–11411.
- 8 M. P. ZACH, K. INAZU, K. H. NG, J. C. HEMMINGER, R. M. PENNER, *Chem. Mater.* **2002**, *14*, 3206–3216.
- 9 Q. LI, M. A. BROWN, J. C. HEMMINGER, R. M. PENNER, *Chem. Mater.* **2006**, in press.
- 10 E. J. MENKE, Q. LI, R. M. PENNER, *Nano Lett.* **2004**, *4*, 2009–2014.
- 11 M. A. ANDERSON, S. GORER, R. M. PENNER, *J. Phys. Chem. B* **1997**, *101*, 5895–5899.
- 12 S. GORER, J. A. GANSKE, J. C. HEMMINGER, R. M. PENNER, *J. Am. Chem. Soc.* **1998**, *120*, 9584–9593.
- 13 S. GORER, G. S. HSIAO, M. G. ANDERSON, R. M. STIGER, J. LEE, R. M. PENNER, *Electrochim. Acta* **1998**, *43*, 2799–2809.
- 14 G. S. HSIAO, M. G. ANDERSON, S. GORER, D. HARRIS, R. M. PENNER, *J. Am. Chem. Soc.* **1997**, *119*, 1439–1448.
- 15 R. M. PENNER, *Acc. Chem. Res.* **2000**, *33*, 78–86.
- 16 Q. G. LI, R. M. PENNER, *Nano Lett.* **2005**, *5*, 1720–1725.
- 17 Q. LI, J. T. NEWBERG, E. C. WALTER, J. C. HEMMINGER, R. M. PENNER, *Nano Lett.* **2004**, *4*, 277–281.
- 18 Q. LI, E. C. WALTER, W. E. VAN DER VEER, B. J. MURRAY, J. T. NEWBERG, E. W. BOHANNAN, J. A. SWITZER, J. C. HEMMINGER, R. M. PENNER, *J. Phys. Chem. B* **2005**, *109*, 3169–3182.
- 19 R. BOWLING, R. T. PACKARD, R. L. MCCREERY, *Langmuir* **1989**, *5*, 683–688.
- 20 R. J. BOWLING, R. T. PACKARD, R. L. MCCREERY, *J. Am. Chem. Soc.* **1989**, *111*, 1217–1223.
- 21 R. J. RICE, R. L. MCCREERY, *Anal. Chem.* **1989**, *61*, 1637–1641.
- 22 Q. G. LI, J. B. OLSON, R. M. PENNER, *Chem. Mater.* **2004**, *16*, 3402–3405.
- 23 A. M. KRESSIN, V. V. DOAN, J. D. KLEIN, M. J. SAILOR, *Chem. Mater.* **1991**, *3*, 1015–1020.

10 Electrochemical Fabrication of Arrayed Nanostructures

Takayuki Homma

10.1 Introduction

Precise fabrication of nanostructures is fundamental for manufacturing various advanced devices and systems. In particular, the fabrication process for well-ordered structures on a Si wafer surface is significant for its broad area of application, such as semiconductor devices and MEMS, etc. These structures have been fabricated mainly using physical (dry) processes such as sputtering, reactive ion etching (RIE) and deep reactive ion etching (DRIE), in combination with photolithographic processes. On the other hand, electrochemical processes have certain advantages and numbers of attempts have been made to develop processes suitable for these applications [1]. In this chapter, electrochemical approaches to the fabrication of well-ordered, arrayed nanostructures onto a Si surface will be described, mainly focusing upon the recent work of the author's group.

10.2 Formation of Metal Nanodots Along the Step Edge of the Si(111) Surface

The hydrogen terminated Si(111) surface has wide and atomically flat terraces separated by steps, one atomic bilayer in height [2, 3], which can be utilized as a "model" for investigating Si wafer surfaces. By using the H-Si(111) surface, the initial nucleation mechanism of trace amounts of metal species, such as Cu, in aqueous fluoride solution was investigated [4].

Figure 10.1 shows a representative STM image of the H-Si(111) surface prepared in Ar-sparged 40% NH_4F solution followed by another immersion in Ar-sparged 40% NH_4F solution for 10 s. By the first immersion, an ideal surface with large, pit-free terraces can be obtained, as is seen in Fig. 10.1(a). Note that the double-immersion procedure is used simply for consistency with subsequent Cu-containing experiments, and follows an initial 15 min immersion in the clean solution.

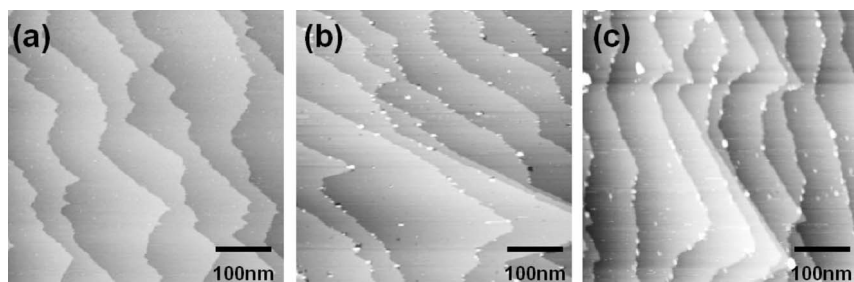


Figure 10.1. STM images of H-Si(111) prepared in argon-sparged 40% NH_4F followed by (a) 10 s immersion in argon-sparged 40% NH_4F ; (b) 10 s immersion in argon-sparged 40% NH_4F with 10 μM CuSO_4 ; (c) 30 s immersion in argon-sparged 40% NH_4F with 10 μM CuSO_4 . Z scale (black to white): 0 to 2 nm [4].

Figures 10.1(b) and (c) show the effect of 10 μM CuSO_4 dissolved in the second solution. After the 10 s immersion (Fig. 10.1(b)), numerous particles, several nanometers in diameter, are observed, located at the step edges. After 30 s immersion in the same solution (Fig. 10.1(c)), the average size of the particles has increased while their number and distribution seem to remain almost unchanged. The results of XPS analysis indicated that these particles are Cu, and such a spontaneous nucleation has been known as a result of electroless-type deposition driven by electrons that accumulate in the Si conduction band during fluoride-enhanced Si dissolution [5–8].

The electrochemical reduction of the cupric ions in the solution to copper metal particles on the silicon surface is generally treated as:

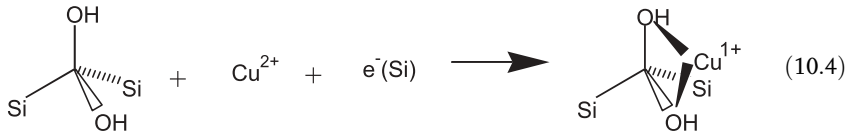


While it is known that the reduction of Cu^{2+} to Cu^0 takes place via Cu^{1+} as follows [9]:



The open circuit potential of H-Si(111) in 40% NH_4F solution was measured to be -0.8 V vs. NHE [3], which is sufficiently negative to the redox potential of $\text{Cu}^{2+}/\text{Cu}^{1+}$ ($+0.159$ V vs. NHE [10]) so that reaction (10.2) is expected to be rapid. Reaction (10.3) is also thermodynamically favorable ($+0.521$ V vs. NHE [10]) and is expected to be rapid if a nucleus of copper is available. However, stable progress of this reaction requires sites which can stabilize the Cu nuclei. Preferential deposition of metals at defect sites such as step edges and pits has been reported, not only for the electrochemical processes but for the dry processes [11–14], and can be explained in terms of the higher local surface free energy or “activity” of these

sites [15]. However, in the case of the Si surfaces described above, they are passivated by hydrogen so that even the step edges on these surfaces are expected to have relatively low surface free energies and would not be the active sites for the deposition. One possibility for the preferential nucleation of Cu at step edges comes from known polynuclear complexes of Cu^{1+} with bridging hydroxide ligands, which form spontaneously in aqueous solution [16]. Based upon this, it is expected that dihydroxy groups at kink sites on the steps on H-Si(111) will bind Cu^{1+} :



The dihydroxy group is a possible intermediate during etching at kink sites on the Si(111) surface [17]. Alternatively, anionic forms of such multivalent surface binding sites may play the key role in localizing copper nucleation at steps. If such sites do bind Cu^{1+} , they could provide the coordination site at which copper is eventually reduced to Cu^0 . The presence of copper at step edges is expected to provide a lower activation barrier for the reaction of other Cu^{1+} ions, resulting in preferential deposition of Cu clusters at step edges. Such a process can be applied to other metal species, such as Ag [18], as well as the formation of continuous particles as “step-edge decoration” [18, 19].

10.3

Maskless Fabrication of Metal Nanodot Arrays using Electroless Deposition Induced by Controlled Local Surface Activities

As described, by utilizing the nature of the Si surface in combination with electrochemical properties, spontaneous formation of metal nanoparticles along the step edges has been achieved. While this process is attractive for the formation of an ordered nanostructure, it has limitation for the design of the patterned structures due to the condition of the step edges. Therefore, processes with flexibility in designing the patterns are required. For this, the “deposition selectivity” at the surface is a significant issue. From this viewpoint, it should be noted that one of the major differences between the physical (dry) and electrochemical deposition processes could be described in terms of the “area selectivity.” In the case of the physical processes, the deposition takes place at the entire surface without area selectivity, so that removal of unnecessary deposits by lift-off or dry/wet etching is required in order to form designed structures. On the other hand, the electrochemical processes take place only at the sites where the electron transfer occurs. Therefore, by supplying electrons to the selected area, patterned formation can be carried out, possibly without photolithography processes. Numbers of processes have been proposed for the “maskless” formation of patterned micro/nano structures via

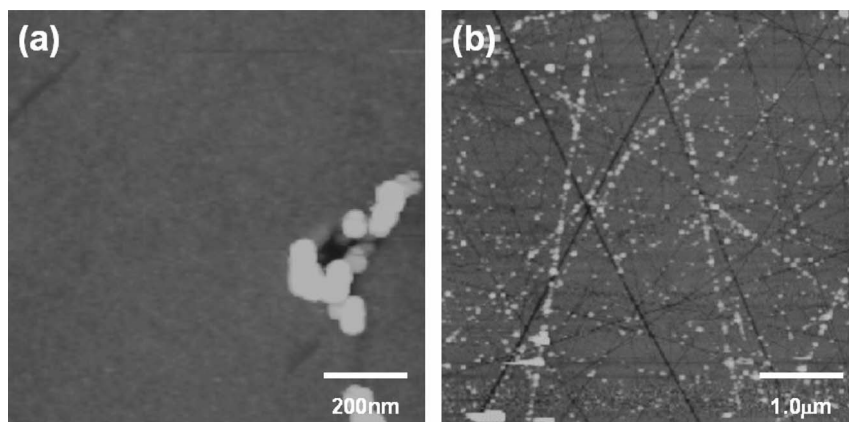


Figure 10.2. TMAFM images of Si(100) wafer surfaces with (a) pit-like defects and (b) scratch-like defects after immersion in DHF solution containing trace amount of metal species. Z scale (black to white): 0 to 10 nm.

electrochemical approaches, using scanning probe microscope and other techniques [20–23]. Furthermore, the electroless deposition process is more advantageous for the formation of patterned nanostructures, since it does not require a current supply using external equipment so that the deposition can take place at electrically isolated regions. In order to carry out the electroless deposition reaction at local sites, for example, irradiation with a laser beam has been proposed [24, 25]. In this case, the temperature of the deposition bath is kept low to prevent spontaneous deposition, the irradiation increases the temperature locally, thus initiating the deposition. Patterned deposition can be achieved by scanning the laser beam.

An alternative approach is to “build-in” the local difference in the activity to designed surface sites. The author’s group has investigated spontaneous deposition process of trace metal species on a Si wafer surface immersed in dilute HF (DHF) solution, and found that preferential deposition takes place at the surface defect sites [26], typically shown in Fig. 10.2. In these specimens, the defects were intentionally formed on the Si wafer surface, either by treating with a jet of SiO₂ slurry to form pit-like defects, or by scratching with diamond slurry. As described above, trace metal ions in aqueous fluoride solution “electrolessly” deposit at the wafer surface by attracting an electron from the Si wafer, these results indicate that the defect sites possess higher activity for the reductive deposition of metal ions.

Such a local difference in surface activity has been investigated using scanning surface potential microscopy (SPoM) [27].

Figure 10.3 shows representative tapping mode atomic force microscopy (TMAFM) and corresponding SPoM images for clean, H-terminated Si(100) wafer surfaces with or without the surface defects. The SPoM image for a wafer surface without the defects, shown in Fig. 10.3(d), represents a uniform feature with no indication of local deviation of the potential at the surface. On the other hand, the

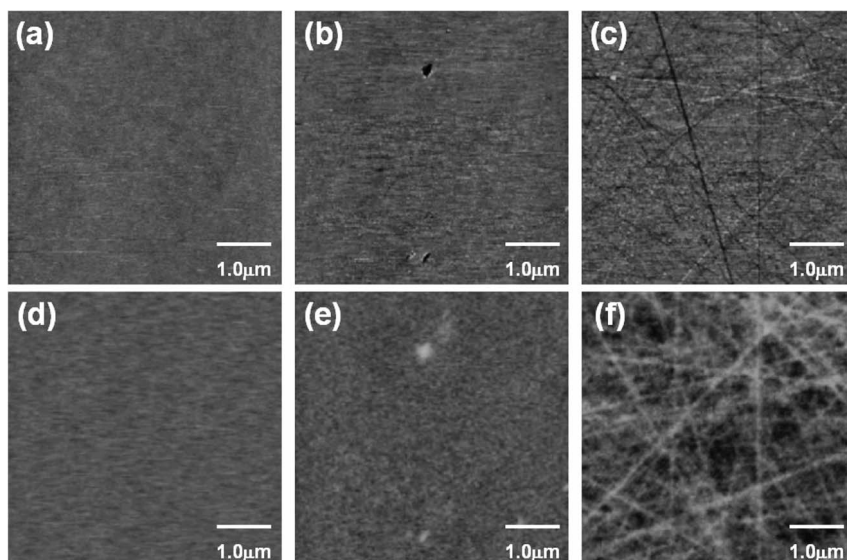


Figure 10.3. TMAFM images, (a)–(c), and corresponding SPoM images, (d)–(f), of clean H-Si(100) wafer surfaces without any defects, (a) and (d); with pit-like defects, (b) and (e); and with scratch-like defects (c) and (f), respectively. Z scale (black to white): 0 to 10 nm, (a)–(c), and 0 to -100 mV, (d)–(f).

surface defect sites possess locally negative potential relative to the non-defect (flat) regions, as is clearly seen in Figs. 10.3(e) and (f), suggesting that such a negative shift in potential enhances the reductive deposition reaction of the metal ion species at the defect sites.

Based upon these results, formation of patterned defects at Si wafer surfaces for fabricating patterned nanostructures was attempted using a nanoindentation technique with an AFM equipped with a diamond probe [27, 28].

Figure 10.4 shows representative TMAFM and SPoM images of the wafers with the surface defects intentionally formed by nanoindentation with various loading forces. The indentation with a larger loading force forms larger pit-like defects, which results in larger shift in the potential. Figure 10.5 plots such a relation, clearly indicating the correlation between the loading force of the indentation, in other words, “the degree of the defect,” and the potential shift.

Based upon these results, attempts were made to achieve the selective deposition of metals using the pre-formed defect sites. In order to achieve spontaneous, i.e., electroless deposition at these sites, the conditions of the solution were optimized. Key parameters were the concentrations of metal ion species and fluoride, as well as the immersing time. In particular, optimization of the fluoride concentration was significant, and it was found that a very low concentration of fluoride was effective in enhancing the selectivity of the deposition at the defect sites. For example, Fig. 10.6 shows TMAFM images of a clean H-Si(100) wafer surface with pat-

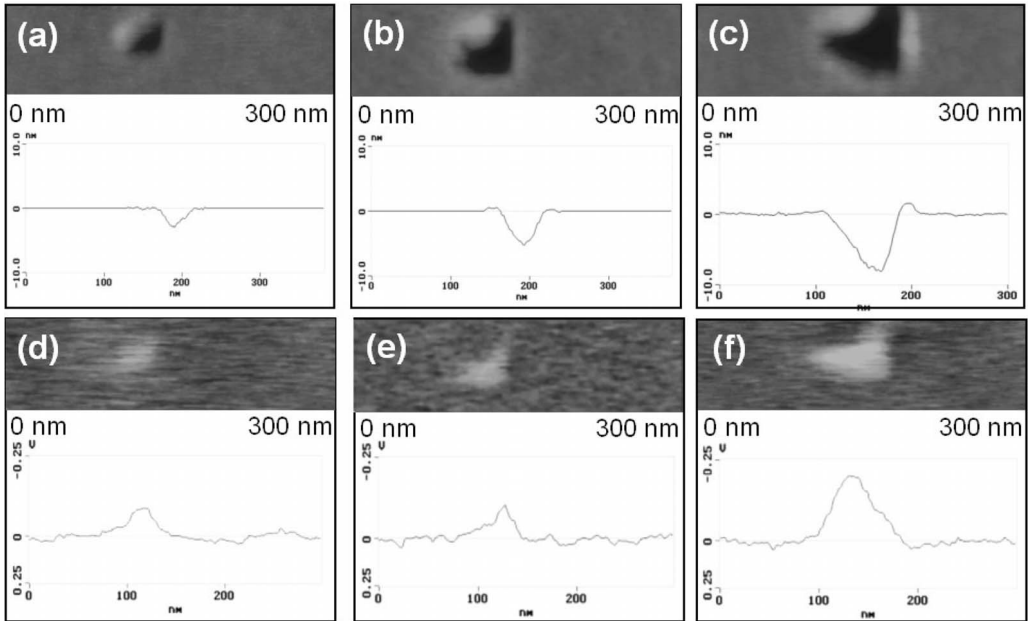


Figure 10.4. TMAFM images, (a)–(c), and corresponding SPoM images, (d)–(f), of clean H-Si(100) wafer surfaces with patterned nanodefects formed by the nanoindentation. The indentation force to form the defects is 16.0 μN (a) and (d), 28.4 μN (b) and (e), and 41.2 μN (c) and (f), respectively. Z scale (black to white): 0 to 10 nm, (a)–(c), and 0 to -200 mV, (d)–(f). Cross sectional profiles for the TMAFM and SPoM images are also shown [27].

terned defect sites formed by nanoindentation, before and after immersing in the 0.025% DHF solution containing 500 ppb of $\text{Cu}(\text{NO}_3)_2$ for 1 min. In spite of such an extremely simple procedure, Cu nanodots are selectively formed exactly at the patterned defect sites. It is considered that, under such a dilute condition of fluo-

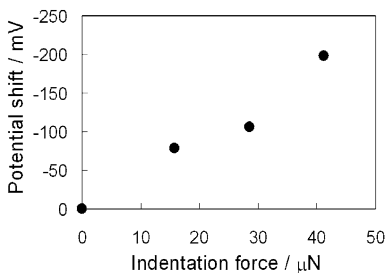


Figure 10.5. Potential shift profile at the defect sites formed by nanoindentation with various loading forces.

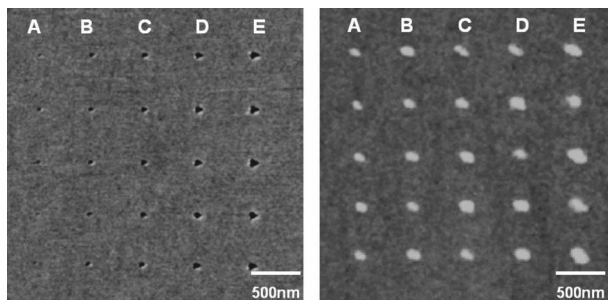


Figure 10.6. TMAFM image of clean H-Si(100) wafer surface with 5×5 patterned defects formed by nanoindentation before and after immersion for 1 min in DHF solution containing a trace amount of Cu. Indentation forces for the rows A to E are 15.8 μN , 22.2 μN , 28.6 μN , 34.7 μN and 41.2 μN , respectively. Z scale (black to white): 0 to 5 nm [27].

ride, most of the surface area of Si is oxidized when immersing in the solution, effectively passivating the reductive reaction of the metal ion species, while the defect sites, which possess locally negative potential, still keep their “activity” to initiate the reductive deposition reaction of metal ion species. In addition, in the 5×5 array of patterned defect sites in Fig. 10.6, the rows indicated as A–E were formed with different loading force and, as is seen in the figure, larger dots are observed at the defect sites formed with larger loading force, i.e., those possessing larger potential shift. Such a trend is plotted in Fig. 10.7. These results indicate the possibility of simultaneous formation of the nanostructures with various feature sizes, which should be advantageous as a nanofabrication process. It was also confirmed that the process could be applied to various metal species such as Cu, Ag, Au, Co, etc. with various feature sizes, as shown in Fig. 10.8.

As described, maskless fabrication of arrayed metal nanostructures onto a Si wafer can be achieved in combination with pre-patterning of nanodeflects and an “electroless” deposition process. This process is extremely simple and does not re-

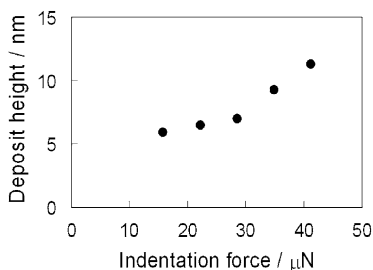


Figure 10.7. Height of the deposits at the nanodeflect sites with respect to the indentation force for their formation.

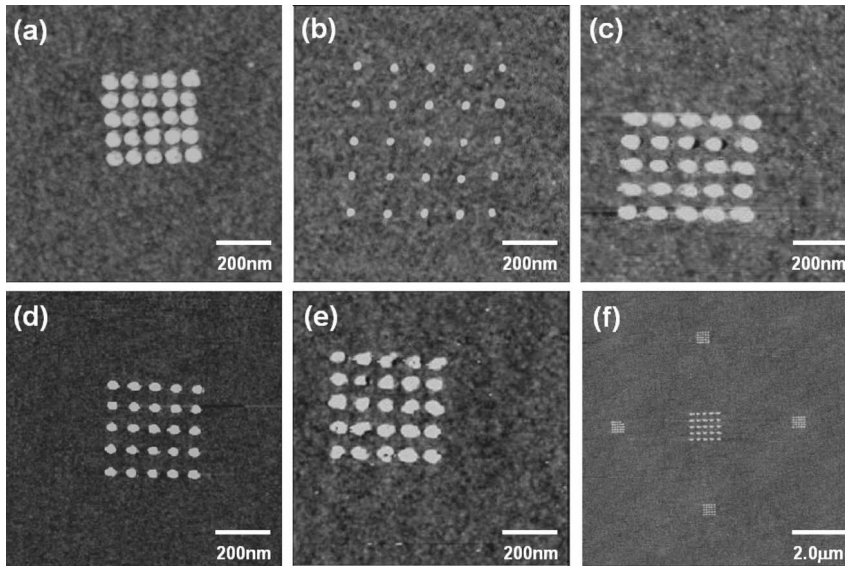


Figure 10.8. TMAFM images of metal nanodot arrays fabricated on the H-Si(100) wafer surface; (a) and (b) Cu, (c) and (d) Ag, (e) Co, and (f) Au [27, 28].

quire photolithography processes or even external current supply, yet precise formation of nanostructures can be easily achieved, which should be advantageous for the formation of various nanostructures and patterns.

10.4

Conclusion

In this chapter, electrochemical processes to fabricate well-ordered, arrayed nanostructures have been described, mainly those for Si wafer surfaces. Investigation of the initial nucleation process of trace amounts of Cu on H-terminated Si(111) surface in aqueous fluoride solution revealed that Cu nucleates preferentially along step edges. It was suggested that $\text{Si}-(\text{OH})_2\text{-Cu}^{1+}$ complexes are formed at the kink sites, resulting in the preferential nucleation of Cu at the step edges. On the other hand, by controlling local activity for the deposition reaction at the Si wafer surface, a maskless and electroless fabrication process of metal nanostructures, such as an array of nanodots, was developed. This consists of the formation of patterned nanodefects at the wafer surface and immersion in a dilute HF solution containing trace amount of metal ion species. The scanning surface potential microscopy (SPoM) analysis clarified that the defect sites locally possessed negative potential, i.e., higher activity for the reductive deposition of metal ions, and fabrication of a nanodot array of Cu, Ag, Au, and Co, was achieved.

These processes demonstrate the capability and possibility of electrochemical processes for nanofabrication, and further precise processes can be developed for various applications, with a deep understanding of the mechanism of the reactions for these processes.

References

- 1 For example, J. W. SCHULTZE, A. HEIDELBERG, C. ROSENKRANZ, T. SCHÄPERS, G. STAIKOV, *Electrochim. Acta*, **2005**, *51*, 775.
- 2 G. S. HIGASHI, Y. J. CHABAL, G. W. TRUCKS, K. RAGHAVACHARI, *Appl. Phys. Lett.*, **1990**, *12*, 656.
- 3 C. P. WADE, C. E. D. CHIDSEY, *Appl. Phys. Lett.*, **1997**, *71*, 1679.
- 4 T. HOMMA, C. P. WADE, C. E. D. CHIDSEY, *J. Phys. Chem. B*, **1998**, *102*, 7919.
- 5 H. MORINAGA, M. SUYAMA, M. NOSE, S. VERHAVERBEKE, T. OHMI, *IEICE Trans. Electron.*, **1996**, *E79-C*, 343.
- 6 O. M. R. CHYAN, J. J. CHEN, H. Y. CHIEN, J. SEES, L. HALL, *J. Electrochem. Soc.*, **1996**, *143*, 92.
- 7 G. J. NORGA, M. PLATERO, K. A. BLACK, A. J. REDDY, J. MICHEL, L. C. KIMERLING, *J. Electrochem. Soc.*, **1997**, *144*, 2801.
- 8 V. BERTAGNA, F. ROUELLE, M. CHEMLA, *Z. Naturforsch., A: Phys. Sci.*, **1997**, *52*, 465.
- 9 J. O'M. BOCKRIS, G. A. RAZUMNEY, *Fundamental Aspects of Electrocrystallization*, p. 36, Plenum Press, New York (1967).
- 10 A. J. BARD, R. PARSONS, J. JORDAN, *Standard Potentials in Aqueous Solutions*, Marcel Dekker, New York (1985).
- 11 R. J. NICHOLS, D. M. KOLB, R. J. BEHM, *J. Electroanal. Chem.*, **1991**, *313*, 109.
- 12 S. A. HENDRICKS, K. T. KIM, A. J. BARD, *J. Electrochem. Soc.*, **1992**, *139*, 2818.
- 13 R. T. POTZSCHKE, C. A. GERVAZI, S. VINZELBERG, G. STAIKOV, W. J. LORENZ, *Electrochim. Acta*, **1995**, *40*, 1469.
- 14 G. M. FRANCIS, I. M. GOLDBY, L. KUIPERS, B. VONISSENDORFF, R. E. PALMER, *J. Chem. Soc., Dalton Trans.*, **1996**, 665.
- 15 E. D. WILLIAMS, N. C. BARTELT, *Science*, **1991**, *251*, 393.
- 16 G. A. ARDIZZOIA, M. ANGARONI, G. LAMONICA, F. CARIATI, M. MORET, N. MASCIOCCHI, *J. Chem. Soc., Chem. Commun.*, **1990**, 1021.
- 17 G. F. CEROFOLINI, L. MEDA, *Appl. Surf. Sci.*, **1995**, *89*, 351.
- 18 N. TOKUDA, N. SASAKI, H. WATANABE, K. MIKI, S. YAMASAKI, R. HASUNUMA, K. YAMABE, *J. Phys. Chem. B*, **2005**, *109*, 12655.
- 19 N. TOKUDA, H. WATANABE, D. HOJO, S. YAMASAKI, K. MIKI, K. YAMABE, *Appl. Surf. Sci.*, **2004**, *237*, 528.
- 20 D. H. CRASTON, C. W. LIN, A. J. BARD, *J. Electrochem. Soc.*, **1988**, *135*, 785.
- 21 D. M. KOLB, R. ULLMANN, T. WILL, *Science*, **1997**, *275*, 1097.
- 22 P. SCHMUKI, L. E. ERICKSON, *Phys. Rev. Lett.*, **2000**, *85*, 2985.
- 23 L. SANTINACCI, T. DJENIZIAN, P. SCHMUKI, *J. Electrochem. Soc.*, **2001**, *148*, C640.
- 24 R. J. VON GUTFELD, D. R. VIGLIOTTI, O. C. WELLS, V. D. KHANNA, E. J. O'SULLIVAN, *Appl. Phys. Lett.*, **1994**, *64*, 348.
- 25 R. J. VON GUTFELD, K. G. SHEPPARD, *IBM J. Res. Develop.*, **1998**, *42*, 639.
- 26 T. HOMMA, C. E. D. CHIDSEY, M. WATANABE, K. NAGAI, *Electrochem. Soc. Proc.*, **1998**, *98(13)*, 250.
- 27 T. HOMMA, N. KUBO, T. OSAKA, *Electrochim. Acta*, **2003**, *48*, 3115.
- 28 N. KUBO, T. HOMMA, Y. HONDO, T. OSAKA, *Electrochim. Acta*, **2005**, *51*, 834.

11

Electrodeposition of Two-dimensional Magnetic Nanostructures on Single Crystal Electrode Surfaces

Philippe Allongue and Fouad Maroun

11.1

Introduction

The energy required to magnetize a ferromagnetic material depends on the direction of the applied field because ferromagnetic materials exhibit ‘easy’ and ‘hard’ directions of magnetization (magnetocrystalline anisotropy) [1]. This anisotropy is used in current hard disk technology. The in-plane magnetic moment of the individual grains is determined from their crystal in-plane orientation. About 1000 grains are necessary to define the *average* direction of magnetization corresponding to the storage of one bit of information (Fig. 11.1(a)) [2]. The magnetic anisotropy may also arise from the shape of the magnetic structure (shape anisotropy). As the easy axis of magnetization lies parallel to the length of a permanent magnet, the direction of magnetization of a nanostructure may be fixed by adjusting its aspect ratio (Fig. 11.1(b)). Another source of anisotropy is the surface of a material or the interface between a ferromagnetic material and another metal. For instance ultra-thin magnetic films sandwiched between two nonmagnetic layers often present *perpendicular* magnetization anisotropy (PMA) below a critical thickness of only a few atomic layers whereas shape anisotropy should favor in-plane magnetization (Fig. 11.1(c)) [3, 4]. The interface anisotropy will be discussed in more detail in this chapter.

The possibility of manipulating the orientation and magnitude of the magnetic moment of atoms through their environment (PMA is one example) is now intensively investigated, in particular to design new recording media. Future recording technology will rely on new media [5] fabricated by assembling nanostructures of controlled structure, size and shape [6] in order to create arrays of macro spins, i.e. monodomain magnets at room temperature, with reproducible characteristics, each of them capable of storing one bit of information. This is a completely new approach with regards to the former strategy used to increase the capability of the hard disk. As explained above, it is not quite possible to reduce the number of grains per bit because of a random surface orientation of the grains (see Fig. 11.1(a)) and it is also not quite possible to further decrease the grain size. Indeed, below a critical size, the grains lose their ferromagnetic properties and become

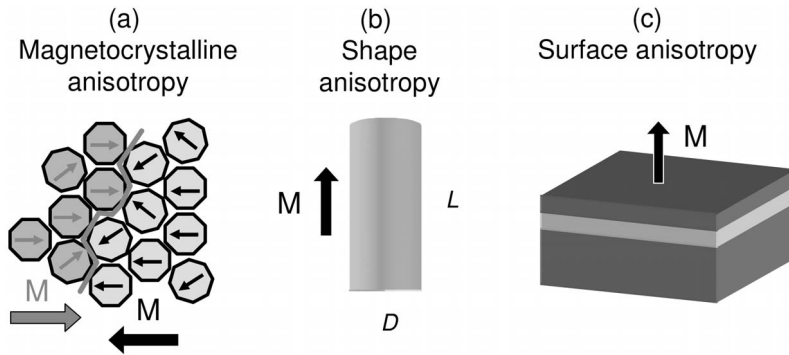


Figure 11.1. The different magnetic anisotropies of ferromagnetic materials. (a) Magnetocrystalline anisotropy determines the mean easy axis of each nanocrystal. About 1000 grains are necessary in current hard disk drives to define one bit, i.e. a well-defined magnetization axis. (b) Shape anisotropy: the aspect ratio L/D of a structure or nanostructure determines the easy axis of magnetization. (c) Surface anisotropy: the moment of an ultrathin ferromagnetic layer sandwiched between layers of a noble metal is often perpendicular to the surface due to surface anisotropy while the shape anisotropy would favor in-plane magnetization (see case (b)).

superparamagnetic, i.e., their magnetization is no longer stabilized in one specific direction but flips randomly due to thermal activation. New materials need therefore to be designed to push the superparamagnetic limit.

The composition, the physical dimensions and the assembly of building blocks, and, equally very important, the crystal structure of all the elementary components and interfaces determine the functionality and performance of a magnetic device. The increasing importance of interfaces and crystal structure justifies the comparison of different growth methods since there is a strong interplay between the crystalline structure of thin films and their elaboration conditions. Physical methods are most often employed for film growth but in a few examples electrochemical deposition has proven its versatility, especially in the context of high technology. Before the inception of GMR sensors, the magnetic heads were, for instance, fabricated by electrochemical deposition of magnetic alloys [7]. Superconformal film growth is presently used for the Cu interconnect in the microelectronic industry [8]. In the academic context, electrodeposition has also proven that it may be complementary to UHV growth. After years of progress with the preparation of clean surfaces of noble metal single crystals at ambient pressure [9] and the advent of the electrochemical STM for *in situ* real time observations of surface processes at a metal [10–12] and semiconductor electrodes [13], a true electrochemical surface science has developed, in particular to investigate the early stages of metal growth on various single crystal electrodes. Concerning magnetic materials a few studies have demonstrated that ultrathin Cu/Co/Au(111) electrodeposited layers exhibit PMA [14, 15] and, in some cases, attempted correlation of the film structure and morphology with their magnetic properties using *in situ* magnetic characteriza-

tions [15–17]. *Self-ordered* metal electrodeposition by replication of atomic scale patterns created on single electrode surfaces has also been achieved by electrodeposition, as reviewed elsewhere [18] and GMR sensors, presenting a significant GMR value, have also been grown electrochemically, as reviewed in Chapter 12.

While the above brief overview indicates that electrodeposition might be a relevant technique to realize two-dimensional nanoscale materials and nanostructures on planar surfaces, there is one domain where the advantage of electrodeposition seems more obvious compared to UHV growth. Electrodeposition is for instance very suitable to grow ensemble or individual nanostructures by template electrodeposition inside nanoscale patterns and, more generally, when one needs to fill a surface with a complex form, as is the case in the top-down approach. A large amount of work has been dedicated to the fabrication and characterization (magnetostatic and magneto-transport properties) of μm long magnetic nanowires and rods of a few tens of nm in diameter grown in nanoporous membranes [19, 20]. These one-dimensional nanostructures could be of great interest in various application fields [21]. Inverse opal structures have also been grown by electrodeposition through self-assembled polystyrene beads [22]. Tip induced cluster deposition with an electrochemical scanning probe microscope (SPM) has been investigated to fabricate arrays of dots within the bottom-up approach [23], with the advantage that the electrochemical environment allows full control and reproducibility of the chemical nature and size of the deposited dots. The reader is referred to Chapter 6 for details on the fabrication methods on metal and semiconductor surfaces.

In this chapter we will focus on the electrochemical growth of *ultrathin* layers of the three iron group metals on a single crystal Au(111) electrode surface. This field was almost unexplored when we started our investigations. We aimed to explore the morphology and structure of electrodeposited magnetic layers and whether they exhibit PMA. We also aimed to compare the performances of electrodeposited systems with those of their counterpart prepared by molecular beam epitaxy (MBE). The published and unpublished results described below outline the strong influence of the deposition conditions on the magnetic properties and the critical role of interfaces and surface chemistry on PMA. This chapter is organized as follows. Section 2 deals with the magnetism of ultrathin films and gives the basic equations describing the systems. A specific sub-section addresses instrumental questions for *in situ* magnetic characterizations in the electrochemical environment. Another sub-section describes how experimental data can be measured and exploited. Section 3 reviews results obtained in our group on the electrodeposition of Ni, Co and Fe on Au(111). In each case, the nucleation and growth is described and the specific magnetic properties outlined in comparison with MBE layers.

11.2

Ultrathin Magnetic Films

Ultrathin magnetic layers are very interesting systems from a fundamental and a technological viewpoint [3, 4]. They often present perpendicular magnetization anisotropy (PMA), i.e. an out-of-plane magnetization, which is one phenomenon

of strong interest for high-density data storage [24–26]. PMA was predicted very early by Néel because of the symmetry breaking at the interface. The amplitude of the phenomenon was however not quite correct and modern experimental studies have evidenced that PMA may have different physical origins [3, 4]. For instance the PMA of Co/Au(111) layers mainly arises from a modification of the magnetic moment of cobalt atoms hybridized with the gold atoms at the Co/Au interface which explains why the cobalt layer must be thinner than $t^* \sim 4$ ML to observe in the UHV an out-of-plane magnetization with Co films evaporated on Au(111) [3]. In the case of Ni/Cu(001) films, the magnetization is perpendicular for Ni layers *thicker* than 7 ML, which is unusual and has prompted many studies. Structural investigations have demonstrated that PMA arises from a modification of the in-plane Ni–Ni atomic spacing (*magnetoelastic* effects) induced by the lattice mismatch between Ni and Cu. The magnetization reorientation transition of Ni/Cu layers may further be manipulated by introducing an oxygen monolayer as surfactant during Ni growth [27]. A reversible switching out of plane \leftrightarrow in-plane orientation of the magnetization was observed via the adsorption/desorption of H₂ on Ni [28].

All the above studies of ultrathin layers outline the strong influence of the atomic scale environment on the moment and anisotropy of magnetic atoms [24]. These parameters have been *experimentally* measured by Gambardella et al. [29] using X-ray magnetic circular dichroism (XMCD) in the case of Co clusters of controlled size deposited on Pt(111). The results proved that the magnetic moment per cobalt atom decreases rapidly with the cluster size and that it reaches its bulk value for clusters composed of more than 15 atoms. The oscillatory magnetic anisotropy in atomic chains of Co atoms decorating a stepped Pt(111) surface is also a remarkable example of the influence of the atomic structure [30]. In the case of two-dimensional monoatomic cobalt islands deposited on Pt(111), recent detailed correlation between STM images and magnetic susceptibility measurements has evidenced a larger magnetic anisotropy of cobalt atoms located at the island perimeter compared to that of cobalt atoms in the islands [31].

The above short overview clearly shows that interface anisotropy depends not only the hybridization of magnetic atoms at the interfaces but also on the crystal-line structure of the magnetic layers (orientation and strain). The morphology of the interfaces (roughness, intermixing, etc.) is also a critical parameter. For these reasons, it is important to compare different growth methods and morphologies of the deposited magnetic layers. It is in this context that we have undertaken the research which is summarized in this chapter.

11.2.1

Magnetic Moment of Ultrathin Films

The orientation of the magnetization vector M of an hcp cobalt layer with the c axis normal to the surface is defined by the tilt angle θ from the surface normal (Fig. 11.2(a)); θ is determined by minimizing the sum of the dipolar (E_d), magnetocrys-

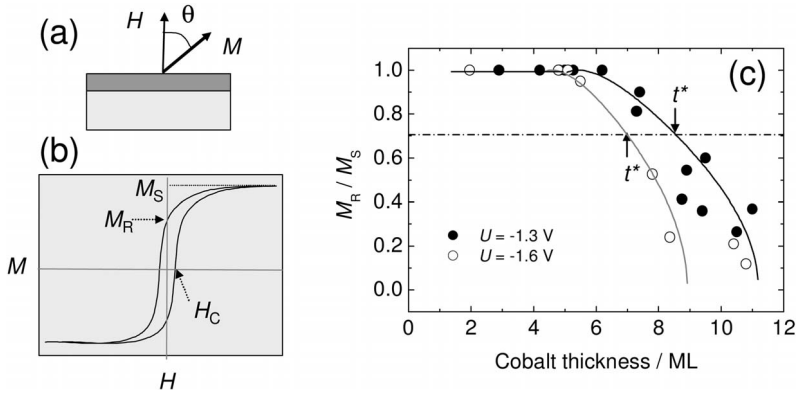


Figure 11.2. (a) Scheme corresponding to Eqs. (11.1)–(11.4). For a field H applied normal to the surface plane, the angle θ between the magnetization vector and the surface normal is given by Eq. (11.5). (b) Schematic hysteresis loop. The loop is open ($H_C \neq 0$) and the remnant magnetization $M_R \neq 0$. In this example, $M_R/M_S \sim 0.5$ which corresponds to $\theta = 60^\circ$. A perfectly square loop ($M_R = M_S$) would be observed when M

is strictly perpendicular ($\theta = 0$). (c) Plots of M_R/M_S as a function of the cobalt thickness for electrodeposited Cu/Co/Au(111) sandwich layers. Symbols correspond to experimental data obtained for Co deposition at -1.3 V/MSE (\bullet) and -1.6 V/MSE (\circ). The solid lines are calculated curves using Eq. (11.7) used to determine the K_S and t^* values. Note the significant influence of the applied potential (see also Table 11.1). After Ref. [15].

talline (E_{mc}), interface (E_S), and Zeeman (E_Z) energies, upon application of an external field H parallel to the surface normal:

$$E_D = -2\pi M_S^2 \sin^2 \theta \quad (11.1)$$

$$E_{mc} = K_1 \sin^2 \theta + K_2 \sin^4 \theta \quad (11.2)$$

$$E_S = (K_S \sin^2 \theta)/t_M \quad (11.3)$$

$$E_Z = -HM_S \cos \theta \quad (11.4)$$

where t_M is the metal thickness and M_S the magnetization at saturation. K_1 and K_2 (both >0) are the bulk magnetocrystalline anisotropy constants of the magnetic material (for metals other than cobalt $K_2 \ll K_1$) [1]. The interface constant $K_S = K_S^{\text{Up}} + K_S^{\text{Down}}$ stands for the contributions of the upper interface (with the outer media, i.e. capping metallic layer, solution etc.) and bottom interface (with the substrate). The term E_D tends to align M in the plane of the layer and E_{mc} tends to align M perpendicular to the surface plane. E_S also favors an out-of-plane easy axis of magnetization if $K_S > 0$. Minimization of the total energy $E(\theta) = E_D + E_{mc} + E_S + E_Z$ with respect to θ at a fixed field H yields:

$$\sin \theta [K_{\text{eff}} + K_2 \sin^2 \theta + HM_S/(2 \cos \theta)] = 0 \quad (11.5)$$

where

$$K_{\text{eff}} = K_1 - 2\pi M_s^2 + K_S/t_M. \quad (11.6)$$

If $K_S > 0$ then K_{eff} may be ≥ 0 when $t_M \rightarrow 0$ (Eq. (11.6)) and the only solution of Eq. (11.5) is $\sin \theta = 0$, i.e. $\theta = 0$, which means that M is strictly perpendicular to the surface plane. Upon film thickening K_{eff} becomes inevitably negative ($K_1 < 2\pi M_s^2$) and the expression in brackets in Eq. (11.5) may be zero for $\theta \neq 0$. This means that, above a critical thickness, which depends on K_S , M is oblique and presents an in-plane component. K_S is experimentally determined by plotting the variations of $M_R/M_S = \cos \theta$ as a function of the ferromagnetic layer thickness, M_R and M_S being the remnant ($H = 0$) and saturation magnetization derived from the M - H hysteresis loop with the field H perpendicular to the film (Fig. 11.2). At zero field, $\sin^2 \theta = -K_{\text{eff}}/2K_2$ from Eq. (11.5). Therefore:

$$M_R/M_S = [1 + (K_1 - 2\pi M_s^2 + K_S/t_M)/(2K_2)]^{1/2} \quad (11.7)$$

The plot M_R/M_S vs. t_M yields the K_S -value by fitting the data with Eq. (11.7) in which K_1 , K_2 and M_S are the bulk values of the considered material. The critical thickness t^* , usually defined as the thickness for which $\theta = 45^\circ$ ($M_R/M_S = \cos \theta = 0.707$) is given by:

$$t^* = K_S/(2\pi M_s^2 - K_1 - K_2) \quad (11.8)$$

The larger K_S the larger t^* and the stronger is PMA. As explained above, the K_S value may originate from quite different physical effects. In the case of a purely *interface* PMA, K_S is essentially phenomenological and it remains very difficult to calculate from *ab initio* calculation [3]. However, when PMA arises from elastic strain, an analytical expression for E_S can be given. In the case of a uniformly (in-plane) strained film and a magnetization perpendicular to the interface:

$$E_S = (3/2)\lambda \varepsilon E_y t_C/t_M = K_S/t_M \quad (11.9)$$

Where λ is the magnetostriction coefficient, E_y the Young's modulus, $\varepsilon = (a_{\text{bulk}} - a_{\text{layer}})/a_{\text{bulk}}$ is the in-plane stress and t_C the critical thickness above which misfit dislocations appear.

As discussed below, in our experiments, the magnetization lies ultimately in the surface plane at zero field above a critical film thickness. However, if a magnetic field is applied perpendicular to the surface the magnetization is tilted out of the surface plane. Therefore the MOKE and AGFM signals are non-zero in the perpendicular configuration of these techniques. For $t_M \gg t^*$, the measured signal is:

$$M \cos \theta = t_M H M_S^2 / (4\pi M_s^2 - 2K_1 - 4K_2) \quad (11.10)$$

This equation shows that the projection of M on the surface normal, measured at a fixed field, is proportional to the film thickness. The proportionality coefficient depends on the deposited material, since M_s , K_1 and K_2 are physical characteristics of

the ferromagnetic metal. The factor increases with increasing magneto-crystalline anisotropy, i.e. with increasing K_1 and K_2 and it decreases with increasing M_S .

11.2.2

In Situ Magnetic Characterizations

Standard characterization techniques of magnetic materials and systems include the magneto optical Kerr effect (MOKE) [32], superconducting quantum interference device (SQUID), ferromagnetic resonance (FMR) [33], vibrating sample magnetometer (VSM) and alternating gradient field or force magnetometer (AGFM) [34]. All these techniques allow the recording of hysteresis loops $M-H$ of macroscopic samples (variations of M as a function of H , see Fig. 11.2). Other techniques, like MOKE microscopy [35] and magnetic force microscopy (MFM) [36], allow local probing, with 500 nm to 100 nm or less lateral resolution, of the magnetization of the sample. Spin polarized STM [37] has recently emerged and allows magnetic characterization at the atomic scale.

In the case of the electrodeposition of iron group metals, fast surface oxidation is anticipated in air, which likely alters the PMA. Hence *ex situ* measurements require capping of the magnetic films with a noble metal [14, 15]. The plots M_R/M_S shown in Fig. 11.2(c) were obtained with electrodeposited Co/Au(111) layers capped *in situ* with a copper layer (CuSO₄ was added to the solution at the end of deposition to deposit Cu at $-1.15 V_{MSE}$ without exposing the sample to air) [15]. The cobalt thickness was measured using Rutherford backscattering for accurate correlations between M_R/M_S and t_{Co} . These curves clearly demonstrate strong PMA since, as discussed later, the K_S values derived from these data are larger than for the corresponding MBE layers (see later, Table 11.1). *In situ* magnetic characterizations present, however, more versatility to investigate independently the two

Table 11.1. K_S and t^* values of Co/Au(111) layers.

Structure ^[a]	t^*/ML	$K_S/erg\ cm^{-2}$	$K_S^{Down}/erg\ cm^{-2}$	$K_S^{Up}/erg\ cm^{-2}$
Cu/Co/Au(111)				
ED ($-1.3\ V$) [15]	7.2	0.78	0.72 ^[b]	–
ED ($-1.6\ V$) [15]	6.2	0.72	0.66 ^[b]	–
MBE ([61])	6.6	0.64	0.58	0.06
Medium/Co/Au(111)				
Sulfate [16]	1.6	0.21	–	$-0.51^{[c]}$
Thiocyanate [16]	4	0.46	–	-0.26
UHV [3]	4		0.58	$-0.28^{[c]}$

^a MBE = molecular beam epitaxy; ED = electrodeposition. ^b Value estimated using $K_S^{Up} = 0.06\ erg\ cm^{-2}$ for the Cu/Co interface. ^c Value estimated using $K_S^{Down} = 0.72\ erg\ cm^{-2}$ for the Co/Au(111) interface.

interfaces (e.g. Co/Au and Co with its outer environment) and therefore explore the influence of surface chemistry on magnetization at the nanoscale, like in UHV studies, provided that the technique is sensitive enough. Another advantage of *in situ* measurements is accurate correlation between the film's thickness and the magnetization without capping the film with a noble metal (see experimental procedure below).

A few groups have developed highly sensitive *in situ* AGFM [16, 17, 38, 39] and MOKE measurements [39–42] whose configuration and operating conditions were adapted to the electrochemical environment. As shown below, our group has achieved sub-monolayer sensitivity with custom built *in situ* AGFM and *in situ* MOKE set-ups. The principle of both techniques and the performances of our experimental set-up are briefly detailed in the following paragraphs.

11.2.2.1 Alternating Gradient Field Magnetometry (AGFM)

For these experiments we used a set-up built at the Laboratory of Magnetism (UFRGS, Porto Alegre, Brazil): the sample is fixed on a glass rod itself held by a piezo-electric element (Fig. 11.3(a)). The alternative magnetic field gradient ∇B is generated by two small coils at a frequency equal to that of the free mechanical resonance of the system “rod + sample” (in the range 10–100 Hz) to apply a force $M \bullet \nabla B$ on the sample and excite the free mechanical oscillations of the system.

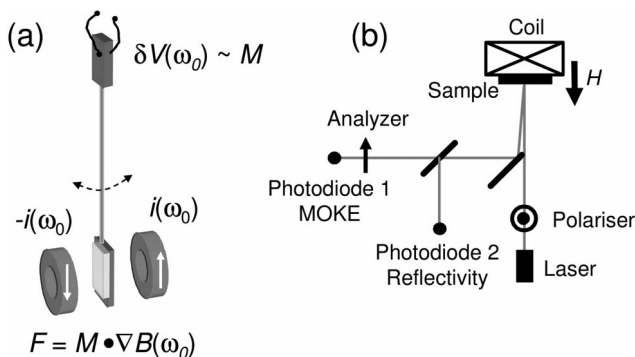


Figure 11.3. (a) Principle of AGFM: a light sample is hanging at the extremity of the glass rod, itself connected to a bimorph piezoelectric element. The alternative field gradient ∇B generated with the two coils in anti-Helmholtz configuration applies a force $F \sim M \bullet \nabla B$ on the sample, which excites the free oscillations of the “rod + sample” ensemble (frequency ω_0) and generates an alternative voltage at the bimorph measured with a lock-in amplifier. Note that $B = 0$ in the middle of the two

coils. The external field H is applied with an electromagnet (not shown). (b) Principle of MOKE: a laser light is linearly polarized with a polarizer illuminates the sample. The reflected beam is splitted into two beams. Photodiode 2 measures the intensity of the first beam and yields the sample reflectivity, and Photodiode 1 measures the intensity of the second beam after crossing the analyser, and yields the MOKE signal multiplied by the reflectivity. A coil in the vicinity of the sample allows application of an external magnetic field.

The amplitude of oscillations is detected by the piezo-electric element through a lock-in amplifier. The AGFM signal is therefore an alternative voltage proportional to the component of M which is parallel to the vector ∇B . The components M_{\perp} (H perpendicular to the surface) and $M_{//}$ (H in the surface plane) are measured with different sample holders. The time resolution of this electrochemical AGFM is 3 data points per second, i.e. a complete hysteresis loop necessitates ~ 3 min, and its sensitivity limit is 0.1 ML of Co.

11.2.2.2 Magneto Optical Kerr Effect (MOKE)

MOKE is based on the rotation of the polarisation of a polarised light when it is reflected on a magnetic material. The Kerr rotation angle θ_{Kerr} is proportional to the vectorial product $M \otimes E$, where E is the electric field of the incident light [43, 44]. In the set-up built at our laboratory (Fig. 11.3(b)), the laser beam which is polarised linearly with a polarizer, reflects onto the sample and then splits into two beams: one for measuring the sample reflectivity and the other, which crosses an analyser, for measuring θ_{Kerr} . At normal incidence, as depicted in the figure, PMOKE ($P = \text{polar}$) is only sensitive to the projection of M on the surface normal. The time resolution of this set-up is 1000 data points per second, i.e. we can acquire a full hysteresis loop in less than 1 s, and its sensitivity limit is 0.1 ML of Co.

11.2.3

Description and Exploitation of *in Situ* Magnetic Measurements

A typical *in situ* AGFM experiment consists in depositing (phase A), stabilizing the deposit (phase B) and stripping the layer (phase C) while recording the transients of current and magnetization at a fixed field H (Fig. 11.4(a)). The example concerns Co deposition on Au(111) with the field parallel to the surface. Because of the slow sampling rate of the AGFM technique, phase B must be a few minutes long to record a complete AGFM hysteresis loop (HL) $M-H$ at a fixed film thickness. An *in situ* MOKE experiment is similar except that one sweeps the field H continuously to record 2 to 5 hysteresis loops per second thanks to the superior sampling rate of the technique. Much more complete information is therefore obtained: Fig. 11.4(b) presents a series of PMOKE $M-H$ loops (H normal to the surface) acquired every second during the growth of the first two monolayers of cobalt on Au(111). After phase B (which may be omitted in MOKE experiments), the film is dissolved by sweeping the potential anodically and the measure of the anodic charge Q_A is converted into a film thickness t_M . By repeating this routine for increasing deposition times, the dependence of the magnetic signal on the layer thickness is obtained.

In situ magnetic measurements give several pieces of information. The first is the magnetization reorientation transition with increasing thickness. In the case of AGFM, it is necessary to record the two transients of magnetization at fixed field with the field perpendicular and parallel to the sample surface (separate experiments). One may also record $M-H$ loops with the routine in Fig. 11.4(a). In the

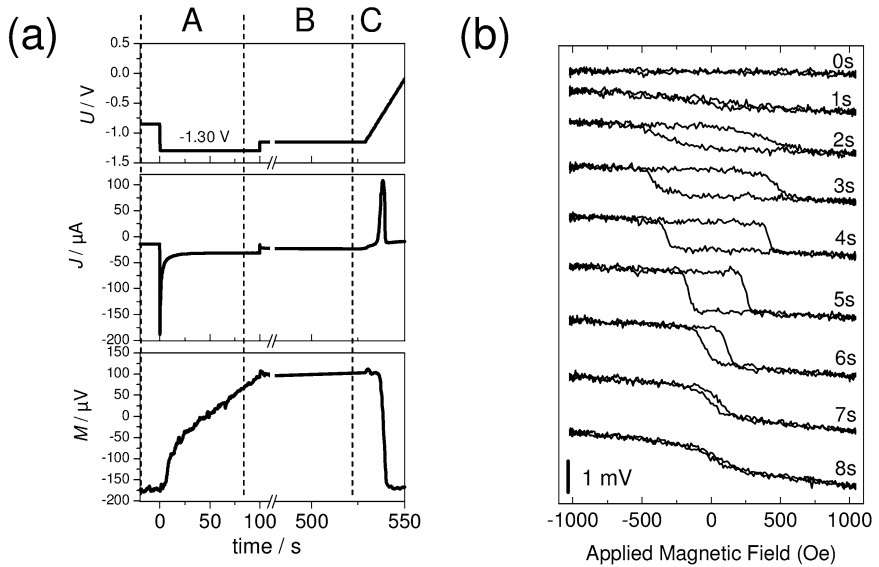


Figure 11.4. (a) Routine of potential used for an *in situ* AGFM experiment. The example concerns Co/Au(111) growth with the field H parallel to the surface plane. The solution composition is 1 mM CoSO_4 , pH = 3.5. In phase A, the potential is stepped negatively to -1.3 V to deposit cobalt; in phase B the potential is stepped back to a rest potential (at -1.15 V) to stabilize the films and record

an hysteresis loop $M-H$. In phase C, the film is dissolved and the charge Q_A is converted into an equivalent cobalt thickness t_{Co} . The potential, the current and the magnetization M at fixed H are recorded. (b) Series of $M-H$ loops recorded every second by *in situ* PMOKE (perpendicular configuration) during the deposition of the first 2 ML of Co on Au(111). Note the open and square loop.

case of MOKE real time recording of the $M-H$ loops provides in one experiment the whole information by measuring the time dependence of the ratio M_R/M_S plus the coercive field. Another important piece of information is the variations of the magnetic moment per atom since, in the case of ultrathin magnetic layers, μ_M may depend on the film thickness [24, 45] and is also influenced by the incorporation of impurities or foreign species and even by the controlled adsorption of molecules on the surface [27, 28]. To determine μ_M the sample must be magnetically saturated. In that case M_S is simply proportional to the deposited volume:

$$M_S = K\mu_M A t_M = R_M t_M \quad (11.11)$$

where A is the electrode surface area and K an instrumental constant. Therefore, measuring $R_M = M_S(t_M)/t_M = AK\mu_M$ gives insights into the thickness dependence of μ_M . Examples of such data exploitation will be presented in the next section.

11.3

Electrochemical Growth and Magnetic Properties of Iron Group Films on Au(111)

In this section we compare the nucleation and growth modes, and the structure of the three metals. We also compare the structural results with previous work on the same films prepared by resistive evaporation in the UHV. These studies showed that the nucleation of Ni [46], Co [47] and Fe [48, 49] on Au(111) is driven by place exchange. Because of the large surface density of nuclei, this specific nucleation process results in rough ferromagnetic layers due to 3D growth (the lateral expansion of the initial clusters is limited by their coalescence).

Another important issue motivating this work is to correlate the structure of electrodeposited *ultrathin* layers with their magnetic properties, which had not been studied before. Indeed, Co and Fe/Au(111) MBE layers present PMA while Ni/Au(111) layers do not present PMA [3]. The *in situ* magnetic measurements described below demonstrate the good quality of the materials grown by electrodeposition, since PMA is observed with Co and Fe, in spite of the strong sensitivity of this phenomenon to interface imperfections and contaminations. Electrodeposited Ni/Au(111) layers present a 6 ML-thick magnetically “dead layer”, likewise the MBE layers [3]. Above this thickness an in-plane magnetization is observed.

11.3.1

Electrochemistry of Au(111) in Iron Group Metal Solutions

In this section all potentials are quoted versus the mercury sulfate electrode (MSE). The voltammograms of Au(111) in the three 1 mM metallic sulfate solutions of pH 3.5 are shown in Fig. 11.5. A common feature is the presence of a cathodic peak at -1.15 V corresponding to the proton reduction reaction ($\text{H}^+ + \text{e}^- \rightarrow \frac{1}{2}\text{H}_2$). The second cathodic peak corresponds to metal deposition ($\text{M}^{2+} + 2\text{e}^- \rightarrow \text{M}$) and the anodic one to the dissolution of the deposited layer ($\text{M} \rightarrow \text{M}^{2+} + 2\text{e}^-$). As the po-

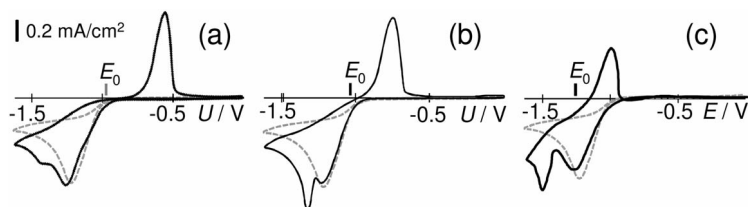


Figure 11.5. Voltammograms of Au(111) in 1 mM NiSO_4 (a), 1 mM CoSO_4 (b) and 1 mM FeSO_4 (c) solutions of pH 3.5 (after Ref. [56]). The sweep rate is 50 mV s^{-1} in all cases. A mercury sulfate electrode is used as a reference. The cathodic peaks correspond to H^+ reduction and metal deposition. The anodic peak corresponds to metal dissolution.

sition of the deposition peak is more negative than that of the proton reduction, the latter reaction takes place in parallel with the deposition of the three metals. For nickel (Fig. 11.5(a)) the deposition peak is positioned at -1.4 V and the dissolution starts at -0.7 V. In the case of cobalt, there are two cathodic peaks for Co deposition: a narrow peak at -1.3 V (Fig. 11.5(b)), which corresponds to the formation of the first cobalt bilayer, and a broader one at -1.4 V, well resolved at a sweep rate of 10 mV s^{-1} (not shown), which corresponds to the growth of additional cobalt atomic planes [50]. The dissolution starts at a more negative potential than for Ni. Iron deposition occurs at an even more negative potential (peak at -1.5 V) and the dissolution peak is also shifted negatively.

Voltammetry evidences therefore that the hydrogen evolution reaction (HER) $\text{H}^+ + \text{e}^- \rightarrow \frac{1}{2} \text{H}_2$ occurs in parallel to the electrodeposition of the three metals. It is a complex multistep reaction involving an adsorption step of H on the metal surface [51]. The role of HER may therefore be critical regarding the magnetic properties and the growth modes of electrodeposited magnetic layers. It is for instance known that H-adsorption on Ni growth in the UHV promotes fast Ni on Ni surface diffusion [52]. The H-adsorption at the electrochemical interface should therefore favor 2D growth. However, as soon an OH layer forms, the greater electronic corrugation of the surface likely reduces surface diffusion [53] and affects the resulting film morphology. Concerning magnetism the HER might, however, be detrimental, since it often leads to H incorporation, a phenomenon that often reduces the magnetization of layers, particularly in the case of Ni and Fe which easily *absorb* hydrogen [51].

11.3.2

Ni/Au(111)

11.3.2.1 Morphology and Structure

UHV studies of Ni/Au(111) MBE growth focused on the nucleation stage which is driven by place exchange of the Au atoms at the elbows of the $22 \times \sqrt{3}$ surface reconstruction surface by Ni atoms. The place exchange is favored by the larger surface energy of Ni compared to Au [46]. No data are available concerning multilayer Ni films. In the electrochemical environment, a place exchange mechanism is also observed at very small overpotentials [54, 55]. On increasing slightly the overpotential a Ni monolayer grows until complete coverage of the surface (Fig. 11.6(a), $U = -1.15$ V). Another characteristic of the sub-monolayer Ni film is the strongly anisotropic needle growth starting from the reconstruction elbows or from the step edges, perpendicular to the domain walls of the reconstruction pattern. The needles are $n \times 11 \text{ \AA}$ in width, with n an integer $1 \leq n \leq 5$. However for $n > 5$, the needles expand laterally and a disordered moiré pattern appears simultaneously. These observations reproduce those reported by Magnussen and coworkers [54, 55]. At potentials more negative than -1.3 V the nucleation becomes homogenous on the gold terraces and the growth of the first monolayer is isotropic (Fig. 11.6(b)). The growth proceeds then in a layer by layer fashion, which results in very smooth films. The ordered hexagonal moiré on the second Ni plane (period $20 \pm 1 \text{ \AA}$) sug-

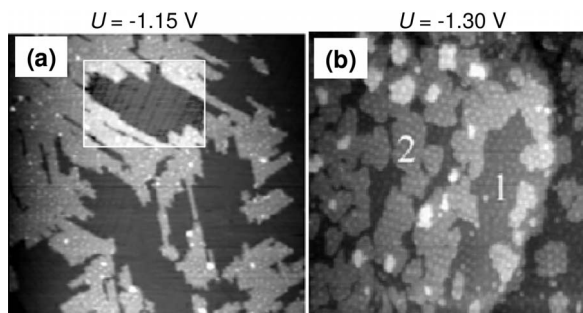


Figure 11.6. *In situ* STM images of Ni growth from a 1 mM NiSO₄ solution at -1.15 V (a) and -1.3 V (b). The numbers in image (b) indicate the local thickness expressed in ML (after Ref. [56]). Frames (a)–(b) are respectively $1040 \times 1080 \text{ \AA}^2$ and $1100 \times 1000 \text{ \AA}^2$. Notice the layer by layer growth.

gests a Ni–Ni spacing distance of 2.5 \AA , which is very close to the bulk value in Ni(111). The moiré orientation pertains further to the alignment of the Ni(111) lattice with the Au(111) lattice. More details can be found in Ref. [56].

11.3.2.2 Magnetic Properties

Likewise evaporated Ni/Au(111) layers [3] electrodeposited Ni films exhibit the same magnetic characteristics. Fig. 11.7(a) shows a series of M – H loops recorded by AGFM during phase B of the routine in Fig. 11.4(a) with H applied parallel to the surface and for increasing film thickness. The data call for three observations: (i) All M – H loops are square (Fig. 11.7(a)) which indicates a fully in-plane magnetization in accordance with previous works in the UHV [3]. (ii) The magnetization at zero field (M_R) drops to zero at about 9 ML (Fig. 11.7(b), open squares). (iii) No magnetic signal is measurable below ~ 6 ML (Fig. 11.7(b), filled circles), which suggests that ferromagnetism vanishes completely below this thickness (the detection limit of our AGFM corresponds to 0.3 ML of nickel or 0.1 ML of cobalt).

The decrease in M_R (Fig. 11.7(b), open squares) may be attributed to the known decrease in the Curie temperature T_C close or below room temperature with decreasing Ni thickness. T_C is the temperature of the ferromagnetic/superparamagnetic transition. A system is ferromagnetic below T_C only. Near T_C the magnetic moment varies as $M \sim (1 - T/T_C)^\beta$ (the value of β depends on the system dimensionality and the number of degrees of freedom for the spin reorientation. In two dimensions theory predicts $\beta = 0.125$) [24], and the theoretical decrease in T_C with decreasing thickness is given by the expression $T_C(t_M)/T_C(\text{bulk}) = 1 - (t_0/t_M)^\lambda$ where t_0 is the critical thickness below which the film is paramagnetic for all temperatures ($T_C = 0$) and the value of the exponent λ depends on the model ($\lambda \sim 1.5$) [24]. Experimentally the critical Ni thickness determined from the decrease in M_R (9 ML) is significantly larger than that observed in

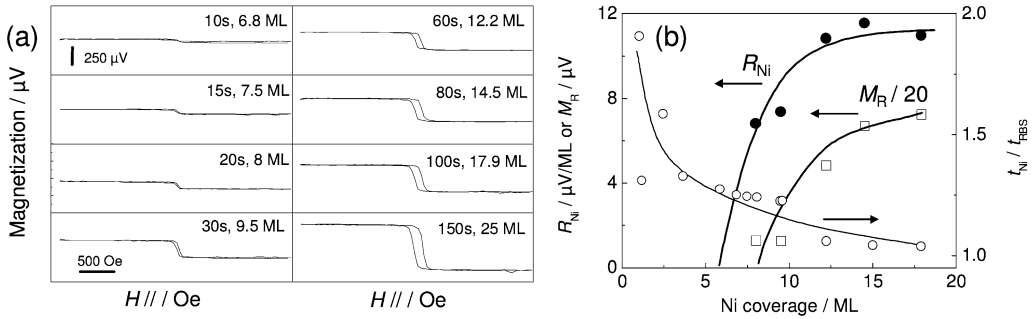


Figure 11.7. *In situ* magnetic properties of Ni/Au(111) layers with the field applied parallel to the surface plane (AGFM measurements): (a) M - H loops recorded during phase B of Fig. 11.4(a), for different layers grown at -1.4 V. (b) Plots of R_{Ni} (●), M_R (□) (left-hand side vertical scale) and t_{Ni}/t_{RBS} (○) (right-hand side vertical scale) as a function of the Ni coverage. The value of M_R was divided by 20 to fit the same vertical scale as R_{Ni} . Note the close correlation between the decrease in R_{Ni} (resp. M_R) below 6 ML (resp. 8 ML) and the incorporation of hydrogen into Ni during the growth of the first 5–6 ML. See text for more explanation. After Ref. [62].

the UHV studies (~ 5 ML) [24, 45]. The reason for this discrepancy is discussed in the next paragraph.

Figure 11.7(b) evidences also that the magnetic moment per atom decreases at low Ni thickness since R_{Ni} (filled circles) decreases with t_{Ni} (see Eq. (11.11)). R_{Ni} drops to zero below 6 ML, which suggests that the first 6 ML can be considered as a magnetically “dead layer”, a phenomenon which has been observed with Ni layers deposited by other techniques and has been investigated theoretically [57, 58]. In our case the incorporation of H into electrodeposited Ni films was proven on comparing the *physical* thickness of the electrodeposited Ni films measured by RBS (t_{RBS}) with that given from the electrochemical dissolution charge of the film (t_{Ni}): The plot of the ratio t_{Ni}/t_{RBS} as a function of t_{RBS} (Fig. 11.7(c), open circles) remarkably evidences the H-incorporation during the growth of the first 5 ML of nickel, which may explain the vanishing of ferromagnetism below this thickness.

11.3.3

Co/Au(111)

11.3.3.1 Morphology and Structure

The nucleation of Co on Au(111) in UHV takes place at the elbows of the Au reconstruction, by the same place exchange mechanism and for the same energetic reasons as for Ni [47], which results in a rough morphology. The replication of the reconstruction pattern was used to self-order Co clusters on vicinal Au(111) surfaces [59].

In the electrochemical environment, Co nucleation takes place also at the elbows of the Au(111) reconstruction. However, this necessitates applying a very small

overpotential, at which the lateral growth becomes hindered after a while, probably because of Co hydroxide formation induced by the increase of the local pH. *In situ* STM measurements show that for an overpotential large enough ($U < -1.25$ V), cobalt grows as *biatomic* islands of apparent height 3.4 Å due to a different tunneling barrier on Au and on Co [56]. The nucleation is selective at the gold step edges for $U < -1.3$ V (Fig. 11.8(a)) and it becomes homogenous on terraces at -1.6 V

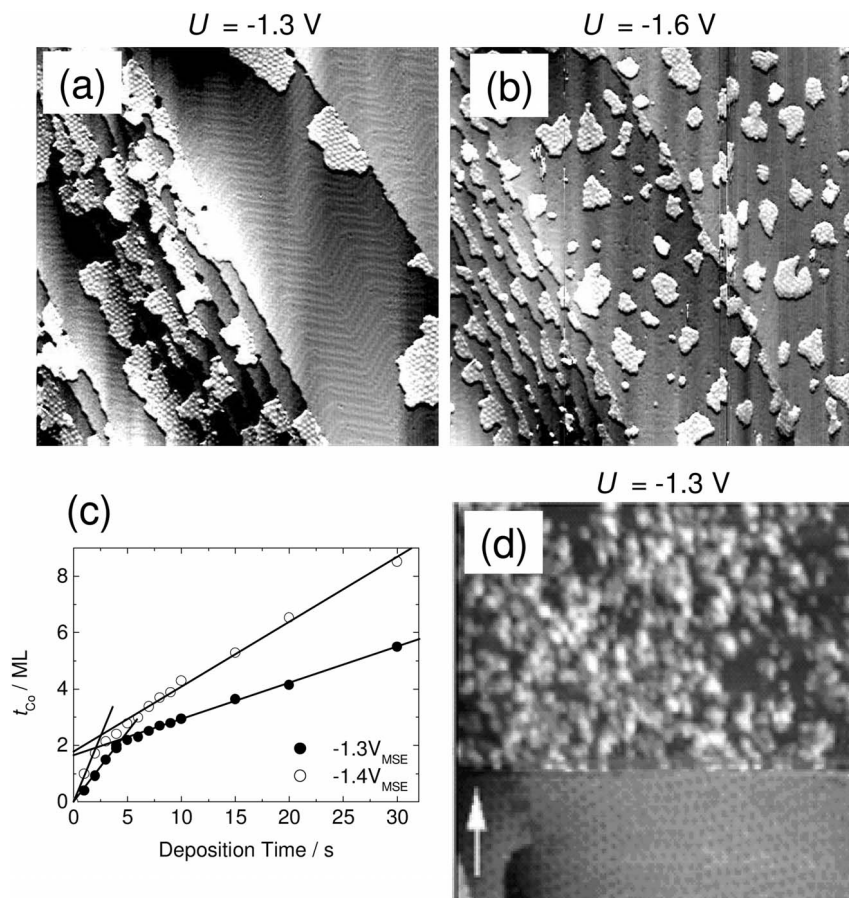


Figure 11.8. Co growth from a 1 mM CoSO_4 sulfate solution, $\text{pH} = 3.5$. (a), (b) *In situ* STM images of submonolayer films deposited at -1.3 V (a) and -1.6 V (b). All islands are biatomic ([60]). Note the different island densities. (c) Plot of t_{Co} as a function of deposition time, showing the larger growth rate of the first 2 ML. (d) *In situ* STM image showing Co growth after addition of thiocyanates to the solution. A Co UPD layer is imaged at -0.8 V (bottom) and 3D growth is observed at -1.3 V (top) (after Ref. [16]). STM frames are respectively $1500 \times 1500 \text{ \AA}^2$ (a), (b) and $900 \times 900 \text{ \AA}^2$ (d).

(Fig. 11.8(b)). As a result, for constant cobalt coverage, the island average size is smaller at -1.6 V. The following growth step is the lateral expansion of the Co islands until complete coverage of the gold surface. Only after the completion of the Co bilayer does the next Co atomic plane start growing and growth proceeds then in a layer-by-layer fashion [15, 56]. Electrochemical measurements confirm that the growth rate depends on the number of deposited atomic layers: the growth rate of the first 2 ML is about 4 times larger than that of subsequent atomic layers (Fig. 11.8(c)). The same trend is observed for all deposition potentials [56]. Adding trace amounts of thiocyanates (SCN^-) results in profound alterations of the above scheme, as shown in Fig. 11.8(d) [16]. In the first place anion-induced Co UPD (under potential deposition) occurs and, atop of this monolayer, 3D nm-sized Co clusters grow randomly.

From a structural viewpoint, the hexagonal moiré pattern (28 \AA) observed by STM on top of the cobalt bilayer grown from the sulfate-containing solution (Fig. 11.8(b)–(c)) indicates the presence of residual strain ($\sim 4\%$), which progressively reduces upon further deposition ($\sim 2.5\%$ for a trilayer) [15]. The strain relief mechanism involves Au/Co intermixing at the interface, as evidenced by the presence of nm-sized alloy islands just after the dissolution of the cobalt layer [15, 56]. *Ex situ* X-ray diffraction and EXAFS measurements [15], after capping Co with Cu or Au, give evidence of the epitaxial growth hcp Co(0001)/Au(111) with the c axis perpendicular to the surface plane and with no rotation of the Co lattice with respect to the gold lattice. No structural information is available for Co layer electrodeposited in the presence of thiocyanates.

11.3.3.2 Magnetic Properties

MBE bare and capped Co/Au(111) layers are a prototype system exhibiting interface PMA which has been investigated in many groups [3]. For Cu-capped Co films deposited on Au(111) an overall interface anisotropy constant $K_S = 0.66 \text{ erg cm}^{-2}$ was found [61]. As shown in Table 11.1, electrodeposited Cu/Co/Au(111) films present also perpendicular anisotropy, which is comparable in strength ($K_S = 0.72$ to 0.78 erg cm^{-2} and $t^* = 6$ to 7 ML) [15]. This result is remarkable because the MBE and electrodeposited layers have quite different morphologies. This is a strong indication that a sharp interface is obtained by electrodeposition since PMA is mainly due to an interface effect in this case. The slightly larger K_S value found for films electrodeposited at -1.3 V (see Fig. 11.2(c) and Table 11.1) is attributed to a contribution of the residual elastic strain at the Co/Au interface. Deposition at -1.6 V promotes a larger density of stacking faults in the cobalt layer due the larger growth rate at this potential, which lowers K_S . After this result we focused on *in situ* magnetic measurements.

In order to probe the presence of PMA in bare Co films electrodeposited on Au(111) we performed *in situ* AGFM and MOKE experiments (with the field applied perpendicularly to the surface H_\perp). Figure 11.9(a) presents a series of transients M -*time* measured at different deposition potentials using electrochemical AGFM at fixed field $H_\perp = 600 \text{ Oe}$. All curves present a sharp peak within the first 10 s of deposition. The amplitude of the peak is almost independent of the applied

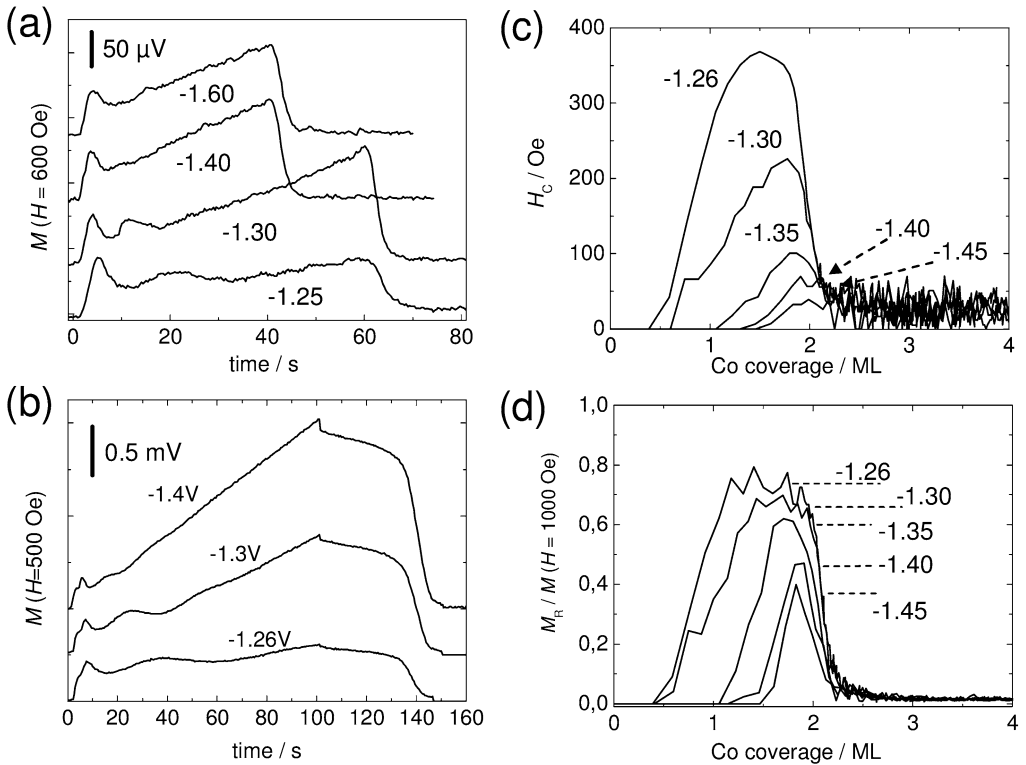


Figure 11.9. Magnetic properties of Co/Au(111) layers. (a) *In situ* AGFM transients of magnetization M -time recorded at different potentials (as indicated in the figure). The field is applied perpendicular to the surface ($H_{\perp} = 600$ Oe). The first peak indicates out-of-plane magnetization. A reorientation transition out-of-plane \rightarrow in-plane magnetiza-

tion occurs above 10 s (after Ref. [62]).

(b)–(d) *In situ* MOKE measurements: Transients M -time at different potentials (b); thickness dependence of H_C (c) and M_R/M ($H = 1000$ Oe) (d) (after Ref. [63]). Notice the potential dependence of the maximum of H_C and of the rise of the M_R/M ($H = 1000$ Oe) (potentials are indicated in the figure).

potential and its maximum corresponds always to an equivalent cobalt thickness of ~ 1.6 ML or a surface coverage 0.8 (the first Co islands are biatomic, see STM observations in Fig. 11.8). *In situ* AGFM hysteresis cycles (not shown) showed that for a Co thickness < 1.6 ML, M is strictly perpendicular to the surface, which is consistent with the fact that the M -time peak amplitude is independent of the applied field. They also show that the peak maximum corresponds also to $M_R/M_S \sim 0.7$, i.e., the Co thickness at the peak maximum is t^* . After the peak, the hysteresis cycles are linear and reversible, indicating an in-plane magnetization. In correspondence, M presents a linear dependence as a function of time as expected from Eq. (11.10). The mean slope is relatively large because of the large K_1 and K_2 values of cobalt. A close inspection of the transients M -time evidences

a second peak when $-1.4 \text{ V} < U < -1.2 \text{ V}$, which is discussed below. The maximum corresponds to 2.6 ML of cobalt. The same transient measurements in the thiocyanate-containing solution also give a peak of perpendicular magnetization, whose maximum corresponds to 4.4 ML [16].

The bottom of Table 11.1 compares the t^* values for Co/Au(111) layers grown in different solutions, determined as the thickness corresponding to the peak maximum of the M -time transient. K_S was then calculated by inverting Eq. (11.8). t^* (or equivalently K_S) is drastically smaller than in the case of capped layers. The decomposition $K_S = K_S^{\text{Down}} + K_S^{\text{Up}}$ evidences that the difference in K_S is due to the upper interface because the anisotropy of the Co/Au interface (K_S^{Down}) is identical for the different systems. The negative value of K_S^{Up} in the sulphate-containing solution means that the cobalt/solution interface tends to align M in the plane of the sample. In the thiocyanate-containing solution, K_S^{Up} is also negative but its contribution is smaller. This difference between the K_S^{Up} values in the sulfate and the thiocyanate solutions might be due to the different Co deposit morphologies. However, we checked that introducing thiocyanate species in the sulfate solution after the deposition of 3–4 ML of cobalt is enough to induce a reorientation transition in-plane \rightarrow out-of-plane of M . This is a direct proof that specific thiocyanate adsorption on cobalt has a strong influence on the overall PMA. Nevertheless, its contribution to PMA remains smaller than that of a Cu capping (see Table 11.1).

One intriguing result derived from AGFM transient measurements is that each of the two peaks in the M -time transient (Fig. 11.9(a)) corresponds to a cobalt thickness (1.6 ML and 2.6 ML) that is independent of the deposition potential. It is difficult to address the origin of the peaks without complementary information. Moreover, no correlation was possible between the observed magnetic behavior and, for example, the size of the Co islands, which depends critically on the deposition potential, as shown by STM. Such details are important to understand the magnetic properties of the electrodeposited Co films, and might be accessed by determining the ratio M_R/M_S as well as the coercive field (H_C) as a function of the Co coverage. The high sampling rate of our MOKE set-up allows the acquisition of hysteresis cycles every 0.5 s and thus gives access to the full cycle at every stages of the growth.

The result of the analysis of a complete sequence of M - H loops is presented in Fig. 11.9(b)–(d). The magnetisation curves at a 500 Oe applied magnetic field as a function of the deposition time present the same features as those obtained by AGFM (Fig. 11.8(b)). This similarity indicates that the data correction we perform to extract the MOKE magnetic signal is quite reliable and correct. The coverage dependence of H_C is a bell curve: starting from zero, H_C goes through a maximum for a coverage ≤ 2 ML, corresponding to the first AGFM peak (Fig. 11.9(a)) and returns to 0 above ~ 2 ML (Fig. 11.9(c)). The key information is that the maximum of H_C increases from 40 Oe to 370 Oe when the deposition potential varies between -1.45 V and -1.26 V , i.e. when the mean size of the Co biatomic islands decreases as observed by STM (Fig. 11.8). The wider the islands the larger is H_C . This behavior resembles that of particles that are small enough (less than 10–100 nm) to be

considered as a macro-spin [64]. However, this kind of direct correlation is difficult because the magnetic interaction energy between neighboring Co islands as well as the magnetic anisotropy should be taken into account for a correct description of this behavior. The second important information is the variation of M_R/M_S with the Co coverage and the deposition potential. Bell curves are again observed: M_R/M_S increases from zero, reaches a saturation value and returns to 0 above ~ 2 ML (Fig. 11.9(d)). The decrease in the maximum value for deposition potentials lower than -1.4 V may be assigned to the fact that the third atomic cobalt plane nucleates atop the Co bilayer before this latter is completed. Trilayer Co islands are indeed expected to have an in-plane magnetization. Another intriguing behavior is that the onset of the rise of M_R/M_S depends on the deposition potential. This onset corresponds to a Co coverage, or equivalently, a Co mean island size, below which the remnant magnetization is zero. In other words, the Co islands must reach a critical size to be ferromagnetic at room temperature. It is reached for a Co coverage of ~ 0.5 ML at -1.26 V and of ~ 1.5 ML at -1.45 V. This is again consistent with the STM observations, because the Co island size decreases with increasing overpotential (Fig. 11.8(a) and (b)). Other studies of the magnetism of small Co particles support this conclusion [65].

The last point to be addressed is the origin of the two peaks in the magnetization transients (Fig. 11.9(a) and (b)). We will not go into the details of the explanation of the first peak because it involves a reorientation of the magnetization, which adds some complication. We only focus on the second peak, which corresponds to a situation where the magnetization is always in the plane, which eases the discussion. Indeed, after the first peak of magnetization the $M-H$ loops (not shown) are strictly linear and therefore pertain to the in-plane orientation of M . Since the cobalt thickness is proportional to time after the growth of the first Co bilayer (see Fig. 11.8(c)), a *linear M-time* plot should be expected from Eq. (11.10). The presence of a second peak indicates therefore a nonlinear dependence of M on the Co thickness. One plausible interpretation is that the anisotropy mainly depends on the number of Co atoms located at the edges of the Co islands composing the third atomic layer. Indeed, during the two-dimensional growth of the third cobalt plane observed by STM [56] the number of step atoms presents a bell dependence with the atomic plane coverage. Recent UHV studies have evidenced a stronger anisotropy of step Co atoms deposited on Pt(111) [31].

11.3.4

Fe/Au(111)

11.3.4.1 Morphology and Structure

Iron MBE growth on reconstructed Au(111) was investigated by STM [48, 49]. Similarly to Ni and Co, Fe clusters nucleate on Au(111) reconstruction elbows and a metastable *pseudomorphic* fcc γ -Fe(111) monolayer (12% strain) is formed (the γ -Fe phase is thermodynamically stable in the temperature range 910–1400 °C). Subsequent iron growth is not layer by layer and the resulting films are rough. Rectangular features are observed above 3.2 ML. This was interpreted as a structural tran-

sition $\gamma\text{-Fe}(111) \rightarrow$ of bcc or $\alpha\text{-Fe}(110)$ because the $[100]_{\text{bcc}}$ lattice spacing of bcc Fe (2.87 Å) is quite close to the $[1-10]_{\text{fcc}}$ Au lattice (2.88 Å). On Cu(111) the same transition occurs for 2.3 ML [66].

In situ STM observations of Fe electrochemical growth on Au(111) show that the growth is 3D for $U > -1.45$ V and 2D for $U < -1.45$ V [67]. We hereby focus on the 2D growth at -1.5 V. The process begins with the formation of 1 ML thick anisotropic features which expand laterally (not shown), whose height is 2.3 Å, in agreement with UHV-STM observations [48, 49]. The absence of moiré pattern on the first 2–3 ML (Fig. 11.10(b)), suggests *pseudomorphic* growth, in analogy with MBE layers, and subsequent growth is nearly a layer-by-layer process, as shown by

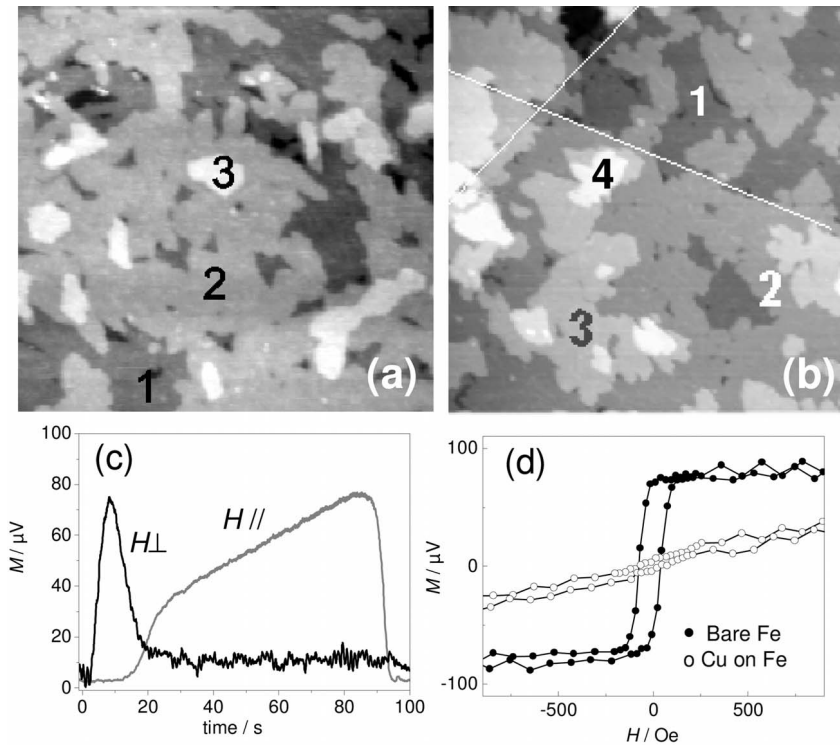


Figure 11.10. Growth and magnetic properties of Fe/Au(111) layers in 1 mM FeSO_4 solution of pH 3.5. *In situ* STM images ≤ 2 ML-thick (a) and ~ 3 ML-thick (b) iron films. Numbers in images are the local thickness in ML (after Ref. [67]). Frames are respectively $1000 \times 1000 \text{ \AA}^2$ and $2300 \times 2300 \text{ \AA}^2$. (c) *In situ* AGFM transients of magnetization with the field perpendicular (black line) and parallel (grey line) to the surface

($H = 600$ Oe in both cases). Note the reorientation transition out-of-plane \rightarrow in-plane magnetization (after Ref. [70]). (d) Hysteresis loops $M-H$ recorded *in situ* of a 2 ML-thick Fe/Au(111) layer before (\bullet) and after (\circ) Cu capping (after [Phys. B 2004]). The field is applied perpendicular to the surface. Note the transition out-of-plane \rightarrow in-plane reorientation upon Cu deposition.

the film morphology in Fig. 11.10(a) and (b). At these coverages, the morphology of electrodeposited films is much smoother than that of MBE layers. In addition rectangular features are not observed below 5 ML. The structural transition $\gamma\text{-Fe}(111) \rightarrow \alpha\text{-Fe}(110)$ seems therefore to appear later than in the UHV.

11.3.4.2 Magnetic Properties

In the UHV, MBE Fe ultrathin films deposited on Au(111) undergo a reorientation transition out-of-plane \rightarrow in-plane of the magnetization around 2.8 ML. The process seems therefore strongly correlated with the structural transition $\gamma\text{-Fe}(111) \rightarrow \alpha\text{-Fe}(110)$ occurring around 3 ML [68]. The same process is observed in the case of Fe/Cu(111) layers [66]. The smaller t^* -value of 2.3 ML for Fe/Cu(111) correlates with the reduced tensile strain in the case of Cu (the mismatch between $\gamma\text{-Fe}$ and Cu is $<1\%$ against 12% with Au). Figure 11.10(c) presents M - $time$ transients recorded with the field perpendicular ($H_{\perp} = 600$ Oe) and parallel ($H_{\parallel} = 600$ Oe) during iron electrodeposition at -1.5 V. Note that the almost nonexistent slope in the M_{\perp} - $time$ after the peak is consistent with the greater M_S value and the smaller K_1 value for iron (Eq. (11.10)). The comparison of the two transients with H_{\perp} and H_{\parallel} pertains to a transition out-of-plane \rightarrow in-plane of the magnetization for a coverage of ~ 2 ML [38, 39], a value which is smaller than that obtained for MBE layers (2.8 ML) (Table 11.2). The difference with respect to MBE layers is, however, that the magnetization reorientation transition (2 ML) occurs *before* the structural transition $\gamma\text{-Fe}(111) \rightarrow \alpha\text{-Fe}(110)$ at 5 ML, which indicates that the Fe/solution interface contributes to align M in the plane, as in the case of cobalt layers. A further difference with MBE films concerns the M - H loops, which are open and square down to an iron coverage of 1.5 ML ($M_R/M_S \sim 1$); by comparison S-shaped loops with $M_R/M_S \ll 1$ are obtained for 1.5 ML-thick MBE layers [68]. The Curie temperature of 1.5 ML-thick layers must therefore be higher for electrodeposited layers than for MBE layers. Above 2 ML, reversible loops are measured. Inverting Eq. (11.8) yields an interface anisotropy constant $K_S \sim 0.72$ erg cm^{-2} (Table 11.2).

We studied the effect of capping a 2 ML-thick Fe/Au(111) layer with a Cu overlayer. Figure 11.10(d) shows two M - H loops recorded with the field applied per-

Table 11.2. K_S and t^* values of Fe/Au(111) layers.

Structure ^[a]	t^*/ML	$K_S/\text{erg cm}^{-2}$
Solution/Fe/Au(111) (ED, -1.5 V) [70]	2.8	~ 0.72 ^[b]
UHV/Fe/Au(111) [68]	2	–
Cu/Fe/Au(111) (ED, -1.5 V) [67]	–	~ 1
Cu/Co/Au(111): MBE multilayer [3]	–	0.72

^a MBE = molecular beam epitaxy; ED = electrodeposition. ^b Value estimated from reversible hysteresis loop (see procedure in Ref. [15]).

pendicular to the surface. The bare layer presents a square and open loop (filled symbols), which means a strictly perpendicular easy axis of magnetization. After Cu capping the magnetization is in-plane since a reversible hysteresis is observed (open symbols). Likewise for MBE Cu/Fe/Au(111) layers [69] reversible hysteresis loops with no remnant magnetization and a small coercive field are obtained with electrodeposited layers. Their analysis yields an anisotropy constant $K_S \sim 1$ erg cm⁻² somewhat larger than the 0.72 erg/cm² measured with Fe/Au(11) multilayers [3]. Table 11.2 summarizes the magnetic anisotropy of different Fe/Au(111) layers. The origin of the rotation of the magnetization easy axis after Cu deposition may be related to structural changes, like the partial strain relaxation of the pseudomorphic γ -Fe layer, upon Cu deposition.

11.4

Concluding Remarks

This chapter demonstrates that electrodeposition is a very suitable technique for growing epitaxial ultrathin magnetic layers on well defined electrode surfaces. In particular *in situ* STM imaging gives valuable information, demonstrating that clean and sharp interfaces are obtained, which was a critical issue in controlling the magnetic anisotropy of such systems. Ni(111), Co(0001) and γ -Fe(111) epitaxial layers are grown by being electrodeposited on Au(111). The morphology of electrodeposited films appears to be much smoother than that of corresponding MBE layers because of a different growth mechanism at the electrochemical interface: the step-flow like mechanism is not observed in the UHV. Instead the nucleation is driven by place exchange in that case, which results in rough layers. An additional favorable factor might be the H-termination of the surface, which enhances adatom mobility and therefore flattening of the topography. Indeed, hydrogen evolution takes place during metal deposition. However, in the case of Ni, hydrogen evolution induces hydrogen incorporation which reduces the magnetization.

From a magnetic viewpoint, these studies have also demonstrated the importance of performing *in situ* characterizations, to investigate in real time the properties of ultrathin layers without capping with a noble metal. In that respect the larger sampling rate of MOKE allows recording of $M-H$ loops during the deposition and yields more complete information. Thanks to *in situ* magnetic measurements, the strong influence of surface chemistry could be evidenced for the first time at ambient in the case of cobalt. After capping with a metal overlayer, the electrodeposited sandwiched Co and Fe layers present an anisotropy constant K_S which is comparable or larger than for MBE layers.

Future perspectives include exploiting further the potential of electrochemistry in the preparation of advanced multilayers and the development of technologically relevant substrates. For instance we have obtained Au(111)/Si(111) buffer films, which can be prepared either ultraflat or divided into a large density of Au(111) dots decorating the steps of a vicinal Si(111) surface [71]. These Au layers and

dots may be used as templates for the growth of magnetic two-dimensional films or dots [18].

Acknowledgments

It is a pleasure to thank past and present students and colleagues at LPMC and formerly at LISE (CNRS, UPR 15) who contributed to this work, in particular: J. Borges, L. Cagnon, R. Cortès, V. Costa-Kieling, C. Gomes, A. Gündel, P. Prod'homme, G. Savidand and J. Peretti for the MOKE set-up. We are deeply indebted to C. Chappert and T. Devolder (IEF, Université Paris Sud, Orsay) who encouraged us to initiate this research and provided expertise with early magnetic measurements on these systems. Last but not least, we are very grateful to J. E. Schmidt, A. Morrone and J. Geshev (Laboratory of Magnetism, UFRGS, Porto Alegre) who manifested strong interest in the project and with whom we performed the first *in situ* AGFM measurements in Porto Alegre. Equally importantly, we thank the Capes/Cofecub exchange program which made possible an active and long lasting cooperation with LAM.

References

- 1 S. CHIKAZUMI, in *Physics of Magnetism*, John Wiley & Sons, New York (1964).
- 2 D. A. THOMPSON, J. S. BENT, *IBM J. Res. Dev.* **44** (2000) 311.
- 3 M. T. JOHNSON, P. J. H. BLOEMENZ, F. J. A. DEN BROEDER, J. J. DE VRIES, *Rep. Prog. Phys.* **59** (1996) 1409–1458.
- 4 D. SANDER, *J. Phys. Condens. Matter* **16** (2002) R603.
- 5 Y. TANAKA, *J. Magn. Magn. Mater.* **287** (2005) 468; Y. NAKAMURA, *J. Magn. Magn. Mater.* **200** (1999) 634.
- 6 J. I. MARTIN, J. NOGUES, KAI LIU, J. L. VICENTE, IVAN K. SCHULLER, *J. Magn. Magn. Mater.* **256** (2003) 449.
- 7 E. I. COOPER, C. BONHÔTE, J. HEIDMANN, Y. HSU, P. KERN, J. W. LAM, M. RAMASUBRAMANIAN, N. ROBERTSON, L. T. ROMANKIW, H. XU, *IBM J. Res. Dev.* **49** (2005) 103.
- 8 T. P. MOFFAT, D. WHEELER, M. D. EDELSTEIN, D. JOSELL, *IBM J. Res. & Dev.* **49** (2005) 19.
- 9 J. CLAVILIER, R. FAURE, G. GUINET, R. DURAND, *J. Electroanal. Chem.* **107** (1980) 205.
- 10 A. A. GEWIRTH, B. K. NIECE, *Chem. Rev.* **97** (1997) 1129.
- 11 K. ITAYA, *Prog. Surf. Sci.* **1998**, **58**, 121.
- 12 O. M. MAGNUSSEN, *Chem. Rev.* **102** (2002) 679.
- 13 P. ALLONGUE, *Scanning Tunneling Microscopy of Semiconductor Electrodes*, Advances in Electrochemical Science and Engineering, H. GERISCHER, C. W. TOBIAS (Eds.), VCH Publishers, Weinheim, Vol. 4, (1995) 1.
- 14 J. L. BUBENDORFF, E. BEAUREPAIRE, C. MÉNY, P. PANISSOD, J. P. BUCHER, *Phys. Rev. B* **56** (1997) R7120; *Appl. Phys. Lett.* **83** (1998) 7043.
- 15 L. CAGNON, T. DEVOLDER, R. CORTES, A. MORRONE, J. E. SCHMIDT, C. CHAPPERT, P. ALLONGUE, *Phys. Rev. B* **63** (2001) 104419.
- 16 L. CAGNON, A. GÜNDEL, T. DEVOLDER, A. MORRONE, C. CHAPPERT, J. E. SCHMIDT, P. ALLONGUE, *Appl. Surf. Sci.* **164** (2000) 22.
- 17 A. GÜNDEL, L. CAGNON, C. GOMES, A. MORRONE, J. E. SCHMIDT, P. ALLONGUE, *Phys. Chem. Chem. Phys.* **3** (2001) 3330–3335.

- 18 P. ALLONGUE, F. MAROUN, *J. Phys. Condens. Matter* **18** (2006) S97.
- 19 Y. HENRY, A. IOVAN, J. M. GEORGE, L. PIRAUX, *Phys. Rev. B* **66** (2002) 184430.
- 20 C. A. ROSS, S. HARATANI, F. J. CASTAÑO, Y. HAO, M. HWANG, M. SHIMA, and J. Y. CHENG, B. VÖGELI, M. FARHOUD, M. WALSH, H. I. SMITH, *J. Appl. Phys.* **91** (2002) 6848.
- 21 L. SUN, Y. HAO, C.-L. CHIEN, P. C. SEARSON, *IBM J. Res. Dev.* **49** (2005) 79.
- 22 P. N. BARTLETT, P. R. BIRKIN, M. GHANEM, *Chem. Comm.* (2000) 1671.
- 23 D. M. KOLB, R. ULLMANN, T. WILL, *Science*, **275** (1997) 1097; G. E. ENGELMANN, J. C. ZIEGLER, D. M. KOLB, *Surf. Sci.* **401** (1998) L420.
- 24 F. J. HIMPEL, J. E. ORTEGA, G. J. MANKEY, R. F. WILLIS, *Surf. Sci. Rep.*, **47** (1998) 511.
- 25 M. F. DOERNER, R. L. WHITE, *MRS Bull.*, September, (1996) 28.
- 26 T. SUZUKI, *MRS Bull.*, September, (1996) 42.
- 27 J. HONG, R. Q. WU, J. LINDNER, E. KOSUBEK, K. BABERSCHKE, *Phys. Rev. Lett.* **92** (2004) 147202.
- 28 D. SANDER, W. PAN, S. OUAZI, J. KIRSCHNER, W. MEYER, M. KRAUSE, S. MÜLLER, L. HAMMER, K. HEINZ, *Phys. Rev. Lett.* **93** (2004) 247203.
- 29 P. GAMBARDILLA, S. RUSPONI, M. VERONESE, S. S. DHESI, C. GRAZIOLI, A. DALLMEYER, I. CABRIA, R. ZELLER, P. H. DEDERICHS, K. KERN, C. CARBONE, H. BRUNE, *Science* **300** (2003) 1130.
- 30 P. GAMBARDILLA, A. DALLMEYER, K. MAITI, M. C. MALAGOLI, S. RUSPONI, P. OHRESSER, W. EBERHARDT, C. CARBONE, K. KERN, *Phys. Rev. Lett.* **93** (2004) 077203; P. GAMBARDILLA, M. BLANC, L. BURGI, K. KUHNKE, K. KERN, *Surf. Sci.* **449** (2000) 93.
- 31 S. RUSPONI, T. CREN, N. WEISS, M. EPPLE, P. BULUSCHEK, L. CLAUDE, H. BRUNE, *Nature Mater.* **2** (2003) 546.
- 32 Z. Q. QUI, S. D. BADER, *Rev. Sci. Instrum.*, **71** (2000) 1243.
- 33 M. FARLE, *Rep. Prog. Phys.* **61** (1998) 755.
- 34 P. J. FLANDERS, *J. Appl. Phys.* **63** (1988) 3940.
- 35 G. PÉNISSARD, P. MEYER, J. FERRÉ, D. RENARD, *J. Magn. Magn. Mater.* **146** (1995) 55.
- 36 P. GRÜTTER, et al., in *Scanning Tunneling Microscopy II*, R. WIESENDANGER, H. J. GÜNTHERODT (Eds.), Springer, Heidelberg, 1992, p. 151; R. PROKSCH, *Curr. Opin. Solid State Mater. Sci.* **4** (1999) 231.
- 37 M. BODE, *Rep. Prog. Phys.* **66** (2003) 523.
- 38 A. GÜNDEL, A. MORRONE, J. E. SCHMIDT, L. CAGNON, P. ALLONGUE, *J. Magn. Magn. Mater.* **226–230** (2001) 1616.
- 39 A. GÜNDEL, T. DEVOLDER, C. CHAPPERT, J. E. SCHMIDT, R. CORTÈS, P. ALLONGUE, *Physica B*, **354** (2004) 282.
- 40 W. SCHINDLER, J. KIRSCHNER, *Rev. Sci. Instrum.* **67** (1996) 3578; *Phys. Rev. B*, **55** (1997) R1989; W. SCHINDLER, O. SCHNEIDER, J. KIRSCHNER, *J. Appl. Phys.* **81** (1997) 3915.
- 41 J. R. HAMPTON, J. L. MARTINEZ-ALBERTOS, H. D. ABRUNA, *Rev. Sci. Instrum.* **73** (2002) 3018; *Langmuir*, **19** (2003) 4309.
- 42 K. M. PODUSKA, S. MORIN, *Rev. Sci. Instrum.* **74** (2003) 4723.
- 43 P. BERTRAND, Thèse de l'École Polytechnique, 1999.
- 44 Z. Q. QIU, S. D. BADER, *Rev. Sci. Instrum.* **71** (2000) 1243.
- 45 R. ZHANG, R. F. WILLIS, *Phys. Rev. Lett.* **86** (2001) 2665; F. HUANG, G. J. MANKEY, M. T. KIEF, R. F. WILLIS, *J. Appl. Phys.* **73** (1993) 6760.
- 46 W. G. CULLEN, P. N. FIRST, *Surf. Sci.* **420** (1999) 53.
- 47 B. VOÏGTLANDER, G. MEYER, N. M. AMER, *Phys. Rev. B* **44** (1991) 10354.
- 48 J. A. STROSCIO, D. T. PIERCE, R. A. DRAGOSSET, P. N. FIRST, *J. Vac. Sci. Technol. A* **10** (1992) 1981.
- 49 B. VOÏGTLANDER, G. MEYER, N. M. AMER., *Surf. Sci.*, **255** (1991) L529.
- 50 P. PRODHOMME, F. MAROUN, P. ALLONGUE, to be published.
- 51 J. O'M BOCKRIS, A. K. N. REDDY, *Modern Electrochemistry*, Plenum Press, New York (1970).
- 52 K. HAUG, Z. ZHANG, D. JOHN, C. F. WALTERS, W. E. PLUMMER, *Phys. Rev. B* **55** (1997) 10233.

- 53 G. HERLICH, F. G. HUDDA, *J. Chem. Phys.* **44** (1966) 1039; R. L. SCHWÖBEL, E. J. CHIPSEY, *J. Appl. Phys.* **37** (1966) 3682; R. L. SCHWÖBEL, *J. Appl. Phys.* **40** (1969) 614.
- 54 A. LACHENWITZER, O. M. MAGNUSSEN, *J. Phys. Chem. B* **104** (2000) 7424.
- 55 F. A. MÖLLER, J. KINTRUP, A. LACHENWITZER, O. M. MAGNUSSEN, R. J. BEHM, *Phys. Rev. B* **56** (1997) 12506; F. A. MÖLLER, O. M. MAGNUSSEN, R. J. BEHM, *Phys. Rev. Lett.* **77** (1996) 3165; *Phys. Rev. Lett.* **77** (1996) 5249.
- 56 P. ALLONGUE, L. CAGNON, A. GÜNDEL, C. GOMES, V. COSTA, *Surf. Sci.* **557** (2004) 41–56.
- 57 E. K. HILL, D. FRUCHART, S. MIRAGLIA, J. TOBOLA, *J. Alloys Comp.* **356–357** (2003) 169.
- 58 G. J. MANKEY, M. T. KIEF, F. HUANG, R. F. WILLIS, *J. Vac. Sci. Technol. A* **11** (1993) 2034.
- 59 V. REPAIN, J. M. BERROIR, S. ROUSSET, J. LECOEUR, *Surf. Sci.* **447** (2000) L152; N. WEISS, T. CREN, M. EPPLE, S. RUSPONI, G. BAUDOT, S. ROHART, A. TEJEDA, V. REPAIN, S. ROUSSET, P. OHRESSER, F. SCHEURER, P. BENCOK, H. BRUNE, *Phys. Rev. Lett.* **95** (2005) 157204.
- 60 F. MAROUN, P. ALLONGUE, unpublished results.
- 61 P. BEAUVILLAIN, A. BOUNOUH, C. CHAPPERT, R. MEGY, S. OULD-MAHFOUD, J. P. RENARD, P. VEILLET, *J. Appl. Phys.* **76** (1994) 6078.
- 62 A. GÜNDEL, C. GOMES, F. MAROUN, J. GESHEV, J. E. SCHMIDT, P. ALLONGUE, in preparation.
- 63 G. SAVIDAND, F. MAROUN, P. ALLONGUE, in preparation.
- 64 J. F. LÖFFLER, J. P. MEIER, B. DOUDIN, J.-P. ANSERMET, W. WAGNER, *Phys. Rev. B* **57** (1998) 2915.
- 65 S. PADOVANI, I. CHADO, F. SCHEURER, J. P. BUCHER, *Phys. Rev. B* **59** (1999) 11887.
- 66 I. SHEN, M. KLAUA, P. OHRESSER, H. JENNICHES, J. BARTHEL, Ch. V. MOHAN, J. KIRSCHNER, *Phys. Rev. B* **56** (1997) 11134.
- 67 L. CAGNON, A. GÜNDEL, F. MAROUN, P. ALLONGUE, to be published.
- 68 O. TOULEMONDE, V. PETROV, A. NAIT ABDI, J. P. BUCHER, *J. Appl. Phys.* **95** (2004) 6585.
- 69 C. CHAPPERT, P. BRUNO, B. BARTENLIAN, P. BEAUVILLAIN, A. BOUNOUH, R. MÉGY, P. VEILLET, *J. Magn. Magn. Mater.* **148** (1995) 165.
- 70 A. GÜNDEL, F. MAROUN, J. GESHEV, J. E. SCHMIDT, P. ALLONGUE, in preparation.
- 71 M. L. MUNFORD, F. MAROUN, R. CORTES, P. ALLONGUE, *Surf. Sci.* **537** (2003) 95.

12 Electrodeposition and Properties of Nanoscale Magnetic/Non-magnetic Metallic Multilayer Films

László Péter and Imre Bakonyi

12.1 Introduction

Driven by technological needs, in the 1980s increased efforts were devoted to improving methods for the preparation of various nanoscale materials including metallic multilayers. Several physical deposition techniques such as evaporation, molecular-beam epitaxy and sputtering were utilized to successfully synthesize multilayers consisting of alternating stacks of magnetic and non-magnetic layers, each having a thickness in the nanometer range. Since films of both the ferromagnetic (FM) Fe-group metals (Fe, Co and Ni) as well as their alloys and the non-magnetic noble elements (Cu, Ag and Au) can be relatively easily deposited by electrochemical methods [1], there was an extended activity also in the field of electrodeposited nanoscale multilayers at the same time (this field was reviewed by Ross [2] up to the early 1990s).

Research on magnetic/non-magnetic multilayers expanded enormously when it was discovered [3, 4] that Fe/Cr multilayers prepared by physical deposition methods can exhibit a very large magnetoresistance effect. This phenomenon was termed “giant” magnetoresistance (GMR) since it was at least an order of magnitude larger than the well-known anisotropic magnetoresistance (AMR) of bulk, homogeneous ferromagnets [5]. It was revealed soon thereafter [6, 7] that sputtered Co/Cu multilayer films can have a similarly large effect even at room temperature and in relatively small fields (≈ 1 kOe). The invention of the spin-valve device [8] utilizing the GMR effect in such nanoscale layered structures then opened the way to applications. Indeed, read-out heads using a GMR spin-valve structure have become a standard in computer hard-disk drives since about 1997. A useful summary of GMR sensor applications can be found in Ref. [9]. Such devices are currently fabricated by one of the physical deposition methods, mainly sputtering.

Research efforts aimed at the production of electrodeposited multilayers with GMR have also been successful. It was demonstrated in 1993 that this relatively simple and cost-effective method is also capable of yielding multilayers exhibiting a large GMR effect, and this finding instigated an extended research activity. Early work was summarized by Schwarzacher and Lashmore [11] and a more recent re-

view [12] of GMR studies on electrodeposited multilayer films provides a complete bibliography of over 90 papers published on this topic by the end of 2004.

The aim of the current overview is to provide a comprehensive introduction to the field of electrodeposition and the properties of magnetic/non-magnetic multilayer films. It was the authors' pronounced intention to offer a didactic insight into the field, putting the emphasis on the production method–property relationship rather than simply listing electrolyte compositions and GMR values in an excessively large number but without a systematic overview. This pursuit will hopefully help one to find one's way in the labyrinth of methods, electrolyte compositions, substrates and layer thicknesses, providing enough guidelines also for the beginners in the field. As far as the properties of nanoscale multilayer films are concerned, this chapter will focus on their structure as well as magnetic and magneto-transport characteristics. It will turn out that all these features are strongly interrelated. The GMR behavior is especially sensitive to microstructural features which, in turn, are determined by the deposition conditions.

It is noted that the electrodeposition of metal and alloy nanowires in porous templates is discussed briefly in Chapter 3. The nanowires can also be electrodeposited such that magnetic and non-magnetic layers alternate along the wire length and these structures can similarly have a GMR effect even larger than in planar multilayer films. There is a vast amount of literature on such multilayered nanowires which is, however, not discussed here and the interested reader is referred to Chapter 3 and to appropriate reviews [11, 13].

12.2

Electrodeposition

Examples of electrodeposition of nanoscale multilayers using a multiple bath method are very scarce. The subsequent deposition of nanoscale layers cannot be performed without the danger of corrosion by repeated immersion into different electrolytes. A system with a rotating cathode combined with a double jet system was the first viable implementation of the multilayer deposition by using alternating electrolytes [14]. Later, various alternating injection methods were also suggested [15, 16]. Nevertheless, the overwhelming majority of nanoscale multilayers have been deposited with the help of a single bath. Therefore, only the single-bath method with aqueous electrolytes will be discussed below. Comparison of the single and dual bath methods can be found elsewhere [2].

12.2.1

Electrolyte Composition

The main components of the electrolytes used for multilayer deposition are the salts of the layer constituent metals. The salt of the less noble metal is usually applied in such a high concentration that the electrolyte is almost saturated with respect to this component. Depending on the actual cation and anion(s), the concen-

tration range of the less noble (magnetic) metal is between 0.6 and 2.3 mol dm⁻³. The relatively high concentration of the less noble metal is important for at least two reasons:

1. The magnetic layer always contains some amount of the more noble non-magnetic metal. If the concentration ratio of the magnetic to non-magnetic metal in the electrolyte is high, the non-magnetic component in the magnetic layer can be decreased to such a level that it does not impact the magnetic properties significantly.
2. At the electrode potentials where the less noble metals (Co, Ni, Fe) can be deposited, hydrogen evolution can also take place (i.e., the free energy change accompanying the hydrogen evolution is negative). The relative importance of the hydrogen evolution can be diminished if the metal concentration is as high as possible.

For the same reason why the concentration of the source compound of the magnetic metal has to be the maximum, the non-magnetic metal has to be applied in a very low concentration, usually between 2 and 50 mmol dm⁻³. Hence, during the formation of the magnetic layer, the amount of codepositing non-magnetic metal can be maintained at a sufficiently low level. The composition range in which the homogeneous alloy of a magnetic and a non-magnetic metal exhibits ferromagnetism can be quite wide. For instance, homogeneous Co–Cu alloys are ferromagnetic down to 33 at.% Co content [17]. However, the non-magnetic metal usually leads to an undesired increase in coercivity. On the other hand, it is difficult to ensure that the magnetic layer is indeed homogeneous, especially when the alloying elements are only limitedly miscible in equilibrium. The consequences of the segregation of the alloying elements will be discussed below, together with the magnetic properties.

It has to be mentioned that when depositing more than one kind of magnetic metal, the composition of the magnetic layer cannot be simply determined from the concentration ratio of the corresponding salts. This is because the codeposition of Fe, Ni and Co takes place in an anomalous manner [18]. The anomalous codeposition means that the metal with lower deposition potential can be codeposited together with the more noble transition metal. Moreover, the molar ratio of the less-noble metal in the deposit is often much higher than the molar ratio with respect to the total amount of magnetic metal salts in the electrolyte. For instance, Co-rich deposits can be obtained by using a Ni-rich electrolyte. It is also worthwhile to note that the composition of the nanoscale magnetic layer is different from that of the bulk magnetic metal deposited at the same conditions with d.c. current. The reason for this deviation is that the mass transport limitation of the deposition of the metal in smaller concentration is pronounced in the case of d.c. deposition, while the depletion of the electrolyte is not significant in the case of pulsed deposition which is interrupted by the deposition of the non-magnetic layer.

Apart from the salts of the metals to be deposited, the electrolyte may have other components. These components are often identical to those applied in d.c. plating processes and can be classified as follows:

1. Ionic compounds that do not take part in any sense in the electron transfer at the cathode, but increase the electrolyte conductivity (for instance, Na_2SO_4). Although such components are usually not essential because of the high concentration of the salt of the magnetic metal, the inactive ionic solute can help to maintain a uniform current distribution.
2. Acids or bases that can ensure the stability of the desired pH. Simple pH regulation without a buffering effect can be performed with the help of a strong acid (such as H_2SO_4) or base (such as NaOH). Weak acids (such as H_3BO_3 or $(\text{NH}_4)_2\text{SO}_4$) are also often used. The role of the weak acid is to prevent hydroxide formation when the electrolyte pH changes in close proximity to the cathode surface. The origin of the pH change is the hydrogen evolution as a side reaction. The importance of the pH stabilization is clearly indicated by the fact that the magnetoresistance of the multilayer deposit proved to be very sensitive to the electrolyte pH in each case studied [19–21]. Although there is no general agreement on the mechanism by which the pH acts as a regulator of the deposit properties, it has been shown that the decrease in pH reduces the Co dissolution from Co-containing deposits [19, 22, 23].
3. Complexing agents. The original idea of applying complexing agents in a plating electrolyte was to make the deposition of a metal possible from a solution in which the metal ion would not be stable or soluble. For instance, complexed alkaline electrolytes can be used for the deposition of metals that form insoluble hydroxides. This concept has so far not been used in electrodeposition of multilayers since practically all studies related to this field applied some more or less acidic electrolytes. Another issue is that in the presence of a complexing agent, the current efficiency is often much higher than without this additive. This can be particularly important in the case of Ni deposition because the overvoltage of the hydrogen evolution is smallest on Ni among the magnetic metals. The complexing agents may also help to bring the deposition potential of the magnetic and non-magnetic metals closer to each other. Although the criterion of the small difference in deposition potentials is rather the prerequisite of the deposition of homogeneous alloys, complex-containing baths developed for alloy deposition are often adapted for multilayer deposition as well. However, it must be mentioned that the increase in concentration of a complexing agent leads to a decrease in the crystallite size of the deposit [24]. This effect is very pronounced when the deposition is carried out by current pulses, and the deposit obtained can even be nanocrystalline [25, 26]. The decrease in crystal size, however, is a disadvantage if the optimization parameter is the magnetoresistance, since the grain boundaries have a large resistivity contribution compared to which the spin-dependent scattering is a smaller and smaller fraction as the grain size is reduced.

4. Surfactants, levelling agents and brighteners. This class of additives (that comprises various organic and inorganic compounds [27]) was developed for the plating industry in order to ensure a bright and even deposit surface. It has been verified that these additives are rather deleterious to the magnetoresistance effect [28–30]. There is no generally accepted theory for the impact mechanism of these additives even for d.c. plating. Possible explanations range from simple physical surface blocking to inhibition of the discharge process [29].

It can be seen from the above that electrolytes suitable for depositing multilayers with GMR have not necessarily been developed from baths used for alloy deposition. This seems quite natural if one takes into account the difference in the optimization target.

12.2.2

Deposition Conditions of the More Noble Layer

Principally, the deposition of the more noble metal can be carried out either by current control or by potential control. Regarding the concentration ratio of the salt of the more noble metal to the other ionic components, one can say that diffusion is the major mass transport process of the more noble metal ions and migration is negligible. Hence, the Nernstian diffusion layer model can be applied. The ion concentration in the vicinity of the cathode is presented in Fig. 12.1 for various deposition conditions.

By applying a current control for the deposition of the non-magnetic metal, the actual layer thickness will certainly be higher than the nominal one (i.e., that calcu-

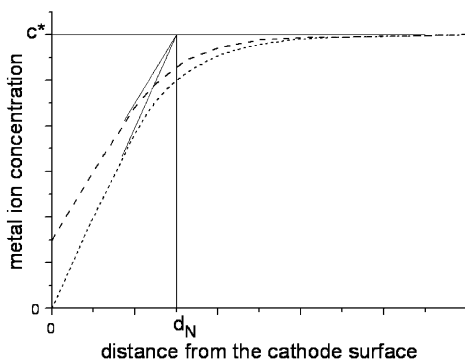


Figure 12.1. Concentration of the ions of the more noble metal as a function of the distance from the cathode surface in steady-state conditions. Dotted line, deposition at the diffusion limited current density; dashed line, deposition below the diffusion limited current density (in both cases, deposition can be controlled either by the current or by applying an appropriate potential). c^* , bulk concentration; d_N , thickness of the Nernstian diffusion layer.

lated from Faraday's law). This is because the leftover ions of the more noble metal (i.e., those not discharged by the fixed current) can oxidize the less noble metal deposited previously. For a Co–Cu/Cu multilayer, this exchange reaction can be written as $\text{Co} + \text{Cu}^{2+} = \text{Co}^{2+} + \text{Cu}$. The reaction stops when the cathode surface becomes completely covered by the more noble metal, regardless of whether the origin of this cover layer is the above described exchange reaction or the electrochemical deposition.

In fact, it is very difficult to maintain accurately the diffusion limited current density by current control. Small concentration fluctuations can lead to either the exchange reaction or the incorporation of the magnetic metal into the non-magnetic layer. Both processes are undesirable. For this reason, potential control can rather be recommended for the deposition of the non-magnetic layer. Nevertheless, remarkably large magnetoresistance ratios can routinely be achieved even by current control [20], although the actual layer thicknesses are usually markedly different from the nominal ones.

In the case of potentiostatic deposition of the non-magnetic layer, the potential can be selected so that dissolution of the previously deposited magnetic layer does not occur. In the most simple approximation, the deposition of the non-magnetic metal should be performed at the rest potential of the less noble metal, as measured in an electrolyte void of the ions of the more noble metal. A more careful potential selection can be performed by analysing the current transients measured during the deposition of the more noble metal [22]. A key figure of this optimization method is presented in Fig. 12.2. Since the standard potential difference between the common magnetic and non-magnetic metals is quite large (several hundreds of millivolts), the deposition of the more noble metal surely takes place in the diffusion-limited current density regime.

The situation can be more complex if the magnetic layer consists of several magnetic elements. In this case, all constituents have different dissolution potentials and whichever conditions are applied for the deposition of the more noble metal, the partial dissolution of the magnetic layer is practically unavoidable. The good strategy in this case is the minimization of the loss of magnetic layer by analysing the current transients. The most simple guideline is that the deposition potential of the more noble metal has to be close to the dissolution potential of the main component of the magnetic layer. A less sophisticated potential selection is also possible if the dissolution of the magnetic layer is hindered: for instance, Ni becomes passive in many electrolytes and hence the potential interval for the deposition of the more noble metal is higher than for non-passivating magnetic layers.

12.2.3

Deposition of the Less Noble Layer

The major constraint for the deposition of the less noble layer is that it has to be magnetic. On the one hand, if the current (or cathodic potential) is too low, the concentration of the non-magnetic metal in the deposit can be so high that the layer does not exhibit ferromagnetic behavior. However, on the other hand, at very

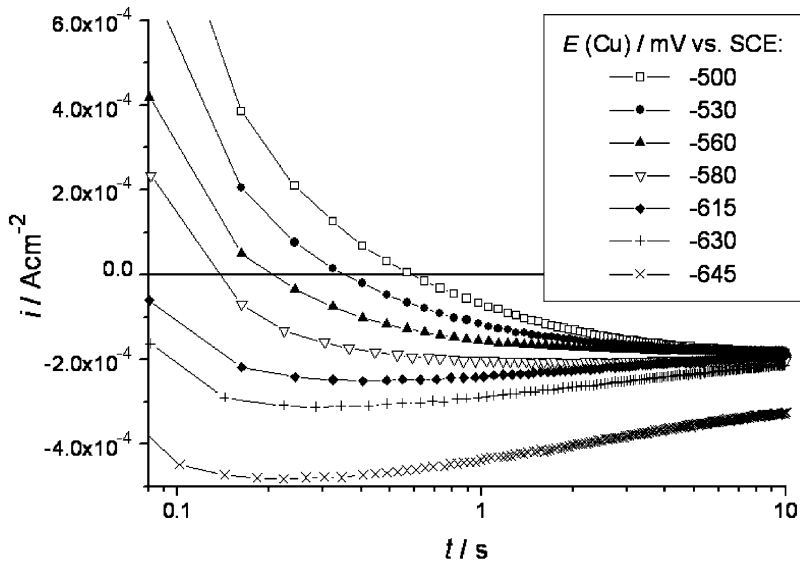


Figure 12.2. Current transients recorded for the potentiostatic Cu deposition pulse during the electrodeposition of Co–Cu/Cu multilayers (reproduced from Ref. 22 with kind permission from Elsevier). Potential intervals: –560 mV or more positive potentials: The initial current transient is long, Co dissolution takes place. –580 mV: Ideal Cu deposition potential. A short and merely capacitive transient can be observed at the beginning of the pulse,

and the cathodic current never exceeds the steady-state current.

–615 mV and –630 mV: Too negative values. Co deposition also takes place at the beginning of the Cu pulse. Co deposition is finished when copper atoms cover the entire electrode surface.

–645 mV or more negative values: Co deposition also takes place in the steady-state.

high current (or cathode potential) the codeposition of hydrogen may be so extensive that finally no magnetic layer is obtained. The fine optimization must also take into account that the mechanical stress in the deposit may depend on the deposition conditions, and the deposit may be spontaneously peeled off from the substrate if the internal stress is too high.

It also may be a problem to overcome the miscibility gap, if any, to obtain a homogeneous magnetic layer at the atomic scale. For instance, Cu is immiscible with Co, and Ag is immiscible with any of the magnetic elements under equilibrium conditions [31]. It is customary to use such electrolytes that promote the formation of metastable solid solutions and not to allow spontaneous separation during the deposition process. If the separation of the elements in the magnetic layer can take place, it gives rise to superparamagnetic behavior (see later).

The deposition mode of the magnetic layer is not as critical as in the case of the non-magnetic layer. Although current control is thought to result in a more uniform layer in the growth direction, potential control also leads to well-defined magnetic layers.

12.2.4

Various Multilayer Deposition Modes

The simplicity of the instrumental background may drive the experimentalist to use the same method for the deposition of each of the alternating layers of a multilayer structure. If both kinds of layers are deposited by current control (or galvanostatic mode, G), the multilayer deposition is termed as G/G mode. Analogously, applying potential control (or potentiostatic mode, P) for the deposition of both layers, it is called the P/P mode. It has been argued [20] that it may be advantageous to use a mixed, G/P mode in which deposition of the magnetic layer is carried out under galvanostatic control and that of the non-magnetic layer under potentiostatic control. Commercially available potentiostats do not usually offer this mixed option which can, however, be realized by using a purpose-made power supply with appropriate computer software control [20]. If the P mode is applied for the deposition of any of the sublayers, the accurate regulation of the sublayer thickness requires that a real time current integration is carried out, while in the G mode the sublayer thickness can be adjusted simply by the pulse length.

Which deposition mode is more suitable for the preparation of multilayers has often been discussed in the literature. In the most recent study on this topic [20], it was found that the deposition parameters in each of the G/G, P/P and G/P modes could be tuned to yield practically the same magnetoresistance curve for electrodeposited Co–Cu/Cu multilayers. However, not necessarily each deposition mode is capable of yielding multilayers with the specific behavior requested. For example, a GMR of about 10% at about 10 kOe can be achieved in Co–Cu/Cu multilayers, even with the G/G mode where the exchange reaction is a very active process of the Cu layer formation. On the other hand, to get the same GMR magnitude in much smaller external magnetic fields (say, in 1 kOe) definitely requires the P/P or G/P mode by which the dissolution of the Co layer can be substantially suppressed. These points will be further elucidated below.

It has also been found [32] that the multilayer deposition mode influences the texture and the microstructure and, thus, indirectly, also the GMR behavior.

12.2.5

Nucleation of the Layers on Each Other

Since the layer thickness in nanoscale multilayers is comparable to the thickness of an atomic monolayer, the layer growth cannot be described with the layer thickness as a simple continuum variable. Although the *average* layer thickness can be accurately controlled down to a fraction of a monolayer by the charge passed through the cathode during the deposition, the uniformity of the layer thickness is not automatically provided. Actually, layer by layer epitaxial deposition is rather rare.

The actual nucleation mode is determined by several parameters. Of great importance are, for instance, the A–A, B–B and A–B interaction free energies (where A and B represent the atoms of the different layers) and the surface free energies at the metal/electrolyte interface. The former is well known and is also related to the equilibrium miscibility of the elements. On the other hand, the latter data are avail-

able for the metal/vacuum interface only [33] and it is difficult to establish them for such a complicated case as the metal/electrolyte interface.

Besides the energetic parameters of the resulting deposit, the kinetic factors also cannot be neglected. While the energetic description of the nucleation can be applied for quasi-equilibrium deposition, the deposition rate during multilayer electroplating can be very high. This is why kinetic parameters such as the surface concentration and mobility of the adatoms and/or the intermediates of the discharge process may also be of importance, since these determine the relative rate of the grain growth and nucleus formation.

The general experience is that the non-magnetic layer has to achieve a critical average thickness in order to ensure a pinhole-free separation of the neighboring magnetic layers. This can be related to the fact that the non-magnetic layer (Cu) is exposed to a compressive stress, and the three-dimensional grain growth is a favorable process as compared to monolayer formation on a surface that is less spacious than the particular crystal surface of pure Cu. For the same reason, a much smaller thickness is sufficient to provide the layer continuity for Co in Co/Cu multilayers. This was revealed from a recent study [34] of electrodeposited Co–Cu/Cu multilayers prepared under conditions completely suppressing the exchange reaction. It has been concluded from the MR behavior and the coercive field values that an average Cu thickness of at least 2.5 nm is required to provide a continuous spacer layer between the magnetic layers. On the other hand, for such thick Cu layers, the multilayer behavior indicated that the magnetic Co–Cu layers remain continuous down to a thickness as small as 1.1 nm. These findings are in line with the results of another study of electrodeposited Co–Cu/Cu multilayers [35] in which continuous spacer layers (and hence significant GMR) developed only for Cu layer thicknesses around 3–4 nm. A minimum sublayer thickness to achieve a full coverage in electrodeposited Fe–Co–Ni–Cu/Cu multilayers was estimated to be 1.5 to 2.2 nm for the magnetic layer on Cu and greater than 3.5 nm for Cu on the magnetic layer [36]. The difference in the critical sublayer thicknesses deduced in the various studies can certainly be attributed to the different deposition conditions. The different nucleation behavior of Co on Cu as compared to that of Cu on Co has also been observed for evaporated Co and Cu layers [37].

The non-uniform layer growth during the electrodeposition of multilayers certainly leads to some undulation of the layer interfaces, although the direct observation of this undulation is very difficult. The undulation of the layers may be partly responsible for the inferior magnetoresistance properties of the electrodeposited multilayers compared to those obtained with some physical methods (see below).

12.3

Properties

12.3.1

Structure

The general rule for the growth of nanoscale multilayers is that a coherent superlattice is obtained [38], in spite of the alternation of layers with different composi-

tions, i.e., with different lattice constants. The formation of a coherent superlattice is easy to elucidate if the components of the layers in elemental form have the same stable crystalline form and the lattice mismatch is small. The typical example is the Ni–Cu pair that both form face-centered cubic (fcc) crystals with a 2% lattice misfit.

Another common case is when the main constituents of the layers can form crystals of the same type, but one of them is metastable. This holds for the Co–Cu pair: Co forms hexagonal close-packed (hcp) crystals at room temperature, but at high temperature the fcc phase is stable. In this case, the Cu layers provide fcc-conform boundary conditions, and the Co layers are also able to adopt this crystalline form since the atomic volume and the total energy of the fcc-Co and hcp-Co phases differ only slightly at room temperature.

Indeed, a well-defined fcc superlattice was observed for electrodeposited Ni–Cu/Cu [21, 39, 40], Co–Ni–Cu/Cu [19, 32] and Co–Cu/Cu [28, 35, 41, 42] multilayers (in the latter system, a few percent fraction with an hcp structure also appears in some cases [41, 42], mainly at the substrate side).

The quality of a multilayer is usually characterized, at least from the structural point of view, by the appearance of satellites on both sides of the major X-ray diffraction (XRD) reflections which was, indeed, observed in many of the reports cited above. These satellites arise due to the bilayer periodicity of the multilayer stacking sequence [38]. It should be noted, however, that the presence of satellite reflections is not at all a prerequisite for the observation of a large GMR. This is exemplified by the work of Kubota et al. [43] on sputtered $\text{Co}_{1-x}\text{Ni}_x/\text{Cu}$ multilayers with $0 \leq x \leq 1$. The authors reported a clear oscillation of both the GMR with the usual large magnitudes and the magnetoresistance saturation field for the whole composition range, whereas the XRD patterns exhibited satellites for Cu layer thicknesses of at least 2.5 nm only and even those satellites were rather faint. It is typical also for electrodeposited multilayers that clear satellites only appear for sufficiently thick Cu spacer layers. A more recent structural study [42] of electrodeposited Co–Cu/Cu multilayers has demonstrated that satellites can be well observed for samples deposited onto smooth Si substrate with thin Ta and Cu seed layers even for the third XRD reflections if the Cu layers are sufficiently thick. However, for multilayers deposited under identical conditions on rough Ti plates, the satellites were completely missing at all Cu layer thicknesses. This study also revealed that the structural quality difference between the two sets of samples, as measured by the appearance of the satellites, does influence to some extent the GMR behavior. However, this influence is manifested not so much in the GMR magnitude but rather in the field dependence, in the sense that multilayers on smoother substrates tend to have lower MR saturation fields. As discussed below, all this means that a better structural quality indicates here a smaller tendency for the formation of superparamagnetic regions in the magnetic layers.

The rule of the formation of a coherent superlattice also holds when the magnetic layer is multicomponent, and some of the elements in the magnetic layer do not have the same crystalline form as that of the non-magnetic “spacer” layer. Simply speaking, the formation of another type of crystal would require a much higher energy than the ordering of the atoms in the magnetic layer in a less favorable manner.

From the viewpoint of structural properties, there is a pronounced difference between the d.c. deposition of an alloy and the pulse-plating of multilayers. First, the d.c. deposit does not exhibit a coherent superlattice, and stable phase(s) of each element can be present. Second, the crystallite sizes in the d.c. deposits and in the multilayers obtained by pulse-plating are markedly different, namely being typically much smaller in the former. Third, while the d.c. deposit consists of randomly oriented small crystals along the growth direction, the multilayers are built up from several hundred nanometer-wide columnar crystals that often extend from the substrate to the electrolyte side and can have a pronounced texture [19, 21, 28, 35, 40–42]. The multilayer texture may vary with substrate orientation as well as with the deposition conditions such as, for example, the deposition mode [32] or the electrolyte composition.

It also has to be noted that the lattice mismatch between the constituent layers can give rise to a significant level of internal stresses, as a result of which the multilayer becomes strained [42, 44]. The degree of strain depends also on the individual layer thicknesses since, evidently, for thick sublayers a part of the stress can relax in the interior of the layers. Such a relaxation cannot occur when both kinds of sublayers have thicknesses of 1 to 3 nm. Therefore, in such cases the multilayer system tries to get rid of the internal stress by forming twin boundaries, by tilting the multilayer planes with respect to the substrate plane or forming smaller grains [32, 40–42].

In multilayer electrodeposition, the growth features are markedly different, depending on whether the substrate is appropriate for an epitaxial growth of the multilayer or not. Of course, in these two cases the resulting multilayer structures will not be the same either, especially as far as a comparison of the substrate side and the solution side is concerned.

If the substrate does not promote epitaxial growth, the multilayer is usually grown to such a thickness that the substrate can be finally removed. This category can be identified as “thick” multilayers. The substrate removal can be performed either by a simple mechanical peeling off procedure or by a more complicated chemical etching, depending on the adhesion to the substrate and the mechanical and chemical stability of the multilayer itself [39]. If the total deposit thickness is higher than 1 μm , the multilayer can be produced in a self-supporting form. Below this limit, the sample has to be fixed to a holder before the removal of the substrate.

If the multilayer is thick, the crystalline properties of the substrate are of minor importance. The deposit growth soon becomes independent of the substrate and will only be determined by the deposition conditions such as the electrolyte composition, electrochemical parameters during the pulses, duty cycle, temperature, and so forth. If the substrate surface does not favor a coherent deposit growth, the deposition starts with a fairly disordered nucleation zone that is followed by a more ordered region with a well-defined texture [41]. The lateral grain diameter in the ordered region is at least an order of magnitude higher than in the initial zone, and the texture is also significantly more pronounced. However, as the deposit is getting thick, the surface roughness increases, and a loss in the preferred orientation can also be observed. In this aspect, the multilayer electrodeposition obeys the

same rules as other deposition processes. Namely, the surface roughness increases with deposition time (i.e., with deposit thickness), and the deposition can be identified as normal or anomalous, depending on the roughness evolution at low length scales [45].

If the deposition is initiated on an appropriate seed layer, the multilayer can readily grow in a quasi-epitaxial way. For instance, the substrate can be a smooth semiconductor wafer with an adhesion layer (Cr, Ta or Ti) and a seed layer (Cu) evaporated onto it. In this case, the surface roughness of the substrate can be very low. The total thickness of the adhesion layer and the seed layer is limited. First, it has to be large enough to ensure continuous coverage and sufficient electrical conductivity for the electrodeposition. Second, it also has to be small enough so that the surface roughness remains similar to that of the semiconductor wafer. Third, it also has to be taken into account that the properties of the deposit will be studied together with the substrate, and hence a thick seed layer may cause a considerable shunting effect during the resistivity measurement. The typical compromise is that the adhesion layer thickness is between 5 and 20 nm, and the seed layer thickness is in the 15–50 nm range.

If the sample is deposited onto a well-defined seed layer, the entire multilayer can be thin. In this case, the growth of the sample can remain epitaxial throughout the total thickness, regardless of whether the texture defined by the substrate is the most favorable or “stable” growth mode for the electrolyte and deposition conditions selected. If the typical bilayer number is between 15 and 50, it is expected that the deviation from the growth mode defined by the substrate will be insignificant.

12.3.2

Magnetic Properties

In magnetic/non-magnetic multilayers with a sufficiently low level of imperfections, conduction electrons in the non-magnetic layers can mediate a coupling between the magnetizations of the neighboring ferromagnetic layers [46]. Depending on the thickness of the non-magnetic spacer, this coupling can be ferromagnetic (FM) or antiferromagnetic (AF) and was found to oscillate with varying spacer layer thickness between the FM and AF type. For Co–Ni/Cu multilayers, for example, a definite AF coupling can be observed at around 1, 2 and 3 nm Cu layer thicknesses [6, 7, 43], with the strength of the coupling rapidly decreasing with increasing Cu layer thickness. In the case of an AF coupling, the magnetizations of the neighboring magnetic layers are aligned antiparallel in the absence of an external magnetic field. A large GMR effect can be observed by applying a magnetic field high enough to ensure a parallel alignment of the layer magnetizations, as will be discussed below.

In an increasing magnetic field, the sublayer magnetizations of AF-coupled multilayers are all gradually aligned along the magnetic field, as depicted in column 3 of Fig. 12.3. The magnetization process does not exhibit a hysteresis since the mag-

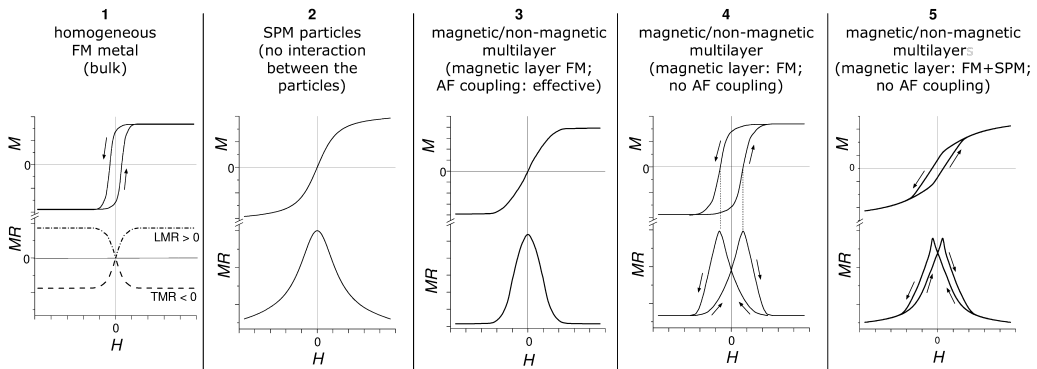


Figure 12.3. Schematic magnetization and magnetoresistance behavior of some magnetic metals and nanostructures. For cases 2 to 5, the LMR and TMR curves are similar in character ($MR < 0$), the saturation value of the TMR being at most 2% larger (in absolute value) than that of the LMR.

netization is zero at $H = 0$. For intermediate Cu layer thicknesses, the coupling is ferromagnetic and typical FM hysteresis loops can be observed here, which is similar to the behavior depicted in column 1 of Fig. 12.3 for a homogeneous bulk ferromagnet. The alternating FM and AF behavior has been well demonstrated for several multilayer systems, for example, for sputtered Co–Ni/Cu [43] and evaporated $\text{Ni}_{83}\text{Fe}_{17}/\text{Cu}$ [47] multilayers. The saturation field (H_s) against the AF-coupling, as evaluated from the magnetoresistance curves of sputtered Co–Ni/Cu multilayers with high Co-content, is about 4 to 5 kOe at around 1 nm Cu spacer layer thickness and rapidly reduces with increasing Ni-content beyond the equi-atomic composition. Thus, H_s reaches a value of about 0.7 kOe for Ni/Cu multilayers whereas it is as low as a few hundred Oe beyond a Cu spacer thickness of 2 nm for all Ni contents [43].

It has also been observed, however, that this ideal behavior is not always obeyed for real multilayers fabricated by any technique (see, for example, Ref. 48 and references therein). The most common deviation is the appearance of a FM hysteresis (Fig. 3, columns 4 and 5) that may occur for several reasons. Thin spacer layers may contain pin-holes through which a local FM coupling may arise at some places. For very thick spacers, the AF coupling may become already very weak and, therefore, the parameters of the individual magnetic layers will dominate the magnetization reversal process. The latter also holds true if the quality of the interfaces between the magnetic and the non-magnetic layers does not permit the development of a substantial AF coupling, even at the optimum spacer layer thickness. A further mechanism leading to FM behavior of the multilayer is the “orange-peel” coupling [35] which is of magnetostatic origin and occurs in multilayers with undulated layer planes or with layer thickness fluctuations. Namely, in such structures the magnetostatic energy is reduced if the magnetic flux lines cross the spacer layer

from a hump of one magnetic layer to a closely spaced valley of the neighboring magnetic layer. Evidently, this will result in an effective FM coupling.

In multilayers with thin magnetic layers, it often happens that some small regions of the magnetic layers become separated (magnetically decoupled) from the rest. Such small regions can exhibit a superparamagnetic (SPM) behavior if their size remains below a critical value [49]. The approach of the magnetization of the SPM regions to saturation can be described with the Langevin function:

$$L(\mu H/kT) = \coth(\mu H/kT) - (\mu H/kT)^{-1} \quad (12.1)$$

where μ is the magnetic moment of an SPM entity. The magnetization curve of an assembly of non-interacting SPM entities is depicted in column 2 of Fig. 12.3.

In electrodeposited multilayers, a FM hysteresis can always be observed. This hints for a weak, if not vanishing, AF coupling between the layer magnetizations. On the other hand, the SPM behavior manifests itself only if the volume fraction of the SPM regions with respect to the FM parts is fairly high, as indicated in column 5 of Fig. 12.3. Also, if the SPM regions are very large and their volume fraction is not significant, their contribution cannot clearly be distinguished from the saturating magnetization of the FM parts of the magnetic layers. The SPM contribution in the magnetization curve is always proportional to the volume fraction of the SPM regions, and thus this contribution can be well separated from the ferromagnetic part (see Fig. 12.4).

An important aspect of the multilayer magnetic characteristics is the coercivity. It is well known for magnetic thin films [49] that the coercive field increases with decreasing film thickness. It was found that this behavior persists also for electrodeposited Co–Cu/Cu multilayers [34].

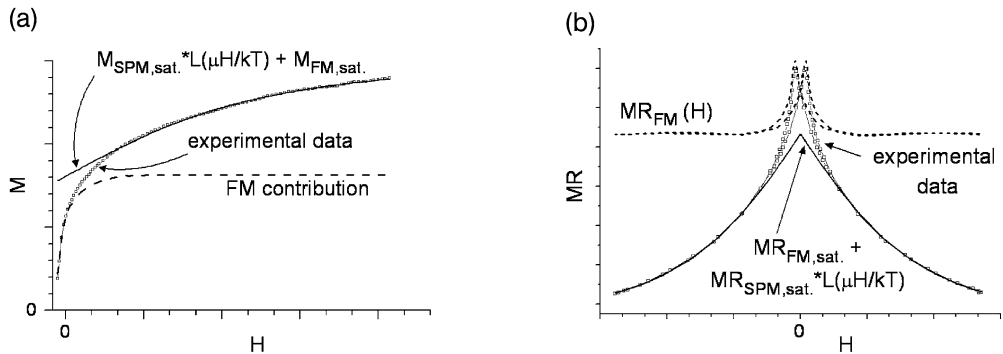


Figure 12.4. Schematic presentation of the decomposition of the magnetization (a) and magnetoresistance (b) into FM and SPM contributions. The separation of the components also offers an opportunity to estimate the size of the SPM entity (μ) that should be identical within the error of the method as obtained from the $M(H)$ and $MR(H)$ curves.

12.3.3

Magnetoresistance

The magnetoresistance is defined as the ratio of the resistivity change due to the external magnetic field to the resistivity measured in zero external field (R_0). It is usually given in percentages:

$$\text{MR}[\%] = 100 \frac{R(H) - R_0}{R_0} \quad (12.2)$$

In some studies, one can also encounter the definition where the normalization is performed with respect to the resistivity at the maximum external field applied. Although R_0 here is formally called the resistivity at zero external field, it may be more appropriate to take the extreme value of the resistance (either maximum or minimum) close to $H = 0$ (this refinement of the definition may be useful for an MR behavior with splitting as a function of H which is the most common case, see columns 4 and 5 in Fig. 12.3).

The magnetoresistance of multilayer films is usually measured in the field-in-plane (FIP), current-in-plane (CIP) configuration. According to the relative direction of the test current (I) and the magnetic field, one can distinguish the longitudinal (L, $H \parallel I$) and the transverse (T, $H \perp I$) magnetoresistance denoted as LMR and TMR, respectively.

Depending on the position of the electrical leads on the multilayer film, the measurement method can be classified as the four-point-in-line method and the van der Pauw method. In the latter mode, the current distribution within the sample is not uniform, and hence there is a slight admixture of the L and T components of the magnetoresistance [11].

The magnetoresistance of a particular multilayer sample depends on several parameters such as the layer thickness, layer composition, undulation of the layers, interface roughness, component distribution within the magnetic layer, and so forth. It has also been found that when the AMR of the magnetic layer material is substantially diminished due to the incorporation of non-magnetic elements, the GMR magnitude of multilayers containing that kind of magnetic layer is also reduced, for example, in Co–Cu–Zn/Cu [50] and Co–Ru/Ru [51] multilayers.

In ideal multilayers in which the magnetic layers exhibit a clear FM behavior with a strong AF coupling, the MR curves exhibit a characteristic bell-shaped field dependence and saturate at a magnetic field necessary to overcome the AF coupling strength (see column 3 of Fig. 12.3).

On the other hand, in a typical granular metal (non-interacting SPM entities embedded in a non-magnetic metallic matrix) the MR curves (column 2 in Fig. 12.3) exhibit a strongly non-saturating behavior. In such cases the field dependence of the magnetoresistance is as follows [52]: $\text{MR}(H) \propto [L(x)]^2$ with the Langevin function $L(x)$ as defined in Eq. (12.1).

If the ferromagnetic layers in a multilayer sample are chemically homogeneous, continuous and sufficiently separated by the non-magnetic spacer layers and there

is only a weak or vanishingly small coupling between the magnetic layers, it can be expected that the magnetic layers will exhibit clear ferromagnetic properties. In other words, the magnetic saturation takes place, in the absence of a significant AF coupling, in the same way as for bulk ferromagnets with identical composition (cf. columns 4 and 1 in Fig. 12.3), and the only difference is that the coercive field is larger due to the thin film effect [34, 49]. In this case, the magnetoresistance curve shows saturation at a similarly small field as the magnetization curve, and the peak position of the MR curve is very close to the coercive field established from the magnetization curve.

A superparamagnetic contribution may arise when some regions of the magnetic layer are magnetically decoupled from the rest of the magnetic layer (see Section 12.3.2). The difficulty in the estimation of the SPM contribution in the magnetoresistance from structural data stems from the fact that the electron scattering probabilities of the FM and SPM regions are not volume-proportional at all but depend on several factors, among which the mutual spatial arrangements of the regions is the most difficult to take into account. Figure 12.5 gives an overview of the magnetoresistance behavior of granular and layered materials with SPM regions. This overview accounts for the character of the magnetoresistance behavior only and is not intended to describe the magnetoresistance value at the saturation.

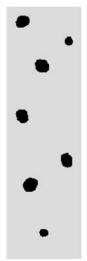




	1	2	3	4	5
					
	SPM	SPM FM	SPM FM	SPM FM	FM
L^2	+	+	+	---	---
L	---	+	+	+	---
MR_{FM}	---	---	+	+	+
	<i>granular materials</i>		?	<i>electrodeposited multilayers</i>	

Figure 12.5. A hypothetical transition from a granular material to a perfect multilayer and the expected magnetoresistance contributions. Structures of types 1 and 2 are obtained during the preparation of granular materials, while structures similar to types 4 and 5 are obtained during the pulse-plating of multilayers. No structure with the intermediate properties (type 3) has yet been identified.

The L^2 -type field dependence of the magnetoresistance in granular systems is related to the fact that both consecutive spin-dependent electron scattering events leading to a GMR effect take place in SPM regions. However, in multilayers the abundance of the SPM regions as compared to the FM regions is much smaller, and hence the consecutive spin-dependent electron scattering events involve at least one FM region. It has been shown for such cases [52] that here the relation $MR(H) \propto [L(x)]$ holds. On the basis of this relation, it was demonstrated that the magnetoresistance of electrodeposited Co–Cu/Cu multilayers could be separated into a FM and a SPM contribution [48]. By this method, one can analyze, via the very sensitive MR measurements, the occurrence of SPM regions in magnetic/non-magnetic multilayers. This is an important progress since the SPM contribution leads to a high saturation field of the magnetoresistance and this results in a reduced magnetic field sensitivity of multilayer field sensor materials. By using the method of optimizing the Cu deposition potential as described in Refs. [20, 22], Gong et al. [36] succeeded in suppressing the formation of SPM regions and thus increasing the GMR sensitivity.

The detailed analysis of the SPM contribution to the magnetoresistance as a function of the preparation parameters performed by Liu et al. [53] for electrodeposited Co–Cu/Cu multilayers suggested that the SPM regions can be visualized as “columnar” objects ranging from one Cu layer to the neighboring one. Another possibility is that the SPM regions responsible for high MR saturation fields are located in the interfacial regions between the magnetic layers, such as depicted in Ref. 54. However, further experimental work is necessary, especially by nanoscale structural and analytical methods, to decide on the actual location and shape of such SPM regions in the multilayer structure.

12.4

Summary

The sections above clearly show that the study of electrodeposited nanoscale multilayers is a highly interdisciplinary field that involves a peculiar blend of electrochemistry and solid state physics. No wonder that many of the articles related to this topic are rather unipolar, depending on whether they deal with mostly electrochemical or physical aspects of the field. However, the preparation conditions and the resulting properties are strongly interrelated. The discussion of the magnetic and magnetotransport properties well demonstrates the interrelation between deposition parameters and deposit properties.

Metallic multilayers in general are often considered as prospective materials because of their favorable mechanical or corrosion properties. These applications can be satisfied with multilayers exhibiting one order of magnitude higher repeat lengths than the electron mean free path where the magnetic and electronic transport phenomena already show the bulk properties. The speciality of the nanoscale multilayers stems from the fact that the repeat length and the electron mean free path are comparable, and this gives rise to properties such as GMR that cannot be observed in the bulk form. This also suggests that if electrodeposited nanoscale

multilayers do come into application, then this might first be expected in the field of sensors based on the GMR effect.

Acknowledgments

This work has been supported by the Hungarian Scientific Research Fund (OTKA) through grants T 037 673 and T 047 094.

References

- 1 A. BRENNER, *Electrodeposition of Alloys*, Vols. I and II, Academic Press, New York, 1963.
- 2 C. A. ROSS, *Annu. Rev. Mater. Sci.* **1994**, *24*, 159–188.
- 3 G. BINASCH, P. GRÜNBERG, F. SAURENBACH, W. ZINN, *Phys. Rev. B* **1989**, *39*, 4828–4830.
- 4 M. N. BAIBICH, J. M. BROTO, A. FERT, F. NGUYEN VAN DAU, F. PETROFF, P. ETIENNE, G. CREUZET, A. FRIEDERICH, J. CHAZELAS, *Phys. Rev. Lett.* **1988**, *61*, 2472–2475.
- 5 R. M. BOZORTH, *Ferromagnetism*, Van Nostrand, New York, 1951.
- 6 S. S. P. PARKIN, R. BHADRA, K. P. ROCHE, *Phys. Rev. Lett.* **1991**, *66*, 2152–2155.
- 7 D. H. MOSCA, F. PETROFF, A. FERT, P. A. SCHROEDER, W. P. PRAIT JR., R. LALOE, *J. Magn. Magn. Mater.* **1991**, *94*, L1–L5.
- 8 B. DIENY, V. S. SPERIOUSU, S. S. P. PARKIN, B. A. GURNEY, D. R. WILHOIT, D. MAURI, *Phys. Rev. B* **1991**, *43*, 1297–1300.
- 9 E. HIROTA, H. SAKAKIMA, K. INOMATA, *Giant Magneto-Resistance Devices*, Springer-Verlag, Berlin, 2002.
- 10 M. ALPER, K. ATTENBOROUGH, R. HART, S. J. LANE, D. S. LASHMORE, C. YOUNES, W. SCHWARZACHER, *Appl. Phys. Lett.* **1993**, *63*, 2144–2146.
- 11 W. SCHWARZACHER, D. S. LASHMORE, *IEEE Trans. Magn.* **1996**, *32*, 3133–3153.
- 12 I. BAKONYI, L. PÉTER, in *Magnetic Materials, Processes and Devices VIII*, S. KRONGELB et al. (Eds.), The Electrochemical Society, PV2004-23, Pennington, NJ, 2006, pp. 227–244.
- 13 L. PIRAUX, A. ENCINAS, L. VILA, S. MATEFI-TEMPFLI, M. MATEFI-TEMPFLI, M. DARQUES, F. ELHOSSINE, S. MICHOTTE, *J. Nanosci. Nanotechnol.* **2005**, *5*, 372–389.
- 14 C. A. ROSS, L. M. GOLDMAN, F. SPAEPEN, *Mater. Res. Soc. Symp. Proc.* **1990**, *160*, 571–576; C. A. ROSS, L. M. GOLDMAN, F. SPAEPEN, *J. Electrochem. Soc.* **1993**, *140*, 91–98.
- 15 N. V. MYUNG, M. SCHWARTZ, K. NOBE, *Plat. Surf. Fin.* **2000**, *87(7)*, 76–82.
- 16 Y. HAYASHI, C. G. LEE, B. H. KOO, T. SATO, M. ARITA, M. MASUDA, *Phys. Status Solidi A* **2004**, *201*, 1658–1661.
- 17 J. R. CHILDRESS, C. L. CHIEN, *Phys. Rev. B* **1991**, *43*, 8089–8093.
- 18 See Ref. 1, Vol. II, pp. 191–193 and pp. 297–298.
- 19 M. ALPER, W. SCHWARZACHER, S. J. LANE, *J. Electrochem. Soc.* **1997**, *144*, 2346–2352.
- 20 V. WEIHNACHT, L. PÉTER, J. TÓTH, J. PÁDÁR, ZS. KERNER, C. M. SCHNEIDER, I. BAKONYI, *J. Electrochem. Soc.* **2003**, *150*, C507–C515.
- 21 M. ALPER, M. C. BAYKUL, L. PÉTER, J. TÓTH, I. BAKONYI, *J. Appl. Electrochem.* **2004**, *34*, 841–848.
- 22 L. PÉTER, Q. LIU, ZS. KERNER, I. BAKONYI, *Electrochim. Acta* **2004**, *49*, 1513–1526.
- 23 P. FRICOTEAUX, J. DOUGLADE, *Surf. Coat. Technol.* **2004**, *184*, 63–68.
- 24 J. W. DINI, *Electrodeposition*, Noyes Publications, Parkridge, NJ, 1993, p. 147.
- 25 H. NATTER, T. KRAJEWSKI, R. HEMPELMANN, *Ber. Bunsenges. Phys. Chem.* **1996**, *100*, 55–64.

- 26 E. TÓTH-KÁDÁR, I. BAKONYI, L. POGÁNY, Á. CZIRÁKI, *Surf. Coat. Technol.* **1997**, *88*, 57–65.
- 27 L. ONICIU, L. MUREŞAN, *J. Appl. Electrochem.*, **1991**, *21*, 565–574.
- 28 S. K. J. LENCZOWSKI, C. SCHÖNENBERGER, M. A. M. GIJS, W. J. M. DE JONGE, *J. Magn. Magn. Mater.*, **1995**, *148*, 455–465.
- 29 E. CHASSAING, *J. Electrochem. Soc.* **2001**, *148*, C690–C694.
- 30 L. PÉTER, Z. KUPAY, Á. CZIRÁKI, J. PÁDÁR, J. TÓTH, I. BAKONYI, *J. Phys. Chem. B* **2001**, *105*, 10867–10873.
- 31 T. B. MASSALSKI (Ed.), *Binary Alloy Phase Diagrams*, 2nd edn. plus updates on CD-ROM, ASM International, Materials Park, Ohio, **1996**.
- 32 Á. CZIRÁKI, J. G. ZHENG, A. MICHEL, Zs. CZIGÁNY, G. NABIYOUNI, W. SCHWARZACHER, E. TÓTH-KÁDÁR, I. BAKONYI, *Z. Metallkde.* **1999**, *90*, 278–283.
- 33 L. Z. MEZEY, J. GIBER, *Jpn. J. Appl. Phys.* **1982**, *21*, 1569–1571; L. VITOS, A. V. RUBAN, H. L. SKRIVER, J. KOLLÁR, *Surf. Sci.* **1998**, *411*, 186–202.
- 34 Q. X. LIU, L. PÉTER, J. TÓTH, L. F. KISS, Á. CZIRÁKI, I. BAKONYI, *J. Magn. Magn. Mater.* **2004**, *280*, 60–74.
- 35 M. SHIMA, L. G. SALAMANCA-RIBA, R. D. McMICHAEL, T. P. MOFFAT, *J. Electrochem. Soc.* **2001**, *148*, C518–C523.
- 36 J. GONG, W. H. BUTLER, G. ZANGARI, *Appl. Phys. Lett.* **2005**, *87*, 012505/1–3.
- 37 Th. ECKL, G. REISS, H. BRÜCKL, H. HOFFMANN, *J. Appl. Phys.* **1994**, *75*, 362–366.
- 38 C. MICHAELSEN, *Philos. Mag. A* **1995**, *72*, 813–828.
- 39 E. TÓTH-KÁDÁR, L. PÉTER, T. BECSEI, J. TÓTH, L. POGÁNY, T. TARNÓCZI, P. KAMASA, I. BAKONYI, G. LÁNG, Á. CZIRÁKI, W. SCHWARZACHER, *J. Electrochem. Soc.* **2000**, *147*, 3311–3318.
- 40 Á. CZIRÁKI, I. GERÓCS, B. FOGARASSY, B. ARNOLD, M. REIBOLD, K. WETZIG, E. TÓTH-KÁDÁR, I. BAKONYI, *Z. Metallkde.* **1997**, *88*, 781–789.
- 41 Á. CZIRÁKI, L. PÉTER, B. ARNOLD, J. THOMAS, H. D. BAUER, K. WETZIG, I. BAKONYI, *Thin Solid Films* **2003**, *424*, 229–238.
- 42 Á. CZIRÁKI, L. PÉTER, V. WEIHNACHT, J. TÓTH, J. PÁDÁR, L. POGÁNY, C. M. SCHNEIDER, T. GEMMING, K. WETZIG, G. TICHY, I. BAKONYI, *J. Nanosci. Nanotechnol.*, **2006**, 2000–2012.
- 43 H. KUBOTA, S. ISHIO, T. MIYAZAKI, Z. M. STADNIK, *J. Magn. Magn. Mater.* **1994**, *129*, 383–388.
- 44 P. BÖDEKER, A. ABROMEIT, K. BRÖHL, P. SONNTAG, N. METOKI, H. ZABEL, *Phys. Rev. B* **1993**, *47*, 2353–2361.
- 45 W. SCHWARZACHER, *J. Phys.: Condens. Matter* **2004**, *16*, R859–R880.
- 46 P. GRÜNBERG, *Acta Mater.* **2000**, *48*, 239–251.
- 47 T. LUCINSKI, F. STOBIECKI, D. ELEFANT, D. ECKERT, G. REISS, B. SZYMANSKI, J. DUBOWIK, M. SCHMIDT, H. ROHRMANN, K. ROELL, *J. Magn. Magn. Mater.* **1997**, *174*, 192–202.
- 48 I. BAKONYI, L. PÉTER, Z. ROLIK, K. KISS-SZABÓ, Z. KUPAY, J. TÓTH, L. F. KISS, J. PÁDÁR, *Phys. Rev. B* **2004**, *70*, 054427/1–10.
- 49 B. D. CULLITY, *Introduction to Magnetic Materials*, Addison-Wesley, Reading, **1972**.
- 50 L. PÉTER, Z. KUPAY, J. PÁDÁR, Á. CZIRÁKI, Zs. KERNER, I. BAKONYI, *Electrochim. Acta* **2004**, *49*, 3613–3621.
- 51 I. BAKONYI, E. TÓTH-KÁDÁR, J. TÓTH, L. F. KISS, L. POGÁNY, Á. CZIRÁKI, C. ULHAQ-BOUILLET, V. PIERRON-BOHNES, A. DINIA, B. ARNOLD, K. WETZIG, *Europhys. Lett.* **2002**, *58*, 408–414; I. BAKONYI, E. TÓTH-KÁDÁR, Á. CZIRÁKI, J. TÓTH, L. F. KISS, C. ULHAQ-BOUILLET, V. PIERRON-BOHNES, A. DINIA, B. ARNOLD, K. WETZIG, P. SANTIAGO, M.-J. YACAMÁN, *J. Electrochem. Soc.* **2002**, *149*, C469–C473.
- 52 B. J. HICKEY, M. A. HOWSON, S. O. MUSA, N. WISER, *Phys. Rev. B* **1995**, *51*, 667–669; N. WISER, *J. Magn. Magn. Mater.* **1996**, *159*, 119–124.
- 53 Q. X. LIU, L. PÉTER, J. PÁDÁR, I. BAKONYI, *J. Electrochem. Soc.* **2005**, *152*, C316–C323.
- 54 I. BAKONYI, L. PÉTER, V. WEIHNACHT, J. TÓTH, L. F. KISS, C. M. SCHNEIDER, *J. Optoelectron. Adv. Mater.* **2005**, *7*, 589–598.

Index

a

accelerator 96, 98ff.
 ac-loop monitoring technique 185
 activity 5
 adatoms 4, 6, 51, 68f., 79, 85
 Ag 3, 17f., 67, 83ff., 100, 102, 106, 174f.,
 196, 215
 Ag(111) 17ff., 35, 36
 Ag_xO 196
 Ag₂S 67, 174f.
 Al 139, 155ff.
 alloys 3, 42, 86, 89ff., 244
 – Co–Al 89ff.
 – Co–Cu 244
 – Ni–Al 89ff.
 – Ni–Fe 3
 – Pd–Au 42
 – phase separation 89
 – Ti–Al 89ff.
 – Zn–Al 86
 – Zn–Au 89
 AlSb 92, 93
 alternating gradient field or force
 magnetometer (AGFM) 223ff., 230, 232
 anion adsorption 81, 83, 94, 179
 anisotropic magnetoresistance (AMR) 242
 anodic barrier film 141
 anodic oxidation 4
 anodic porous alumina 139ff.
 – ideally ordered 148ff.
 – self-ordered 139ff.
 – with 3D periodicity 154f.
 anomalous codeposition 244
 aspect ratio 20, 96
 atomic force microscopy (AFM) 4, 18, 22
 atomic scale contacts 168ff.
 atomic switch 175
 atomistic nucleation theory 9
 Au 62ff., 100, 196, 215

Au(100) 17f.
 Au(111) 35f., 42, 57, 66, 70ff., 83, 84ff., 92,
 119, 130, 132, 134, 218ff.

b

ballistic magnetoresistance (BMR) 182
 Bi 62, 70ff.
biatomic islands 231
 Bi₂Te₃ 196, 200, 202ff.
 1-1'-biphenyl-4-thiol (BPT) 63
 blocking agent 98
 Brownian dynamics (BD) 54f.
 Brownian equation 55
 burst-like dissolution 131f.

c

cathodic overpotential 6f.
 CdS 196
 CdSe 196, 200, 203
 CdTe 3
 classical nucleation theory 8
 cluster stability 40ff., 66
 Co 64, 89, 122, 132, 134, 215, 220, 226, 227,
 230ff., 247, 250f., 253f.
 cohesive energy 41
 competitive adsorption 89ff., 99, 101
 compound semiconductor 92f.
 computer simulation techniques 31
 Coulomb blockade 189
 Cu 3, 35f., 64, 100ff., 174, 196, 209, 215, 220,
 247ff.
 Cu₂O 198
 curvature enhanced accelerator coverage
 (CEAC) 20, 97, 98, 100, 106, 109, 110

d

Damascene processing 103, 109
 DC-loop monitoring system 186
 deposition current 101

- deposit–substrate misfit 17
diffusion-controlled growth 198
diffusion limited current density 125, 246
- e**
effective tunneling barrier height 91
electric field strength 141, 143, 146ff.
electrical double layer 187
electrochemical atomic layer epitaxy (EC-ALE) 19
electrochemical dissolution 6, 125
electrochemical etching 128, 173
electrochemical jet cell 62
electrochemical potential 4
electrochemical step edge decoration (ESED) 195ff.
electrochemical supersaturation 6f.
electrochemical undersaturation 6
electrodeposition 3f., 17
– anodic deposition 4
– cathodic codeposition 3
– cathodic deposition 3
– double-pulse technique 17
electroless deposition 210ff.
electromigration 184
electron beam lithography (EBL) 168
electron transport 177
electrooxidation 204f.
embedded atom method (EAM) 35, 52, 56
epitaxial growth 252
equiconcentration surfaces 123f., 126
equilibrium potential 5ff.
exchange current density 15, 103
- f**
Faraday currents 118
Fe 227, 235ff.
ferromagnetic resonance (FMR) 223
field emission/sputtering 128f.
first order phase transition 6
first-order phase transition 47
focus ion beam (FIB) 168
- g**
Galvani potential 4
galvanic displacement 20
giant magnetoresistance (GMR) 182, 242, 253, 258
glassy carbon 13f.
growth of 3D nanoclusters 15f.
– diffusion control 16
– planar diffusion zones 16
– zones of reduced nucleation rate 16
growth rate 20
- h**
high-electric-field anodization 145, 147
highly oriented pyrolytic graphite (HOPG) 83, 195f.
honeycomb structure 138
- i**
ionic liquids (ILs) 80ff.
– *In situ* electrochemical STM 81f.
– electrochemical properties 80
– interfacial characteristics 80
– potential window 80f.
ionic/electronic mixed conductor 67
– Ag₂S 67
- j**
jump-to-contact 36, 66, 118f., 121
- k**
kinetically controlled growth 198
kink sites 42, 47, 51ff., 210
- l**
Landauer formula 178
Langevin dynamics (LD) 54ff.
Langevin equation 54
layer-by-layer growth mode 20, 57
localized anodic oxidation 22f.
localized electrodeposition 7, 22, 121ff., 131ff.
low-dimensional metal phases 7, 18f., 47, 68, 70
– 0D phases 47
– 1D phases 18f., 47, 70
– 2D phases 7, 18f., 47
– thermodynamics 68f.
- m**
magnetic anisotropy 217f.
– magnetocrystalline anisotropy 217f.
– shape anisotropy 217, 218
– surface anisotropy 218
magnetic force microscopy (MFM) 223
magnetization 220ff., 253ff.
magneto optical Kerr effect (MOKE) 223ff., 232
magnetoresistance 254ff.
magnetostriction coefficient 222
maskless fabrication 214
mechanically controllable break junction (MCBJ) 167, 184
metal dissolution by STM tip electrochemical nanoelectrodes 125
metal–insulator–metal (MIM) structures 23

- MnO₂ 196, 198
 Mo 196
 MOKE microscopy 223
 molecular beam epitaxy (MBE) 219
 molecular dynamics simulations 32f.
 – ab initio 33
 – Cartesian coordinates 32
 – Newton's equation 32f.
 – tip induced local metal deposition (TILMD) 33ff.
 molecular junctions 190
 monatomic steps 18f.
 monolayer electrocatalysts 20
 mononuclear growth 20f.
 Monte Carlo method 37, 38ff., 44
 – Grand Canonical simulations 41
 – (Grand Canonical) simulations 40
 – lattice models 40, 44ff.
 – off-lattice models 40ff.
 – partition function 37f.
 – transition probability 39
 MoO₂ 196, 198f., 203f.
 MoS₂ 196, 202ff.
 multilayers 19
 multinuclear growth 21
- n**
- nanodot arrays 215
 nanodots 208f.
 nanogaps 184ff.
 nanoindentation 150, 212ff.
 nanoparticles 17, 19f., 65, 189, 195, 197, 199
 nanoscale multilayers 242f., 249f.
 nanoscale polyaniline junction switch 188
 nanostructuring 20f., 23f., 67, 118
 nanowires 21, 62f., 83, 195ff., 243
 natural lithography 157, 160
 Nb 23f.
 Nb₂O₅ 23f.
 Nernst equation 5
 Nernst potential 123, 126f.
 Nernstian diffusion layer 246
 Ni 35, 89, 174, 220, 227ff., 250ff.
 n-Si (111):H 132, 135
 nucleation rate 20
 nucleus formation 7ff.
 – active sites 10ff.
 – critical nucleus 8f., 11, 15
 – critical overpotential 17
 – Gibbs–Thomson equation 8f.
 – instantaneous 16f.
 – multiple 16
 – nucleation rate 10ff., 15, 17
 – nucleation work 7, 9
 – progressive 16f.
 – Zeldovich factor 10
- o**
- 1-octadecanethiol (ODT) 63
 order/disorder transition 85
- p**
- Pb 17f., 36, 57, 132, 135, 174, 196
perpendicular magnetization anisotropy (PMA) 217ff., 222, 232
 phase-coherence length 177
 place-exchange 19
 point of zero charge (pzc) 70
 polycarbonate track-etched (PCTE) membrane 62
 potential-induced conductance modulation 179
pseudomorphic growth 236
 p-Si 22
 Pt 20, 196
 Pt(111) 220
 pulse-plating 252, 257
- q**
- quantized conductance 119, 178
- s**
- Sb 92, 196
 scanning electrochemical microscope (SECM) 118, 120f.
 scanning electron microscopy (SEM) 127, 140
 scanning probe microscopy (SPM) 4, 21f.
 scanning surface potential microscopy (SPoM) 211ff.
 scanning tunneling microscopy (STM) 4, 18, 72
 scanning tunneling spectroscopy (STS) 90f., 93
 self-assembled monolayers (SAMs) 63
 self-ordering voltage 142ff.
 self-terminated method 172
 Si 157f., 160f.
 Si(100) 211ff.
 Si(111) 208ff.
 single-atom memory device 181
 SiO₂ 22
 solid state electrochemical reaction 174
 spatial distribution of nanoclusters 13
 spinodal decomposition 86, 89
 standard potential 5
 step edges 21, 63, 90, 195f., 209f., 231
 step sites 51ff.

- STM tip apex 119, 122ff., 129
- STM tip current 118
- STM tip electrochemical nanoelectrodes 120ff.
- STM tip-generated 0D nanocavities 70, 72
- Stranski–Krastanov growth model 70
- stripping 200
- superconducting quantum interference device (SQUID) 223
- superconformal film growth 107ff.
 - shape change simulations 107, 109
 - shape-change simulations 108
 - stability analysis 110f.
- superfilling 96ff.
- superlattices 19
- surface alloying 40, 86ff.
- surfactant mediated growth 19

- t**
- tapping mode atomic force microscopy (TMAFM) 211ff.
- templates 20f., 61ff., 140, 155
- thermodynamic equilibrium 4
- transmission electron microscopy (TEM) 128, 149

- tunneling current 91, 118
- tunneling magnetoresistance (TMR) 182
- twin boundaries 252
- two-step anodization 149

- u**
- underpotential deposition (UPD) 7, 19, 34, 46f., 68, 70ff., 82f., 86
- UPD monolayers 17f., 70
 - commensurate 17f., 70
 - incommensurate 17, 18

- v**
- vibrating sample magnetometer (VSM) 223

- x**
- X-ray magnetic circular dichroism (XMCD) 220

- y**
- Young's modulus 222

- z**
- Zn 86ff.

Related Titles

Ohno, H. (ed.)

Electrochemical Aspects of Ionic Liquids

2005

Hardcover

ISBN 0-471-64851-5

Izutsu, K.

Electrochemistry in Nonaqueous Solutions

360 pages with 150 figures and 62 tables

2002

Hardcover

ISBN 3-527-30516-5

Butt, H.-J., Graf, K., Kappl, M.

Physics and Chemistry of Interfaces

2003

Softcover

ISBN 3-527-40413-9

Hodes, G. (ed.)

Electrochemistry of Nanomaterials

2001

Hardcover

ISBN 3-527-29836-3

Advances in Electrochemical Science and Engineering

Volume 8

2003

Hardcover

ISBN 3-527-30211-5

Wang, J.

Analytical Electrochemistry

2000

Hardcover

ISBN 0-471-28272-3